IDŐJÁRÁS

QUARTERLY JOURNAL
OF THE HUNGARIAN METEOROLOGICAL SERVICE

CONTENTS

****

http://omsz.met.hu/english/ref/jurido/jurido_en.html

VOL. 108 * NO. 1 * JANUARY - MARCH 2004

IDŐJÁRÁS

Quarterly Journal of the Hungarian Meteorological Service

Editorial Office: P.O. Box 39, H-1675 Budapest, Hungary or
Gilice tér 39, H-1181 Budapest, Hungary
E-mail: prager.t@met.hu or *antal.e@met.hu*
Fax: (36-1) 346-4809

Subscription by

mail: IDŐJÁRÁS, P.O. Box 39, H-1675 Budapest, Hungary
E-mail: prager.t@met.hu or *antal.e@met.hu*; *Fax: (36-1) 346-4809*

IDŐJÁRÁS

Quarterly Journal of the Hungarian Meteorological Service
Vol. 108, No. 1, January–March 2004, pp. 1–10

Radiative forcing tendency due to anthropogenic aerosol particles and greenhouse gases in Hungary

Tivadar Feczkó[1], Ernő Mészáros[1] and Ágnes Molnár[2*]

[1]*University of Veszprém, H-8201 Veszprém, P.O. Box 158, Hungary*
[2]*Air Chemistry Group of the Hungarian Academy of Sciences, H-8201 Veszprém, P.O. Box 158, Hungary; E-mail: amolnar@almos.vein.hu*

(Manuscript received March 14, 2003; in final form November 19, 2003)

Abstract—Radiative forcings of aerosol components and greenhouse gases were studied by a box model in Hungary. Direct climate forcing of aerosol was calculated by using chemical, optical, and meteorological data found in the examined region, while the forcing of greenhouse gases was determined by formulas with global constants and regional concentrations. The climatic effects of these species were compared with their forcings estimated for the beginning of eighties. The climatic effect of ammonium sulfate and carbon dioxide varied significantly during the last two decades. Positive forcing of carbon dioxide increased by 60%, while cooling effect of anthropogenic ammonium sulfate aerosol decreased by 45%. That is, both important trace components in the air helped the warming of regional climate during this period.

Key-words: climate forcing, ammonium sulfate aerosol, carbon dioxide.

1. Introduction

Both aerosol and gaseous components can affect the radiation transfer processes in the atmosphere. Thus, aerosol particles influence *directly* the amount of short-wave radiation reaching the Earth's surface. On the other hand, aerosol can change the climate *indirectly* by modifying microphysical properties of clouds which enhances the cloud reflectivity. This implies that increased concentration of aerosol particles serving as cloud condensation nuclei can change the radiative properties and lifetimes of clouds. Consequently, aerosol produces substantial cooling in the climate system.

* corresponding author

In contrast, greenhouse gases absorb the long-wave radiation emitted by the Earth's surface causing warming of the climate. Estimation of such climatic effects has become an important issue during the last decades, since human activities modify both aerosol and greenhouse gas concentration in the air. We have to take into account in this respect, however, that climate forcing of aerosol particles differs significantly from that of greenhouse gases. This is due to the fact that, while greenhouse gases distribute rather uniformly over the Earth, the concentration of aerosol varies spatially and temporally very much owing to its short atmospheric residence time.

It is well known that radiative forcing of greenhouse gases is generally calculated by global models (*Hansen et al.*, 1988; *WMO*, 1999; *IPCC*, 2001). Similarly, a lot of global climate models have been applied to estimate the direct and indirect radiative forcing of anthropogenic sulfate aerosols (*Charlson et al.*, 1992; *Boucher* and *Lohmann*, 1995; *IPCC*, 1994). The regional behavior of aerosol climate forcing was also studied by high resolution regional climate models (*Ekman*, 2002). In a summarizing work, *Myhre et al.* (2001) show how the anthropogenic and natural climate forcing mechanisms have changed globally from the industrial revolution until present days.

Previously, *Práger* and *Kovács* (1988) worked out a radiative-convective model for average hemispheric circumstances. Using this model by adopting it for Hungary, *Mika et al.* (1993) examined the effect of extra aerosol emission, derived from antropogenic and natural sources, on Hungarian atmospheric radiation balance considering different states of carbon dioxide content. Their radiative-convective model adopted for average atmospheric conditions of Budapest used hypothetical aerosol and gas concentration.

In the present paper the direct aerosol forcing by ammonium sulfate and carbonaceous particles is examined for rural air in Hungary. In addition, the variation of sulfate aerosol forcing estimation is compared with the effect of changes in greenhouse gas concentrations during the last two decades. Aerosol properties and most of the forcing parameters are supposed to be representative for Hungary. The estimation of indirect forcing of aerosol particles will be discussed in a future publication.

2. Data used in the study

2.1 The box model

Both radiative-convective models and box models are used for calculating regional climatic effect of atmospheric compounds. In radiative-convective models the vertical distributions of species are taken into consideration, while to estimate the tropospheric average radiative forcing of aerosol and

greenhouse gases, box models can be applied (*Charlson*, 1991). Considering that data demand of box models is not high, and our results from field measurements can be fitted easily into this model, in our study we applied a simple box model to calculate various forcing mechanisms. The box is imagined as the troposphere over Hungary closed by the tropopause. Since several input data (aerosol extinction, carbon dioxide concentration, incoming solar radiation, etc., see later) refer to K-puszta station or its surroundings, representing Hungarian background air, the simplified box is supposed to describe the air mass over Hungary. It is assumed that the net horizontal transport of measured components is zero, that is, the composition of incoming and outgoing air is chemically equivalent. On the other hand, the air mass is vertically well mixed in the box. For estimating climate forcing, aerosol and greenhouse gas field measurements as well as satellite and meteorological data were used.

2.2 Direct forcing of aerosol

In order to estimate the radiative forcing of aerosol components, their chemical and optical properties were examined simultaneously at K-puszta station, in central Hungary. K-puszta station belongs to GAW and EMEP networks, and the concentrations of different atmospheric constituents (aerosol particles, trace gases) are thought to be characteristic of Hungarian background air. To determine the mass extinction coefficient (the extinction caused by unit aerosol mass) of aerosol components, which is necessary for estimation of direct climate forcing (cf. Appendix), mass concentration of aerosol compounds and extinction coefficient were parallel measured. Aerosol samples were collected by a cascade impactor of two stages separating fine and coarse particles with a cut-off diameter of 1 μm. Ammonium sulfate was analyzed by capillary electroforesis (for more details: *Krivácsy* and *Molnár*, 1998), while total carbon was determined by the catalytic combustion method. It must be noted that only samples taken from morning to evening were analyzed considering the fact that aerosol influences the radiation only in daylight. At the same time scattering and absorption coefficients of fine aerosol particles were monitored at K-puszta station. The scattering coefficient was measured by an integrating nephelometer (M 903, Radiance Research Inc., operating at a wavelength of 550 nm), while the absorption coefficient was observed by a continuous light absorption photometer (model PSAP, Radiance Research Inc., operating at a wavelength of 565 nm).

The direct forcing of aerosol particles caused by the scattering and absorption of light, generally produces negative climatic effect, especially in rural air. This is due to the fact that the great majority of the extinction is

caused by scattering (*Mészáros*, 1999) determined by particles having a size comparable to the wavelength of the light. For this reason only fine particles with diameters between 0.1 μm and 1 μm are taken into account. Our measurements and many other information indicate that under these circumstances the so-called optically active fine aerosol is composed mainly of ammonium sulfate and carbonaceous compounds. Ammonium sulfate and organic species take part in scattering processes exerting cooling influence on climate, while black carbon content of aerosol is mostly responsible for absorption, which results in warming.

Applying the simple box model mentioned, the direct radiative forcing of aerosol in Hungarian rural air was estimated. In this model (for more details see *Feczkó et al.*, 2002) both meteorological parameters and aerosol properties (*Table 1*) were considered, as far as possible by applying regional data.

Table 1. Yearly averaged parameters necessary for calculating the direct climate forcing of aerosol

Parameter	Value
F_0' (W m^{-2})	300
A_c	0.70
R_s	0.21
T_a	0.76
β	0.29

The solar energy change in an air column (called climate forcing) was calculated (see the Appendix) by using the following data: incident solar radiation flux at the top of the atmosphere (F_0'), the fraction of the surface covered by clouds (A_c) – the annual values were gained from satellite observations (ERBE, ScaRaB, METEOSAT). The satellite grid we took into account included K-puszta station, where the aerosol measurements (filter sampling, measurements of scattering and absorption coefficients) were made. The albedo of the underlying Earth's surface (R_s) was derived from the estimation of Hungarian Meteorological Service (*Dávid et al.*, 1990). The fractional transmittance of atmosphere (T_a) above the aerosol layer and the upscattered fraction by aerosol (β) were only considered as global averages.

As mentioned previously, in the model average values are applied, although important seasonal variation could be found in the case of incident solar radiation flux, cloud coverage, and surface albedo (see *Table 2*).

The annual average values were composed of considering seasonal variation of these parameters.

Table 2. Seasonal variation of parameters for calculating direct climate forcing of aerosol

	Spring	Summer	Autumn	Winter
F_0' (W m^{-2})	379	439	231	132
A_c	0.750	0.500	0.625	0.875
R_s	0.177	0.213	0.190	0.267

Multiple regression analysis was used to calculate dry mass scattering coefficients of ammonium sulfate and total carbon as well as the mass absorption coefficient of total carbon from chemical and optical data. The results are presented in *Table 3*. The dependence of mass scattering coefficient on the relative humidity was considered on the basis of results on hygroscopic growth of aerosol particles (*Imre,* 2002).

Table 3. Mass extinction coefficients of main aerosol components

Component	Mass scattering coefficient (m^2 g^{-1})	Mass absorption coefficient (m^2 g^{-1})
Ammonium sulfate	6.1 ± 0.7	–
Total carbon	3.2 ± 0.9	1.0 ± 0.2

2.3 Radiative forcing of greenhouse gases

The effect of well-mixed greenhouse gases on climate in the box can be determined by radiative transfer models (*IPCC*, 1994). These type of calculations generally estimates the climatic effect of greenhouse gases by comparing their concentration to the concentration level before the industrial revolution. We applied the simplified expressions (*Hansen et al.*, 1988; see Appendix) for the calculation of radiative forcing due to CO_2, CH_4, and N_2O, as given in *IPCC* (2001). It should be noted that constants of these expressions refer to global conditions. For the calculation concentrations of gases listed in *Table 4* were used. These concentrations of greenhouse gases were measured in K-puszta and Hegyhátsál, Hungary (the data were kindly provided by *L. Haszpra*).

Table 4. Yearly average abundances of greenhouse gases used in the calculation of climate forcing ([a] estimated over the world, [b] measured in Hungary, *not measured)

Gas	Abundance (year 1750)[a]	Concentration (in 1982)[b]	Concentration (in 2000)[b]
CO_2	278	340	373
CH_4	700	*	1873
N_2O	270	*	315

3. Results and discussion

The main goal of this paper is to examine how the climatic effect of main anthropogenic aerosol components and greenhouse gases has changed during the last two decades in Hungary under rural circumstances. It must be noted that the reliability of forcing estimations for these two classes of atmospheric components are very different. While the uncertainty of calculation of forcing by greenhouse gases can be characterized by a factor of 1.2, the total uncertainty factor of aerosol direct effect is about 2.5 (*Penner et al.*, 1994). Furthermore, the uncertainty of aerosol indirect forcing estimation is probably even more larger. Thus, the comparison of climate forcing of aerosol particles and greenhouse gases directly can be considered with caution owing to the big difference in the uncertainty of forcing estimations.

By taking in mind this discussion, direct climate forcing of main aerosol components was calculated. These calculations show that ammonium sulfate particles cause an important direct aerosol effect on climate in Hungarian rural air (*Table 5*). The yearly average of direct forcing of these particles was found to be $-0.95\ W\ m^{-2}$ *for 2000*. Anthropogenic fraction of ammonium sulfate was determined on the basis of previous sulfur budget calculation for Europe (*Mészáros* and *Várhelyi*, 1982), according to which in 1982 about 10% of sulfate particles originated from sulfur gases emitted by natural sources. Taking into account this sulfate concentration, and assuming that the natural contribution did not change substantially, the anthropogenic climate forcing caused by sulfate particles is equal to $-0.82\ W\ m^{-2}$ *for 2000*. The forcing of ammonium sulfate was also examined for the first half of 1980s, when the sulfur dioxide emission was much stronger than at present as the result of different industrial conditions. According to our estimation, the yearly mean value of anthropogenic ammonium sulfate forcing *in the eighties* was about $-1.45\ W\ m^{-2}$ derived from human activities. In the case of direct climatic effect of carbon, we got smaller value (*Table 5*), it was equal to $-0.6\ W\ m^{-2}$ *in 2000* owing to light scattering, which was decreased by about 15% due to warming

effect by absorption. Unfortunately, we have no reliable estimation about anthropogenic fraction of carbonaceous aerosol for Hungary, and in the lack of previous carbon measurements, we are not able to determine its forcing for the beginning of 1980s.

Table 5. Yearly average direct forcing (W m^{-2}) of ammonium sulfate and total carbon in aerosol (* not determined)

	Ammonium sulfate	**Total carbon**
Natural and anthropogenic (in 2000)	- 0.95	- 0.6
Anthropogenic (in 2000)	- 0.82	*
Anthropogenic (in 1982)	- 1.45	*

According to our estimations for greenhouse gases, the positive climate forcings of carbon dioxide, methane, and nitrous oxide are *1.6, 0.5,* and *0.15 W* m^{-2} (*Table 6*), respectively, *in 2000* relative to the pre-industrial situation. The effect of these gases, which have both natural and human sources, are giving about 85 % of total anthropogenic greenhouse effect (see *IPCC*, 2001). The concentration and consequently climate forcing of carbon dioxide has changed substantially during the last two decades, while the increase of the concentration of the other two greenhouse gases did not cause high effect in this period. The anthropogenic forcing of carbon dioxide was estimated to be *1 W* m^{-2} *at the beginning of 1980s.*

Table 6. Yearly average effect (Wm^{-2}) of greenhouse gases (* global estimation)

	Carbon dioxide	**Methane**	**Nitrous oxide**
Anthropogenic (in 2000)	1.6	0.5	0.15
Anthropogenic (in 1982)	1.0	*0.45	*0.10

We can conclude that the change of climatic effect of ammonium sulfate and carbon dioxide was important in particular during the last two decades in our region. It can also be established that in the time interval *between 1982 and 2000 anthropogenic climatic effect of carbon dioxide increased with a factor of 1.6*, while *for ammonium sulfate it decreased nearly by 45%* owing to the concentration variation of these two components. This means that during the last two decades both atmospheric species contributed to the warming of

local climate in this region. It is noted in this respect that *Myhre et al.* (2001) examined worldwide all natural and anthropogenic forcing mechanisms. They found that radiative forcing between 1945 and 1970 decreased somewhat in spite of the increase in greenhouse gas concentrations. The authors referred explained this primarily by the strong sulfur dioxide emission and its conversion to sulfate aerosol. This global trend surely has been even more significant in the region of central-eastern Europe because of the lack of effective air pollution management. Our results show that the impact of aerosols could have been comparable with the forcing of greenhouse gases in the 80s and probably in the previous decades. On the other hand, significant decline of aerosol forcing has occurred in the last years, therefore, increasing warming effect of greenhouse gases can be expected in the near future. This does not mean, however, that high sulfate concentration would be desirable to compensate climatic impacts of greenhouse gases. Other effects of sulfur emissions like acid rain in regional areas and health damages on local urban scale do exclude such a possibility. Thus, the only solution would be the mitigation of the anthropogenic release of greenhouse gases.

Finally, it is noted that the climate forcing of atmospheric species can be converted to temperature change by a factor, which is called climate sensitivity. This factor is considerably variable in the case of different compounds. Its value depends on the feedback mechanisms considered. If the feedback processes are not taken into account, the climate sensitivity is estimated to be 0.3 K W^{-1} m^2 for both aerosol and greenhouse gases (*Hansen et al.*, 1981; *Charlson et al.*, 1991), which means that 1 W m^{-2} variation in the climate forcing changes the average temperature with 0.3 K.

Acknowledgements—The authors are indebted to *L. Haszpra* from Hungarian Meteorological Service for making available the data sets of carbon dioxide, methane, and nitrous oxide concentrations.

This work was financially supported by the Hungarian Scientific Research Fund (OTKA; project number TS 40903), Hungarian Academy of Sciences (AKP; project number 2000-34 2,5), and National Program on Research and Improvement (NKFP; project number 3/005).

APPENDIX

A. Calculation of direct radiative forcing of aerosol:

due to scattering (*Charlson et al.*, 1991):

$$\Delta F_i^s = -F_0' T_a^2 (1 - A_c) (1 - R_s)^2 \beta \tau_i^s, \quad (1)$$

where $\tau_i^s = \alpha_i^s m_i'$, $\alpha_i^s = \alpha_i^{s,RH} f(RH)$ and $m_i' = m_i H$;

due to absorption (*Haywood* and *Shine*, 1995):

$$\Delta F_i^a = F_0' \, T_a^2 \, (1 - A_c)\omega\beta\tau_i^a \, [(1 - R_s)^2 - 2R_s/\beta(\omega^{-1} - 1)], \tag{2}$$

where $\tau_i^a = \alpha_i^a \, m_i'$; ΔF_i is solar energy change (climate forcing) owing to the scattering/absorption; F_0' is the incident solar radiation flux at the top of the atmosphere; T_a is the fractional transmittance of atmosphere above the aerosol layer; A_c is the fraction of the surface covered by clouds. R_s is the albedo of the underlying Earth's surface; β is the upscattered fraction by the aerosol; τ_i is the aerosol optical depth of ith scattering/absorbing component in aerosol. Further: m_i' is the aerosol column burden of the corresponding component, α_i is the mass scattering/absorption coefficient. $\alpha_i^{s,RH}$ is defined as light-scattering efficiency at a low relative humidity; $f(RH)$ is the relative increase in scattering cross section because of humidity change. The column burden of a given aerosol constituent can be determined as the product of mass concentration (m_i) and the corresponding scale height (H). ω is the single-scattering albedo.

B. Calculation of climate forcing of greenhouse gases

due to CO_2:

$$\Delta F = \alpha \, [g(C) - g(C_0)], \tag{3}$$

where C is CO_2 concentration in ppm, α=3.35 (constant), $g(C)$=ln(1+1.2C+ 0.005C^2+1.4 × $10^{-6}C^3$);

due to CH_4:

$$\Delta F = \alpha(\sqrt{M} - \sqrt{M_0}) - [f(M, N_0) - f(M_0, N_0)], \tag{4}$$

where M is CH_4 concentration in ppb, α = 0.036 (constant);

due to N_2O:

$$\Delta F = \alpha(\sqrt{N} - \sqrt{N_0}) - [(f(M_0, N) - f(M_0, N_0)], \tag{5}$$

where N is N_2O concentration in ppb, α = 0.12 (constant),

$$f(M,N) = 0.47 \ln[1 + 2.01 \times 10^{-5}(MN)^{0.75} + 5.31 \times 10^{-15}M(MN)^{1.52}]. \tag{6}$$

References

Boucher, O. and *Lohmann, U.*, 1995: The sulfate-CCN-cloud albedo effect: a sensitivity study with two general-circulation models. *Tellus 47B*, 281-300.

Charlson, R.J., Langner, J., Rodhe, H., Leovy, C.B., and *Warren, S.G.*, 1991: Perturbation of the northern hemisphere radiative balance by backscattering from anthropogenic sulfate aerosols. *Tellus 43AB*, 152-163.

Charlson, R.J., Schwartz, S.E., Hales, J.M., Cess, R.D., Coakley Jr., J.A., Hansen, J.E, and *Hofmann, D.J.*, 1992: Climate forcing by anthropogenic aerosols. *Science 255*, 423-430.

Dávid, A., Takács, O., and *Tiringer, Cs.*, 1990: Distribution of radiative balance over Hungary (in Hungarian). Országos Meteorológiai Szolgálat Kiadványa, No. 66, Budapest.

Ekman, A.M.L., 2002: Small scale patterns of sulfate aerosol climate forcing simulated with a high-resolution regional climate model. *Tellus 54B*, 143-162.

Feczkó, T., Molnár, A., Mészáros, E., and *Major, G.*, 2002: Regional climate forcing of aerosol estimated by a box model for a rural site in Central Europe during summer. *Atmospheric Environment 36*, 4125-4131.

Hansen, J., Johnson, D., Lacis, A., Lebedeff, S., Lee, P., Rind, D., and *Russell, G.*, 1981: Climate impact of increasing atmospheric carbon dioxide. *Science 213*, 957-966.

Hansen, J., Fung, I., Lacis, A. Rind, D., Lebedeff, S., Ruedy, R., Russell, G., and *Stone, P.*, 1988: Global climate changes as forecast by Goddard Institute for Space Studies 3-dimensional model. *J. Geophys. Res. 93*, 9341-9364.

Haywood, J.M. and *Shine, K.P.*, 1995: The effect of anthropogenic sulfate and soot aerosol on the clear sky planetary radiation budget. *Geophys. Res. Lett. 22*, 603-606.

Imre, K., 2002: Study on the higroscopic properties of atmospheric aerosol (in Hungarian). Diplomamunka, Veszprémi Egyetem.

IPCC, 1994: Radiative forcing of climate change. In *Climate Change 1994* (eds.: *J.T. Houghton, L.G. Meira Filho, J. Bruce, H. Lee, B.A. Callander, E. Haites, N. Harris*, and *K. Maskel*). Cambridge University Press, New York.

IPCC, 2001: *Climate Change 2001* (eds.: *J.T. Houghton, Y. Ding, D.J. Griggs, M. Nouger, P.J. van der Linden, X. Dai, K. Maskell*, and *C.A. Johnson*). Cambridge University Press, U.K.

Krivácsy, Z. and *Molnár, A.*, 1998: Size distribution of ions in atmospheric aerosols. *Atmospheric Research 46*, 279-291.

Mészáros, E., 1999: *Fundamentals of Atmospheric Aerosol Chemistry*. Akadémiai Kiadó, Budapest.

Mészáros, E. and *Várhelyi, G.*, 1982: An evaluation of possible effect of anthropogenic sulfate particles on the precipitation ability of clouds over Europe. *Időjárás 86*, 76-81.

Mika, J., Kovács, E., and *Bozó, L.*, 1993: The effect of anthropogenic and natural changes of the atmospheric aerosol content on the radiation balance in the Carpathian basin (in Hungarian). *Beszámolók az 1993-ban végzett tudományos kutatásokról*. Orsz. Meteorológiai Szolgálat, Budapest, 81-89.

Myhre, G., Myhre, A., and *Stordal, F.*, 2001: Historical evolution of radiative forcing of climate. *Atmospheric Environment 35*, 2361-2373.

Penner, J.E., Charlson, R.J., Hales, J.M., Laulainen, N., Leifer, R., Novakov, T., Ogren, J., Radke, L.F., Schwartz, S.E., and *Travis, L.*, 1994: Quantifying and minimizing uncertainty of climate forcing by anthropogenic aerosols. *Bull. Amer. Meteorol. Soc. 75*, 375-400.

Práger, T. and *Kovács, E.*, 1988: Investigation of the climate modifying effects of atmospheric trace gases and aerosol particles by a radiative-convective model (in Hungarian). *Időjárás 92*, 153-162.

WMO, 1999: *Scientific Assessment of Ozone Depletion: 1998*. Global Ozone Research and Monitoring Project. World Meteorological Organization. *Report No. 44*, Geneva, Switzerland.

IDŐJÁRÁS

Quarterly Journal of the Hungarian Meteorological Service
Vol. 108, No. 1, January–March 2004, pp. 11–32

Influence of rain and other meteorological parameters on trace metals in size fractionated particles in polluted urban atmosphere

Antonio J. Fernández Espinosa and **Miguel Ternero Rodríguez**

Department of Analytical Chemistry, Faculty of Chemistry, University of Seville, C. Professor García González s/n, E-41012 Seville, Spain; E-mail: anjose@us.es

(Manuscript received January 3, 2003; in final form June 19, 2003)

Abstract—Relationships between meteorological variables and particles, metals and their size fraction concentrations were determined from samples collected in different climatic situations. Special attention was focused on the effect of rain. Single correlation and multiple regression statistical methods were performed on samples from both rainy and dry days. Coarse particle concentrations diminished linearly when rainfall increased. The metals Fe, V, Ni, Ti, and Mn diminished as well. A substantial concentration effect was produced by the temperature on TSP, Fe, Ti, and Mn concentrations in fine particles. Also, a dispersion effect was produced by the atmospheric pressure on TSP, Mn, Fe, Ti, Ni, and V concentrations in these particles. Besides, there was a dispersion effect by the wind speed on TSP and Cd concentrations. The fine particles and metals between 1.3 and 0.6 micrometers are those best correlated with meteorological parameters. Multiple linear regression was demonstrated to be a powerful tool to explain the particle and metal levels in relation to size distribution and meteorology.

Key-words: size distribution, metals, suspended particles, meteorology, rain, multiple linear regression.

1. Introduction

Suspended atmospheric particles have long lifetimes depending on size and meteorological conditions. Size distribution depends on aerosol sources, but it is also affected by prevailing meteorological conditions. Apart from additional factors, meteorology is the most determinant factor in the removal or dispersion mechanisms of particles and metals in the air. Many studies have

investigated the relationship between meteorological conditions and airborne particles (*Elsom* and *Chandler*, 1978; *Witz* and *Moore*, 1981; *Brooks* and *Salop*, 1983). The latter two used multiple linear regression analyses to relate meteorological parameters to particle and several metal concentrations in the USA, specifically in Los Angeles city and Southeastern Virginia State. We carried out a similar study on particles and lead in Seville (*Melgarejo et al.*, 1986) using single and multiple correlations. The relation between meteorology and particle size distribution has also been the subject of numerous recent and earlier works, such as *Choularton et al.* (1982) in Manchester (UK), *Väkevä et al.* (2000) in Helsinki, and *Despiau et al.* (1996) in a Mediterranean zone of France (Toulon), all of them using single correlations on particles.

To study the nature and magnitude of the meteorology effect on different particle sizes, the first tool is the statistical analysis of correlations (single linear regression). Thus, the first objective is to know, how meteorology influences different sizes, focusing specially on fine particles and toxic metals, which are the most harmful.

As a second important objective, multiple linear regression was considered as a statistical technique for the best information for particle and metal behavior caused by the meteorological parameters.

2. Experimental section

2.1 Measurement sites

This study was done in Seville (38°12'-36°51'N, 4°39'-6°32'W, 10 m a.s.l.), the largest city in southern Spain. Analytical data were obtained from a network of twelve sampling stations already used in our previous works (*Usero et al.*, 1988; *Fernández et al.*, 1999 and 2000). The stations have different traffic intensities and different industrial activities, as well as zones with clean air. Seville is located in the centre of the Guadalquivir Valley, which opens toward the ocean at the base of the triangle that the valley forms.

The city has a warm and dry Mediterranean climate with mean annual temperature of 18°C, rainfall 600 mm, atmospheric pressure 1014 hPa, relative humidity 65%, and wind speed 2 m s^{-1}. Seville is characterized by high temperatures and low wind speeds. Prevalent air currents come from the SW-NE direction. All these data are averaged from the 1961-1990 period (*MMA*, 1997). Predominant winds proceed from the Atlantic Ocean (southwest). Therefore, the situation of this sampling network in Seville

represents the meteorological effects of a Mediterranean zone influenced by the African winds as in other cities of southern Europe.

2.2 Particulate sampling

Atmospheric particles were collected with a high-volume sampler (MCV, Model CAV-A/HF) equipped with a five-stage cascade impactor plus a back-up filter (MCV, Model IC/CAV), which effectively separates the particles. It has the following equivalent cut-off diameters at 50% efficiency (D_p): >10 μm (A particles), 10–4.9 μm (B particles), 4.9–2.7 μm (C particles), 2.7–1.3 μm (D particles), 1.3–0.6 μm (E particles), and <0.6 μm (backup, F particles). For A to E stages, five cut filters (14.2 cm × 14.2 cm) were used, and for the backup filter an uncut filter (20.3 cm × 25.4 cm) was used. Cut and uncut micro-fibre glass filters were purchased from WHATMAN (GF/A).

Granulometric fractions are in accordance with the particle size fraction definitions for health-related sampling (*ISO 7708*, 1995), which defines the fine particles as the fraction below 1 μm. Thus, stages B to F can be associated with PM10 particles, stages D to F with PM2.5 particles, and stages E plus F with PM1 particles (*Fernández et al.*, 2001). The flow rate should be set at the value of 68 $m^3\ h^{-1}$ to get the size separation. The flow rate is calibrated every three months at the Andalusian Reference Laboratory for the Air Quality (LARCA) in Seville.

Care was taken in handling the fibreglass filters in order to avoid contamination problems, and all filter materials and samples were handled within a vertical laminar airflow cabinet, for ensuring air cleanliness standards of class 100 according to Federal Standard 209E.

Forty-one samples were collected in 1996, and three to four samples were usually taken at each sampling station. The sampling time-frame was usually 48 h (about 3264 m^3), and a weekly sample was taken on different days during the following week, so that a possible distorting effect could be avoided.

2.3 Reagents and apparatus

Vertical laminar airflow cabinet with a HEPA filter was from INDELAB (Model IDL-48V). Water bath was from JULABO (Model SW-20C). Centrifuge was from SIGMA (Model 3-15). Standard solutions for metals and acids were from MERCK. Ultra-pure water was from WATERS-MILLIPORE (Milli-Q-grade, Model Plus).

Samples were analyzed for eleven metals (Ca, Fe, Mg, Pb, Cu, Mn, Ti, V, Ni, Co, Cd) by atomic emission spectrometry with inductively coupled plasma (ICP-AES) using a Fisons-ARL 3410 sequential multi-element

instrument. Determinations in the multi-element analysis were done in triplicate for each sample.

2.4 Methodology for the chemical analysis

Samples and blank filters used were stored, treated in a dark room and analyzed individually (A-F) for metal concentrations as in our previous work, *Fernández et al.* (2001). The particle concentration of each stage of suspended particles (FSP) was expressed in μg m^{-3}. The total suspended particles concentration (TSP) was then calculated by summing the particle concentrations of the six fractions (FSP) of each sample.

The metal concentration of each filter (FM) was expressed in ng m^{-3}. The total metal concentration (TM) was then calculated by summing the concentration of the six fractions (FM) of each sample. To differentiate between the different size fractions, these were numbered from 1 to 6, e.g., Fe1 and Fe6 corresponded to the metal Fe collected in stages A and F, respectively.

2.5 Meteorological data

Meteorological data were provided daily by our local service of the National Institute of Meteorology (INM) in Seville. These data correspond to the same periods of each particulate sampling. These values for each sampling correspond to the average hourly data provided throughout the sampling periods. Rainfall values were summed with the hourly data during the sampling period. The meteorological data are represented as follows: precipitation (PP) in mm, ambient temperature (AT) in C, atmospheric pressure (AP) in hPa, wind speed (WS) in m s^{-1}, and wind direction (WD) according to the cardinal points.

In this study we considered the rainy and dry days separately in two matrices, after dividing the "total matrix", which showed some interesting results. The "dry days matrix" was formed by samples collected on non-rainy days, "rainy days matrix" was formed the by samples collected on rainy days.

2.6 Multivariate statistical analyses

On the basis of the results, basic and multivariate statistical analyses were applied to the analytical and meteorological data. For these analyses the STATISTICA (*StatSoft,* 1999) software package was used.

Correlation studies were carried out by applying the simple linear regression (SLR) technique. Because a high correlation coefficient does not necessarily imply linearity, linearity was verified by graphical examination.

Any non-linear case was discarded. The procedure for this not only consisted of choosing the highest correlation coefficients, but also verifying the linearity by observing the linear profile of the points, i.e., the pairs of data x-y. Sometimes, high correlation coefficients do not give a real linearity on a graph, because their line is formed by accumulation of points at the extreme of their linear range and a lone point at the other extreme. In these cases, the correlation coefficients are due to only one sample and not all the experimental data. Outliers are misleading and should therefore be discarded.

Later on, multiple linear regression (MLR) analysis was used to relate the analytical variables, statistically significant in the SLR, to the meteorological parameters, through mathematical multivariate linear functions. For both SLR and MLR, when the correlation coefficient (r) was not sufficiently high, a two-tailed t-test was applied with a 95% confidence level to assess whether $r \neq 0$ was significant. Thus, if the calculated t of the student test was greater than the t tabulated, then r was significantly greater than zero.

From the first calculations of the data, we observed, that in Seville rain is the parameter with the greatest influence on particle and metal levels as opposed to the other parameters. The heterogeneity and distortion factor introduced by the washing effect of the rain makes the conclusions unreliable and justifies the need to treat each situation separately.

The statistical studies took into consideration, firstly, the effect of rain on total suspended particles and total metal concentrations and their size distributions, and secondly, the effect of the remaining meteorological parameters on particle and metal concentrations and their size distributions.

3. Results and discussions

3.1 Meteorological characteristics of the sampling period

During the whole year in 1996, a total of 916.8 mm of rainfall was registered, which represents a considerable increase compared to the previous years (580 mm in 1993, 327 mm in 1994, and 503 mm in 1995). Meteorological parameters recorded only for the sampling period are presented in *Table 1*. The mean rainfall on rainy days was 13.6 mm. Mean wind speed was low, 2.2 m s^{-1}, although it was sufficient to cause the resuspension of soil particles in the air. Depending on maximum values, the effect can reach the dispersion of pollution. It should be noted also, that the temperatures were high. With regard to the frequency of the wind direction, the most common winds were south-westerly or southerly, although, the strongest winds came from the west (*Fig. 1-a*). This was to be expected, because the wind blows up the axis of the Guadalquivir Valley (SW-NE).

Table 1. Mean values of the analytical and meteorological variables corresponding to the sampling period

Variable	Mean	Range	Units	RSD (%)
Meteorological variables				
PP*	13.6	(1.2 - 141.0	mm	167.8
WD	SW	(NW - W)		27.0
WS	2.2	(0.6 - 4.2)	$m\ s^{-1}$	44.3
AT	21.0	(15.3 - 29.8)	°C	20.5
AP	1010.5	(1003.7 - 1018.4)	hPa	0.4
Total and fractionated particle variables				
TSP	78.7	(31.1 - 158.1)	$\mu g\ m^{-3}$	44.0
A	12.1	(3.1 - 27.3)		53.6
B	12.4	(6.6 - 21.1)		33.4
C	4.9	(2.8 - 7.5)		26.9
D	4.0	(2.0 - 6.0)		31.2
E	3.6	(0.8 - 7.1)		46.4
F	41.7	(11.7 - 104.5)		57.0
Total metal variables				
Ca	2956	(345 - 8680)	$ng\ m^{-3}$	81.6
Fe	689	(131 - 1974)		58.3
Mg	366	(200 - 669)		29.2
Pb	97	(15 - 1335)		60.0
Cu	28.0	(8.3 - 74.2)		51.5
Mn	19.8	(4.1 - 141.0)		52.6
Ti	7.4	(1.7 - 16.9)		52.0
V	5.9	(0.6 - 18.0)		76.5
Ni	1.97	(0.47 - 4.31)		58.9
Co	0.56	(0.09 - 2.01)		76.7
Cd	0.44	(0.09 - 4.73)		61.4

*: Mean rainfall on rainy days, RSD: Relative standard deviation in percentage, WD: wind direction

The relationship between wind speed, rainfall, atmospheric pressure, and temperature is an important climatic feature. Thus, the correlation analysis is a good tool, because it shows meteorological behavior, for example, the well known relations between the rain, the decrease of temperature and atmospheric pressure, and the increase of wind speeds. Other results show that mild warm winds come from the south (proceeding from Africa) and slightly less warm winds from the Southwest (the Atlantic Ocean). The coldest winds are also the

strongest, those coming from the west (the Atlantic Ocean crossing Portugal). The highest rainfall values are correlated with south-westerly winds, because the moisture easily penetrates into the valley.

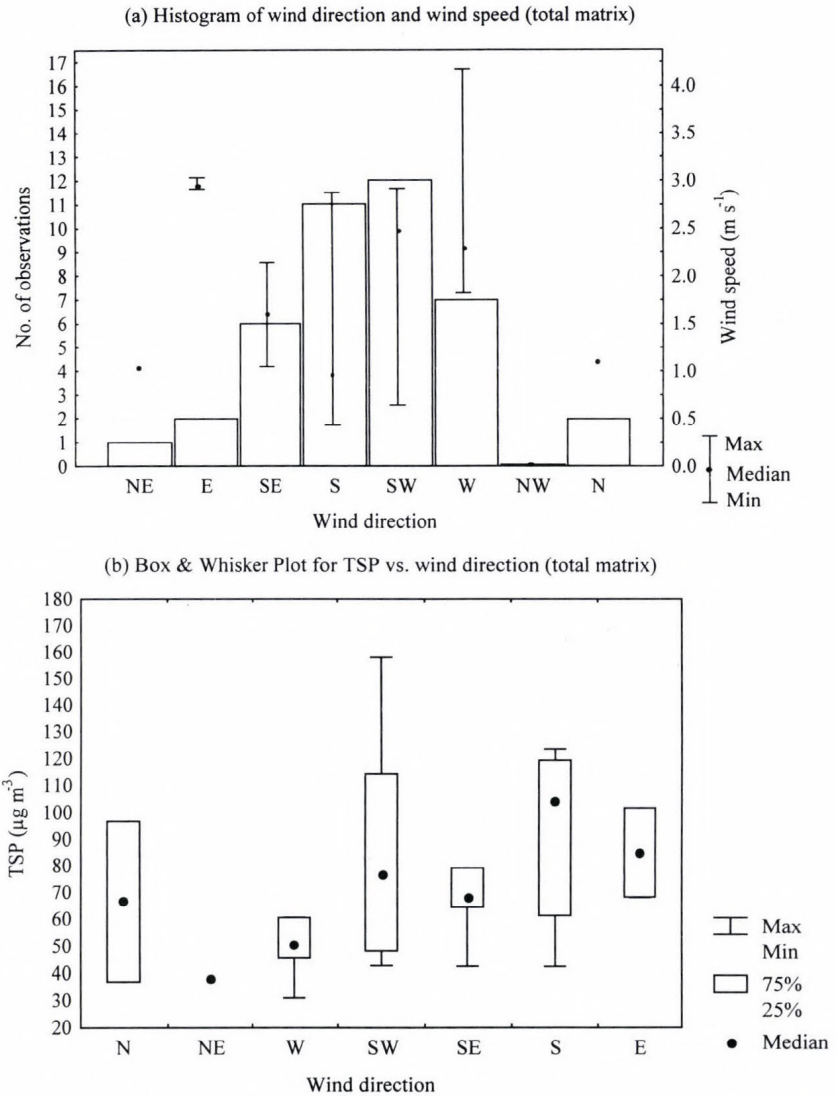

Fig. 1. (*a*) Frequency of wind direction, values of median, maximum, and minimum for wind speeds for all samples. (*b*) Distribution of TSP levels according to the wind directions with values of median, maximum, minimum, and quartiles.

3.2 Basic analytical parameters

In order to know the levels of particles and metals, they are also included in the basic statistics of *Table 1*. The mean value of 78.7 μg m^{-3} for TSP is from 50–150 μg m^{-3}, that would correspond to an "acceptable" air quality according to European directive 1999/30/EC for PM10 particles, but not a "good" air quality (under 50). If the mean value of A particles is subtracted from TSP, the resulting mean value, which would correspond to PM10 particles (sum of B to F stages), is 66.6 μg m^{-3}, still above 50 μg m^{-3}, the final limit value for 24 h. Two samples of TSP exceeding 150 μg m^{-3}, corresponds to a "poor" air quality, although no PM10 value exceeds this value. 23 samples of 41 exceed the limit value for 24 h in PM10 particles, but additionally 16, 12, and 12 samples exceed this value in PM2.5, PM1, and F particles, respectively. The F particles, with D_p<0.6 μm, reaches a maximum value of 104.5 μg m^{-3}. This is relevant, because this size has a high probability of depositing in the alveolar region of the lungs. Remember, that 40% of these 41 samples were collected in rainy days. It is known that the sum of particle concentration of various consecutive filters from a cascade impactor contains errors attributed to a possible accumulation of mass from conversion of gas to particles into the filters. This way, mainly particles lower than 1 μm from this conversion are bound to each stage, increasing the mass of each filter but not changing significantly their percentages regarding the sum. Although this fact exists, it is clear that numerous sum values are much higher than the limit for PM10 particles, even in the sum values corresponding to PM2.5, PM1, and F particles. Because of this effect of accumulation of mass in the sum, we cannot include these PM concentrations as analytical variables in the statistical treatment, except for these comparisons.

In relation to the total metal concentrations, the lead value is five times lower (0.097 ng m^{-3}) than the limit established by the European Community, however, three samples collected near a foundry exceed this limit of 0.5 μg m^{-3}. Therefore, although lower levels of lead are emitted by leaded fuel driven vehicles, high values can be detected locally in the proximity of foundries, for example the maximum value in *Table 1*. These high mean values of particles and low mean values of metals indicate the important influence of the North Western African particles from the Sahara desert.

3.2.1 Total particle content, size distribution, and the effect of rain

In order to study the differences introduced by the rain in particle and metal levels, *Fig. 2* shows the averaged values of concentrations by comparing dry days and rainy days. The great influence of rain is expressed as percentage.

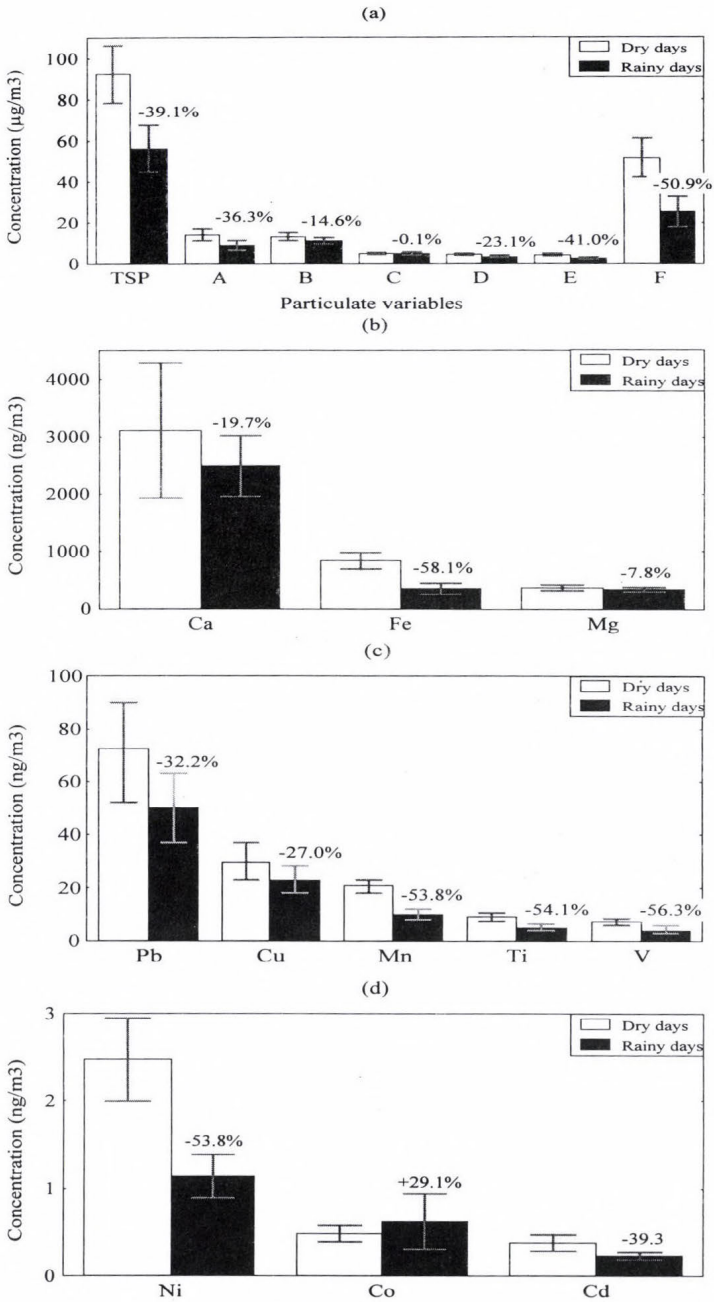

Fig. 2. Averaged values of (*a*) total suspended particles, TSP, and fractionated suspended particles, FSP, and (*b*), (*c*), (*d*) total metal concentration, TM. Effect or rainfall comparing dry days and rainy days.

Table 2. Correlation coefficients (r) for the three matrices of data formed by the meteorological variables, the total suspended particles (TSP), and their size distribution (FSP, A to F), and the metals (TM)

Meteorological variables				Total and fractionated particle variables							Total metal variables										
WS	AT	AP	PP	TSP	A	B	C	D	E	F	Ca	Fe	Mg	Pb	Cu	Mn	Ti	V	Ni	Co	Cd
(a) Total matrix																					
WS	1.00	−0.53	−0.48	0.54	−0.39	−0.43	−0.25	−0.07	−0.37	−0.40	−0.35	−0.13	−0.46	0.01	−0.37	−0.38	−0.47	−0.51	−0.41	−0.50	0.10	−0.56
AT	−0.53	1.00	0.38	−0.51	0.62	0.46	0.35	0.22	0.54	0.61	0.64	−0.30	0.61	0.09	0.37	0.47	0.64	0.59	0.35	0.51	−0.32	0.51
AP	−0.48	0.38	1.00	−0.66	0.12	0.02	−0.16	−0.30	0.00	0.10	0.21	0.01	0.27	−0.10	0.11	0.07	0.28	0.30	0.14	0.20	−0.09	0.16
PP	0.54	−0.51	−0.66	1.00	−0.48	−0.46	−0.31	0.07	−0.24	−0.37	−0.48	−0.05	−0.56	−0.06	−0.20	−0.31	−0.57	−0.54	−0.47	−0.50	0.37	−0.28
(b) Dry days matrix																					
WS	1.00	−0.21	0.03	–	0.03	−0.25	−0.07	0.01	−0.02	0.06	0.13	−0.01	−0.01	0.20	−0.27	−0.36	−0.08	−0.07	−0.12	−0.17	0.06	−0.47
AT	−0.21	1.00	−0.28	–	0.47	0.31	0.28	0.40	0.53	0.50	0.46	−0.48	0.35	0.01	0.29	0.44	0.46	0.32	0.06	0.24	−0.65	0.40
AP	0.03	−0.28	1.00	–	−0.67	−0.62	−0.65	−0.53	−0.62	−0.67	−0.56	−0.15	−0.61	−0.39	−0.21	−0.33	−0.69	−0.57	−0.55	−0.57	0.06	−0.27
(c) Rainy days matrix																					
WS	1.00	−0.13	0.63	0.03	−0.36	−0.24	−0.39	−0.33	−0.46	−0.66	−0.29	−0.37	−0.25	−0.07	−0.08	0.04	0.01	−0.39	−0.22	−0.30	−0.10	−0.43
AT	−0.13	1.00	−0.01	−0.42	0.50	0.45	0.37	−0.16	−0.15	−0.13	0.59	−0.45	0.61	0.01	−0.12	0.18	0.20	0.40	0.60	0.31	0.04	0.04
AP	0.63	−0.01	1.00	−0.24	−0.16	−0.15	−0.37	−0.49	−0.50	−0.41	−0.02	−0.29	0.02	−0.17	−0.29	−0.09	0.37	−0.03	0.15	−0.22	0.11	−0.15
PP	0.03	−0.42	−0.24	1.00	−0.35	−0.61	−0.52	0.16	0.21	0.15	−0.28	0.30	−0.44	0.19	0.15	−0.29	−0.41	−0.24	−0.54	−0.38	0.42	0.07

WS: wind speed, AT: ambient temperature, AP: atmospheric pressure, PP: precipitation

Also, single correlations of particles and metals with meteorological parameters are shown in *Table 2*. This table highlights the positive and negative correlation coefficients that indicate the linear behavior between particle and metal concentrations and meteorological parameters. In *Fig. 2-a*, the decrease in concentration of the fine particles (E particles: - 41%, and mainly F particles: - 51%) is greater than that of coarse particles (A particles: 36%, B particles: 15%). However, in *Table 2-c*, the higher anticorrelation with rainfall can be observed for particles larger than 4.9 μm, mainly the A particles > 10 μm (r = - 0.61); meanwhile, the value for F particles is low (r = - 0.28). This fact seems to be a contradiction, but one observes an easy explanation: the fine particles are those that are eliminated in large proportion (-51 % in *Fig. 2-a*) independently of the quantity of rain (- 0.28 in *Table 2-c*). Meanwhile, the coarse particles are those that respond more linearly to the removal and washing effect of the rain (-0.61 in *Table 2-c*). Thus, fine particles are removed from the atmosphere independently of the amount of rain, whereas elimination of coarse particles is dependent on rainfall values.

On the other hand, in *Table 2-c*, the negative correlation between TSP and rainfall was not as significant as might be expected (r = - 0.35). This fact can be explained by the differences in the correlation coefficients of the different size fractions (from - 0.61 for A particles to + 0.21 for D particles). This is one of the aspects that justifies the importance of studying the particle sizes for meteorological and environmental interpretations.

Regarding the influence of rain on metal contents, the lowest values were observed again for the rainy days (*Fig. 2-b,c,d*, *Table 3*). The percentages for the size fractions of metals can be seen in *Table 3*. In the last file, the highest negative percentages of total concentrations were found for Fe (-58.1%), vanadium (-56.3%), Ni (-53.8%), Ti (-54.1%), and Mn (-53.4%), but on the contrary, high positive percentages of cobalt (+29.1%) were found. The higher values are for fine particles, except for vanadium (-67.0%) and calcium (-51.8%), which are for coarse particles. The high percentages found in rainy samples correspond to the majority of size fractions of cobalt, mainly the E particles, and several fractions of magnesium and cadmium.

We assign these decreases in percentages mainly to two causes: the effect of washing of particles, depending on their size, the solubility of the particles, and the metal compounds contained in them (*Mészáros*, 2002). About their size distribution, we know through our studies on the same samples, that the metals are more associated with the smallest size fraction (F particles) regarding the TSP concentrations, such as Ni (73%), V (70%), and Co (56%), although, other metals also have notable percentages, such as Mg (48%), Mn (44%), Ti (42%), and Fe (37%), always higher than in the percentages of coarse particles (*Fernández et al.*, 2001). These percentages would explain the large washing

effect on metals in the rainy day situations, including Fe and Ti, mainly on fine particles.

Table 3. Percentages of decreases of the concentrations of particles and metals by the rain regarding the dry days

	TSP	Ca	Fe	Mg	Pb	Cu	Mn	Ti	V	Ni	Co	Cd
A	-36.3	-51.8	-54.5	-9.8	-39.1	-29.8	-49.9	-50.4	-67.0	-44.7	+9.7	-22.9
B	-14.6	-47.3	-43.1	+16.4	-16.6	-17.7	-45.3	-42.0	-45.4	-49.2	-4.2	+14.2
C	+0.1	-3.7	-36.1	+26.3	-25.2	-2.9	-39.2	-39.5	-55.0	-22.2	+37.5	-10.7
D	-23.1	-2.4	-49.9	+5.4	-41.7	-1.7	-51.2	-50.6	-50.7	-39.0	+23.6	-20.9
E	-41.0	-2.2	-62.2	-17.4	-49.8	-11.1	-54.7	-61.1	-48.0	-44.7	+82.4	-38.3
F	-50.9	+6.5	-71.1	-20.2	-30.6	-45.7	-59.9	-62.2	-57.6	-57.4	+33.2	-48.4
Total	**-39.1**	**-19.7**	**-58.1**	**-7.8**	**-32.2**	**-27.0**	**-53.8**	**-54.1**	**-56.3**	**-53.8**	**+29.1**	**-39.3**

With regards to solubility, we know through our chemical speciation studies corresponding to these fine particles samples, that the metals with higher percentages in the soluble chemical forms regarding the total concentrations are those of V (50%), Ni (40%), Co (35%), and Mn (33%), but not those of Fe (4%), Ti (8%), and Mg (18%) (*Fernández et al.*, 2002). These percentages would explain the large decreases in the sample concentrations for the metals V, Ni, and Mn in rainy day situations, specially regarding the high soluble capacity of vanadium. The metals Fe and Ti are not particularly soluble, however, both are removed well enough by rain. Their percentages of decrease in the fine fraction are 71.1% and 62.2%, respectively, higher than V, Ni, and Mn (*Table 3*). Therefore, in the case of Fe and Ti, the removal effect that prevails is the physical washing, since their percentages of the fine fraction from the TSP is greater than the 37%, as mentioned above.

Thus, the removal mechanism most probably combines the physical effect of washing by the drops of rain that fall, together with the solvent effect of the drops of water, which dissolve the soluble compounds that form particles and metals. Additionally, the dissolved and washed metals and particles can also haul other chemical forms and particles with them.

With regard to cobalt metal, it is a highly soluble metal and accumulates in the fine particles, however, with higher concentration in the rainy samples. We found an explanation for this contrary behavior: There is a well-known special characteristic of the complexes of cobalt formed by cobalt (II) chloride and water molecules, they reflect pink colors with water and blue colors without water. If there is increasing rain, the concentration of water molecules

that surround the cobalt salts and complexes also increases, and the cobalt mixes with the humid air.

On the other hand, correlations of the rainy days matrix (*Table 2-c*) show only the total concentration of vanadium is clearly dependent on rain quantity ($r = -0.54$), and the higher anticorrelations of its size fractions (*Table 4-c*) correspond to particles larger than 4.9 μm, mainly the V2 fraction ($r = -0.60$) and V6 fraction ($r = -0.57$). Although, other size fractions are anticorrelated, as in the case of magnesium >4.9 μm ($r = -0.66$ for Mg1 fraction), Fe >10 μm ($r = -0.60$), Mn >4.9 μm ($r = -0.58$ for Mn1 and Mn2 fraction), and Ti >10 μm ($r = -0.57$), showing that the correlation is always with coarse sizes. Elimination of those sizes is dependent on the value of rainfall, with the exception of vanadium.

Both indicators of decreases in particle-metal levels by rain, percentages (*Fig. 2* and *Table 3*), and correlation coefficients (*Tables 2* and *4*) show that these fractionated particles and metals cited are those that have the same response in the rain. In general, it has been possible to observe that particles and metals of different sizes show different behavior in the rain. Differential responses from other parameters should be verified, as has been done for rain.

3.2.2 Influence of the remaining meteorological parameters on particle and metal concentrations and their size distributions

Firstly, the highest TSP values were observed proceeding from the most frequent wind direction, south and mainly southwest, but not from the strong western winds nor the low eastern winds, as can be seen in the Box & Whisker plot of *Fig. 1b*. Another six Box & Whisker plots, which are not represented here for all particle size fractions show, that F particles follow the same wind direction pattern as TSP with higher levels from the south. This trend is also sharper for A particles but mainly for B particles, both are coarse particles.

The effect, that the wind speed could reduce the TSP concentrations in the air by a removal effect from the airborne particles, is an anticorrelation, but it could also increase their levels if the wind resuspends coarse soil particles, showing positive correlation. This opposite effect should be the cause of the correlation coefficient between the two variables, both being low, although it is negative ($r = -0.39$) in the total matrix and rainy situations ($r = -0.36$), and null in dry situations ($r = +0.03$, *Table 2*). However, observing the size fraction data, in the rainy day situations only the fine particles between 1.3 and 0.6 μm present a clear negative coefficient (*Table 2-c*, $r = -0.66$). Therefore, these particles are those that were better dispersed by winds only in rainy situations. In *Table 2-a* the rain have a relationship with high wind speed

(r = + 0.54) and anticyclonic conditions, i.e., lower temperatures (r = - 0.51) and atmospheric pressures (r = - 0.66).

Regarding the total metal concentrations, *Table 2* shows in the total matrix that Cd was the most easily eliminated by the wind (r = - 0.56). Other metals have similar but lower anticorrelations, such as Ti (r = - 0.51), Ni (r = - 0.50), Mn (r = - 0.47), and Fe (r = - 0.46) in the same matrix, and Cd again (r = - 0.47) in dry samples. Cd is the only metal that appears with high anticorrelations in the three matrices.

Table 4. Results of the single linear regression (SLR) for the fractionated metals (FM) in function of the meteorological variables. Table contains the higher values of the coefficient r for each metal

Variable	Equation (Y = a + b X)	Correlation coefficient (r)	t_{calc}	Degrees of freedom	t_{tab}
	(a) Total matrix (41 samples)				
Mn4	Mn4 = - 0.63 + 0.08 AT	+0.69	5.95	39	2.02
Fe5	Fe5 = - 24.89 + 2.57 AT	+0.66	5.49	39	2.02
Ti5	Ti5 = - 0.23 + 0.03 AT	+0.66	5.49	39	2.02
Cd6	Cd6 = 0.39 - 0.02 WS	- 0.50	3.61	39	2.02
Ti5	Ti5 = 0.56 - 0.03 WS	- 0.66	5.49	39	2.02
Ni1	Ni1 = 0.31 - 0.02 WS	- 0.55	4.11	39	2.02
Mn5	Mn5 = 1.47 - 0.07 WS	- 0.54	4.01	39	2.02
Fe5	Fe5 = 50.18 - 2.66 WS	- 0.56	4.22	39	2.02
	(b) Dry days matrix (25 samples)				
Co3	Co3 = 0.18 - 0.01 AT	- 0.58	3.41	23	2.07
Mn1	Mn1 = 495.14 - 0.49 AP	- 0.70	4.70	23	2.07
Fe5	Fe5 = 3357.00 - 3.30 AP	- 0.60	3.60	23	2.07
Ti5	Ti5 = 29.57 - 0.03 AP	- 0.56	3.24	23	2.07
Ni6	Ni6 = 172.41 - 0.17 AP	- 0.54	3.08	23	2.07
V5	V5 = 86.93 - 0.09 AP	- 0.58	3.41	23	2.07
Cd5	Cd5 = 0.08 - 0.01 WS	- 0.50	2.77	23	2.07
Ni1	Ni1 = 0.37 - 0.03 WS	- 0.60	3.60	23	2.07
	(c) Rainy days matrix (16 samples)				
V2	V2 = 0.56 - 0.01 PP	- 0.60	2.81	14	2.15
V6	V6 = 3.69 - 0.11 PP	- 0.57	2.60	14	2.15
Mg1	Mg1 = 79.01 - 1.44 PP	- 0.66	3.29	14	2.15
Fe1	Fe1 = 120.23 - 3.02 PP	- 0.60	2.81	14	2.15
Mn1	Mn1 = 3.01 - 0.08 PP	- 0.58	2.66	14	2.15
Mn2	Mn2 = 2.57 - 0.05 PP	- 0.58	2.66	14	2.15
Ti1	Ti1 = 1.25 - 0.03 PP	- 0.57	2.60	14	2.15
Fe1	Fe1 = - 361.40 + 24.93 AT	+0.62	2.96	14	2.15
V1	V1 = - 1.55 + 0.10 AT	+0.64	3.12	14	2.15
Cd6	Cd6 = 0.29 - 0.01 WS	- 0.62	2.96	14	2.15
Ti2	Ti2 = 1.84 - 0.08 WS	- 0.57	2.60	14	2.15

About their size fractions, Cd was associated with the fine particles, <0.6 μm, in the total matrix ($r = -0.50$, *Table 4-a*) and in rainy situations ($r = -0.62$, *Table 4-c*), and with the fine particles between 1.3 and 0.6 μm in dry situations ($r = -0.50$, *Table 4-b*). This latter size, the E fraction was also associated with other metals, such as Ti, Mn, and Fe ($r = -0.66$, $r = -0.54$, and $r = -0.56$, *Table 4-a*). Ni was the only metal found in the coarse particles, >10 μm, ($r = -0.55$, *Table 4-a*; $r = -0.60$, *Table 4-b*). Finally, Ti presented high anticorrelations in rainy situations (*Table 4-c*) in the coarse particles, between 10 and 4.9 μm ($r = -0.57$). The majority of anticorrelations correspond to fine particles, <1.3 μm, mainly the E particles, except for the coarse particles, >4.9 μm, of Ni and Ti. Therefore, the particles most easily removed by the wind, as in the effect of rain, are the PM1 particles, fortunately.

On the other hand, significant positive correlations were found between temperature and TSP levels, i.e., the particle levels being high when temperatures were also high or vice versa. This correlation is well highlighted in the total matrix ($r = +0.62$), but also on the rainy days ($r = +0.50$) and slightly on the dry days ($r = +0.47$) (*Table 2*), therefore, this effect is marked and frequent. The mechanism is logical: when temperature is high, the density and viscosity of air diminish, and this favors the resuspension of particles. In the total matrix, particles smaller than 2.7 μm better correlated with the temperature, mainly the F particles ($r = +0.64$). In the dry samples, the particles <2.7 μm again better correlated with the temperature ($r = +0.53$ for D particles), and in the rainy situations only particles <0.6 μm ($r = +0.59$), correlated the best with the temperature. Therefore, the effect of temperature is more accentuated in the particles of less than 2.7 μm, although this would not be applied to extremely fine particles (e.g., $D_p < 0.1$ μm), because at this size there is not any resuspension.

The resuspension of particles by high temperatures could be attributed to a drying effect on earth crustal particles of soils and additionally to a decrease in air density and viscosity. Both reasons could facilitate the suspension of particles in the air. Our Regional Government is also aware of these episodes, since the particle concentration often exceeds the level of "not acceptable air quality" in its Air Control and Monitoring Stations. The other coherent explanation could be the Saharan particles coming from the North African warm winds. Also, at high temperatures an important production of fine particles occurs. Therefore, all three suppositions can be valid, and the third is in agreement with the experience of our regional episodes. The first two explanations are in agreement with the present particle size study, because it is most likely that the Saharan particles are coarse when they reach the continent (*Schütz* and *Sebert*, 1987; *Molinaroli et al.*, 1993). This problem exists not only in our city but also in other cities of our region of Andalusia. The

Saharan input represents a problem in other Mediterranean countries, including as far away as Central Europe. Therefore, the new Directive contemplates the possibility of keeping in focus the different geographical situations (Article 5.4 of the *Council Directive 1999/30/EC*, 1999).

Studying the relationship between temperatures and metal concentrations, one found that earth crustal metals such as Mn, Fe, and Ti had high concentrations at high temperature values ($r = +0.64$, $r = +0.61$, $r = +0.59$, respectively, *Table 2-a*). This fact supports the two explanations above mentioned, because both particle sizes are coming from earth crustal sources. When we studied their size distribution (*Table 4-a*), we observed that the effect rebounded on Fe5 particles ($r = +0.66$), Mn4 particles ($r = +0.69$), and particles of Ti <2.7 μm, mainly Ti5 ($r = +0.66$), i.e., the fine metal fractions again, contained in PM2.5. However, in rainy samples (*Table 4-c*), the size fractions, that have high correlation, are the particles >10 μm, such as Fe1 ($r = +0.62$) and V1 ($r = +0.64$), i.e., the coarse particles that respond to high temperatures in rainy situations.

On the other hand, we observed (*Table 2-b*), that, contrarily, cobalt was negatively correlated with temperature ($r = -0.65$), showing behavior opposite to that of TSP, Mn, Fe, and Ti. The size fraction that followed this trend was represented by particles between 4.9–2.7 μm ($r = -0.58$, *Table 4-b*). The explanation could be related to the stability of the cobalt complexes in the rainy situations mentioned above. Since temperature is negatively correlated with rainfall and cobalt is positively correlated with rainfall, logically cobalt is anticorrelated with temperature.

Regarding the atmospheric pressure parameter, the correlation study also reveal a dispersion effect on TSP (*Table 2-b*, $r = -0.67$). This effect of he anticyclonic conditions was strongest for the fine E particles (*Table 2-b*, $r = -0.67$), but the anticorrelations are high for all size fractions.

There were also several anticorrelations for metal concentrations (*Table 2-b*), with Mn ($r = -0.69$), Fe ($r = -0.61$), Ti ($r = -0.57$), Ni ($r = -0.57$), and V ($r = -0.55$). Studying their size distribution (*Table 4-b*) we found, that predominant size fractions for Mn were particles >4.9 μm ($r = -0.70$ for Mn1 particles), particles < 1.3 μm for Fe ($r = -0.60$ for Fe5 particles), Ti5 particles ($r = -0.56$), Ni6 particles ($r = -0.54$), and V5 and V6 particles ($r = -0.58$ for V5 particles).

One can observe that the metals having correlations or anticorrelations with the main meteorological parameters are always the earth crustal elements Fe, Ti, and Mn. In these cases not only fine particles were highly correlated, but also the coarse particles in several metals.

Correlations and anticorrelations of particles metals, and their size fractions were found, which could explain several relationships with

meteorological parameters. Atmospheric pressure has shown stronger dispersion effect than wind speeds on suspended particles and metals, and temperature shows a contrary effect on concentration. But, in some analytical variables there are negative and positive correlations at the same time. For example, in the rainy matrix, vanadium is correlated with ambient temperature and anticorrelated with atmospheric pressure, and the same fact occurs in total and dry matrices with TSP, Fe, Mn, Ti, and Ni concentrations. Therefore, what will the global behavior of these elements be, faced with both parameters at the same time? This question can not be answered by single correlations, but with multiple regressions.

3.3 Multiple linear regression analysis to correlate the behavior of variables with meteorological conditions

In the previous section, we found significant correlations between analytical variables and meteorological data through simple linear regression (SLR) analyses, mainly with rainfall, temperature, and atmospheric pressure. As expected, it was also possible to find multivariate equations to relate only the correlated variables in the SLR (*Tables 2* and *4*) with all the meteorological parameters at the same time using the multiple linear regression (MLR) analysis (*Fernández et al.*, 2000). These equations can be useful in verification if the concentrations in the air can follow a basic model of behavior for particles metals, and their size fractions, and if this model is more accurate than the SLR. Therefore, applying the *Statistica* package we obtained these equations for the three matrices (*Table 5*). This table shows, also underlined, the significant coefficients for meteorological parameters.

One can observe in *Table 5*, that the equations that give the worst correlation coefficients for TSP concentrations are those obtained for the rainy days matrix ($r = 0.60$). Consequently, the coefficient is lower for the total matrix ($r = 0.71$), which contains rainy samples, than for the dry days matrix ($r = 0.74$), without rainy samples. This is also evidence, that rain situations distort the study of atmospheric pollution a lot by total suspended particles. This difference can be verified in *Fig. 3-b,c*, where the poor capacity of prediction of the equation on rainy days can be seen in relation to the dry days. This fact should be due to the different behaviors of the different size fractions in rainy situations most influenced by the rain. Thus, variability (*Table 1*) in rainfall variable (168 %) is greater than wind speed (44%) for example, and, therefore, the success of prediction is lower. Only several fractions of soluble elements such as magnesium or vanadium (*Fig. 3-f*) have a better capacity for prediction in rainy day matrices.

Table 5. Results of the multiple linear regression (MLR) for the TSP, FSP, TM, and FM variables in function of all meteorological variables. The table underlines the significant coefficients for meteorological parameters

Variable (Y)*	a	b_1	b_2	b_3	b_4	Correlation coefficient (r)	t_{calc}	Degrees of freedom	t_{tab}
(a) Total matrix (41 samples)									
TSP	3469.328	-1.787	-0.672	4.091	-3.426	0.7128	6.35	36	2.028
F	1334.967	-1.015	0.208	3.036	-1.339	0.6855	5.88	36	2.028
Mn	497.983	-0.427	-0.264	0.914	-0.491	0.7212	6.50	36	2.028
Mn4	1.569	-0.013	-0.020	0.056	-0.001	0.7372	6.81	36	2.028
Fe	22467.817	-19.666	-13.169	35.747	-22.125	0.7001	6.12	36	2.028
Fe5	469.961	-0.509	-1.124	1.720	-0.461	0.7323	6.72	36	2.028
Ti	166.131	-0.154	-0.230	0.311	-0.161	0.6766	5.74	36	2.028
Ti5	3.216	-0.004	-0.018	0.015	-0.003	0.7655	7.43	36	2.028
Cd	8.653	0.001	-0.027	0.016	-0.008	0.6323	5.10	36	2.028
Cd6	4.314	0.000	-0.016	0.014	-0.004	0.5874	4.53	36	2.028
Ni	90.505	-0.055	-0.096	0.069	-0.088	0.6448	5.27	36	2.028
Ni1	8.579	-0.001	-0.022	0.001	-0.008	0.5891	4.55	36	2.028
(b) Dry days matrix (25 samples)									
TSP	7485.992	-	1.414	2.663	-7.367	0.7421	6.91	21	2.080
E	363.016	-	0.091	0.145	-0.358	0.7606	7.32	21	2.080
Co	13.169	-	-0.006	-0.038	-0.012	0.6682	5.61	21	2.080
Co3	-1.808	-	0.000	-0.006	0.002	0.5902	4.57	21	2.080
Mn	1830.889	-	-0.017	0.525	-1.799	0.7448	6.97	21	2.080
Mn1	468.513	-	-0.199	0.046	-0.459	0.7741	7.64	21	2.080
Fe	74643.533	-	6.169	17.149	-73.283	0.6445	5.26	21	2.080
Fe6	34607.535	-	16.263	10.551	-34.147	0.6710	5.65	21	2.080
Ti	681.318	-	-0.020	0.137	-0.667	0.5946	4.62	21	2.080
Ti5	25.812	-	-0.012	0.007	-0.025	0.6597	5.48	21	2.080
Ni	242.965	-	-0.059	0.017	-0.237	0.5917	4.58	21	2.080
Ni1	23.130	-	-0.031	-0.004	-0.022	0.7211	6.50	21	2.080
V	1064.356	-	-0.220	-0.145	-1.039	0.5769	4.41	21	2.080
V1	103.101	-	-0.064	-0.019	-0.100	0.6781	5.76	21	2.080
Cd	16.048	-	-0.032	0.014	-0.016	0.5874	4.53	21	2.080
Cd5	1.352	-	-0.006	0.002	-0.001	0.5707	4.34	21	2.080
(c) Rainy days matrix (16 samples)									
TSP	255.600	-0.453	-3.053	7.313	-0.287	0.5996	4.68	11	2.201
B	715.802	-0.182	-0.108	0.285	-0.701	0.7330	6.73	11	2.201
V	-416.026	-0.074	-0.410	0.943	0.406	0.7308	6.69	11	2.201
V2	-2.096	-0.010	-0.048	0.058	0.002	0.8293	9.27	11	2.201
Mg1	6487.662	-1.840	5.547	-1.105	-6.403	0.8180	8.88	11	2.201
Fe	-16502.994	-3.521	-24.701	78.671	15.682	0.6804	5.80	11	2.201
Fe1	-2304.284	-1.997	-5.962	16.904	2.163	0.7630	7.37	11	2.201
Mn1	-214.868	-0.071	-0.134	-0.006	0.218	0.6949	6.03	11	2.201
Ti1	-56.542	-0.019	-0.107	0.064	0.057	0.7333	6.74	11	2.201
Cd6	-3.824	0.000	-0.017	0.000	0.004	0.6364	5.15	11	2.201

*: Equation: $Y = a + b_1 PP + b_2 WS + b_3 AT + b_4 AP$

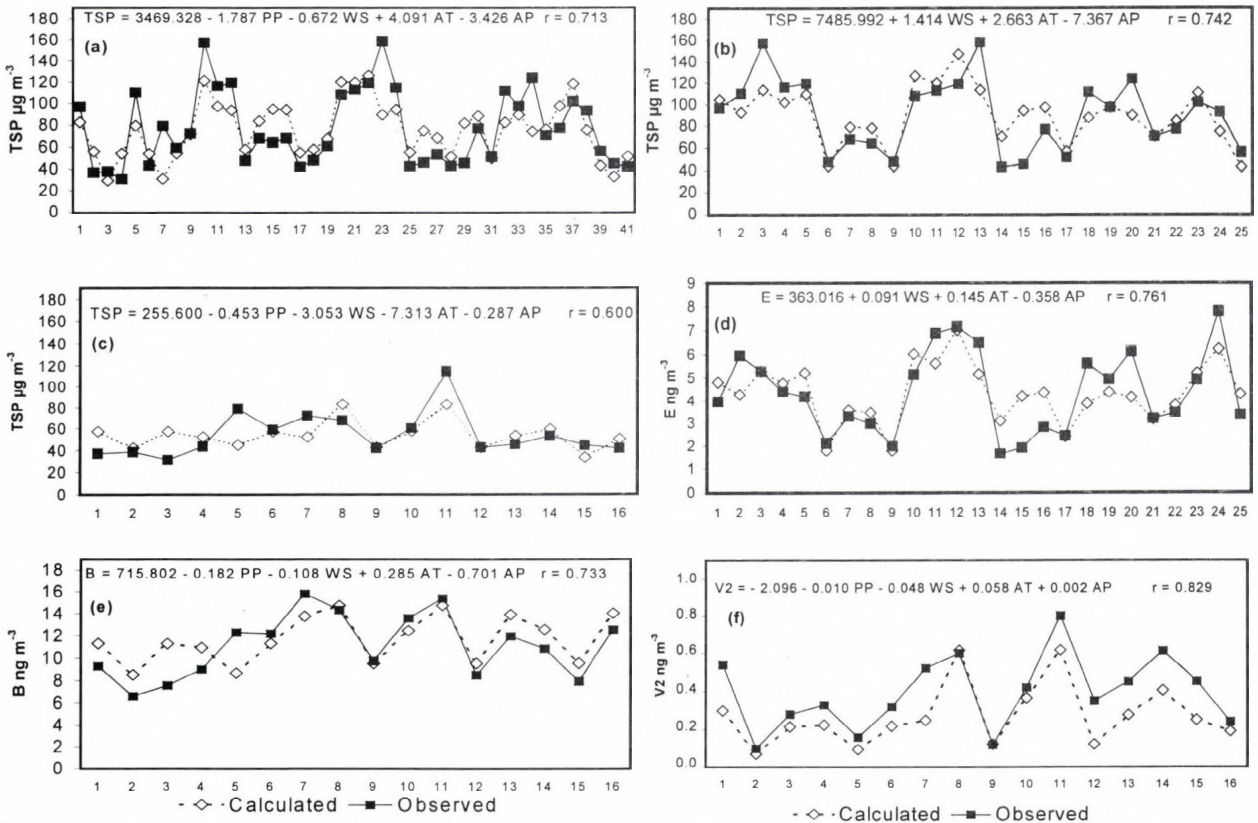

Fig. 3. Comparison between concentrations of the experimental values of analytical parameters and the corresponding predicted values for (*a*) TSP in total matrix, (*b*) TSP in dry days matrix, (*c*) TSP in rainy days matrix, (*d*) E particles in dry days matrix, (*e*) B particles in rainy days matrix, and (*f*) V2 in rainy days matrix.

Regarding the size fractions of particles, in the dry days matrix, the E particles are most highly correlated (r = 0.76). These particles are those, in which more correlation and anticorrelation were found, therefore, they are the particle sizes most influenced by meteorological parameters. In both, total and dry matrices, the fine particles (E and F fractions) are the most easily predicted (*Fig. 3-d* for the E particles). However, in rainy situations, the coarse particles are the best correlated, the A and B particles instead of fine particles (*Fig. 3-e* for B particles). This fact is in accordance with the fact that the coarse particles are those that respond positively to the amount of rainfall, although the fine particles are those that are best removed by the rain independently of the rainfall. Thus, the rainy situations introduce a major difficulty when predicting the behavior or concentrations of fine particles, which are the most harmful.

Regarding the total metal and their size fraction concentrations, in dry and total matrices the metal with the highest correlation is manganese (r = + 0.74 and r = + 0.72, *Table 5*), but on rainy days vanadium (r = + 0.73) is the metal that was found to be a model of behavior more accurate than the SLR. Meanwhile, manganese does not appear in the rainy days matrix because of its low coefficient (r is significantly equal to zero). The metal iron is the only one that appears with a coefficient higher than 0.64 in the three matrices, and is also the only one that has a higher correlation coefficient in the rainy days matrix (r = + 0.68), although with smaller differences, than in the dry days matrix (r = + 0.64).

The corresponding size fractions of metals have generally higher coefficients than the total concentrations, except for several cases, such as Cd6 and Ni1 in the total matrix, and Co3 or Cd5 in the dry days matrix. Many of these coefficients are high or extremely high, for example, Ti5, Mn4, and Fe5 in the total matrix, Mn1 and Ni1 in the dry days matrix, and Fe1, Ti1, and mainly V2 and Mg1 in rainy days matrix, with coefficients higher than 0.82. These metal fractions are the best explained in both matrices (*Table 5*).

These results confirm again the importance of the relationship of the meteorological parameters with the particles and metals depending on their corresponding sizes.

4. Conclusions

Interesting interrelations were found that explain the behavior of particles and metals of different sizes in different meteorological conditions: the effect of temperature on the increase of particle concentrations, the effect of

atmospheric pressure and wind speed on the dispersion of particles, and the elimination of particles by the rain.

Multiple linear regression technique was notably useful to confirm the poor capacity of prediction on rainy day conditions for particles and metals. The best prediction was observed for metals that can be in soluble forms in the air, such as magnesium and vanadium. The particles lower than 1.3 micrometers are the most easily predicted when studying the size distribution of particles. The metal concentrations with the highest correlation coefficients in the MLR were observed for fine particles, such as the Fe, Mn, and Ti metals, or coarse particles, such as the Mn, Ni, Mg, Fe, V, and Ti metals.

We conclude that rainfall is the meteorological parameter that most affects particle elimination and metal pollution by physical and chemical washing away of particles. The other meteorological parameters were also observed influencing the presence of different size particles in the air (wind speed, temperature, and pressure). These effects are different for different size fractions.

It would be interesting to extrapolate from these methods, if used in other regions and countries, to the possible data, checking the differences and similarities with their results. Although, our first objective after this study will be to repeat this research for a longer time period with a larger number of samples and several additional meteorological parameters. The study of the size distribution and meteorological parameters constitutes a way to increase the information about the lifetimes of pollutants in the urban air. The satisfactory results of the multiple linear regression technique should be checked into a context of a wide research with a wide sampling period.

Acknowledgements—We would like to thank the "Consejería de Medio Ambiente de la Junta de Andalucía" for their financial assistance in carrying out this research project.

References

Brooks, L. and *Salop, J.*, 1983: Chemical and meteorological characteristics of atmospheric particulates in southeastern Virginia utilizing multi-variant analysis. *J. Air Control Association 33*, 222-224.

Choularton, T W., Fullarton, G., and *Gay, M.J.*, 1982: Some observations of the influence of meteorological variables on the size distribution of natural aerosol particles. *Atmospheric Environment 16*, 315-323.

Council Directive 1999/30/EC of 22 April, 1999: Relating to limit values for sulphur dioxide, nitrogen dioxide and oxides of nitrogen, particulate matter and lead in ambient air. Official Journal L163, 41-60.

Despiau, S., Cougnenc, S., and *Resch, F.*, 1996: Concentrations and size distributions of aerosol particles in coastal zone. *J. Aerosol Science 27*, 403-415.

Elsom, D.M. and *Chandler, T.J.*, 1978: Meteorological controls on ground level concentrations of smoke and sulphur dioxide in two urban areas of the U.K. *Atmos. Environ. 12*, 1543-1554.

Fernández, A.J., Ternero, M., Barragán, F.J., and *Jiménez, J.C.*, 1999: Source characterization of airborne particles in Seville (Spain) by multivariate statistical analyses. *Időjárás 103*, 261-273.

Fernández, A.J., Ternero, M., Barragán, F.J. and *Jiménez, J.C.*, 2000: An approach to characterization of urban airborne particles sources through heavy metals speciation. *Chemosphere 2*, 123-136.

Fernández, A.J., Ternero, M., Barragán, F.J., and *Jiménez, J.C.*, 2001: Size distribution of metals in urban aerosols in Seville (Spain). *Atmospheric Environment 35*, 2595-2601.

Fernández, A.J., Ternero, M., Barragán, F.J., and *Jiménez, J.C.*, 2002: A chemical speciation of trace metals for fine urban particles. *Atmospheric Environment 36*, 773-780.

ISO 7708, 1995: *Air Quality - Particle Size Fraction Definitions for Health-related Sampling*. ISO Publications, First Edition 1995-04-01.

Melgarejo, P.L., Ternero, M., and *Gracia, I.*, 1986: A study of the atmospheric lead pollution in Sevilla, Spain. Influence of meteorology and traffic, and relationship with other traffic-generated pollutants. *Int. J. Env. Analytical Chemistry 24*, 283-296.

Mészáros, E., 2002: Atmospheric wet deposition as a nutrient supply for the vegetation. *Időjárás 106*, 103-111.

MMA, Ministerio de Medio Ambiente, 1997: *Guía resumida del clima en Espa a 1961-1990.* Dirección General del Instituto Nacional de Meteorología. Edita Secretaría Técnica de Medio Ambiente, Madrid.

Molinaroli, E., Guerzoni, S., and *Rampazzo, G.*, 1993: Contribution of Saharan dust to the Central Mediterranean basin. In *Proc. Controlling the Composition of Clastic Sediments* (eds.: *M.J. Johnsson* and *A. Basu*). *Geological Society of America. Bulletin* Special Paper, 303312.

Schütz, L. and *Sebert, M.*, 1987: Mineral aerosols and source identification. *J. Aerosol Science 18*, 1-10.

StatSoft, Inc., 1999: *STATISTICA' 99* Edition for Windows (Computer program), Kernel release 5.5. Tulsa, OK, USA.

Usero, J., Rosa, F., Ternero, M., and *Gracia, I.*, 1988: A determination of the sources in the Seville urban aerosol. *Int. J. Env. Analytical Chemistry 33*, 233-244.

Väkevä, M., Hämeri, K., Puhakka, T., Nilsson, E.D., Hohti, H., and *Mäkelä, J.M.*, 2000: Effects of meteorological processes on aerosol particle size distribution in an urban background area. *J. Geophysycal Research 105(D8)*, 9807-9821.

Witz, S. and *Moore, A.B.*, 1981: Effect of meteorology on the atmospheric concentrations of traffic-related pollutants at a Los Angeles Site. *J. Air Pollution Control Association 31*, 1098-1101.

IDŐJÁRÁS

Quarterly Journal of the Hungarian Meteorological Service
Vol. 108, No. 1, January–March 2004, pp. 33–49

Nowcasting of the precipitation type Part II: Forecast of thunderstorms and hailstone size

István Geresdi[1], **Ákos Horváth**[2] and **Árpád Mátyus**[1]

[1]*University of Pécs, Institute of Geography,*
Ifjúság u. 6, H-7624 Pécs, Hungary; E-mail: geresdi@ttk.pte.hu

[2]*Hungarian Meteorological Service,*
Vitorlás u. 17, H-8600 Siófok, Hungary; E-mail: horvath.a@met.hu

(Manuscript received May 23, 2003; in final form December 22, 2003)

Abstract—The purpose of this research was to develop a numerical model to estimate the occurrence of thunderstorms and hailstones on the ground. This model is a part of the nowcasting system (MEANDER) developed by the Hungarian Meteorological Service. The formation of the thunderstorms was estimated by running a one-dimensional, steady state model at every grid point of the mesh covering the Carpathian Basin. Using sounding and surface data over a grid with 3 km horizontal resolution initialized the model. The outputs of the model are: vertical profile of temperature and updraft velocity of the ascending air parcel, furthermore, the size of the largest hailstone on the ground. Convective Available Potential Energy (CAPE) is also calculated to estimate convective activity. The predicted occurrence of the thunderstorms was compared to radar observations. The calculated maximum hailstone sizes were checked by using reports of the voluntary observers. The comparisons show that nowcasting system overestimates the occurrence of the thunderstorm formation; about 20% of the alarms were false. In most cases the nowcasting system forecasted the formation of the thunderstorms one hour before they appeared.

Key-words: nowcasting, numerical simulation, thunderstorm, hailstone, radar observation.

1. Introduction

In the second part of this series the results about the convective activity are published. In the first part (*Geresdi* and *Horváth*, 2000) we dealt with the winter precipitation. Now, we are focusing on the characteristic phenomenon of the summer weather, the thunderstorm. Strong convective storms frequently

produce large hail and intensive outflow. Both phenomena are consequence of very complicated and strongly interacting dynamics and microphysical processes. Two possible approximations could be used to simulate the development of convective storms. It is obvious that the mesoscale models with high horizontal resolution (distance between grid points in the horizontal direction should be about 1 km) and sophisticated microphysical description could be the most appropriate for modeling of this process (e.g., *Pilke et al.*, 1992; *Colle* and *Clifford*, 2000). Although the mesoscale models have number of advantages, because of the necessary high horizontal resolution, it takes order of hours to give a three-hour forecast. Another possibility is the application of a highly parameterized scheme to simulate the dynamics (e.g., *Aleksic et al.*, 1991), and using the available computer capacity to give a more detailed microphysical description about the process we focus on. In this project we chose the second way. The dynamics of the convective clouds is characterized by the output of a one-dimensional steady state cloud model with bulk microphysics. A detailed microphysics is used to calculate the melting rate of the falling hailstone.

The output data of the model occurrence of thunderstorms and maximum hailstone size - was compared with radar observation, and surface reports of hailstones. The output of the thunderstorm nowcasting is described by presentation of a case study.

2. Description of the model

One-dimensional steady state cloud model is used to characterize the updraft region of convective clouds. The updraft velocity (w) of the ascending air parcel is determined by the buoyancy, lateral entrainment and weight of the hydrometeors:

$$\frac{dw}{dz} = \frac{g}{w}\left(\frac{T_{vc} - T_{ve}}{T_{ve}} \frac{1}{1+\alpha} - q\right) - \mu w, \tag{1}$$

where q is the mixing ratio of hydrometeors, T_{vc} and T_{ve} are the virtual temperature inside and outside of the air parcel, respectively. α is a correction parameter (0.5), which compensates the neglect of nonhydrostatic pressure perturbations (*Anthens*, 1977). The entrainment rate (μ) is directly proportional to the updraft velocity (w) and inversely proportional to the radius of the air parcel. The entraining air with cooler temperature and lower vapor content effects the total water content and temperature of the air parcel as well. Beside the water vapor, five types of water substances are considered: cloud water, cloud ice, snow, rain, and hail/graupel. Interactions between these substances

are simulated by bulk microphysics. The fall out of the precipitation particles is not allowed. The heat released during the freezing of supercooled drops, condensation, and deposition increases the temperature of the ascending air parcel. For estimation of the convective activity, the CAPE was calculated by taking into consideration that the temperature of the air parcel in addition to the releasing latent heat of condensation is affected by the entrainment of the cooler and dryer environmental air and by the releasing latent heat of fusion. More details about the model could be found in *Zoltán* and *Geresdi* (1984).

The one-dimensional steady state simulation describes the dynamics of the updraft core. Modifying the initial parameters of the ascending air parcel (e.g., temperature, radius, updraft velocity), it could be achieved that the calculated cloud top height agrees well with the radar observation (*Marwitz*, 1970). While the height of the cloud top is well observable parameter, unfortunately only a few measurements are available for the vertical updraft profile in convective storms. The reason of the absence of this type of data is that synchronization of two or three Doppler radars is necessary for measurement of the three-dimensional velocity field. The basic theory of the application of one-dimensional models for estimation of convective activity is that the good agreement between the observed and calculated maximum cloud top height means that the model calculates well the maximum updraft velocity as well (*Foot* and *Mohr*, 1979). The updraft velocity has a strong effect on the precipitation formation in convective clouds. The fast lifting of the air may results in low precipitation formation efficiency of the convective clouds (*Fankhauser*, 1988).

Although the hailstones spend most of their life time outside of the most intensive area of the updraft core, their size seems to be well correlated with the maximum of updraft velocity. However, the size of the hailstone on the ground is not only effected by the intensity of the storm, but the mass of the hail could be significantly reduced due to the melting between the 0°C level and the ground. A numerical model, which involves both of the above mentioned effects, was developed to estimate the maximum size of hailstones on the ground. The equation for initial radius of the largest hail particle comes from the assumption that the terminal velocity of the largest hailstones – could form in the cloud – is equal to the maximum of the updraft velocity:

$$w_{\max} = \sqrt{\frac{2\rho_h g d_{\max}}{3\rho_a c_d}}, \tag{2}$$

where $w_{\max}$ is the calculated maximum updraft velocity. The right side of this equation is the terminal velocity of the hailstone with diameter of $d_{\max}$.

The density of the hailstone (ρ_h) generally changed between 450 kg/m^3 and 950 kg/m^3. Low density particles form when the hailstone formation is initiated by aggregation of ice crystals, and the structure of the hailstone becomes porous. The density can increase over that of bulk ice if the melted water fills the pores. If hailstone forms from supercooled water drops with size of few millimeters and grows by collection of supercooled drops, its density is near to that of bulk ice. For simplicity, density of 900 kg/m^3 was used during the simulation. ρ_a is the density of air and c_d is drag coefficient (0.6).

Previous laboratory results show that the meltwater sheds from the ice core if the diameter of the hailstone is greater than 9 mm, and only a thin liquid layer remains on the surface of the hailstone (*Rasmussen et al.*, 1984). It is supposed that the falling particle does not collect either liquid or solid hydrometeors. Sensitivity studies made by *Rasmussen* and *Heymsfield* (1987b) shows that while collection of the liquid water hardly affects the melting rate, the low relative humidity significantly reduces it. If the heat transfer from the collected particles could be neglected, the melting rate depends only on the heat transfer from the ambient air and the heat released due to the diffusion of water vapor from the surface of the particle (*Rasmussen* and *Heymsfield*, 1987a):

$$\frac{dm_h}{dt} = \frac{1}{L_f}\{-4\pi r_h k_a (T_\infty - T_s) f_h - 4\pi r_h L D_v (\rho_{v,\infty} - \rho_{v,s}) f_v\}, \qquad (3)$$

where r_h is the radius of the hailstone, k_a and D_v are heat conductivity of air and vapor diffusion coefficients in air, respectively. T_∞ and T_s are the temperatures in the environment and on the surface of the graupel, $\rho_{v,\infty}$ and $\rho_{v,s}$ are the vapor densities far from the graupel and on its surface, respectively. The surface temperature of the melting hailstone is 273.15 K, and the vapor density at the surface is given by the saturation vapor pressure at the melting point. L_v and L_f are the latent heat of condensation and that of fusion, respectively. f_v and f_h are ventilation coefficients for vapor and heat transfer (*Pruppacher* and *Klett*, 1997), respectively:

$$f_v = 0.78 + 0.308 N_{Sc}^{1/3} N_{\mathrm{Re}}^{1/2},$$

$$f_h = 0.78 + 0.308 N_{Pr}^{1/3} N_{\mathrm{Re}}^{1/2},$$

where N_{Sc} and N_{Pr} are the Schmidt and Prandtl numbers. The first term between the brackets in Eq. (3) is the heat transfer due to the conduction; the

second term is the releasing latent heat due to vapor diffusion. The hailstone with initial size of d_{max} (Eq. (2)) starts to fall down from the height of the melting level. The time period, the melting particle spends between the melting level and the ground, depends on the terminal velocity of the falling particle and the strength of the downdraft. The terminal velocity is a function of the Reynolds number and was calculated on the base of the paper of *Rasmussen* and *Heymsfield* (1987a). Unfortunately, generally we have no data about velocity, vapor, and water content in the descending air. In the downdraft, due to the fall out effect and the strong mixing with environmental air, the water content could be significantly smaller than the adiabatic value. Because of this uncertainties the collision between the melting hailstones and water drops was not taken into consideration. Although the sensitivity studies show that the vapor content is an important parameter, unfortunately we have no information about how it changes in space and time. It is supposed that due to the evaporation of the raindrops the vapor content in the downdraft is near to the saturation value. This may not be true at the time, when the precipitation elements start to fall out from the cloud, but later the relative humidity should be near 100%. The ambient temperature of the falling hailstone was given by wet adiabatic descend starting from the level of -10°C, and the velocity of the descending air was supposed to be 5 m/s. In the downdraft of intensive storms this value could be higher, but it is generally less than 10 m/s. Underestimation of the downdraft overestimates the time period necessary for the hailstone to reach the ground, that is the melting of the hailstone is overestimated.

Fig. 1 shows the possible effects of these uncertainties on the calculated hailstone size. The effect of the downdraft intensity and that of the subsaturation were investigated by using three different downward velocities (0, 5, and 10 m/s) and three different values of relative humidity (80, 90, and 100%). The hailstone started to fall at height of 3.5 km with initial radius of 10 mm. That means that maximum updraft velocity in the convective storm where the hailstone formed was about 18 m/s. Due to the adiabatic warming the temperature of the air inside the downdraft increased from 0°C to 27°C. The hailstone lost only a few percent of its mass above the level of 2 km in every case. The explanation of the acceleration of the melting near to the ground is the larger air temperature and the increase of surface/mass ratio due to the melting. The shorter falling time period due to the increased downdraft velocity resulted in about 20% larger final hail size on the ground. The consequence of the lower of vapor content was also larger hail size. The larger the cooling rate caused by the evaporation from the surface of the hailstones, the larger the size of the hailstone was on the ground. Calculation was made also by relative humidity of 50%. In this case the size of the hail particle

hardly decreased and it was about 8.3 mm on the ground. However, low relative humidity like this is rarely observed in precipitation shaft.

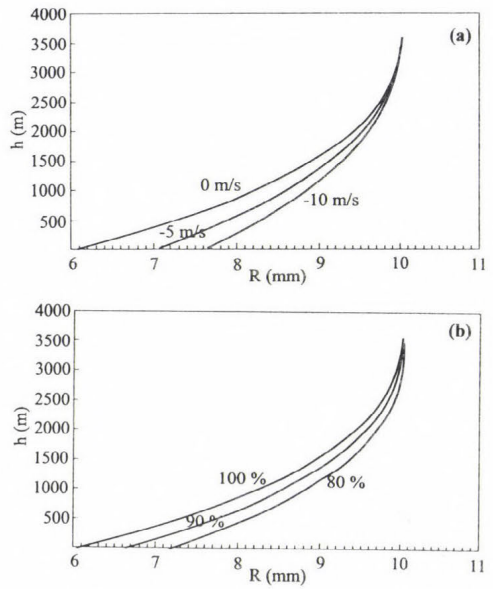

Fig. 1. Effect of downdraft (*a*) and relative humidity (*b*) on the melting of the hailstones. The calculation was made at three velocities of 0, 5, and 10 m/s, and with relative humidity of 100, 90, and 80%. The curves are denoted by the appropriate numbers. The downdraft was 0 m/s in all of the three cases in Fig. 1b.

3. Initialization

Input data of the model are produced by nowcasting system developed at the Hungarian Meteorological Service. The system uses real time data of surface observations (SYNOP), forecasted fields of a limited area model ALADIN (*Horányi et al.,* 1996), and calculates the objective analysis using optimal interpolation for data assimilation. Radar reflectivity data are also applied for analysis of relative humidity. The MEANDER (Mesoscale Analysis Nowcasting and Decision Routines) system produces high resolution (dx = dy = 3 km and dz = 200 m) 3D fields of basic parameters: pressure, geopotential height, temperature, relative humidity, and wind. We refer the reader to *Horváth* and *Geresdi* (2003) for more information about MEANDER.

The height and temperature of the condensation level are calculated by using dry adiabatic ascend from the ground. It is supposed that the air layer

above the ground is well mixed. The potential temperature and vapor content of the ascending air parcel are given by the following equations:

$$\bar{q}_{v,0} = \frac{1}{200}\int_0^{200} q_v(z)dz, \qquad \bar{\Theta}_0 = \frac{1}{200}\int_0^{200} \Theta(z)dz, \tag{4}$$

where the values of the $q_v(z)$ and $\Theta(z)$ functions are given by interpolation technique applied in MEANDER to calculate the parameters near the surface. The air parcel is initiated from the condensation level with radius of 5 km and updraft velocity of 5 m/s.

4. Application

Model output was compared with observations between May 1 and September 30, 2002, in southern part of Transdanubia (area of this region is about 840,000 ha). In this region of Hungary (target area) hail suppression has been carried out since early 90's. (Hungary is in central region of Europe bounded by longitudes of 16°19' and 22°48' and latitudes of 45°48' and 48°36'.) More details about the applied technique for the hail suppression could be read in *Dessens* (1986). S-band radar has been used to detect thunderstorms over the region. It was supposed that a thunderstorm formed if the maximum reflectivity of a cell reached 45 dBZ. Radar observations are compared with the calculated occurrence of thunderstorms. Reports of hail from the locations of the ground based generators are used to check the forecasted maximum hailstone size. (The mean distance between the generators is less than 10 km.) The nowcasting output is presented by a case study. On the August 4, 2002, an intensive precipitation system crossed the western part of the Hungary in southwest-northeast direction. This squall line was forecasted neither of the mesoscale models applied at the Hungarian Meteorological Service.

4.1 Case study of August 4

The synoptic analysis of the following case study is based on mean sea level pressure (mslp) and upper level (850 and 500 hPa) data of ECMWF analysis. In the morning of August 4, 2002, a cold front passed the Alpine region. At 06 UTC a prefrontal squall line appeared in the western part of Hungary (*Fig. 2a*). This squall line was indicated by line organized thunderstorms and moved from southwest to northeast. On the 850 hPa level, temperature and wind fields do not show significant cold or warm advection at 6 UTC (*Fig. 2b*), but on the 500 hPa level, massive cold advection can be recognized (*Fig. 2c*). At 12 UTC on the mslp chart, the squall line can be clearly divided from the cold

front (*Fig. 2d*). The cooling of the low level troposphere, caused by thunderstorms of the squall line, decreased the temperature gradient of cold front, that was the reason why only weak cold advection occurred on the 850 hPa level at 12 UTC above the investigated area (*Fig. 2e*). On the 500 hPa level, a characteristic cold trough could be recognized above the Carpathian Basin which was isolated from the western cold air mass (*Fig. 2f*). Definitely this high level, fast moving cold trough was responsible for increasing of convective components (*Horváth* and *Geresdi*, 2000), and after all for the formation of heavy thunderstorms. The height of the 0°C level was at about 3400 m (AGL) during the day.

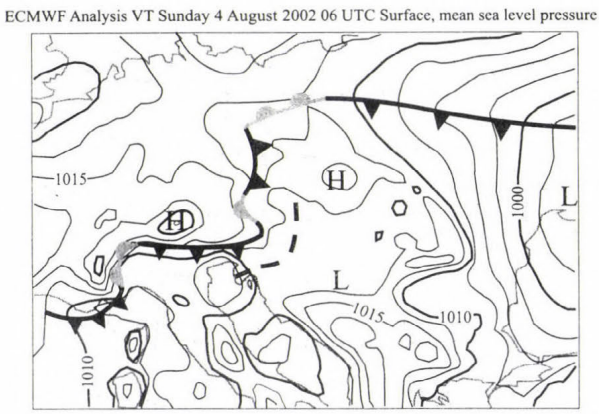

Fig. 2a. Mean sea level pressure field and front analysis at 06:00 UTC, August 4, 2002
The prefrontal squall line is close to the cold front.

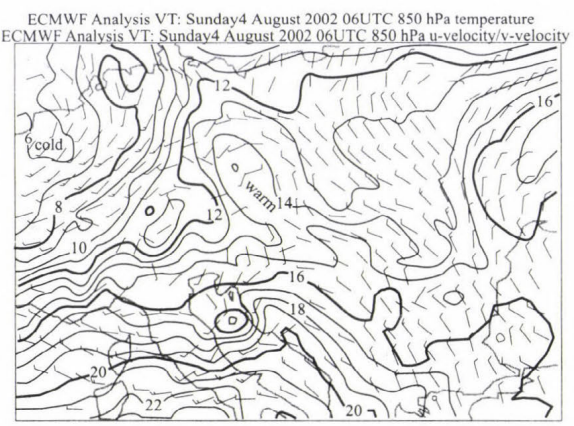

Fig. 2b. 850 hPa temperature and wind fields at 06:00 UTC, August 4, 2002.
There is no significant temperature advection.

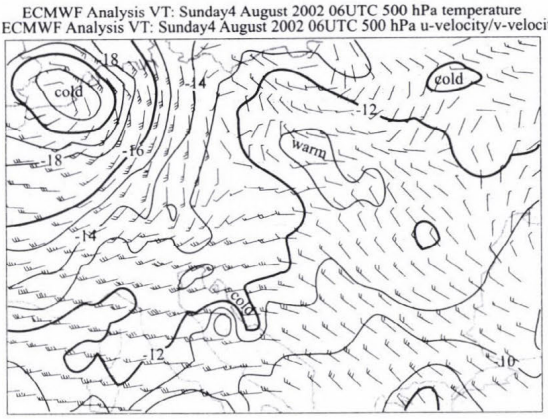

Fig. 2c. 500 hPa temperature and wind fields at 06:00 UTC, August 4, 2002. Characteristic cold advection can be recognized above the Carpathian Basin.

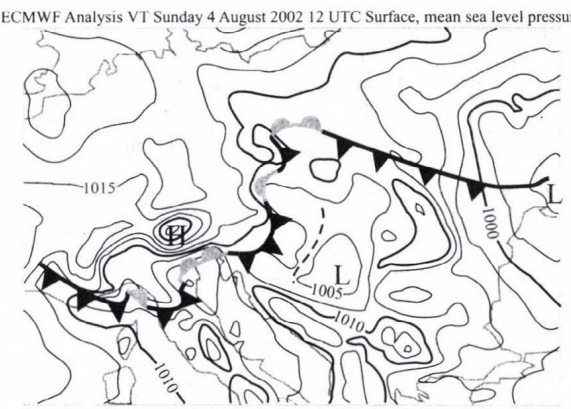

Fig. 2d. Mean sea level pressure field and front analysis at 12:00 UTC, August 4, 2002. The prefrontal squall line is well separated from the cold front.

The typical output of the nowcasting system are shown in *Fig. 3* and *Fig. 4*. The convective activity is characterized by the CAPE (*Fig. 3*), which was calculated by the one-dimensional, steady state numerical model. This figure shows the isolines for the CAPE at the time when the convective activity reached its daily maximum. Due to the large instability, formation of severe thunderstorms could be expected in an about 100 km wide region crossed Transdanubia in the direction of north-west – south-east. The model forecasted the formation of the thunderstorms one hour before the appearance of the first thunderstorm cells. The thunderstorms started to form at about 8 a.m. (UTC),

and cells with large reflectivity were observed until midnight. Although the convective activity significantly decreased after 10 p.m., a few cells were observed even the next morning. The time evolution of the maximum reflectivity and the number of the cells observed with reflectivity larger 45 dBZ are presented in *Table 1*. The maximum reflectivity was higher than 50 dBZ until 20:30. Large number of cells were observed in the morning between 9:30 and 10:30 and in the evening between 18:30 and 20:30. While the first maximum of the convective activity was the consequence of the approaching convergence line, the second maximum was due to the cold front.

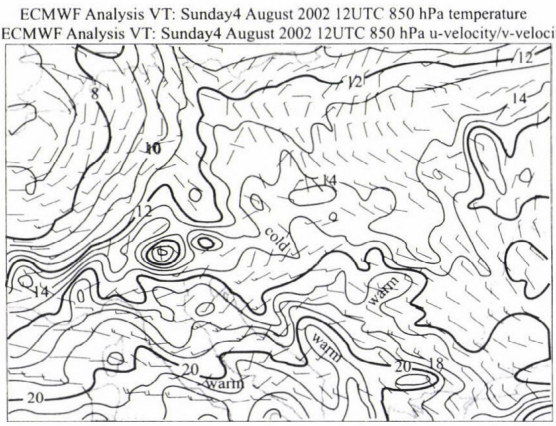

Fig. 2e. 850 hPa temperature and wind fields at 12:00 UTC, August 4, 2002. Thunderstorms of the prefrontal squall line decreased the temperature gradient of the cold front.

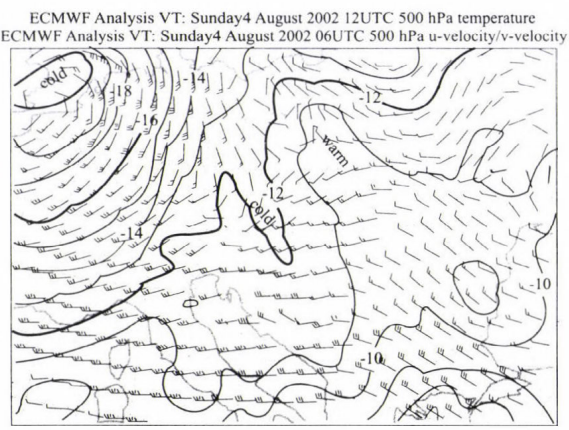

Fig. 2f. 500 hPa temperature and wind fields at 12:00 UTC, August 4, 2002. The high level cold trough of the prefrontal squall line is well separated from the main western cold air mass.

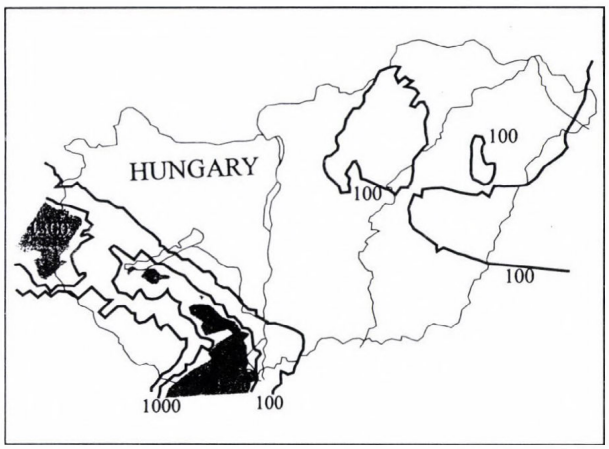

Fig. 3. CAPE calculated by the nowcasting system for the forecast of thunderstorm formation. This figure was released at 10:00 UTC, August 4, 2002. The numbers at the isolines denote the value of CAPE. The dark areas denote the region where the CAPE is larger than 1300 J/kg.

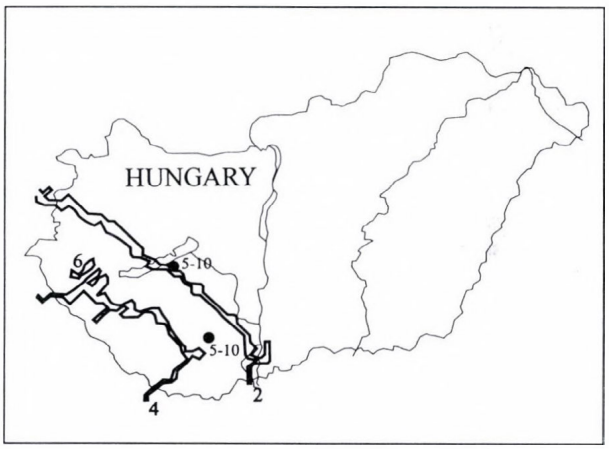

Fig. 4. Isolines of the maximum hailstone size at 10:00 UTC. The numbers at the isolines denote the diameter of the largest hailstones that could reach the ground. The black dots denote the places of the hail reports this day. The numbers at the black dots mean the observed size of the hailstones.

In the last column the reported maximum hailstone sizes are given. It is embarrassing that in spite of high reflectivity observed by S-band radar, only a few hail reports were sent this day. This discrepancy questions the applicability of the voluntary reports for verification of the model results. Comparison of

hailpad and radar observation shows that possibility of hail on the surface is large if the reflectivity is over 55 dBZ (*Dye* and *Martner*, 1978). The calculated maximum hailstone size (third column in *Table 1*) correlates well with the measured maximum reflectivity. (The model gives the maximum hailstone size in different size categories to make the comparison easier between model results and observations.) The isolines of the forecasted maximum hailstone sizes are also involved in the outputs of the nowcasting system (*Fig. 4*). (Note, that hailstone is defined as a bulk ice particle larger than 5 mm, the smaller ones are considered graupel particles.) The numbers next to the dots in this figure denote the reported hailstone sizes in mm. Although these data agree well with the calculated values, the verification of the output for the hailstone size needs more observations.

Table 1. Comparison of model results and observations on August 4, 2002. The first column gives the time in UTC. In the fifth column the number of cells with maximum reflectivity larger than 45 dBZ is given. d_{max} denotes the calculated and observed maximum hailstone size

Time	Model results		Observation		
	Thunder-storm	d_{max} (mm)	Max. refl. (dBZ)	N (cells)	d_{max} (mm)
7:30	yes	5 – 10	34.0	0	–
8:30	yes	5 – 10	45.0	1	–
9:30	yes	5 – 10	58.0	11	5 – 10
10:30	yes	10 – 30	55.0	10	5 – 10
11:30	yes	10 – 30	59.0	5	–
12:30	yes	10 – 30	52.0	5	–
13:30	yes	10 – 30	52.0	3	–
14:30	yes	10 – 30	57.0	1	–
15:30	yes	10 – 30	58.0	3	–
16:30	no	5 – 10	50.0	2	–
17:30	yes	5 – 10	53.0	4	–
18:30	yes	5 – 10	59.0	9	–
19:30	yes	5 – 10	54.0	12	–
20:30	yes	5 – 10	54.0	9	–
21:30	yes	5 – 10	54.0	7	–
22:30	yes	3 – 5	47.0	3	–
23:30	yes	3 – 5	39.0	0	–
0:30	no	–	43.0	0	–
1:30	yes	3 – 5	41.0	0	–
2:30	yes	3 – 5	37.0	0	–
3:30	yes	3 – 5	37.0	0	–
4:30	yes	–	43.0	0	–
5:30	yes	–	43.0	0	–
6:30	yes	–	48.0	1	–
7:30	no	–	44.0	0	–
8:30	no	–	45.0	2	–
9:30	no	–	40.0	0	–
10:30	no	–	42.0	0	–
11:30	no	–	29.0	0	–
12:30	no	–	31.0	0	–

Structure of the radar reflectivity pattern (*Fig. 5*) shows similarity to that of calculated CAPE. The direction of the band is similarly north-west – south-east, however, the cells characterized by high reflectivities lie about 50 km north of the calculated CAPE isolines. It is surprising that in spite of the very large value of the CAPE, no radar echoes were observed in southern part of Transdanubia, and low values of reflectivity were observed at the Hungarian-Austrian border. This disagreement emphasizes the importance of the initialization. It is strongly believed that the large values of the CAPE in the cloud free region are the consequence of the incorrect surface data. The check of the possible reasons needs further research.

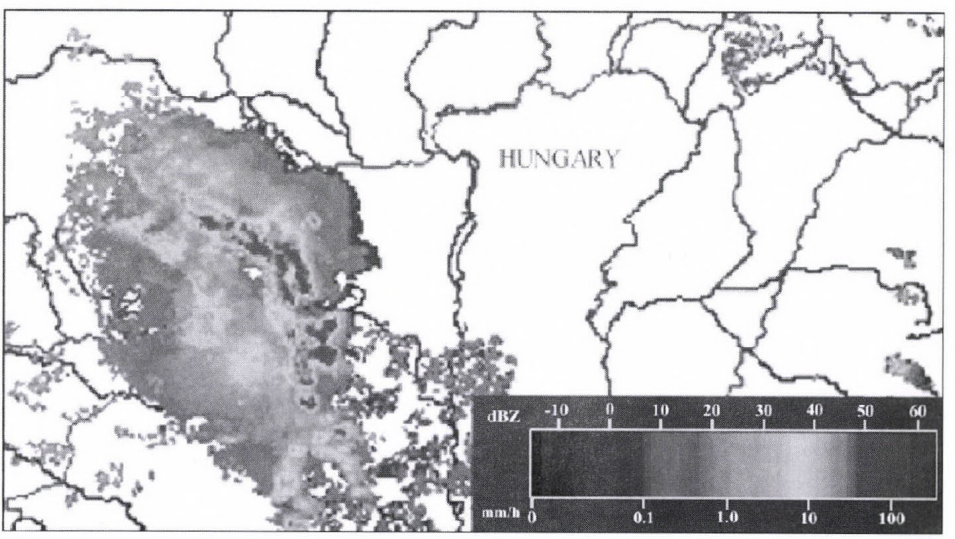

Fig. 5. Radar observation at 10:00 UTC.

5. Verification of model results

The content of *Tables 2* and *3* summarizes the comparison between the observation, based radar measurement and surface report of hail, and model results. The data were gathered over the whole season, between May 1 and September 30, 2002. The nowcasting system sent a report in every hour. These reports contained the warning of the thunderstorm formation and the maximum hailstone size could occur. The nowcasting system issues thunderstorm warning if one of the radars of the Hungarian Meteorological Service detects a thunderstorm cell, and the calculation of the cell movement

(see details in *Horváth* and *Geresdi*, 2003) predicts the appearance of the thunderstorm over the target area. This kind of the thunderstorm forecasting could be unreliable in the case of formation of the airmass thunderstorms. This type of thunderstorms rarely produces large hail, but because of the slow movement, it can result in flood.

Table 2. Observations versus model results for one hour forecast of the thunderstorms

Model	Observations	
	Yes	No
Yes	288	277
No	102	3075

Table 3. Observations versus model results for one hour forecast of the maximum hailstone size

Model	Observations	
	Yes	No
Yes	38	440
No	6	3188

Between May 1 and September 30 the maximum radar reflectivity was larger than 45 dBZ on 61 days. From these days the nowcasting system issued thunderstorm warning on 56 days, that is the system missed the forecast of thunderstorm on six days. Additional analysis of radar observation shows that although the maximum reflectivity was larger than 45 dBZ on these days, the structure of the radar pictures were very similar to that of stratified layer clouds, sometimes with weak embedded convective cells. That means that the nowcasting system forecasts the thunderstorm formation with high reliability on the days when environmental conditions promote this process. However, number of the days with thunderstorms was overestimated by the nowcasting system. Although thunderstorms were not observed by radar over the southern part of the Transdanubia, thunderstorm warning was issued on additional 15 days. This relatively larger ratio (about 25%) could be the consequence of the dissipation of the storm cells before they could reach the target area.

A more detailed analysis of the reports is presented in *Table 2* and in *Table 3* 3672 reports were sent by the nowcasting system during the season.

As *Table 2* shows, the formation of thunderstorm was forecasted 1 hour before the thunderstorms appeared over the target area on 288 occasions. False alarms were sent on 277 occasions. About two third of these reports was sent when the intensity of the thunderstorms decreased as they approached the target area (the maximum reflectivity decreased below 45 dBZ). This situation can be observed between 23:30 and 4:30 in *Table 1*. The convective cells were observed by the radar out of the target area, but their intensity gradually decreased as they approached the target area.

The remaining one third of the reports were released when due to the low activity of the convective cells, they completely dissipated before they reached the target area, or the propagation speed was not calculated correctly. This later case frequently occurred when the convective cells formed in airmass. The missing of the alarm on 102 occasions could be critical. As it is mentioned in the paragraph above, detailed analysis of the radar pictures shows that these situations mostly occurred when the clouds became stratified, and sometimes the maximum reflectivity increased slightly above the threshold value (see, e.g., report at 8:30 in *Table 1*).

Comparison of the hailstone size calculated by the model with that of reported by voluntary observers concludes that the model overestimates both the maximum size and frequency of hail occurrence (*Table 3*). However, as it was mentioned in the case study, we believe that these reports could not be considered to be representative. So further research is necessary for verification of the maximum hailstone size forecast.

6. Conclusion

The numerical model proved to be a useful tool for nowcasting of thunderstorm formation. As the case study showed, the shape of calculated CAPE field is very similar to the radar picture. However, it is not clear why no thunderstorm formation occurred in the southern part of Hungary and near the Austrian-Hungarian border, although the calculated instability was quite large in these regions. One possible explanations may be the inconsistency in the objective analysis between the hourly refreshing surface data and the higher levels forecasted fields which are predicted from the 00 UTC objective analysis. The coupling between the measured surface and forecasted upper level fields can produce physically deformed vertical profiles, when the calculated parameters differ considerably from that of the real atmosphere. The inadequate simulation of the dynamics of squall line could be another reason of the overestimation of the area where intensive thunderstorms formed. (The applied mesoscale model is a hydrostatic model.) In the future, a non-

hydrostatic numerical model is intend to be used, and also a more frequent (about in every 3rd hour) run of the model is planned to give the necessary initial parameters for nowcasting system. The case study shows that if the MEANDER forecasts the convective activity only on the base of calculated CAPE values, the frequency of the thunderstorm formation would be overestimated. The number of these false warnings are reduced by taking into consideration the earlier radar observations. Unfortunately this technique is not efficient in the case of the slowly moving airmass thunderstorms and for longer time period.

The contingency tables show that the reliability of the nowcasting system is high for one hour forecast, but considering the two or three hours forecast, the ratio of the false alarms gets larger.

Although the calculated maximum hailstone sizes correlate well with the large reflectivity values measured by the radar, the comparison with surface hail reports shows that the model significantly overestimates both the frequency of hail occurrence and the maximum hailstone size. This could be the consequence of the very simple model dynamics, and also the neglect of the collision between the water drops and hailstones in the precipitation shaft may lead to the overestimation of the maximum hailstone size. However, the comparison of the radar observations and the surface hail reports allows us to suspect that the reliability of these reports is questionable. The hailpad network, applied during the 80's, may be a more efficient way for surface observation of hailstones (*Székely* and *Zoltán*, 1984).

Acknowledgements—The authors are grateful to Nefela South Hungarian Association for Hail Suppression for providing the radar data and hail reports. The research was supported by the Hungarian Scientific Research Fund (T043010).

References

Aleksic, N., Nikolic, I., and *Jovanovic, D.*, 1991: Forecasting of convective activity using a one-dimensional steady-state cloud model. *Month. Weather Rev. 119*, 3099-3103.

Anthens, R.A., 1977: A cumulus parametrization scheme utilizing a one-dimensional cloud model. *Month. Weather Rev. 105*, 270-278.

Colle, B.A. and *Clifford F.M.*, 2000: The 5-9 February 1996 Flooding Event over the Pacific Northwest: Sensitivity Studies and Evaluation of the MM5 Precipitation Forecasts. *Monthly Weather Review 128*, 593–617.

Foote, G.B. and *Mohr, C.G.*, 1979: Results of a randomized hail suppression experiment in Northeast Colorado. Part VI: Post Hoc stratification by storm intensity and type. *J. Appl. Meteor. 18*, 1589-1600.

Frankhauser, J.C., 1988: Estimates of thunderstorm precipitation efficiency from field measurements in CCOPE. *Month. Weather Rev. 116*, 663–684.

Dessens, J., 1986: Hail in Southwestern France. II: Results of a 30-year hail prevention project with silver iodide seeding from the ground. *J. Climate Appl. Meteor. 25*, 48-58.

Dye, J.E. and *Martner B.E.*, 1978: The relationship between radar reflectivity factor and hail at the ground for northeast Colorado thunderstorms. *J. Appl. Meteor. 17*, 1335-1341.

Geresdi, I. and *Horváth, Á.*, 2000: Nowcasting of precipitation type. Part I: Winter precipitation. *Időjárás 104*, 241-252.

Horányi, A., *Ihász, I.*, and *Radnóti, G.*, 1996: ARPAGE/ALADIN: A numerical weather prediction model for Central-Europe with the participitation of the Hungarian Meteorological Service. *Időjárás 100*, 277-301.

Horváth, Á. and *Geresdi, I.*, 2000: Severe convective storms and associated phenomena in Hungary. *Atmospheric Research 56*, 127-146.

Horváth, Á. and *Geresdi, I.*, 2003: Severe storms and nowcasting in the Carpathian Basin. *Atmospheric Research 67-68*, 319-332.

Marwitz, J.D., Middleton, J.R., Auer, Jr., A.H., and *Veal, D.L.*, 1970: The dynamics of updraft vaults in hailstorm as inferred from the entraining jet model. *J. Atmos. Sci. 27*, 1099-1102.

Pielke, R.A., Cotton, W.R., Walko, R.L., Tremback, C.J., Lyons, W.A., Grasso, L.D., Nicholls, M. E., Moran, M.D., Wesley, D.A., Lee, T.J., and *Copeland, J.H.*, 1992: A comprehensive meteorological modeling system – RAMS. *Meteorol. Atmos. Phys. 49*, 69-91.

Pruppacher, H.R. and *Klett, J.D.*, 1997: *Microphysics of Clouds and Precipitation*. Kluwer Academic Publisher.

Rasmussen, R.M. and *Heymsfield, A.J.*, 1987a: Melting and shedding of graupel and hail. Part I: Model physics. *J. Atmos. Sci. 44*, 2754-2763.

Rasmussen, R.M. and *Heymsfield, A.J.*, 1987b: Melting and shedding of graupel and hail. Part II: Sensitivity study. *J. Atmos. Sci. 44*, 2764-2782.

Rasmussen, R.M., Levizzani, V., and *Pruppacher, H.R.*, 1984: A wind tunnel and theoretical study on the melting behavior of atmospheric ice particles. Part III. Experiment and theory for spherical ice particles of radius < 500 μm. *J. Atmos. Sci. 41*, 381-388.

Székely, Cs. and *Zoltán, Cs*, 1984: The hailpad possibilities of its usefulness. *Időjárás 88*, 32-45.

Zoltán, Cs. and *Geresdi, I.*, 1984: A one-dimensional steady-state jet model for thundercloud. *Időjárás 88*, 21-31

IDŐJÁRÁS

Quarterly Journal of the Hungarian Meteorological Service
Vol. 108, No. 1, January–March 2004, pp. 51–63

Implementation of CO_2 Q band line mixing computations into line-by-line atmospheric radiative transfer codes

Ferenc M. Miskolczi*[1] and **Martin G. Mlynczak[2]**

[1]*Analytical Services & Materials Inc.,*
One Enterprise Parkway, Suite 300 Hampton, VA 23666, U.S.A.
E-mail: f.m.miskolczi@larc.nasa.gov

[2]*NASA Langley Research Center, Mail Stop 420, Hampton, VA 23681-2199, U.S.A.*

(Manuscript received March 24, 2003; in final form February 12, 2004)

Abstract—In this paper, we discuss the computational difficulties of merging line-mixing models into line-by-line computations. We present the technical details of the upgrade of the High-resolution Atmospheric Radiative Transfer Code (HARTCODE) into an accurate reference line-by-line code for line mixing computations in the Q branches of the CO_2. The implementation of line mixing was based on the model, database, and software that were developed at the Laboratoire de Physique Moleculaire et Applications (LPMA), and the HITRAN2K database absorption line compilation. In the recent version of the line mixing database 306 vibrational bands of eight CO_2 isotopes are included, and there are provisions for calculations using the first order and the more accurate relaxation operator method. The successful integration of the line mixing computations has been validated using airborne and ground-based high-resolution HIS radiance measurements. This exercise can also be regarded as the validation of the line mixing database for high resolution, nadir viewing thermal emission measurements.

Key-words: HITRAN, line mixing, HARTCODE.

1. Introduction

According to comparisons of the high-resolution spectral radiance simulations with measurements, ignoring the CO_2 Q band line mixing effects could be responsible for errors of about 20 per cent in the computed outgoing long wave spectral radiance (*Haskins et al.*, 1999). Line mixing is a term to describe the effect of the pressure on the closely packed absorption lines belonging to the same

* Corresponding author. Tel: 757-827-4627; Fax: 757-825-8659

vibrational band. Whenever the line spacing is comparable to the pressure broadened half width, the lines will overlap and collision will broaden and mix the lines creating interference terms in the band shape. More detailed theoretical description and quantitative analysis of line mixing can be found in the literature, see for example *Armstrong* (1982).

Here we shall focus only on the technical details of how line mixing may be implemented into a line-by-line (LBL) atmospheric radiative transfer code. In particular, how the LPMA line mixing model (*Rodriguez et al.*, 1999; *Jucks et al.*, 1999) was implemented into the HARTCODE (*Miskolczi et al.*, 1990; *Rizzi et al.*, 2002).

The size of the most recent version of the LPMA distribution archive is about 17 MB (un-compressed), representing the situation of the database in May 2002. In the database the absorption line and line mixing parameters of 18708 CO_2 Q lines in the 468–6936 cm^{-1} spectral range are organized into 918 files. The structure of the archive is very clear and compact, see *Fig. 1*. The SOFT_Q directory contains software that is ready for use for any homogeneous CO_2 path. In DATA_Q the BANDINF.DAT file gives a summary of the included vibrational transitions. Files $S_1 \ldots S_{306}$, $Y_1 \ldots Y_{306}$, and $W_1 \ldots W_{306}$ are the spectroscopic information, first order line mixing coefficients, and the elements of the relaxation operator, subsequently. The TEST_Q directory contains precomputed cases for the consistency check of the full database. The sub-branches of the asymmetric CO_2 molecules are treated as separate bands. The number of the 'true' Q branches is 271. The LPMA database and software are not optimized for LBL radiative transfer computations in the atmosphere.

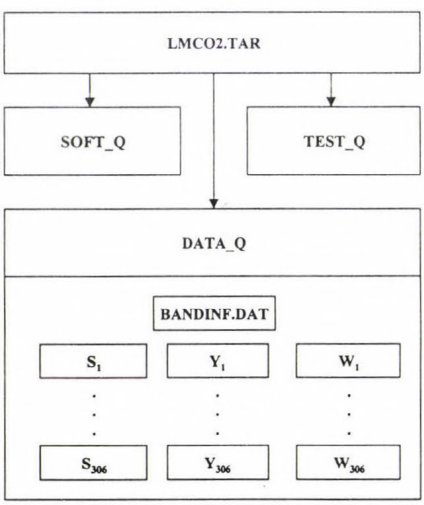

Fig. 1. Structure of the LPMA CO_2 Q band line mixing archive.

HARTCODE is a general purpose software for optical depth, transmittance, radiance, and flux density computations in a spherically stratified refractive atmosphere using the LBL method. The schematic diagram of the code is presented in *Fig. 2*. The LAYER–1 section processes the input atmospheric profile and may output details of the slant path, layering, and viewing geometry. The spectral quantities are read in the wave number loop, and this is the place where line mixing parameters will enter. LAYER–2 module computes the monochromatic optical depth over an appropriate wavenumber grid which is necessary for the wavenumber integration. This part of HARTCODE has been substantially modified to accommodate line mixing computations. In the LAYER–3 module the spectral mean quantities of the output parameters are computed for any required viewing geometry. HARTCODE uses a unique input absorption line file, which is prepared by a preprocessing code. This file is shaped for fast and efficient use with a given radiative transfer problem.

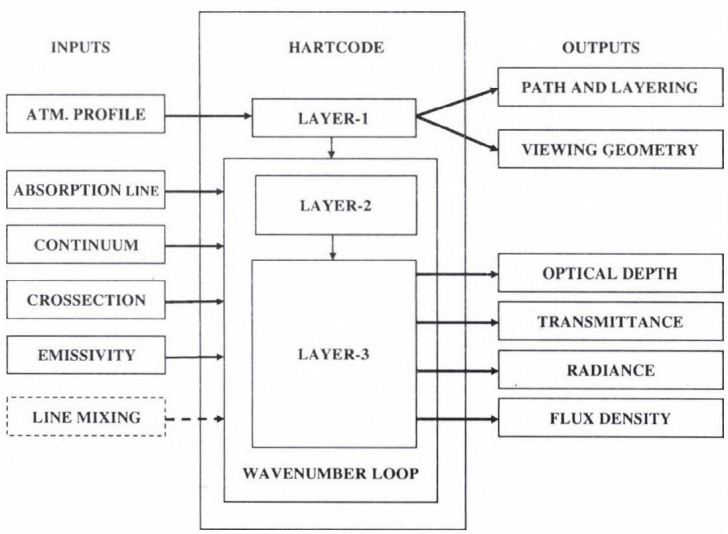

Fig. 2. Schematic structure of the High-resolution Atmospheric Radiative Transfer Code.

In this work the input absorption lines were taken from the HITRAN2K database (*HITRAN2K,* 2002). This compilation contains over a million transitions of 38 different absorbers, but the CO_2 Q lines are identical to those of present in the 1996 edition (*Rothman et al.*, 1998). The HITRAN2K database contains several improvements, among others, improved water vapor line parameters, which are important when comparing simulated and measured radiance spectra.

Regarding the CO_2, we have altogether 60802 transitions, out of these 11694 are Q lines of 328 Q bands. Although, in its original form, the HITRAN2K absorption line file is suitable for line-by-line computations, for efficient use, and for line mixing computations it must be re-shaped.

Implementation of line mixing into HARTCODE was taken in two steps. First the LPMA and HITRAN2K databases were treated to make them suitable for direct HARTCODE access. Next, the subroutines to compute line-mixing with the first order or the relaxation operator method were added, together with the necessary changes in some existing HARTCODE modules.

2. Modifications related to the LPMA and HITRAN2K databases

In HARTCODE the grid structure for wave number integration over a given resolution is non-uniform, and is set up by using the absorption line positions present in the input line file. The LPMA and HITRAN2K databases were created by using different sources of theoretical and experimental spectroscopic data, therefore, the first step was to solve line compatibility problems between the two databases. HITRAN2K contains several Q bands which are not included in the LPMA, while most of the coincidental Q bands contain more absorption lines in the LPMA than in the HITRAN2K. In *Fig. 3* the absorption lines in the coincidental Q bands are plotted in the 500–1000 cm^{-1} spectral range. Apparently, most of the excessive LPMA Q lines are weak. In case the wave number grid points are generated using the HITRAN2K lines, grid points would be missing for these weak lines. On the other hand, merging thousands of very weak LPMA Q lines into the input line file would introduce unnecessary computational burden, which should be avoided. However, the line mixing computation of the monochromatic absorption coefficient requires all rotational lines of a given vibrational transition that were included in the development of the LPMA parameterization.

The simple practical solution to the above problem is to use two properly organized and filtered data files. The first one is an ordinary line file which contains all transitions of all absorbers that have significant contributions to the absorption coefficients. Also, it should contain a kind of complex flag which identifies the Q bands for which line mixing coefficients are available in the LPMA database. This first file will control the setup of the wavenumber grid. The second file contains all LPMA Q lines and the line mixing coefficients sequentially organized into blocks by the minimum wave number of the rotational lines in the contributing vibrational bands. To create these two files, the HARTCODE line preprocessing software was modified. The modified code is performing the following tasks:

- Checks the original HITRAN2K data file for unhandled transitions.
- Determines the coincidental Q bands and marks the related transitions.
- Re-organizes the LPMA database into a blocked sequential file.
- Merges the LPMA database to the HITRAN2K.
- Applies filters on the combined database and creates the final line file.

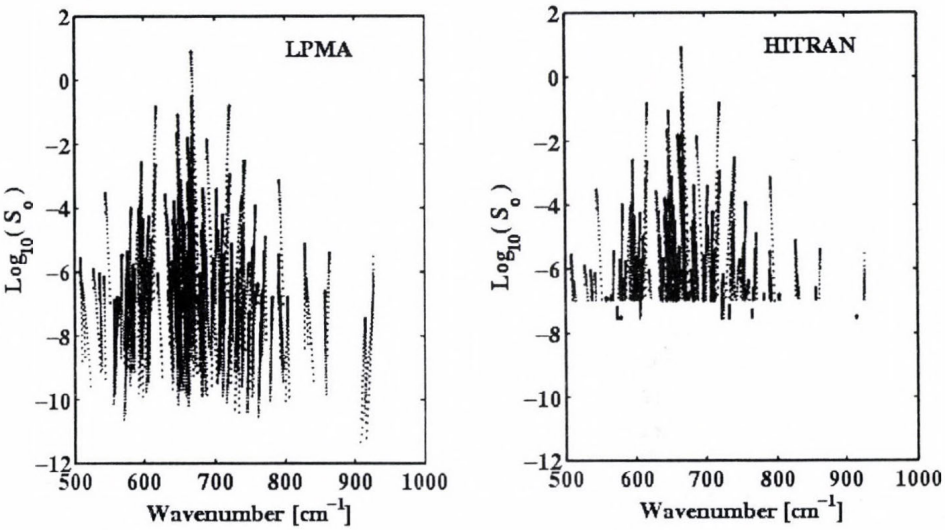

Fig. 3. Intensity distributions of the LPMA and HITRAN2K Q lines in the coincidental Q bands. S_o [cm^{-1} (atm-cm$_{STP}$)$^{-1}$] is the line intensity at 296 K.

As an example of the operation of the pre-processing code, some numerical results for a spectral radiance simulation problem in the 450–3550 cm^{-1} spectral range, using a vertical path trough the whole USS 76 atmosphere are given. In this case the filters were set to keep only those transitions which contribute more than 10^{-2} per cent to the total Voigt monochromatic absorption coefficients at the line centers. As a result, there remained 98994 transitions in the final absorption line file (with 21336 CO_2 and 8740 coincidental CO_2 Q lines), and 11968 transitions in the LPMA line mixing file. Ten other molecular species, H_2O, N_2O, CO, CH_4, O_2, NO, SO_2, NO_2, and N_2 were also contributing to the final number of transitions. These line files were used at the validation of the line mixing model with the High-resolution Interferometer Sounder (HIS) measurements.

In case of interest, a complete set of five FORTRAN line processing routines are available from the authors. These codes may be used to process the LPMA database with the different HITRAN editions or other absorption line archives.

3. Modifications in HARTCODE

Major modifications of the HARTCODE were needed for two reasons. Firstly, the nature of the computation of the line mixing with the first order or relaxation operator method requires the interruption of the strict sequential reading of the input absorption line file, and jump into a reading sequence, based on the positions and widths of the vibrational bands. Since Q bands have complex overlapping structure, the treatment of the ordinary lines and the marked Q lines is rather complex. Secondly, the mathematical representations of the line mixing computations require the efficient evaluation of the complex probability function and library routines for handling complex operators. A summary of the equations relevant to the line mixing computations is given in the Appendix.

Introducing the line mixing option into the HARTCODE resulted in significant increase of the size of the code. The new version of HARTCODE contains about 1700 more program lines. Eleven subroutines have been added. The first six are performing the following tasks: read the LPMA Q line file; evaluate the complex probability function; compute the transition population, first order line mixing coefficients, Lorentz half widths, and relaxation matrix elements for the current temperature and pressure; compute the absorption coefficients; compute the equivalent Q lines. The other six routines are from the LPMA Mathematical Library and their tasks are to diagonalize and invert complex operators. Some of the above routines are the slightly modified versions of the codes available in the SOFT_Q directory of the LPMA distribution archive. During the implementation major efforts were devoted to resolve the synchronized reading of the two absorption line files and to develop consistent line wing cut–off concept for the coincidental Q lines.

As an illustration, the effect of the code modifications is shown in *Figs. 4* and *5*, where monochromatic layer optical depth computations are compared with- and without applying line mixing. In *Fig. 4* the unmodified code results are presented. In *Fig. 5* the difference between the two curves at the top shows the effect of the line mixing on the total optical depth. The maximum difference is about 50 per cent and it occurs at around 618.5 cm^{-1}. The set of curves at the middle of *Fig. 5* represents the optical depth from the LPMA Q lines, and the bottom set of curves are the contributions from the other molecules and non-LPMA Q lines. Each curve in the sets shows the variation of the optical depth of an atmospheric layer between the altitudes of 0 and 20 km.

The spectral interval has a width of 1.0 cm^{-1} and contains 1332 grid points for the wavenumber integration.

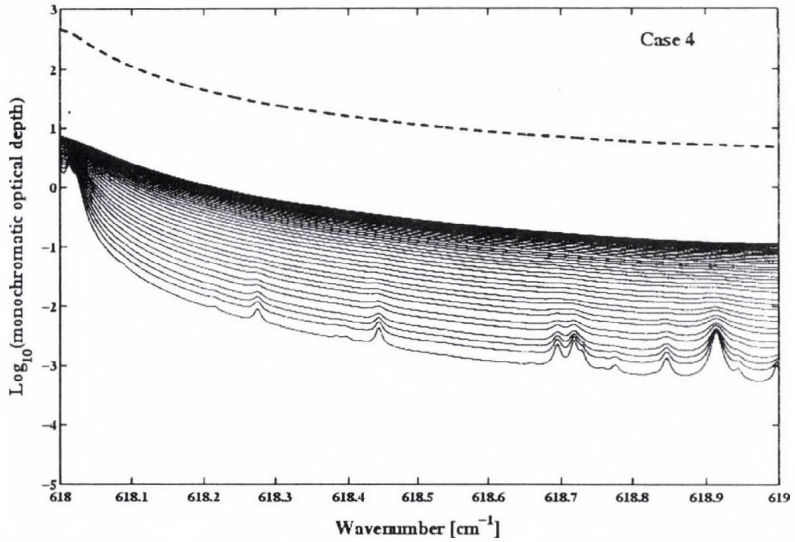

Fig. 4. Monochromatic optical depth of the atmospheric layers at different altitudes. Computed for the UWITRA93 case 4 without line-mixing. Dashed line is the total optical depth through the 20 km vertical path.

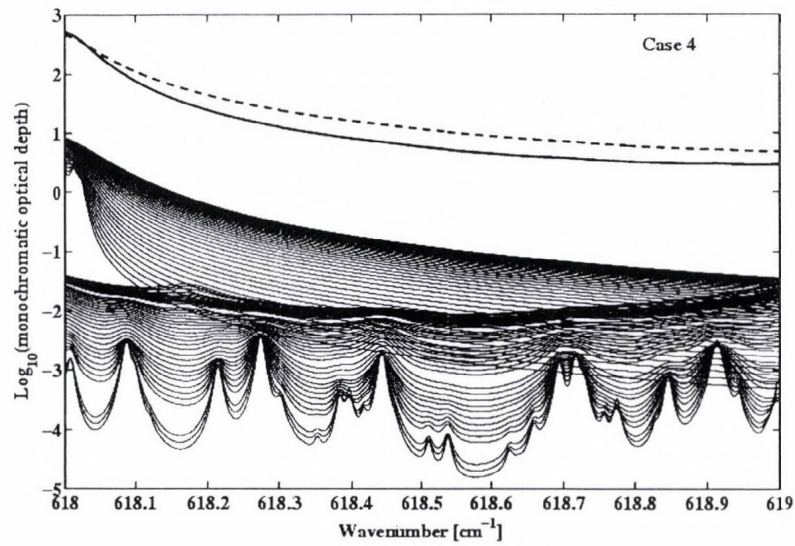

Fig. 5. Monochromatic optical depth of the atmospheric layers at different altitudes. Computed for the UWITRA93 case 4 with line-mixing. The top two lines are the total optical depths with- and without line-mixing. The two set of curves are the results of the separation of the absorption lines into LMPA Q lines and other absorption lines.

4. Validation

To validate the newly implemented line mixing algorithm for atmospheric applications, we selected the UWITRA93 data set (*Knuteson,* 1993). Since HARTCODE was participating in the 1993 ITRA exercise, the atmospheric profiles and the radiance measurements were ready for immediate use, see *Figs. 6* and *7*. In the data set there are two up-looking (ground based), and two down-looking (airborne) measurements. The unapodized spectral resolution of the HIS instrument in the band 1 (600–1080 cm^{-1}) is about 0.3 cm^{-1}. HARTCODE radiances, with- and without applying first order line mixing computations, were computed with 0.005 cm^{-1} spectral resolution. The relative differences in the downward radiances, (cases 1 and 2), are about 20 to 50 per cent, but for Q bands closer to the window region it may exceed 80 per cent, see *Fig. 8*. The line-mixing effects on the upward radiances, (cases 3 and 4), are considerably less, and remain below 20 per cent. This is mainly due to the significant contributions to the radiances from the surface.

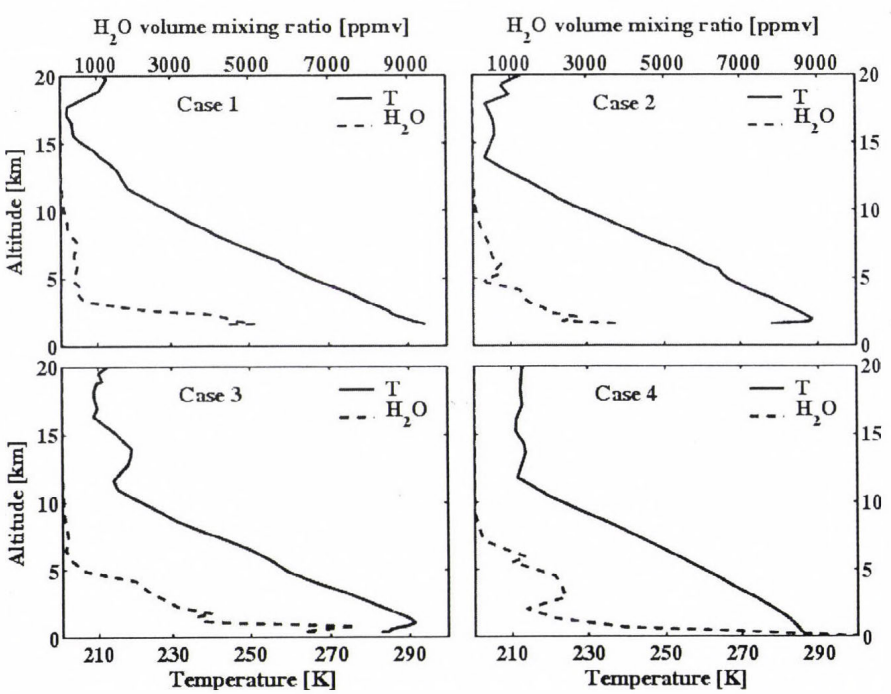

Fig. 6. Temperature and H_2O volume mixing ratio profiles of the UWITRA93 data set. Cases 1 and 2 were used for the ground based HIS simulations and cases 3 and 4 were used for the simulations of the aircraft measurements.

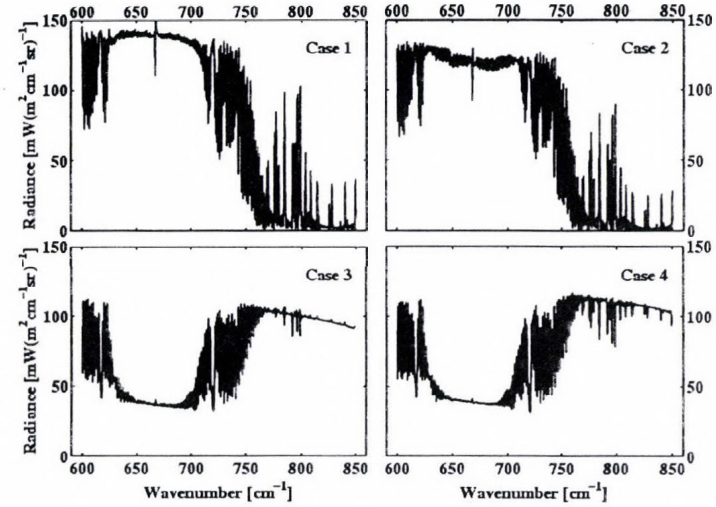

Fig. 7. High-resolution Interferometer Sounder radiance measurement in band I for the UWITRA93 cases. These radiances were used for the validation of the line-mixing model and its implementation into HARTCODE. The spectral resolution is 0.36 cm^{-1}.

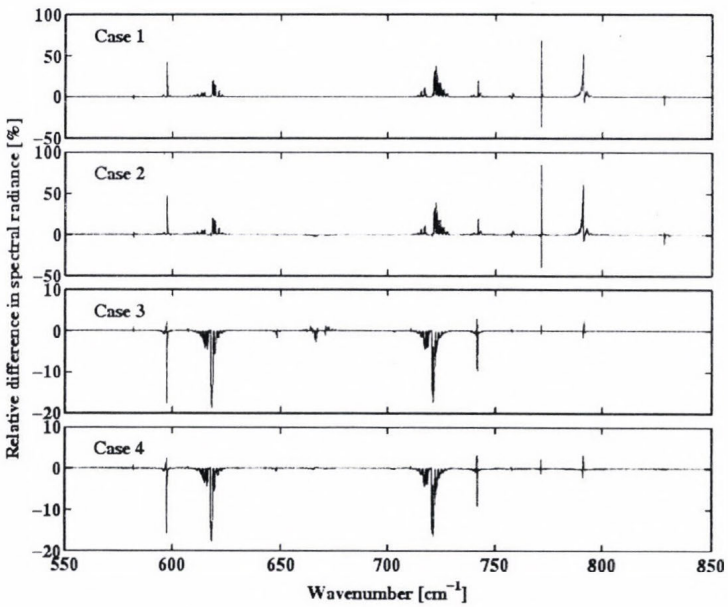

Fig. 8. Effect of line-mixing on the high-resolution simulated spectra. UWITRA93 cases, 0.005 cm^{-1} spectral resolution. The relative difference is defined as $100(R-R_x)/R_x$, where R is the radiance without line-mixing and R_x is with line-mixing.

To model the HIS measurements, the HARTCODE radiances were evaluated using the FFT method, which involves interpolation, smoothing, fast Fourier transform, truncation, zero filling, and inverse Fourier transform. Here we used linear interpolation for 2^{19} discrete wavenumber points. Since unapodized radiances can have zero or negative values, relative errors can not be computed. In *Fig. 9* the differences in the simulated and measured radiances are displayed. The upper curves in case 1 and 2 and the lower curves in case 3 and 4 are the differences without line mixing. The other four curves in the plots (they are vertically offset by +/–10 units for better view) show the differences when the line mixing effect was considered. Here we are not going into the quantitative details of the comparison, our purpose is merely to show that the LPMA line mixing model works properly within HARTCODE. Apparently, there are large improvements by introducing the line-mixing, actually bringing the differences close to the instrument noise. Line-mixing computations with the relaxation operator method produced very similar results, (not shown here), but with considerably longer computing time. Obviously, line mixing computation has a price. The computer time necessary to run a case was increased by a factor of three for the first order method, and a factor of six for relaxation operator method. Note, that one single HARTCODE run in the 450–3500 cm^{-1} spectral range, (with 0.005 cm^{-1} resolution and using 80 atmospheric layers), without line mixing takes about 15 minutes on a 2.8GHz HP PC.

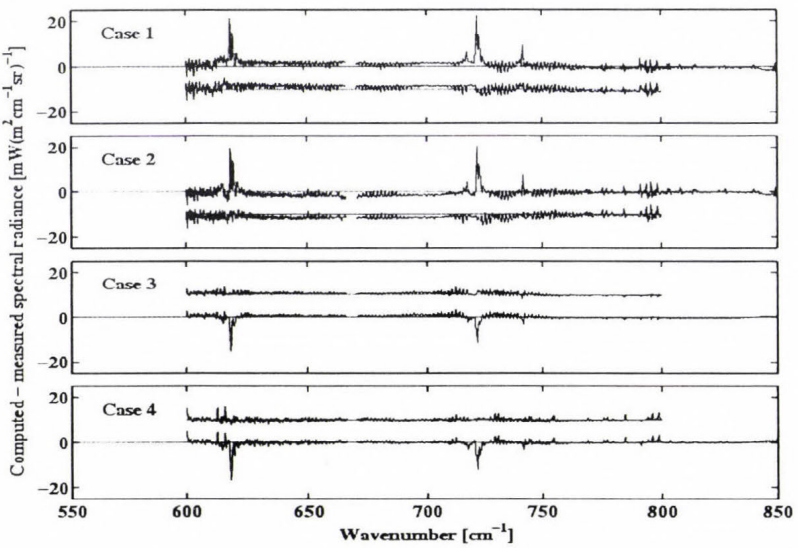

Fig. 9. Effect of line-mixing on the simulation errors. The longer curves in the plots were computed without line-mixing. The shorter curves, with +/–10 units vertical offsets, are the errors when line-mixing was considered in the calculations.

5. *Conclusions*

Here we have demonstrated that the LPMA line mixing model can be effectively implemented and used within a line-by-line atmospheric radiative transfer code. The key to the LPMA data base was to make it suitable for simultaneous sequential processing with the HITRAN2K absorption line file. It appears that the development of an interface code which is unique for the LPMA database, (or for any other line mixing database with different structure), is always necessary. The excellent documentation of the LPMA archive made this job relatively easy. Once this code is developed, the use of further editions of the HITRAN database with different CO_2 lines, or using a new LPMA edition (with better line mixing parameters, but with the same structure) will be a matter of re-running the software. The increased computer time of the LBL calculations has little importance when the accuracy is the primary concern.

The scientific community, engaged with molecular spectroscopy and atmospheric radiative transfer, has long time been awaiting for readily available line mixing parameters and algorithms that are included into the further editions of the HITRAN database. Regarding the number of existing line mixing models and parameterizations, see for example *Hoke et al.* (1994), *Strow et al.* (1994), *Timofejev et al.* (1997), the evaluation, selection, and implementation could take a long time. Meanwhile, as the most recent and most comprehensive CO_2 line-mixing archive, the LPMA model may be used alternatively.

Acknowledgements—We are very grateful to *J. M. Hartmann* for the most recent version of the LPMA line mixing archive and to *R. O. Knuteson* for the HIS measurements and the related documentation.

APPENDIX

Formulas relevant to line-mixing computations

Line intensity definition in HITRAN (in units of cm^{-1} (molecules $cm^{-2})^{-1}$):

$$S_i^0 = \Pi_i(T_0) D_i^2 \nu_i (1 - \exp(-c_1 \nu_i / T_0)).$$

Voigt monochromatic absorption coefficient for non-LPMA Q lines and other CO_2 lines:

$$k_\nu(p,T) = \mathrm{X}_{CO_2} \frac{T_S p}{p_S T} L_0 \sum_{i=1}^{N} S_i^0 \frac{\left(1 - e^{-c_1 \frac{\nu}{T}}\right) F_i(T_0)}{\left(1 - e^{-c_1 \frac{\nu_i}{T_0}}\right) F_i(T)} \sqrt{\frac{\ln 2}{\pi}} \frac{e^{-c_1 E_i \frac{T_0 - T}{T_0 T}}}{c_3 \sqrt{\frac{T}{M_i}} \nu_i} [V(x,y)]^{RE}.$$

First order line mixing absorption coefficient for LPMA Q lines:

$$k_v^F(p,T) = A_v(p,T)\sum_{i=1}^{N} B_v^i(T)\left(\left[V(x,y)\right]^{RE} - Y_i(T)\left[V(x,y)\right]^{IM}\right).$$

Absorption coefficient for the equivalent Q lines:

$$k_v^R(p,T) = A_v(p,T)\sum_{i=1}^{N} \frac{\left([SE_i]^{RE}[V(x,y)_i]^{RE} - [SE_i]^{IM}[V(xx,yy)_i]^{IM}\right)}{c_3\sqrt{\frac{T}{M_i}}},$$

where

and

$$A_v(p,T) = \mathrm{X}_{CO_2}\frac{T_S p}{p_S T}L_0(1-e^{-c_1\frac{v}{T}})\sqrt{\frac{\ln 2}{\pi}},$$

$$B_v^i(T) = \Pi_i(T_0)\frac{F_i(T_0)}{F_i(T)}D_i^2\frac{e^{-c_1E_i\frac{T_0-T}{T_0T}}}{c_3\sqrt{\frac{T}{M_i}}}.$$

List of symbols

$\Pi_i(T_0)$	Population at temperature T_o
D_i	Dipole moment
v_i	Resonance wavenumber, cm^{-1}
c_1	1.4387686
T_0	296.00 K
X_{CO2}	CO_2 volume mixing ratio
T_s	273.15 K
p_s	1013.25 hPa
T	Temperature, K
p	Pressure, hPa
L_o	2.68710×10^{19}
v	Wave number, cm^{-1}
N	Total number of the Q lines of all contributing bands
$F_i(T)$, $F_i(T_0)$	Partition functions of the CO_2 isotope
E_i	Ground state energy
c_3	3.58128×10^{-7}
M_i	Molecular weight of the CO_2 isotope
$V(x,y)_i$	Complex probability function
$x = (v - v_i)(\ln 2)^{1/2}/\alpha_D$	Real part of the argument of V
$y = \alpha_L/\alpha_D(\ln 2)^{1/2}$	Imaginary part of the argument of V
$\alpha_D = c_3(T/M_i)^{1/2}v$	Doppler half width
$\alpha_L = \alpha_o^i(p/p_s)(T_0/T)$	Lorentz half width

Γ	Temperature coefficient of the ith transition
α_o^i	Lorentz half width at T_o and p_s
$xx = (H^R + \nu_i^* - \nu)(\ln 2)^{1/2}/\alpha_D$	Real part of the argument of V for the equivalent lines
$yy = H^I (\ln 2)^{1/2}/\alpha_D$	Imaginary part of the argument of V for the equivalent lines
H^R	Positions of the equivalent lines
H^I	Half width of the equivalent lines
SE_i	Complex intensities of the equivalent lines
ν_i^*	Population-averaged wave number.

The superscripts *RE* and *IM* refers to the real and imaginary part of the V complex probability function and $Y_i(T)$ is the first order line mixing coefficient. The sums in the above equations are extended to all the lines of all contributing Q bands at a particular wavenumber. Detailed explanation of H^R and H^I can be found in *Rodriguez et al.* (1999).

References

Armstrong, R.L., 1982: Line mixing in the ν_2 band of CO_2. *Applied Optics 21*, 2141-2145.

HITRAN2K. 2002; http://cfa-www.Harvard.edu/HITRAN/hitrandata.

Haskins, R., Goody, R., and *Chef, L.*, 1999: Radiance covariance and climate models. *J. Climate 12*, 1409-1422.

Hoke, M. L., Clough, S.A., Kneizys, F.X., and *Anderson, G.P.*, 1994: Line coupling in fifteen micron carbon dioxide Q-branches: Review and implementation in FASCOD3. *Proc. SPIE 2309*, 170-183.

Jucks, K. W., Rodriguez, R., LeDoucent, R., Claveau, C., Traub, W.A., and *Hartmann, J.M.*, 1999: Model, software, and data-base for computation of line-mixing effects in infrared Q branches of atmospheric CO_2. II. Minor and asymmetric isotopomers. *J. Quant. Spectros. Radiat. Transfer 63*, 31-48.

Miskolczi, F., Bonzagni, M., and *Guzzi, R.*, 1990: High resolution atmospheric radiance - transmittance code (HARTCODE). In *Meteorology and Environment Sciences: Proc. of the Course on Physical Climatology and Meteorology for Environmental Application*. World Scientific Publ. Co. Inc., Singapore, 743-790.

Rodriguez, R., Jucks, K.W., Lacome, N., Blanquest, G., Valrand, J., Traub, W.A., Khalil, B., LeDoucent, R., Valentin, A., Camy-Peyret, C., Bonamy, L., and *Hartmann, J.M.*, 1999: Model, software, and data-base for computation of line-mixing effects in infrared Q branches of atmospheric CO_2. I. Symmetric isotopomers. *J. Quant. Spectros. Radiat. Transfer 61*, 153-184

Rizzi, R., Matricardi, M., and *Miskolczi, F.*, 2002: Simulation of uplooking and downlooking high-resolution radiance spectra with two different radiative transfer models. *Applied Optics 41*, 940-956.

Rothman, L.S., Rinsland, C.P., Goldman, A., Massie, T., Edwards, D.P., Flaud, J.-M., Perrin, A., Camy-Peyret, C., Dana, V., Mandin, J.-Y., Schroeder, J., Cann, A., Gamache, R.R., Wattson, R.B., Yoshio, K., Chance, K.V., Jucks, K.W., Brown, L.R., Nemtchinov, V., and *Varansi, P.*, 1998: The HITRAN molecular spectroscopic database and HAWKS (HITRAN atmospheric workstation): 1996 edition. *J. Quant. Spectrosc. Radiat. Transfer 60*, 665-710.

Strowe L.L., Tobin D.C., and *Hannon S.E.*, 1994: A compilation of first-order line-mixing coefficients for CO_2 Q-branches. *J. Quant. Spectrosc. Radiat. Transfer 52*, 281-294.

Timofejev Y.M., Polyakov A V., Tonkov M.V., and *Filippov N.N.*, 1997: Line-mixing influence on the slant path transmittance and limb atmospheric radiation in different IR absorption bands. IRS'96: Current Problems in Atmospheric Radiation. *Proc. of IRS'96*, Fairbanks, Alaska, USA, 1004-1007.

IDŐJÁRÁS

Quarterly Journal of the Hungarian Meteorological Service
Vol. 108, No. 1, January–March 2004, pp. 65–75

Aerodynamic properties of air layer above maize canopy during windy conditions

Taťjana Hurtalová[1], František Matejka[1], Blanka Chalupníková[2] and Jaroslav Rožnovský[3]

[1]*Geophysical Institute of the Slovak Academy of the Sciences, Dúbravská cesta 9, 845 28 Bratislava 45, Slovak Republic; E-mail: geoftahu@savba.sk*

[2]*Czech Hydrometeorological Institute, Kroftova 43, 616 67 Brno, Czech Republic; E-mail: chalupnikova@chmi.cz*

[3]*Department of Landscape Ecology, Mendel University of Agriculture and Forestry, Zemědělská 1, 613 00 Brno, Czech Republic; E-mail: roznovsky@chmi.cz*

(Manuscript received April 5, 2002; in final form February 7, 2003)

Abstract—The analysis of the wind speed profile measurements carried out above maize canopy during the whole growing season were used for dependence parameterization of the dynamic roughness length z_0 as well as aerodynamic resistance r_a on the wind speed $u(z)$. The investigated experimental field is situated in Žabčice, Czech Republic (49°01'N, 16°37'E, 179 m a.s.l.). The zero plane displacement d, the roughness length z_0, and the aerodynamic resistance r_a values were determined during the whole maize growing season. On the basis of these values, the dependence of the z_0 and ra values on the wind speed was found and quantitavely expressed for this canopy surface. For zero plane displacement d we accepted the fact, that the relation $d = (2/3)h$ is well representative for agricultural crop covered surfaces. The average roughness length of closed maize canopy was from 0.24 m in August to 0.19 m in October with mean canopy height of 2.24 m and 2.15 m, respectively. The dependence of friction velocity u^* on the wind speed $u(0.5\ \mathrm{m})$ can be fitted as $u^* = 0.62[u(0.5\,\mathrm{m})]^{0.69}$. The function $z_0 = f(u)$ can be analyzed as the dependence of the relative roughness length $\xi_0 = z_0/h$ on the nondimensional speed $\Gamma = u(h)/u^*$. For this dependence the analytical relationship was found in the form: $\xi_0 = 0.162 \exp(-0.306\,\Gamma)$. The aerodynamic resistance decreases with increasing wind speed. This dependence is more complicated, because the r_a-values depend also on the rougness length and atmosphere's thermal stratification.

Key-words: wind speed profile, friction velocity, roughness length, zero plane displacement, aerodynamic resistance, maize.

1. Introduction

A coupling of the airflow and the canopy surface takes place above a flexible vegetation during windy conditions. This builds up the waving form of the canopy surface in addition to producing streamlining and fluttering phenomena. Consequently, it may be estimated that the aerodynamic properties vary with the wind speed. This is one of the most striking phenomena of the airflow above a surface formed by vegetation (*Brutsaert,* 1982; *Hayashi,* 1983).

In the analysis of wind structure in the lowest layers of the atmosphere, it is advantageous to regard some horizontal layers where individual relationships of physical amount are established. The surface boundary layer is defined as the lower friction layer, in which the wind structure is strongly influenced by the surface morphologic and thermal conditions. In addition to this fact, it is possible to observe the formation of a new boundary layer generated under the surface boundary layer, if the surface is covered by vegetation.

So it has been noted, that the values of the roughness length and the zero plane displacement change systematically with the wind speed, when they are determined from wind speed profiles measured above a stand of vegetation. Many observations on this phenomenon have been done for different plant canopies (*Saugier* and *Ripley*, 1978; *Hayashi,* 1983; *Mölder,* 1997; *Mölder et al.*, 1999; *Hurtalová* and *Matejka,* 1999). The concept of the roughness length has become a simple and useful tool for parameterization of the surface momentum, sensible heat, and latent heat fluxes (*Brutsaert,* 1982; *Mölder,* 1997). Hence, the roughness length is an important imput parameter in many mathematical models simulating the surface fluxes of mass and energy, as well as in numerical modeling from mesoscale models to long-term climate analyses including general circulation models (*Jasinski* and *Crago,* 1999). Consequently, there is an urgent need to estimate the values of the roughness length for various kinds of earth surfaces with required accuracy and reliability.

The aim of this study was the determination of the zero plane displacement d, the roughness length z_0, and the aerodynamic resistance r_a values during the whole maize growing season. On the basis of these values, the dependence of the z_0 and r_a-values on the wind speed $u(z)$ can be found and quantitatively expressed for this canopy surface.

2. Theory and methods

The generally accepted theory of exchange between the land surface and the lower atmosphere layers is based on the works of *Monin* and *Obukhov* (1953, 1954). With the help of the universal functin $\phi(z/L)$ of Monin-Obukhov, it is

possible to describe the vertical wind speed profile $u(z)$, considering the atmosphere thermal stratification, by relationship

$$\frac{d\overline{u}}{dz} = \frac{u^*}{\kappa z}\phi\left(\frac{z}{L}\right), \tag{1}$$

where u^* is the friction velocity, κ is the Kármán constant, and L is the Monin-Obukhov length. Under neutral conditions, introducing the values of z_0 and d, the vertical wind speed profile is represented by the integrated form of Eq. (1)

$$\overline{u}(z) = \frac{u^*}{\kappa}\ln\left(\frac{z-d}{z_0}\right). \tag{2}$$

Additional basic equations valid in the canopy sublayer are (*Hayashi,* 1983)

$$\tau = \rho K_M \frac{d\overline{u}}{dz}, \tag{3}$$

$$\frac{d}{dz}\left(\frac{\tau}{\rho}\right) = a\, LAD\, C_d \overline{u}^2, \tag{4}$$

$$K_M = \beta \xi_0^{\,m}\, \overline{u} h(1 - rLAD), \tag{5}$$

where K_M is called the eddy exchange coefficient of momentum, $\tau = \rho(u^*)^2$ is the vertical transfer of momentum, ρ is the air density, h is the mean vegetation height, $\xi_0 = z_0 / h$ is the relative roughness length, C_d is the drag coefficient for individual roughness elements, LAD is the leaf area density, r is the luxuriant length, which was defined by *Hayashi* (1983), and a, β, m are nondimensional constants.

Using these relationships and provided that K_M changes continuously and $LAD = 0$ on the level $z = h$, we obtained the relationship for the z_0-values as a function of the nondimensional speed $\Gamma = u_h/u^*$ in the form (*Hayashi,* 1983; *Hurtalová* and *Matejka,* 1999)

$$\frac{z_0}{h} = \xi_0 = \left(\frac{\kappa}{\beta\Gamma}\right)^{\frac{1}{m-1}} \exp\left(\frac{\kappa\Gamma}{m-1}\right), \tag{6}$$

where $m \neq 0$.

The zero plane displacement d can be determined from analysis of the results of the wind speed profile measurements in case of a neutral atmosphere

stratification (*Brutsaert,* 1982). Consequently, in the absence of wind speed profile data at neutral atmosphere stratification, we can use the relationship $d = f(h)$, where h is a mean canopy height increasing during the growing season. The mean of data presented in literature is $d/h = 0.68$, with extremes of 0.53 and 0.83 (*Brutsaert,* 1982; *Mölder et al.,* 1999). Again, it is clear that the ratio d/h also can not really be a constant. But $d = (2/3)h$ appears to be fairly representative for closed vegetation canopy surfaces. The zero plane displacement is the height of the active surface, where the radiation is reflected and transformed into other energy kinds.

The roughness length values can be determined by the analysis of the wind speed profiles measured over an active surface at minimum three levels at different thermal atmosphere stratifications (*Hurtalová et al.,* 1987). Each wind speed profile $u(z)$ can be approximated by the relationship (*Monin* and *Obukhov,* 1954; *Hurtalová et al.,* 1987)

$$u_i(z) = A_i(\gamma + \log(z)) + C_i z\,, \tag{7}$$

where i is the profile number. A_i, γ, C_i are parameters which can be determined by the least squares method for each wind speed profile. Using known values of these parameters, the z_0-values can be estimated by formula

$$z_0 = 10 - \gamma\,. \tag{8}$$

The physical sense of A_i and C_i parameters can be deduced from relationships which are valid for each wind speed profile:

$$u^* = \kappa\, A_i / \ln(10) \quad \text{and} \quad \beta^* / L = C_i \ln(10) / A_i\,, \tag{9}$$

where β^* is Monin-Obukhov's universal semiempirical constant.

The transfer through the canopy air and in the air above it can be represented by an aerodynamic resistance r_a (*Brutsaert,* 1982). The r_a-values can be calculated using simple method on the base of the wind speed profile analysis (*Hurtalová* and *Szabó*, 1985). The aerodynamic resistance to water vapor r_a is defined from relationship (*Brutsaert,* 1982)

$$E = \rho \frac{q_s - q_a}{r_a}\,, \tag{10}$$

where E is the water vapor flux, q_s and q_a are the specific humidity of air at the surface and at the reference height, respectively. Further, let's consider the

definition of the eddy exchange coefficient of momentum K_M (*Hurtalová* and *Szabó,* 1985). For r_a, the relation $r_a = 1/K_M$ is valid. Then, coming out from Monin-Obukhov's theory and considering thermal stratification of the atmosphere for r_a, the following relationship can be found (*Hurtalová,* 1995)

$$r_a = \frac{\ln\left(\frac{z}{z_0}\right) + \frac{\beta^*}{L}(z - z_0)}{\kappa\, u^*}. \tag{11}$$

The atmospheric stratification in Eq. (11) is defined by parameter β^*/L. The values of z_0, u^*, and the parameter β^*/L can be determined by the analysis of the wind speed profiles, according to Eq. (9).

3. Experimental site and data

The experimental site of Žabčice is located in the southern part of Moravia, Czech Republic, in a warm agroclimatological macroregion with a predominantly moderate winter (*Rožnovský* and *Svoboda,* 1995). The average annual temperature is 9.2°C, the average temperature during vegetation season is 15.7°C. The growing season, which is limited by biological zero for maize canopy (8.0°C), in average starts on March 31 and ends on October 20.

The investigated plant species was maize (*Zea maize L.*), for which canopy structure and architecture is changing significantly during the growing season. Plant density was 12 plants/m^2 and row spacing was 0.7 m. The maize "STIRA" variety is middle lateness, two-line hybrid with mark FAO 390. This cultivar is typical one having good economic properties and high harvests, plants are not sensitive to droughts.

The wind speed measurements were part of microclimatic profile measurements above the investigated maize canopy. Anemometers were installed at 0.5 m, 1.0 m, and 2.0 m above the zero plane displacement level on a metallic mast. The values of wind speed were continuously measured by automatic measuring equipment with data logger and anemometers A100L in 15-minute intervals of measurements. For the analysis we selected the wind speed hourly average values, which fulfilled the condition $u(0.5\,\mathrm{m}) \geq 1.0$ m s^{-1}. From this it follows the assumption, that we analyzed the vertical wind speed profiles under the conditions of turbulence development. It can be expected that the shape of a wind speed profile depends on the value of the mean wind speed at level close to canopy height (*Matejka et al.,* 2001).

The analyzed wind speed profiles were measured from May 10 to October 18, 2000. The year 2000 was very dry during the growing season, namely in April the monthly sum of precipitation was altogether 1.6 mm, and during the first part of May (till May 17) it rained only 7.8 mm (*Rožnovský et al.*, 2000). This fact definitely influenced plant growth and development, as well as the closing of maize canopy.

4. Results and discussion

The vertical wind speed profiles, measured in and above maize canopy during the whole growing season fulfilling the condition $u(0.5\text{m}) \geq 1.0$ m s^{-1}, were analyzed. This analyzed series contained 1255 hourly mean wind speed profiles measured from May 10 to October 18, 2000.

As it was mentioned above, April was very dry and this fact importantly influenced the plant growth and structure of maize canopy, namely at the beginning phase of maize. In May the experimental field formed only a bare soil surface. At the end of June this surface was covered by the maize canopy with leaf area index LAI $\sim$ 2.0 m^2 m^{-2}. The surfacewas covered by closed maize canopy, LAI $>$ 3.0 m^2 m^{-2}, from the end of July. The maximum height of the closed maize canopy reached the 2.32 m.

Only few analyzed profiles were measured in neutral atmosphere stratification. Therefore we accepted the fact, that relation $d = (2/3)h$ is good representative of agricultural crop covered surfaces (*Brutsaert,* 1982; *Mölder et al.*, 1999).

Seasonal course of daily average values of canopy height h and $(d+z_0)$ is indicated in *Fig. 1*. It is known, that the roughness length is dependent on the canopy structure and architecture, as well as on the wind speed. Therefore, the dependence of z_0-values on the wind speed will be analyzed above closed maize canopy (August 1–October 18, 2000). During this time, the changes of canopy height and plant green mass density are not so dynamic as at the start of the growing season (*Fig. 1*), and also their influence on the roughness length are minimal. The monthly average z_0-values were: $z_0 = 0.24$ m of the mean canopy height 2.24 m in August, $z_0 = 0.23$ m of $h = 2.20$ m in September, and $z_0 = 0.19$ m of $h = 2.15$ m in October. The roughness length of canopy surface is very often expressed as the fraction of the roughness elements height above the zero plane displacement, $(h - d)$. *Garratt* (1992) suggests that $z_0/(h - d)$ equals to 0.2–0.4. *Mölder* (1997) found for the barley field that $z_0 = 0.3(h - d)$. In our case, the monthly average values of $z_0/(h - d)$ for investigated maize stand equal to 0.32 in August and September, and 0.27 in October. This is well corresponded with the values found in literature.

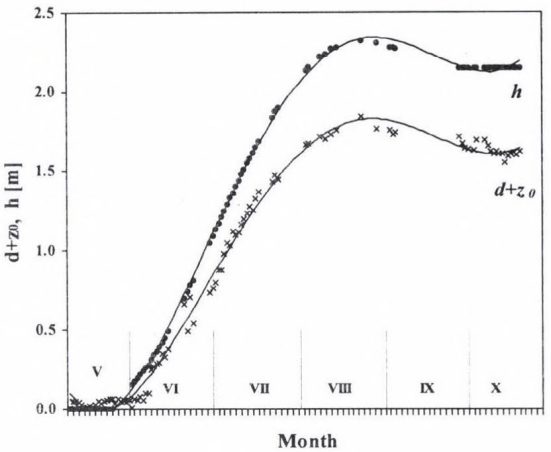

Fig. 1. Seasonal course of daily average values of canopy height h and $(d+z_0)$, where d is the zero plane displacement height and z_0 is the roughness length of the maize canopy.

At first the dependence of the friction velocity u^* on the wind speed measured at the level of plant height, $u(h)$ ~u(0.5 m) at closed maize canopy, was analyzed. Assuming z_0 and d are constant with the wind speed, the linear equation, $u^* = Au(h)$, where A is constant, is followed from the log law. Then, as it was introduced by Hayashi, the canopy is in an aerodynamical steady state (*Hayashi,* 1983). In this case the z_0 and d values are not dependent on the wind speed. But for a real canopy, the friction velocity settles down and deviates from the linear equation. The u^* values were calculated from the wind speed profile analysis, Eq. (9). In our case, on the basis of the analyzed observations, the wanted function for investigated maize canopy during August 1–October 18, 2000 can be fitted as follows, $u^* = 0.62[u(0.5\text{m})]^{0.69}$ (*Fig. 2*). The correlation coefficient between u^* calculated by this equation and calculated from the wind speed profiles was 0.68. It is necessary to be aware, that u^* values depend not only on the wind speed but also on z_0. It may be an explanation for the dispersion of experimental points in *Fig. 2*. From this analysis it follows, that this closed maize canopy was in an aerodynamically variable state, and so the z_0 values will be dependent on the wind speed. The function $z_0 = f(u)$ can be analyzed as the dependence of the relative roughness length ξ_0 on the nondimensional speed Γ Then the dependence $\xi_0 = f(\Gamma)$ for investigated closed maize canopy from August 1 to October 18, 2000 can be expressed by analytical relationship in the form (*Fig. 3*):

$$\xi_0 = \frac{z_0}{h} = 0.162 \exp(-0.306\,\Gamma). \tag{12}$$

The correlation coefficient between z_0 calculated by Eq. (12) and calculated from the wind speed profiles was 0.96.

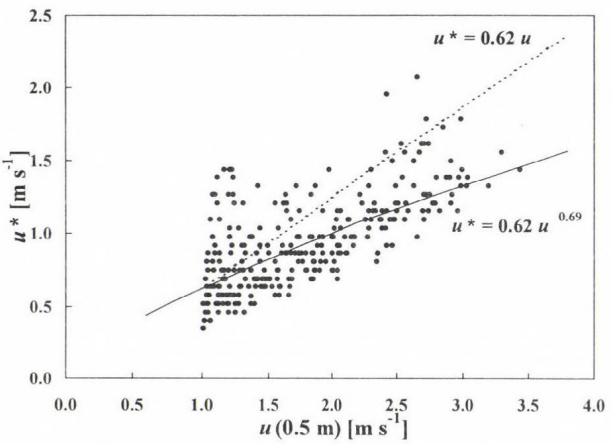

Fig. 2. Dependence of the friction velocity u^* on the wind speed $u(0.5\ \mathrm{m})$.

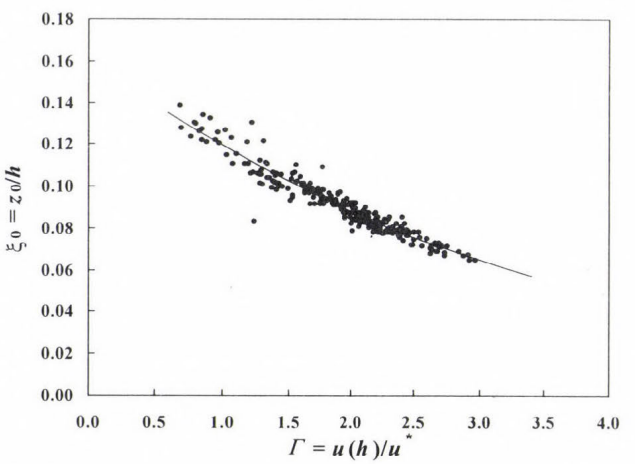

Fig. 3. Dependence of the relative roughness length ξ_0 on the nondimensional speed Γ for closed maize canopy.

From wind speed profile analysis also the r_a values were calculated using Eq. (11). The dependence of the r_a values on the wind speed $u(2\ \mathrm{m})$ above maize canopy during the whole growing season is shown in *Fig. 4*. The fitted line has the form of the 3-order polynomial with correlation coefficient 0.51.

During this period, the r_a values (daily averages) were from the interval 1.38–63.48 s m^{-1} (*Fig. 5*). Maximum value of aerodynamic resistance over closed

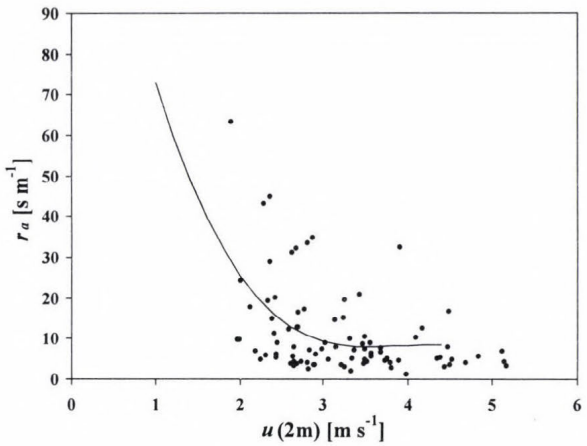

Fig. 4. Variation in the aerodynamic resistance r_a with the wind speed u(2 m) above maize canopy during the growing season.

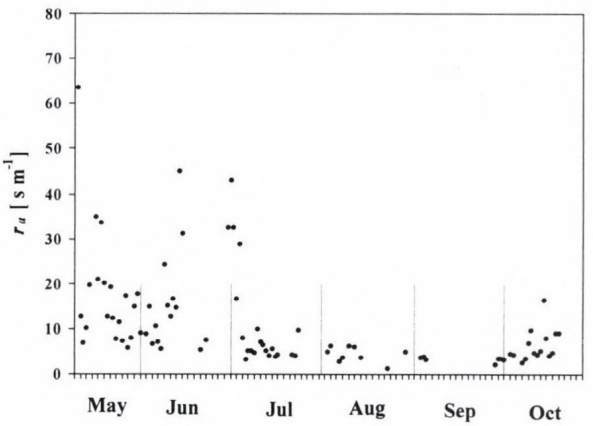

Fig. 5. Seasonal variations in the aerodynamic resistance r_a above maize canopy during the growing season.

canopy surface (August, September) was only 6.27 s m^{-1}. In October the r_a values were higher with maximal value of 16.52 s m^{-1}. As it was written before, the aerodynamic resistance also can represent the water vapor transfer through the canopy air and in the air above this canopy (*Brutsaert,* 1982;

Hurtalová, 1995). It may be seen, that the r_a values are high over bare soil (May) and above surface covered by canopy with low *LAI*-values (June), and they are low above closed canopy surface (August, September). In October, when *LAI* of the maize stand decreases, the r_a values have grown a little. Further it can be seen, that the aerodynamic resistance decreases with increasing wind speed. However, this dependence is more complicated, because the r_a values depend also on the roughness length and the atmosphere's thermal stratification. The experimental points dispersion in *Fig. 4* is the evidence of this fact. This is well in comformity with results found in literature (*Wallace et al.,* 1984).

5. Conclusion

The zero plane displacement, roughness length, and aerodynamic resistance values were determined during the whole maize growing season. The average roughness length of closed maize canopy was from 0.24 m in August to 0.19 m in October, with mean canopy height of 2.24 m and 2.15 m, respectively. The monthly average values of $z_0/(h - d)$ for closed maize canopy equaled to 0.32 of mean canopy height of 2.22 m. Further, the results showed that values of the roughness length determined for maize canopy during the whole growing season were practically independent of the mean height of this canopy. It has as a result that the often used estimation of the roughness lengths as $0.1h$ is not always appropriate.

This study confirms that aerodynamic properties of air layer above maize canopy surface vary with wind flowing. On the basis of the wind speed profile analysis it was found, that the dependence of friction velocity u^* on the wind speed $u(0.5\text{m})$ above investigated closed maize canopy was expressed by the relationship $u^* = 0.62[u(0.5\text{m})]^{0.69}$. It means, that maize canopy was in an aerodynamically variable state, and the roughness length values depend on the wind speed. Further it was shown, that Eq. (12) well approximates the changes of z_0 values of investigated maize canopy surface with the air flow.

The aerodynamic resistance decreases with increasing wind speed. This dependence is more complicated, because the r_a-values depend also on the rougness length and the atmosphere's thermal stratification. Maximum value of aerodynamic resistance over closed canopy surface (August, September) was only 6.27 s m^{-1}. In October the r_a values were higher with maximal value of 16.52 s m^{-1}.

Acknowledgements—The authors are grateful to the Slovak Grant Agency VEGA (Grant No 2/2093/22) and the Ministry of Education, Youth and Sports of Czech Republic (Grant No J08/98:432100001) for partially supporting this work.

References

Brutsaert, W.H., 1982: *Evaporation Into the Atmosphere.* D. Reidel Publishing Company, London.

Garratt, J.R., 1992: *The Atmospheric Boundary Layer.* Cambridge University Press, Cambridge.

Hayashi, Y., 1983: *Aerodynamical Properties of an Air Layer Affected by Vegetation. Environm. Res. Center Papers, 3.* ERC the University of Tsukuba, Ibaraki.

Hurtalová, T., 1995: Aerodynamic resistance role in plants-atmosphere system. *Contr. Geophys. Inst. SAS, Ser. Meteorol. 15*, 52-61.

Hurtalová, T., Janičkovičová, L., and *Matejka, F.*, 1987: Dynamic roughness - an aerodynamic characteristic of the active surface. *Contr. Geophys. Inst. SAS, Ser. Meteorol. 18*, 56-64.

Hurtalová, T. and *Matejka, F.*, 1999: Surface characteristics and energy fluxes above different plant canopies. *Agric. and Forest Meteorol. 98-99*, 491-500.

Hurtalová, T. and *Szabó, T.*, 1985: Die Abhängigkeit des Integralkoeffizienten der turbulenten Diffusion von ausgewählten meteorologischen Parametern. *Z. Meteorol. 35*, 354-358.

Jasinski, M.F. and *Crago, R.D.*, 1999: Estimation of vegetation aerodynamic roughness of natural regions using frontal area density determined from satellite. *Agric. and Forest Meteorol. 94*, 65-77.

Matejka, F., Hurtalová, T., Rožnovský, J., and *Chalupníková, B.*, 2001: Effect of soil drought on evapotranspiration of maize field. *Contrib. to Geophysics and Geodesy 31*, 455-466.

Monin, A.S. and *Obukhov, A.M.*, 1953: Dimensionless characteristics of turbulence in the atmospheric surface layer (in Russian). *Doklady AN SSSR 93*, 223-226.

Monin, A.S. and *Obukhov, A.M.*, 1954: Basic turbulent mixing law in the atmospheric surface layer (in Russian). *Trudy Geofiz. Inst. AN SSSR*, 24(151), 163-187.

Mölder, M., 1997: Parametrization of exchange processes over a barley field. *Boundary-Layer Meteorol. 84*, 341-361.

Mölder, M., Grelle, A., Lindroth, A., and *Halldin, S.*, 1999: Flux-profile relationships over a boreal forest - roughness sublayer corrections. *Agric. and Forest Meteorol. 98-99*, 645-658.

Rožnovský, J. and *Svoboda, J.*, 1995: Agroclimatological characteristics of Žabčice region (in Czech). *Folia, Series A.* Mendel Agricultural and Forestry University, Brno.

Rožnovský, J., Svoboda, J., Žalud, Z., and *Šťastná, M.*, 2000: Meteorological characteristics of dry spring 2000. In MZLU to Growers, Žabčice 2000. *Proc. of Contributions from Field Days.* MZLU in Brno, 72-75.

Saugier, B. and *Ripley, E.A.*, 1978: Evaluation of the aerodynamic method of determining fluxes over natural grassland. *Quart. J. Roy. Meteorol. Soc. 104*, 257-270.

Wallace, J.,S., Lloyd, C.,R., Roberts, J., and *Shuttleworth, W.,J.*, 1984: A comparison of methods for estimating aerodynamic resistance of heather in the field. *Agric. and Forest Meteorol. 32*, 289-305.

BOOK REVIEW

Wilfried Schröder (editor): **Meteorological and Geophysical Fluid Dynamics (A book to commemorate the centenary of the birth of Hans Ertel)**. Science Edition, D-28777 Bremen-Rönnebeck, 2004, 417 pages. Price: 20 EUR.

Professor Hans Richard Max Ertel was born in 1904 and died in 1971. He is a highly recognised scientist for his work related to geophysics, meteorology, and hydrodynamics. His earlier research covered a much wider range, it touched even the cosmology. The German Commission for the History of Geophysics and Cosmical Physics decided to collect into one volume tributes and greetings (25), as well as scientific papers (34) dedicated to Professor Ertel. The book contains the first and last papers written by himself, the greeted scientist.

The papers deal with every aspect of geophysics, the authors represent several countries as it can be expected in the case of a memorial book. This way the reader will have a possibility to be informed of several fraction of geophysics and hydrodynamics. It seems, Dr. Schröder's editorial work very well serves both: Professor Ertel's tribute and the readers interests.

G. Major

GUIDE FOR AUTHORS OF *IDŐJÁRÁS*

The purpose of the journal is to publish papers in any field of meteorology and atmosphere related scientific areas. These may be

- research papers on new results of scientific investigations,
- critical review articles summarizing the current state of art of a certain topic,
- short contributions dealing with a particular question.

Some issues contain "News" and "Book review", therefore, such contributions are also welcome. The papers must be in American English and should be checked by a native speaker if necessary.

Authors are requested to send their manuscripts to

Editor-in Chief of IDŐJÁRÁS

P.O. Box 39, H-1675 Budapest, Hungary

in three identical printed copies including all illustrations. Papers will then be reviewed normally by two independent referees, who remain unidentified for the author(s). The Editor-in-Chief will inform the author(s) whether or not the paper is acceptable for publication, and what modifications, if any, are necessary.

Please, follow the order given below when typing manuscripts.

Title part: should consist of the title, the name(s) of the author(s), their affiliation(s) including full postal and E-mail address(es). In case of more than one author, the corresponding author must be identified.

Abstract: should contain the purpose, the applied data and methods as well as the basic conclusion(s) of the paper.

Key-words: must be included (from 5 to 10) to help to classify the topic.

Text: has to be typed in double spacing with wide margins on one side of an A4 size white paper. Use of S.I. units are expected, and the use of negative exponent is preferred to fractional sign. Mathematical formulae are expected to be as simple as possible and numbered in parentheses at the right margin.

All publications cited in the text should be presented in a *list of references*, arranged in alphabetical order. For an article: name(s) of author(s) in Italics, year, title of article, name of journal, volume, number (the latter two in Italics) and pages. E.g., *Nathan, K.K.,* 1986: A note on the relationship between photo-synthetically active radiation and cloud amount. *Időjárás 90,* 10-13. For a book: name(s) of author(s), year, title of the book (all in Italics except the year), publisher and place of publication. E.g., *Junge, C. E.,* 1963: *Air Chemistry and Radioactivity*. Academic Press, New York and London. Reference in the text should contain the name(s) of the author(s) in Italics and year of publication. E.g., in the case of one author: *Miller* (1989); in the case of two authors: *Gamov* and *Cleveland* (1973); and if there are more than two authors: *Smith et al.* (1990). If the name of the author cannot be fitted into the text: *(Miller,* 1989); etc. When referring papers published in the same year by the same author, letters a, b, c, etc. should follow the year of publication.

Tables should be marked by Arabic numbers and printed in separate sheets with their numbers and legends given below them. Avoid too lengthy or complicated tables, or tables duplicating results given in other form in the manuscript (e.g., graphs)

Figures should also be marked with Arabic numbers and printed in black and white in camera-ready form in separate sheets with their numbers and captions given below them. Good quality laser printings are preferred.

The text should be submitted both in manuscript and in electronic form, the latter on diskette or in E-mail. Use standard 3.5" MS-DOS formatted diskette or CD for this purpose. MS Word format is preferred.

Reprints: authors receive 30 reprints free of charge. Additional reprints may be ordered at the authors' expense when sending back the proofs to the Editorial Office.

More information for authors is available: antal.e@met.hu

Information on the last issues: http://omsz.met.hu/irodalom/firat_ido/ido_hu.html

Published by the Hungarian Meteorological Service

Budapest, Hungary

INDEX: 26 361

HU ISSN 0324-6329

IDŐJÁRÁS

QUARTERLY JOURNAL
OF THE HUNGARIAN METEOROLOGICAL SERVICE

CONTENTS

****

http://omsz.met.hu/english/ref/jurido/jurido_en.html

VOL. 108 * NO. 2 * APRIL – JUNE 2004

IDŐJÁRÁS

Quarterly Journal of the Hungarian Meteorological Service

Editorial Office: P.O. Box 39, H-1675 Budapest, Hungary or
Gilice tér 39, H-1181 Budapest, Hungary
E-mail: prager.t@met.hu or *antal.e@met.hu*
Fax: (36-1) 346-4809

Subscription by

mail: IDŐJÁRÁS, P.O. Box 39, H-1675 Budapest, Hungary;
E-mail: prager.t@met.hu or *antal.e@met.hu*; *Fax: (36-1) 346-4809*

IDŐJÁRÁS

Quarterly Journal of the Hungarian Meteorological Service
Vol. 108, No. 2, April–June 2004, pp. 79–94

Theoretical approach of a continuous flow particle counter by condensation of ambient humidity

Evelyne Géhin[1*] and **André Renoux**[2]

[1]*Centre d'Etudes et de Recherches en Thermique Environnement et Systèmes (CERTES), Université Paris XII, Avenue du Général de Gaulle, 94010 Créteil, France; E-mail: gehin@univ-paris12.fr*

[2]*Laboratoire de Physique des Aérosols et Transfert des Contaminations (LPATC), Université Paris XII, Avenue du Général de Gaulle, 94010 Créteil, France; E-mail: renoux@univ-paris12.fr*

(Manuscript received January 16, 2003; in final form October 6, 2003)

Abstract—A new principle of a continuous flow particle counter is presented. It uses the natural presence of water vapor in ambient air to cause particle growth by condensation. The water vapor condensation is started by a continuous subsonic expansion in a nozzle with its outlet set into vacuum by pumping. The reached saturation depends on relative air humidity, nozzle throat cross section, and parameters of the system (mass flow rate, downstream pressure, and upstream temperature). The COPACHA (Continuous Particle Counter by Condensation of Ambient Humidity) enables to detect particles with size equal to or larger than 10 nm for relative humidity >20%. Downstream pressure shall be between 600 and 700 hPa, and the minimum nozzle throat length must be 20 cm.

Key-words: CNC, heterogeneous condensation, growth rate, nozzle, air-water vapor expansion, saturation.

1. Introduction

Measurement of the atmospheric particulate pollution needs to take into consideration the ultrafine aerosol ($d_p < 0.1$ μm) more and more. For this aim, the Condensation Nucleus Counter (CNC) is the most suitable device as much

* Corresponding author

for the detection of this aerosol as for its size distribution measurement, in connection with an electrical aerosol analyzer or a diffusion battery (*Götz et al.*, 1991; *Renoux* and *Boulaud,* 1998). All CNCs are based on the principle of particle growth by condensation in order to make them detectable. Boulaud (*Renoux* and *Boulaud*, 1998) classified them into three categories according to the methods applied to induce the supersaturation: adiabatic expansion, mixing of cold and warm fluids, cooling by circulation in a cold-walled pipe. These different techniques have led to the development of many types of continuous or discontinuous flow CNCs (*McMurry*, 2000). Another classical technique to perform supersaturation is the process of expansion in a nozzle (*Stodola*, 1927). For example, this technique has been applied to produce monodispersed aerosols (*Turner et al.*, 1988) or superfine powders (*Tom* and *Debenedetti,* 1991). Several researchers have studied particle growth by heterogeneous condensation in a nozzle (*Johnston* and *Wexler*, 1995; *Mallina* and *Wexler*, 1997; *Yang et al.*, 2000a, *Jurski* and *Géhin,* 2003). Apparently, *Yang et al.* (2000b) have been the only ones until now, who used this method to design and perform a continuous operating type CNC. They mixed the initial aerosol with air saturated by clean water. The mixing was followed by expansion in a nozzle. In this way one can detect particles with a diameter exceeding 40 nm. According to the authors, this technique reduces losses due to diffusion, and there is little condensation on nozzle walls contrary to the systems involving wall cooling. Furthermore, let us add, that, as the velocity profile in a nozzle is practically flat, parameters such as temperature, total pressure, and vapor pressure show little variation within a given section, thus avoiding the necessity to consider the exact trajectory of the particle (in a classical CNC, particles are injected into the center to avoid variations due to the temperature profile in a given section of the condenser pipe). Consequently, this approach seems to be promising because of its simplicity, and we shall demonstrate that it can be further simplified by using ambient humidity naturally present in the air. Our system (COPACHA, Continuous Particle Counter by Condensation of Ambient Humidity, see *Fig. 1*) makes use of the natural presence of water vapor in ambient air to cause particle growth. Water vapor condensation on aerosol results from a continuous subsonic expansion in a nozzle with outlet set into vacuum by pumping. The saturation reached depends on relative humidity of air and operating parameters of the system (flow rate, downstream pressure, initial fluid temperature). It is possible to get saturation ratio around 3 by adjusting these parameters so that particles with diameter over 4 nanometers can theoretically be activated. The aerosol growth can be emphasized after activation by throat lengthening, that enables to increase the transit time and consequently the final diameter. The particles are detected at throat outlet by a classical system using light scattering.

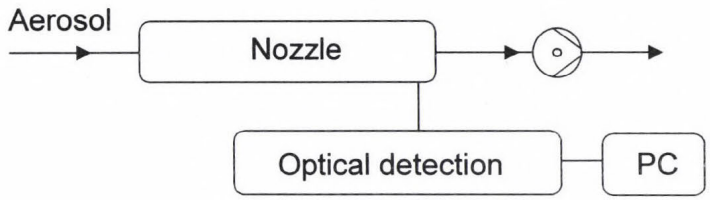

Fig. 1. COPACHA skeleton diagram.

2. Particle growth by condensation in a nozzle

Let us assume, that particles are spherical, uniformly distributed in the gas phase, and they are present in low concentration ($< 10^5$ particles cm^{-3}). Gas phase consists of a mixture of air and water vapor. As an indication, absolute humidity is under 0.015 kg of water kg^{-1} of dry air for moist air at standard atmospheric pressure and a temperature of 20°C. Because of the low water vapor content and particle concentration, we can consider the effect of drop or wall condensation upon the global parameters (total pressure, temperature, gas density) as insignificant. This approximation is justified (*Barrett* and *Clement*, 1986), when the particle concentration is low or the condensable mass is insignificant compared to total fluid mass. Then, the mix of both phases is processed as a pseudo-fluid, and the flow can be described by the same equations as those of a one phase flow.

The study of the compressible fluid flow in a nozzle is based on a few classical assumptions. Thus, we assume that the flow is one dimensional, permanent, adiabatic (low flow transit time in the nozzle justifies this considering that there are no exchanges with outside during expansion), the interactions with walls can be neglected (contact friction, thermal transfers), and the fluid is a perfect one. Under these circumstances, solving the equations of mass, motion, and energy conservation, as well as the fluid state equation, we obtain the classical expression of the variations of the different flow characteristics related to the Mach number (M_{ach}):

$$\left[1+\frac{(\gamma-1)}{2}M_{ach}{}^2\right]=\frac{T_i}{T}=\left(\frac{p_i}{p}\right)^{\left(\frac{\gamma-1}{\gamma}\right)}=\left(\frac{\rho_i}{\rho}\right)^{\gamma-1}, \quad M_{ach}=\frac{v}{a}, \quad a=\sqrt{\gamma r T}, \qquad (1)$$

where T_i, p_i, ρ_i are the temperature, pressure, density of the generating state, that is the characteristics of the fluid sampled at the entrance of the nozzle.

Further, T, p, ρ, M_{ach}, v are the temperature, pressure, density, Mach number, velocity of the fluid in a given nozzle section. a is the sound velocity. Finally, γ and r are the ratio of gas specific heats and the ideal gas constant. Furthermore, considering the above mentioned conditions:

$$p = p_{as} + p_v \approx p_{as}, \qquad \rho = \rho_{as} + \rho_v + \rho_a \approx \rho_{as}, \tag{2}$$

where the subscripts *as*, *v*, *a* denote dry air, vapor, and aerosol.

To Eq. (1), we must add the conservation of total mass flux rate, q, in every nozzle section:

$$q = \rho A v, \tag{3}$$

where A is the section area at a given nozzle section.

As the saturated vapor pressure, p_{vs}, is always low compared to total pressure, the saturation, S, is given by:

$$S \approx H = \frac{p_v}{p_{vs}}, \tag{4}$$

where H is the relative humidity of moist air. Water vapor pressure, p_v, in a given section of the nozzle is calculated for monodispersed aerosol with initial diameter, D_i, and by assuming of no extra condensation on the walls:

$$p_v = \left[\frac{p}{P_i} p_{vi}\right] - (D^3 - D_i^3)\frac{\pi \rho_l N}{6}\frac{r_{gp} T}{M_v}. \tag{5}$$

In this equation p_{vi} is the initial vapor pressure, D and N are the diameter and concentration of the droplet in the nozzle, while ρ_l, r_{gp}, and M_v are the water density, universal gas constant, and water vapor molecular mass, respectively. With the assumption of no coalescence phenomena or over losses in the nozzle, wich is a good approximation according to the short residence time of flowing particles in the system, N is calculated with the following equation:

$$N = N_i \frac{\rho}{\rho_i}. \tag{6}$$

2.1 Particle activation and critical saturation

Since there is no initial thermal unbalance between different phases, the Kelvin equation gives the minimum diameter of the nuclei activated at a given saturation and temperature:

$$D_{min} = \frac{4\,\sigma_l\,M_v}{\rho_l\,r\,T\,\ln(S)}. \tag{7}$$

In the case of soluble particle consisting of, for example, salt, the condensation process is initiated at saturation ratio lower than that described in Eq. (7), leading to a decrease of D_{min}. For non-wettable particles, the vapor tends to deposit in very small droplets; when the particle surface is completely covered, a uniform liquid film appears, the nucleus is then entirely coated (*Fletcher,* 1962). This phenomenon tend to increase the activation saturation and consequently D_{min}. In the first step this phenomenon is neglected and Eq. (7) will be used.

According to *Ahn* (1988), the critical saturation ratio, corresponding to the threshold at which the homogeneous condensation appears, can be determined by calculating the value of S for which $I = 1\ \mathrm{m^{-3}\ s^{-1}}$ (I is the nucleation rate). We obtain:

$$S_{cr} = \exp\left[\frac{16\,\pi}{3}\left(\frac{\sigma}{KT}\right)^3 \frac{v_m^2}{\ln\left(2v_m\left(\frac{p_v}{KT}\right)^2\left(\frac{\sigma}{2\pi m_v}\right)^{1/2}\right)}\right]^{1/2} \tag{8}$$

In this equation σ, v_m, and m_v are the surface tension, vapor molecule volume, and mass, respectively. This saturation factor shall not be exceeded, otherwise condensation nuclei could appear, resulting in an overestimation of the particle number.

2.2 Particle growth

Heat and mass transfer phenomena between particle and surrounding medium depend on Knudsen number:

$$Kn = \frac{2\lambda}{D},$$

where λ is the mean free path of carrying gas molecules. Calculations of Knudsen number for particles with a diameter of 10 nm gives values from 1 to 10 in our conditions. According to the classification given by *Devienne* (1958), the corresponding flow regime is consequently the transient one (Knudsen regime).

Diameter variation of a sphere is linked to J, the water vapor mass flow reaching the droplet:

$$\frac{dD}{dt} = \frac{J}{\frac{\pi}{2} D^2 \rho_l}. \tag{9}$$

Fuchs and *Sutugin* (1970) give the expression of water vapor mass flow reaching the drop for the transient regime. With the correction for relative motion between gas and droplet (*Hughmark,* 1967), J is given by:

$$J = C(Kn_v)\, Sh\, D_{vg}\, \pi D \left(\frac{p_{v\infty} M_v}{r_{gp} T_\infty} - \frac{p_{vd} M_v}{r_{gp} T_d} \right), \tag{10}$$

where $p_{v\infty}$, T_∞, p_{vd}, T_d are the vapor pressure and fluid temperature, respectively, far from the droplet and at the droplet surface.

$$p_{vd} = p_{vs}(T_d) \exp\left(\frac{4\sigma_l M_v}{\rho_l r_{gp} T_d D} \right), \tag{11}$$

where D_{vg} is the vapor diffusion coefficient in the gas (Appendix), while Sh is the Sherwood number (Appendix). In Eq. (10) $C(kn_v)$ is the Fuchs's correction coefficient defined by (*Fuchs,* 1959):

$$C(Kn_v) = \frac{1 + Kn_v}{1 + 1.7104\, Kn_v + \frac{4}{3} Kn_v^2} \quad \text{and} \quad Kn_v = \frac{2\lambda_v}{D}, \tag{12}$$

where λ_v is the mean free path of water vapor molecules in air. It is defined by the Meyer's formula:

$$\lambda_v = \frac{3 D_{vg}}{V}. \tag{13}$$

In Eq. (13) V is the average thermal velocity at temperature T:

$$V = \left(\frac{8KT}{\pi m_v} \right)^{1/2}, \tag{14}$$

where K is the Boltzmann constant, while m_v is the mass of a water molecule.

2.3 Particle temperature

If we assume an isothermal droplet and take into account the correction for relative motion, the droplet temperature evolution for Knudsen regime is given by:

$$\rho_l C_{pl} \frac{dT_d}{dt} = \frac{6}{\pi D^3}(Q_l - Q_c), \tag{15}$$

where C_{pl} is the specific heat at constant pressure for water, Q_c is the heat release by conduction in the gas, and Q_l is the condensation heat:

$$Q_c = \pi D k (T_d - T_\infty) C(kn) Nu, \tag{16}$$

$$Q_l = JL, \tag{17}$$

where Nu is the Nusselt number (Appendix), k is the thermal conductivity of gas, while $C(kn)$ is the Fuchs's correction coefficient for the carrying gas defined by:

$$C(kn) = \frac{1 + Kn}{1 + 1.7104 Kn + \frac{4}{3} Kn^2}. \tag{18}$$

2.4 Particle motion

Drag and pressure forces can be considered as the only external forces acting on flowing particles, then the particle motion can be described by the following equation:

$$\left(\frac{\pi D^3 \rho_l}{6}\right) \frac{dv_d}{dt} = -\frac{6\pi \mu C_D Re_d D}{48 C_c}(v_d - v) - \frac{dp}{dx}\frac{\pi D^3}{6}, \tag{19}$$

where Re_d is the droplet Reynolds number defined by:

$$Re_d = \frac{|v_d - v| D\rho}{\mu}. \tag{20}$$

Further, the values of the drag factor, C_D, are the following (*Kurten et al.*, 1966):

$$C_D = \begin{cases} \dfrac{24}{Re_d} & \text{for} \quad Re_d < 0.1 \\ 0.28 + \dfrac{6}{Re_d^{0.5}} + \dfrac{21}{Re_d} & \text{for} \quad 0.1 < Re_p < 4000 \end{cases} \tag{21}$$

Finally, in Eq. (19) C_c is the Cunningham factor. It can be expressed as a function of the particle diameter and mean free path of gas molecules, λ (*Seinfeld,* 1986):

$$C_c = 1 + \frac{2\lambda}{D}\left[1.257 + 0.4\exp\left(\frac{-1.1D}{2\lambda}\right)\right]. \tag{22}$$

2.5 Solving method

Fluid pressure, temperature, density, and velocity in the nozzle are first calculated with Eqs. (1), (2), (3). Then the particle concentration is estimated at each position in the nozzle with Eq. (6). Then, Eqs. (5), (9), (15), and (19) are solved at all points of the nozzle by the Runge-Kutta method.

3. Discussion

The aims of our study are to show that:

- saturation values, that can be reached by using this device in ambient air with relative humidity $>20\%$, enable us to activate particles with a diameter over 10 nm,
- saturation values reached remain under the critical saturation value,
- growth of activated particles is sufficient to have them detected.

In the calculations presented, we consider that the nozzle has a circular cross section and its diameter linearly varies from inlet diameter d_i to throat diameter d_{th} (*Fig. 2*). Pressure and temperature in generating state are $p_i = 10^5$ Pa and $T_i = 288$ K, respectively. We consider different throat lengths in order to obtain sufficient retention times for particles growth.

3.1 Particle activation in COPACHA

Fig. 3 shows how the saturation varies in relation to cross section ratios in the nozzle for different initial and downstream pressure ratios. The saturation ratio

remains almost constant for normalized sections over 1.4, but its variation becomes significant for normalized sections under 1.2. This indicates that condensation in the nozzle appears exclusively for sections very near to the nozzle throat. This phenomenon is confirmed by *Fig. 4*, that gives the variation of the minimal activation diameter in relation with the normalized section for different pressure drops. The activation of particles under 10 nm exclusively occurs for normalized sections under 1.15.

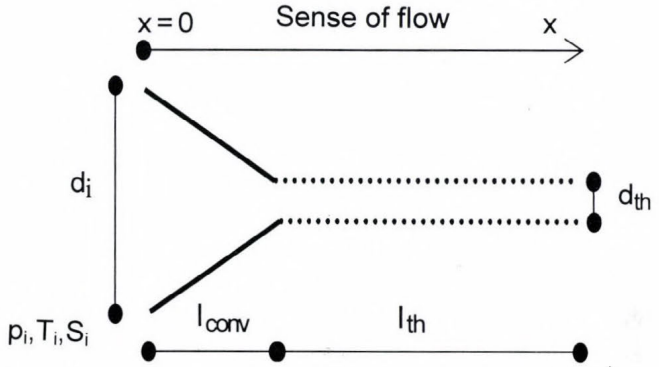

Fig. 2. Geometry used for theoretical study. p_i, T_i, S_i are the initial pressure, temperature, and saturation ratio, while d_i and d_{th} are the entrance and throat nozzle diameters, l_{conv} and l_{th} are the convergent zone and throat length, respectively.

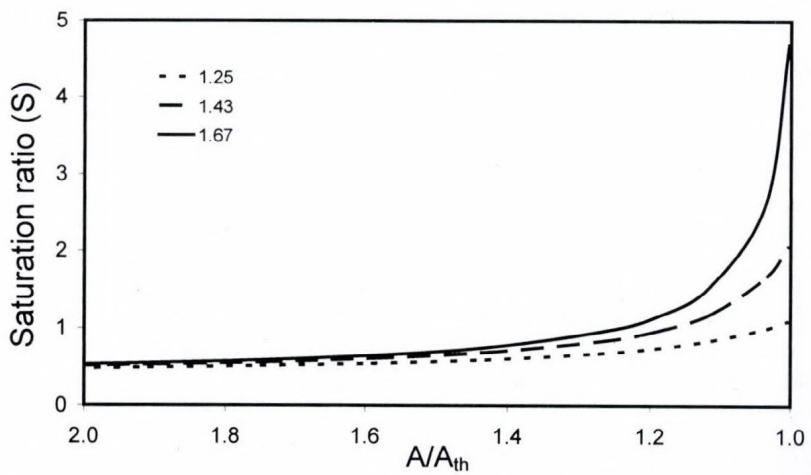

Fig. 3. Saturation in the nozzle (without condensation) in relation to section ratios (A/A_{th}) for different pressure drops ($p_i/p_{downstream}$), where $A_i/A_{th} = 796$, $S_i = 0.4$.

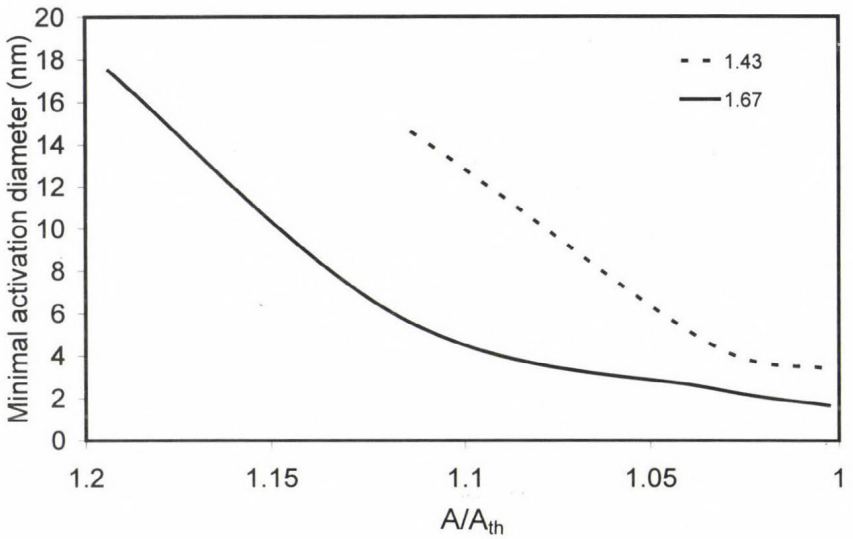

Fig. 4. Minimal activation diameter in relation to normalized section (A/A_{th}) for different pressure drops ($p_i/p_{downstream}$), where $A_i/A_{th} = 796$, $S_i = 0.4$.

According to nozzle geometry, drop growth in the convergent zone can be either significant (long convergent zone) or practically negligible (short convergent zone). It is to be noted, that the maximal saturation is reached in the nozzle throat, implying that the particles, that are not activated at the throat inlet, do not grow by condensation and they remain indetectable by optical system. *Fig. 4* shows that minimal activation diameter decreased according to the normalized section in the nozzle. Thus, to know the minimal diameter of the particles that will be activated in the nozzle, we must study the minimal diameter of activation in the nozzle throat.

Table 1 shows saturation variations reached in the nozzle throat in relation to relative humidity at the nozzle inlet and to downstream pressure. For downstream pressure of 600 hPa, the saturation in the nozzle throat always exceeds 2.4, corresponding to a minimal diameter of activated particles around 3 nm (*Table 2*). For relative humidity of 50%, the limit for critical saturation rate is exceeded, so in that case it is a risk to activate molecule aggregates and consequently to count more particle than there actually are. When the downstream pressure equals to 800 hPa, the saturation is still too low to activate particles with diameter under 10 nm (*Tables 1* and *2*) except at relative humidity of 50%. For downstream pressure of 700 hPa, the critical saturation ratio is never reached and particles with diameters of 10 nm are always activated for relative humidity values between 30 and 50%.

Table 1. Saturation in relation to downstream pressure (p) and relative humidity (H), and the critical saturation (S_c) in the nozzle throat (A_i / A_{th} = 44.4)

$H/p_{downstream}$ (%)	600 hPa	700 hPa	800 hPa
20	2.4	1.1	0.5
30	3.6	1.6	0.8
40	4.8	2.1	1.1
50	5.9	2.6	1.4
S_c	5.0	4.5	4.2

Table 2. Minimal activation diameter in relation to downstream pressure (p) and relative humidity (H)

$H/p_{downstream}$ (%)	600 hPa (nm)	700 hPa (nm)	800 hPa (nm)
20	3.0	40.5	-
30	2.0	5.3	-
40	1.6	3.3	24.4
50	-	2.5	7.5

Those effects are summed up in *Fig. 5*. The operating area of the system is included between the upper curve corresponding to (H_i, $p_{downstream}$), producing a critical saturation in the nozzle throat, and the lower curve represents the activation of particles with diameter of 10 nm in the nozzle throat.

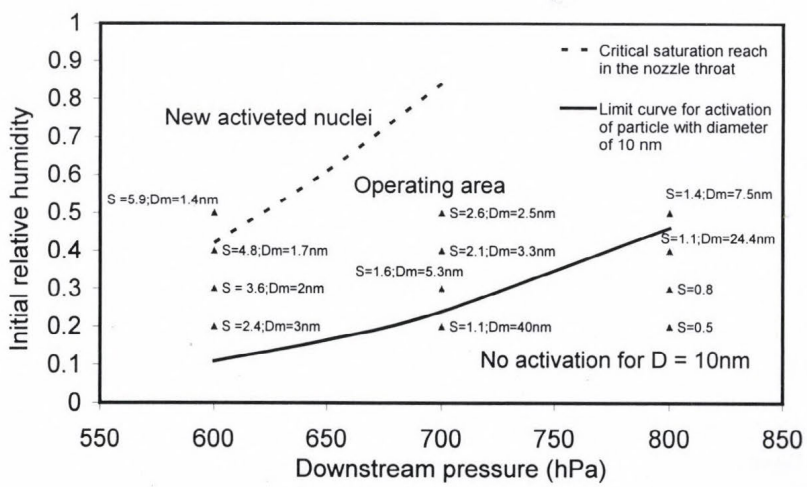

Fig. 5. Operating area of the system in relation to the downstream pressure and relative humidity at the nozzle inlet and downstream pressure (A_i / A_{th} = 44.4).

3.2 Particle growth in COPACHA

After the condensation process had been started, particles must grow in the nozzle until they reach an optically detectable diameter. Let us recall, that the minimal classically detectable diameter by optical particle counters is about 0.15 μm. In our system, since the particle growth occurs mainly in the nozzle throat, the retention time in the throat is an essential parameter. For initial droplet diameters between 10 nm and 100 nm, the relative velocity between the gas and the droplet increases in the first part of the nozzle and falls to zero in the throat. *Tables 3* and *4* indicate the final diameter of drops at nozzle outlet for different retention times and relative humidity values for aerosols with initial diameter of 10 nm.

Table 3. Final diameter of drops for different retention time (t_s, in ms) and relative humidity (H) values ($p_{downstream}$ = 700 hPa, D_i = 10 nm, A_i/A_{th} = 44.4)

H/t_s	**0.34**	**0.55**	**0.8**	**1**
%		**μm**		
30	0.06	0.10	0.14	0.17
40	0.11	0.18	0.25	0.30
50	0.16	0.25	0.34	0.41

Table 4. Final diameter of drops for different retention time (t_s, in ms) and relative humidity (H) values ($p_{downstream}$ = 600 hPa, D_i = 10 nm, A_i/A_{th} = 44.4)

H/t_s	**0.28**	**0.46**	**0.64**	**0.82**
%		**μm**		
20	0.06	0.09	0.12	0.15
30	0.10	0.16	0.21	0.26
40	0.15	0.22	0.29	0.36

Table 3 shows that for downstream pressure of 700 hPa and retention time exceeding 0.8 minutes, particles with an initial diameter of 10 nm grow sufficiently to be detected when the relative humidity remains within 30% and 50%. On the over hand, one can see from *Table 4* that for downstream pressure of 600 hPa and retention time of 0.82 minutes, the same particles grow sufficiently large to be detected when relative humidity is within 20% and 40%. *Table 5* gives the final size of drops in relation to the initial nucleus diameter. This table also shows that the influence of the initial diameter on the exit diameter is low. It is to be noted, that the effect of initial particle

concentration on saturation in the nozzle can be neglected for concentrations below 10^5 cm^{-3}. For higher particle concentration, the vapor content in the gas falls very quickly in the throat of the nozzle, which slows down the condensation on the droplet.

Table 5. Final diameter (D_f, in μm) of particles for different initial diameters (D_i) ($p_{downstream}$ = 700 hPa, H = 40%, t_s = 1 ms)

D_i	10 nm	20 nm	40 nm	60 nm	80 nm	100 nm
D_f	0.30	0.31	0.32	0.34	0.36	0.37

4. Conclusion

We have designed a new type of CNC that uses ambient humidity as working fluid. Our study indicates that COPACHA (Continuous Particle Counter by Condensation of Ambient Humidity) is able to detect particles with sizes larger than or equal to 10 nm for relative humidity values above 20%. It is also demonstrated that the operation downstream pressure must be between 600 and 750 hPa, and the minimal retention time at the nozzle throat must be about 0.8 minutes.

APPENDIX

The mean free path can be determined by the following equation (*Willeke,* 1986):

$$\lambda = \lambda_0 \left(\frac{\mu_{as}}{\mu_{as0}} \right) \left(\frac{p_0}{p} \right)^{\gamma} \sqrt{\frac{T_0}{T}},$$

where $\lambda_0 = 0.0653$ μm, $p_0 = 10^5$ Pa, $\mu_{as0} = 1.81 \times 10^{-5}$ Pa s, $T_0 = 293$ K.

The dynamic viscosity of air is calculated by the Sutherland's rule:

$$\mu_{as} = \mu_0 \sqrt{\frac{T}{T_0}} \frac{\left(1 + \frac{c}{T_0}\right)}{\left(1 + \frac{c}{T}\right)},$$

where $c = 123.6$ K, $\mu_0 = 171.1 \times 10^{-6}$ (Pa s), $T_0 = 273$ K.

Diffusion coefficient of water vapor in air (D_{vg}) is given by *Fuller et al.* (1966) as follows:

$$D_{AB} = \frac{10^{-3}\ T^{1.75}}{p\left(U_A^{1/3} + U_B^{1/3}\right)^2} \left(\frac{1}{M_A} + \frac{1}{M_B} \right)^{1/2},$$

where D_{AB} is given in $cm^2\ s^{-1}$, T in K, p in atm, while U values represent the atomic diffusion volumes given by *Fuller et al.* (1966). $U_{Air} = 20.1\ cm^3\ g^{-1}\ mol^{-1}$, $U_{water} = 9.44\ cm^3\ g^{-1}\ mol^{-1}$.

Sherwood and Nusselt numbers (*Hughmark,* 1967) can be tabulated as given below:

Re_d	Sc or Pr	Sh or Nu
$1 < Re_d < 450$	Sc or Pr < 250	Sh or Nu $= 2 + 0.6\ Re_d^{0.5}$ (Sc or Pr)$^{1/3}$
$1 < Re_d < 17$	Sc or Pr > 250	Sh or Nu $= 2 + 0.5\ Re_d^{0.5}$ (Sc or Pr)$^{0.42}$
$17 < Re_d < 450$	Sc or Pr > 250	Sh or Nu $= 2 + 0.4\ Re_d^{0.5}$ (Sc or Pr)$^{0.42}$

List of symbols

A	Nozzle surface at cross section x [m^2]
a	Sound velocity in fluid [$m\ s^{-1}$]
C_p	Specific heat at constant pressure
d	Nozzle diameter at cross section x [m]
D	Diameter of particles or drops [m]
D_{vg}	Vapor diffusion coefficient in gas [$m^2\ s^{-1}$]
H	Relative humidity
I	Nucleation rate [$m^{-3}\ s^{-1}$]
J	Mass flow of vapor onto a drop [$kg\ s^{-1}$]
k	Thermal conductivity of fluid [$W\ m^{-1}\ K^{-1}$]
K	Boltzmann's constant
Kn	Knudsen number
L	Latent heat [J kg]
l_{th}	Throat length [m]
l_{conv}	Convergent length [m]
M_{ach}	Mach number
M	Molecular weight [$kg\ mol^{-1}$]
m_v	Mass of a vapor molecule [$kg\ mol^{-1}$]
N	Particle concentration [m^{-3}]
Nu	Nusselt number for a sphere
p	Pressure [Pa]
Pr	Prandtl number
q	Total mass flux rate in the nozzle [$kg\ s^{-1}$]
Q_l	Condensation heat release [$J\ s^{-1}$]
Q_c	Conduction heat release [$J\ s^{-1}$]
r	Ideal gas constant [$J\ kg^{-1}\ K^{-1}$]
Re	Reynolds number
Re_d	Droplet Reynolds number
r_{gp}	Ideal gas constant [$J\ K^{-1}\ mol^{-1}$]
S	Saturation ratio
Sc	Schmidt number
Sh	Sherwood number
T	Temperature [K]
t_s	Retention time [s]
v	Fluid speed [$m\ s^{-1}$]
V	Average thermal velocity [$m\ s^{-1}$]
v_m	Molecule volume [m^3]
x	Abscissa in nozzle [m]
ρ	Density [$kg\ m^{-3}$]
γ	Ratio of gas specific heats
σ	Surface tension [$N\ m^{-1}$]
λ	Mean free path [m]
μ	Dynamic viscosity [Pa s]

Indices

as	Reference fact to dry air
a	Reference fact to aerosol
d	Reference fact to droplet
i	Reference fact to generator state

l	Reference fact to liquid phase
t	Reference fact to Knudsen regime
th	Reference fact to nozzle throat
v	Reference fact to vapor
vs	Reference fact to saturating vapor state
∞	Reference fact to state far from the droplet.

References

Ahn, K.H., 1988: Ultrafine aerosol measurement and particle activation and droplet growth processes in condensation nucleus counters. *Ph.D. Thesis*, University of Minnesota.

Barrett, J.C. and *Clement, C.F.*, 1986: A soluble one-dimensional problem for coupled heat conduction and mass diffusion with aerosol formation in a vapor-gas mixture. *J. Aerosol Sci. 17*, 129-143.

Devienne, M., 1958: *Frottement et échanges thermiques dans les gaz raréfiés*. Gauthier-Villars, Paris.

Fletcher, N.H., 1962: *The Physics of Rainclouds*. Cambridge University Press.

Fuchs, N.A., 1959: *Evaporation and Droplets Growth in Gaseous Media*. Pergamon, New York.

Fuchs, N.A. and *Sutugin, A.G.*,1970: *Highly Dispersed Aerosols*. Ann Arbor Science Publishers, Ann Arbor, Michigan.

Fuller, E.N., Schettler, P.D., and *Giddings, J.C.*, 1966: A new method for prediction of binary gas-phase diffusion coefficients. *Ind. Eng. Chem.*58, 19-26.

Götz, G, Mészáros, E., and *Vali, G.*, 1991: *Atmospheric Particles and Nuclei*. Akadémiai Kiadó, Budapest.

Hughmark, G.A.,1967: Mass and heat transfer from rigid spheres. *Am. Inst. Chem. Engng. J. 13*, 1219–1221.

Johnston, M.V. and *Wexler, A.S.*, 1995: Mass spectrometry of individual aerosol particles. *Analyt. Chem. 67*, 721A-726A.

Jurski, K. and *Gehin, E.*, 2003: Heterogeneous condensation process in an air water vapour expansion through a nozzle-experimental aspect. *Int. J. of Multiphase Flow 29*, 1137-1152.

Kurten, H., Raash, J., and *Rump, F.H.*, 1966: *Chem. Ing. Tech. 38*, 941-948.

Mallina, R.V. and *Wexler, A.S.*,1997: Particle growth in high speed particle beam inlets. *J. Aerosols Sci. 28*, 223-238.

McMurry, P.H., 2000: The history of Condensation Nucleus Counters. *Aerosol Sci. Technol. 33*, 297-322.

Renoux, A. and *Boulaud, D.*,1998: *Les aérosols, physique et métrologie*. Lavoisier ed, Paris.

Seinfeld, J.,H.,1986: *Atmospheric Chemistry and Physics of Air Pollution*. Wiley, New York.

Stodola, A.,1927: *Steam and Gas Turbines*. McGrawHill, New York.

Tom, J.W. and *Debenedetti, P.G.*, 1991: Particle formation with supercritical fluids. *J. Aerosol Sci.* 22, 555-584.

Turner, J.R., Kodas, T.T., and *Friedlander, S.K.*, 1988: Monodisperse particle production by vapor condensation in nozzles. *J. Chem. Phys. 88*, 457-465.

Willeke, K.,1986: Temperature dependence of particle slip in gaseous medium. *J. Aerosol Sci. 5*, 191-204.

Yang, J., Jaenicke, R., Dreiling V., and *Peter, T.*, 2000a: Rapid condensational growth of particles in the inlet of particle sizing instruments. *J. Aerosol Sci. 31*, 773-788.

Yang, J., Jaenicke, R., and *Dreiling, V.*, 2000b: A continuous nozzle CNC for CN and CCN counting. *J. Aerosol Sci. 31*, 809-810.

IDŐJÁRÁS

Quarterly Journal of the Hungarian Meteorological Service
Vol. 108, No. 2, April–June 2004, pp. 95–122

Application of a cloud model in simulation of atmospheric sulfate transport and redistribution Part II. Numerical experiments and discussion of results

Vlado Spiridonov[1] and **Mladjen Curic**[2]

[1]*Institute of Physics, Faculty of Natural Sciences and Mathematics, St. Cyril and Methodius University, Skopje, Macedonia; E-mail: vspiridonov@mol.net.mk*

[2]*Department of Meteorology, Faculty of Physics, University of Belgrade, Serbia E-mail: curic@ff.bg.ac.yu*

(Manuscript received September 25, 2002; in final form November 19, 2003)

Abstract—The simulation of the so called summer case with continental polluted field initialization has revealed that convective thunderstorm generates strong vertical transport of gases and particulate compounds from the planetary boundary layer (PBL) to the upper troposphere (UT), perturbation of physical and chemical properties of aerosol, modification of pollutant concentration, and change of the spatial distribution of chemical species. The early formation of precipitation and enhanced scavenging have contributed to formation of approximately 2.5 times greater equivalent air concentration of sulfate in precipitation near the surface, than that found in the air at this level. The key microphysical processes that transfer the dissolved matter to the resultant frozen hydrometeors are: the accretion of cloud water by snow, accretion of cloud ice by snow, depositional growth of snow, wet and dry growth of graupel, accretion of cloud water by graupel, and auto-conversion (aggregation) of snow.

The so called spring case numerical experiment with chemical background taken from Macedonia provided an insight into the potential influence on the long-range transport of atmospheric pollutants and ascertained quantitative-qualitative assessments about processes by which acidic species are incorporated into precipitation. The parameters computed by the model are in fairly good agreement with observations. The average equivalent cloud water pH and rainwater pH were about 5.0 and 4.5, respectively, when the most acidic precipitation occurred.

The results of the sensitivity tests of cloud chemistry to the physical processes in continental non-polluted and polluted environments indicate, that in-cloud nucleation and scavenging of aerosols account for 27% and 20% of the total sulfur mass removed by wet deposition in non-polluted and polluted cases, respectively. Sub-cloud scavenging contributes for about 35% and 29% of the total sulfur mass removed by wet deposition. Liquid-phase in-cloud oxidation contributes for about 35% and 32%, while

sub-cloud oxidation accounts for about 40% and 35% of the total sulfur mass deposited for non-polluted and polluted cases, respectively. Neglecting the ice phase when considering chemistry in continental non-polluted and polluted clouds may lead to overestimation by about 140% and 150% of the total sulfur mass removed by wet deposition. The assumption of Henry's law equilibrium for these types of clouds results in overestimation of about 148% and 133%, respectively.

Key-words: cloud modeling, chemical processes, microphysics, sulfate transport.

1. Introduction

Numerical experiments and model sensitivity tests have been performed utilizing a relatively sophisticated dynamical cloud model with simple sulfur chemistry (*Spiridonov* and *Curic*, 2003, hereafter referred as Part I). In Part II, we continue with examination of the dependence of the chemical fields upon the physical processes, which take place in the in-cloud and near-cloud environment. In this way, one can study the effects of deep convection on the redistribution of atmospheric pollutants and clarify some primary relationships among dynamical, microphysical, and chemical processes in three-dimensional space and complex cloud environment.

Here we present the results of the numerical experiments. Three-dimensional cloud chemistry simulations have been performed in order to understand the transport and transformations processes, and to investigate the modification of the sulfate concentration in the in-cloud and near-cloud environments. Two basic parameter sets have been used to initialize the cloud chemistry model.

2. Three-dimensional numerical experiments

In this section, mainly the microphysical and chemical parts of the results of numerical experiments, i.e., results of the solution of the equations formulated in Sections 2 and 3 of Part I are discussed. As it was mentioned, in order to understand the transport and redistribution processes of chemical species inside convective clouds and in the near-cloud environment, and to explore the changes of pollutant concentrations, three-dimensional simulations of the chemistry of such clouds have been performed. Of course, 3D runs are also important dynamically for studying the relationship between wind shear and veering, rotation and orientation of updrafts and downdrafts, cloud movement relative to the mean direction, and flow of environmental wind around the cloud.

2.1 Boundary conditions and numerical technique

Boundary conditions are specified along all sides of the integration domain, since the computations take place within a finite model domain. Along the bottom of the model domain the normal velocity w is set to zero. The open top boundary condition is applied in the model in order to eliminate strong internal gravity waves (*Klemp* and *Durran*, 1983). Also the normal second derivatives for the eddy mixing terms are set to be zero along the boundaries. This provides vertical gradients in the mean state so the profiles are not distorted due to eddy mixing near the boundaries. The lateral boundaries are open and time-dependent, so that disturbances can pass through with minimal reflection. Two different cases with regard to the wind velocity are considered, after *Durran* (1981). When the velocity component normal to the boundary is directed inside the domain (inflow boundary), normal derivatives are set to zero. At outflow boundaries, the normal velocity component is advected out through the boundary with an estimated propagation speed which is averaged in the vertical, and weighted at each level by the approximate local amplitude of the wave. Boundary conditions for the pressure are calculated from other boundary values to maintain consistency.

Model equations are solved on a standard spatially staggered grid. All velocity components, u_i are defined at one-half grid interval $0.5\,\Delta x_i$, while scalar variables are defined at the midpoint of each grid. The horizontal and vertical advection terms are calculated by centered fourth- and second-order differences, respectively.

Since the model equations are compressible, a time splitting procedure is applied to achieve numerical efficiency. With this procedure the sound wave terms are solved separately using a smaller time step, while all other processes are treated with a larger time step, Δt, which is appropriate to the time scales of physical interest. The small and large time steps are applied as follows. The scalar prognostic equations, except the pressure equation, are solved from $t-\Delta t$ to $t+\Delta t$ by a single leap-frog step. The terms which are not responsible for sound wave generation in the equations of motion and the pressure equation, are evaluated at the central time level t. Finally, the wind and pressure prognostic variables are stepped forward from $t-\Delta t$ to $t+\Delta t$, with forward time differencing by the small time step. In grid points adjacent to lateral boundaries, the normal horizontal advection terms are approximated using second-order differences instead of the fourth-order ones used elsewhere. At lateral boundaries, the normal derivatives for all prognostic variables are calculated with first-order accuracy, through one-sided differences lagged at time $t-\Delta t$ to provide stability.

2.2 Initial conditions and initialization procedure

Fig. 1 shows the representative radio-sounding for simulation of a moderate air mass thunderstorm which occurred on July 6, 1995. This is referred hereafter as summer case. The main characteristic of the sounding is a stable dry layer limiting cloud growth. The atmosphere was moist to the height of 350 hPa, with two thin layers of great thermal stability. The wind profile is characterized by weak wind velocity near the surface, veering at the sub-cloud layer, enhanced wind shear at the mid-level, and strong zonal wind at the upper levels. The initial mixing ratios of rain and solid water are set to zero at all levels. The initial values of the number concentration of cloud droplets, $N_1 = 1000$ cm^{-3}, and dispersion, $D_0 = 0.40$, used in this study for the computation of auto-conversion are consistent with the nature of continental clouds.

Table 1 lists the chemical field initialization used to simulate two environments: (i) continental non-polluted background and (ii) continental polluted one.

The initial fields of temperature, humidity, horizontal wind velocity, and chemical data giving the input for the April 3, 2000 case (spring case) are depicted in *Fig. 2*. The concentrations of SO_2, H_2O_2, O_3, and NH_4^+ and SO_4^{2-} aerosols are assumed to fall exponentially with height, e.g.,

$$q_i(z) = q_i(0)\mathrm{e}^{-z/H}, \tag{1}$$

where $q_i(0)$ is the mixing ratio of component i at the lowest model level; H is the model scale height.

Initial impulse for convection is an ellipsoidal warm bubble of the form

$$\Delta T = \Delta T_0 \cos^2 \frac{\pi}{2}\beta \qquad \text{for} \quad \beta < 1, \tag{2}$$

where

$$\beta = \left[\left(\frac{x - x_c}{x_*}\right)^2 + \left(\frac{y - y_c}{y_*}\right)^2 + \left(\frac{z - z_c}{z_*}\right)^2\right]^{1/2}. \tag{3}$$

Here, the subscript c refers to the location of the center of the perturbation, while x_*, y_*, z_* are radial dimensions of the bubble. Values used for these simulations are $x_c = 12$ km, $y_c = 6$ km, $z_c = 0.5$ km, $x_* = y_* = 2.8$ km, $z_* = 0.5$ km, and the temperature perturbation is maximum in the bubble center, distinguishing $T_0 = 4$°C for the summer case simulation and $T_0 = 3.6$°C for the spring case, and exponentially decreasing to zero on the bubble boundary.

The initial perturbation of water vapor mixing ratio, caused by this initial temperature perturbation, is calculated with assumption that relative humidity has the same value as it had before the perturbation.

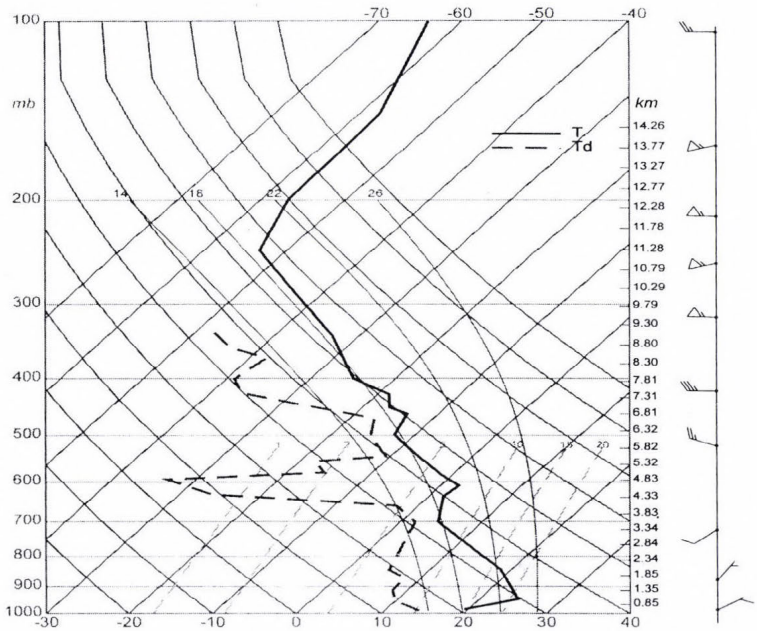

Fig. 1. The 00:00 UTC atmospheric sounding for Skopje, on July 6, 1995. Coordinate lines denote pressure (hPa) and temperature (°C). The solid line represents the temperature profile and the dashed line represents the moisture profile. Symbols on the right side of the same figure denote wind profile (direction and velocity).

Table 1. Initial fields of chemical species involved in sulfate production, for continental non-polluted and continental polluted background, based on *Taylor* (1989b)

Chemical species expressed through mixing ratios	$q_i(0)$ [μg kg^{-1}(air)]		H (km)
	Continental non-polluted clouds	Continental polluted clouds	
q_{SO_2}	4.42	21.0	2.0
$q_{SO_4^{2-}}$	3.1	16.0	3.5
$q_{NH_4^+}$	0.58	3.0	3.5
$q_{H_2O_2}$	0.59	0.59	-
q_{O_3}	82.8	82.2	-

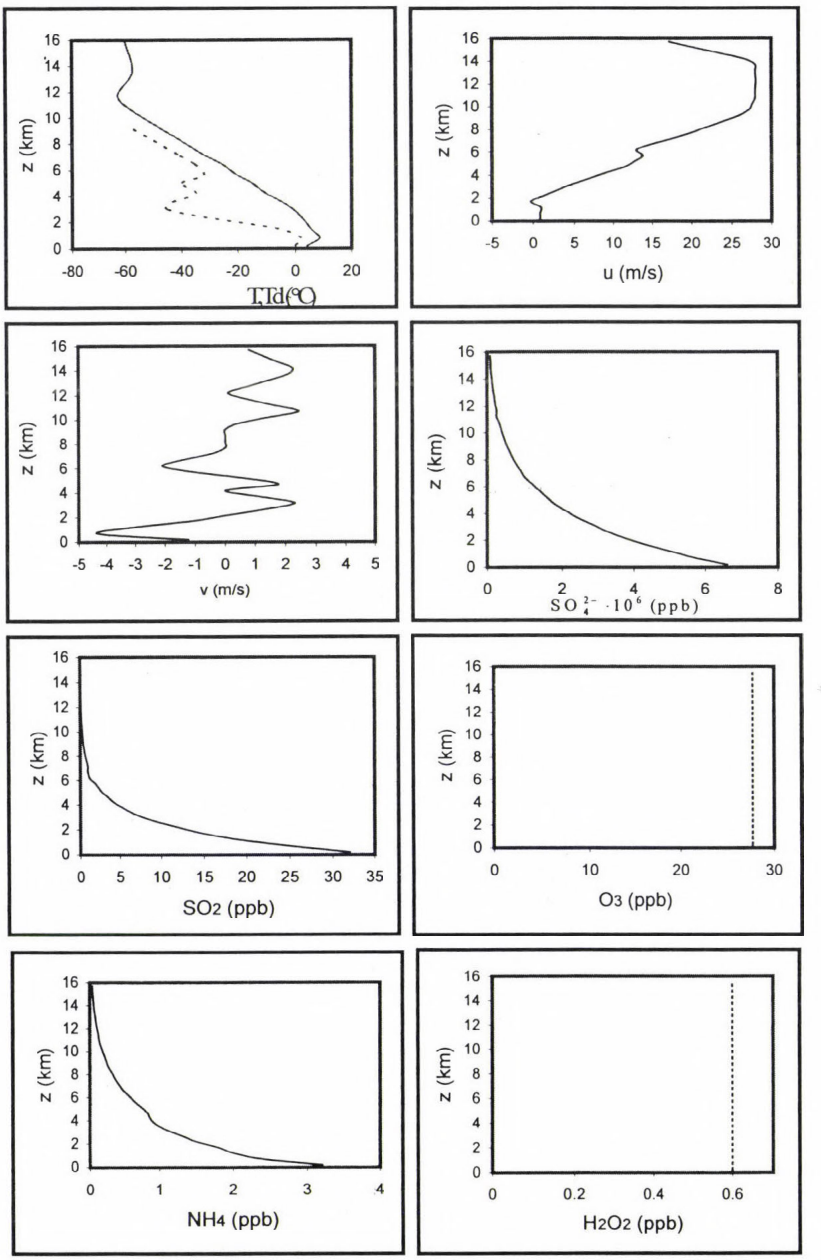

Fig. 2. The initial fields of temperature, humidity, u and v the horizontal wind velocity components and the chemical data set input of SO_4^{2-}, SO_2, O_3, NH_4^+, and H_2O_2 (in ppb), for April 3, 2000.

The model domain for the summer case simulation is 45 km × 45 km × 15 km. The model for the spring case is configured to a 24 km × 24 km × 12 km domain. The horizontal resolution of the model is 1 km, while the vertical one is 0.25 km for the summer case and 0.5 for the spring case run. The temporal resolution of the model is 5 and 10 s for integration of the dynamics, microphysics, and chemistry, and a smaller one is 0.2 and 2 s for solving the sound waves. The same temporal resolution is taken for solving aqueous phase chemistry and transport of chemical species.

3. Results

A number of case studies have been performed in the past to verify and document the value of the present cloud model in contributing to the understanding of convective storm dynamics and microphysics (e.g., *Telenta* and *Aleksic*, 1988; *Curic et al.*, 1999; *Spiridonov* and *Telenta*, 2000).

3.1 The summer case simulation of July 6, 1995

Numerical simulation results shown in *Fig. 3* indicate development of the model cloud starting at time 12.5 min. after initialization. Strong updrafts rapidly move the cloud towards the super-cooled zone, forming traces of ice crystals. After 23 min. the simulated cloud could be described as Cu med. with cloud water mixing ratio 7.5 g kg^{-1} and two minutes later raindrops occur with mixing ratio of 0.3 g kg^{-1}. Hail occurs in the 28th min and snow in the 29th, when the cloud could be identified as Cu cong. with depth about 9.6 km. Soon after that massive formation of graupel gives the intensive vertical development of the cloud an important energy source. In 40 minutes simulation time, hail reaches its maximum mixing ratio 16.0 g kg^{-1}. In 45 minutes the cloud top penetrates the tropopause, soon after that our 3D run indicates rapid transformation of graupel to rain, while the melting graupel also enhances precipitation, and the mixing ratio of rain increases to its maximum value of 12.7 g kg^{-1}. The mature stage of the simulated storm comes after 70 min. of integration when extensive precipitation occurs. The fallout of hydrometeors weakens the updraft intensity and cuts off the supply of moisture from the surface, so the cloud top spreads horizontally forming the characteristic anvil. The weakened surface convergence indicates the entering of dissipation stage, although, remaining anvil survives for a much longer time. After 120 minutes, only fragmented structure of the cloud remains in the integration domain. The maximum accumulated rain is 175 mm, and accumulated hail is 1.3 kg m^{-2}. In summary, the three-dimensional simulation indicates a moderate air mass thunderstorm with appearance of large amount of precipitation.

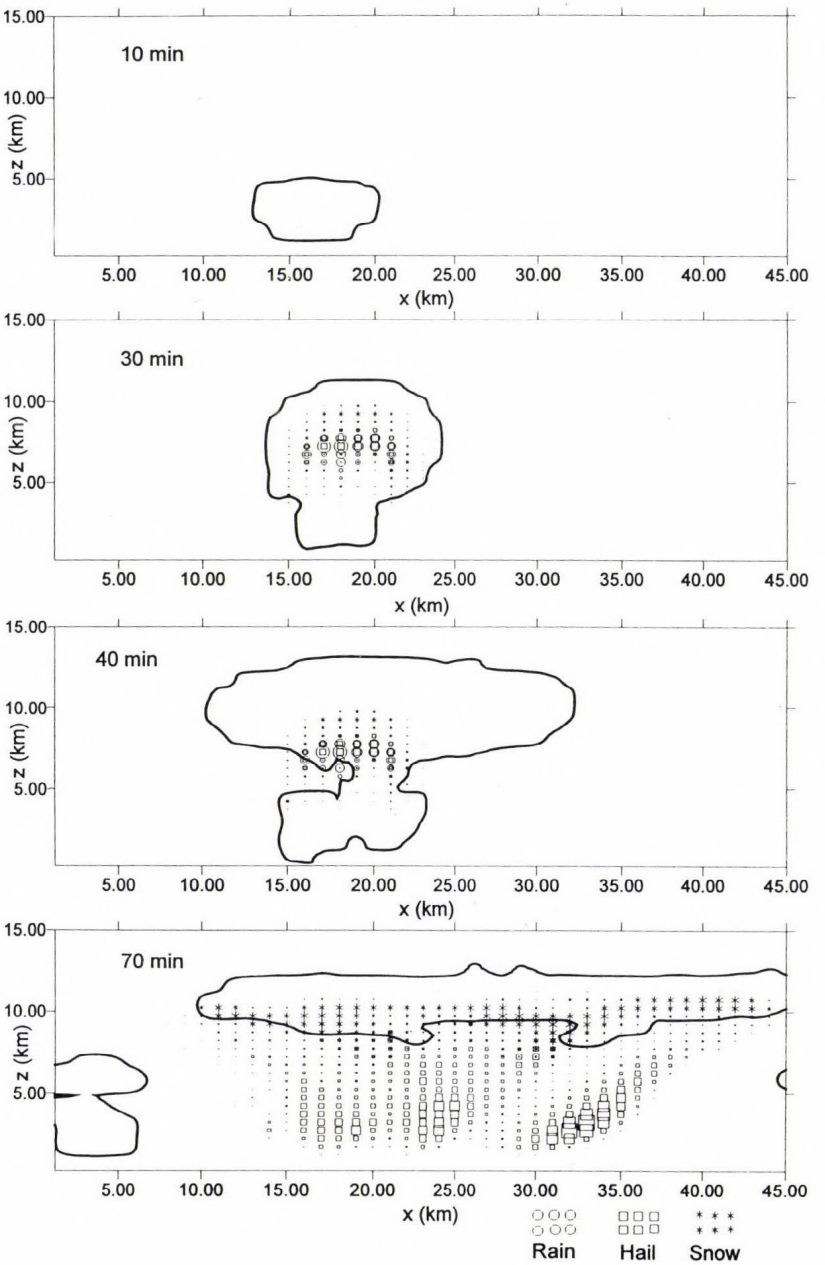

Fig. 3. General cloud appearance at 10, 30, 40, and 70 min. in $x - z$ plane at $y = 8.0$ km. Cloudy areas are outlined by the solid line with cloud water mixing ratio = 0.01 g kg^{-1}. Dots and rectangular boxes indicate rain and hail mixing ratios greater than 0.5 g kg^{-1}, respectively. The asterisks denote the snow mixing ratio greater than 0.5 g kg^{-1}.

The real microphysical structure of the storm chosen for numerical simulation was examined through calculations of the maximum radar reflectivity factor. The time evolution of the radar reflectivity maps are shown in *Fig. 4*. Dominant features are the temperature perturbation and appearance of the first radar echo 12 min. after the initialization. Then one can note rapid growth and spread of the radar reflectivity in the super-cooled zone of the cloud model domain. This phase of cloud evolution is characterized by intensive microphysical transformations. The formation of precipitation is evident on the radar reflectivity patterns from 30 to 50 min., when maximum radar reflectivity is found in the warm sector of the model domain. *Table 2* shows the comparison between some simulated and observed parameters for the analyzed case.

Vertical cross-sections of the integrated SO_4^{2-} aerosol mixing ratio in the simulated storm built up in 10, 30, 40, and 50 minutes are presented in *Fig. 5*. A three-dimensional view of sulfate transport and redistribution inside the convective cloud volume is shown in *Fig. 6*. It is conspicuous that sulfate transport and changes of its spatial distribution go parallel with cloud formation and evolution. Convergence near the cloud base is the result of mass transfer by nucleation scavenging and Brownian diffusion. The formation of rain leads to a more uniform distribution of aerosol mass. After this, the updrafts are no longer sufficient to maintain the mass flux, and scavenging by rain successively reduces the mass of cloud-dissolved sulfate. The equivalent air concentration of sulfate in the precipitation near to the surface is approximately 2.5 times higher than the concentration in the air at this level. It suggests that both processes, oxidation by O_3 and H_2O_2 in rainwater and scavenging by rain, contribute to the formation of excess sulfate near to the surface. We found that after 40 min. simulation time, sulfate reaches the ground leading to wet deposition. Small portion of sulfate mass, which is not scavenged by hydrometeors, is advected by flows at upper cloud levels led by the basic tropospheric wind. As time elapses, evaporation from precipitation becomes so important, that a fraction of the sulfate is transferred back into the air.

Evolution of the pH factor in cloud water and rainwater after 20, 30, 40, and 50 min. of simulation time is shown in *Fig. 7a,b*. The dashed curves delineate the cloud and rainwater boundary, while solid lines display the pH factor distribution in cloud and rainwater, respectively. The strong gradient of cloud water acidity in early stages of cloud development is due to mass convergence and dissolution of pollutants in cloud water close to the central part of the cloud. In the mature stage, successive weakening of the gradient followed by slight lowering of cloud water acidity can be seen. Subsequently, the formation of precipitation induces rain scavenging and dissolution of pollutants, contributing to much more uniform pH distribution. The average

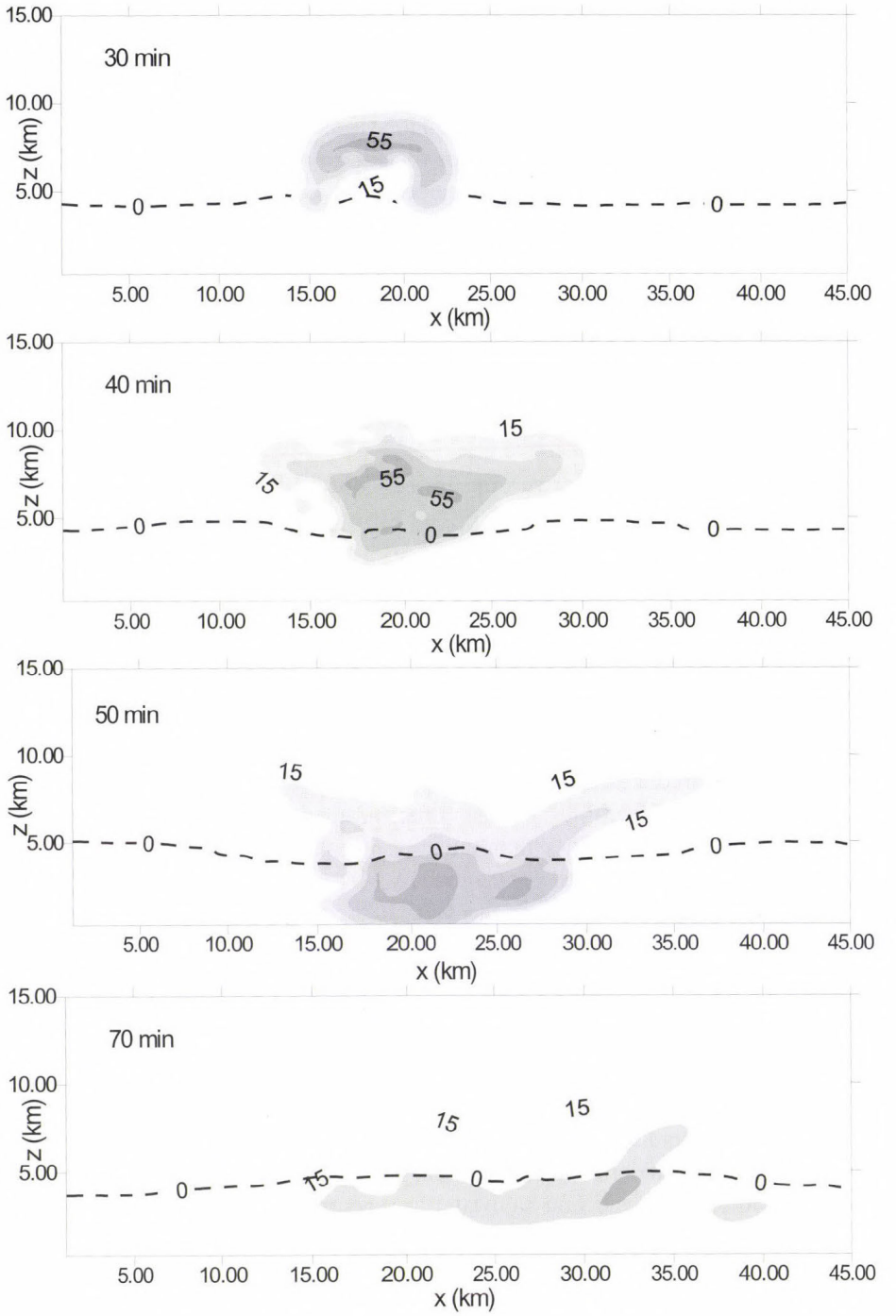

Fig. 4. The radar reflectivity history maps (dBz) in $x - z$ plane at $y = 8.0$ km at 30, 40, 50, and 70 min. Dashed lines denote distribution of 0°C isotherm.

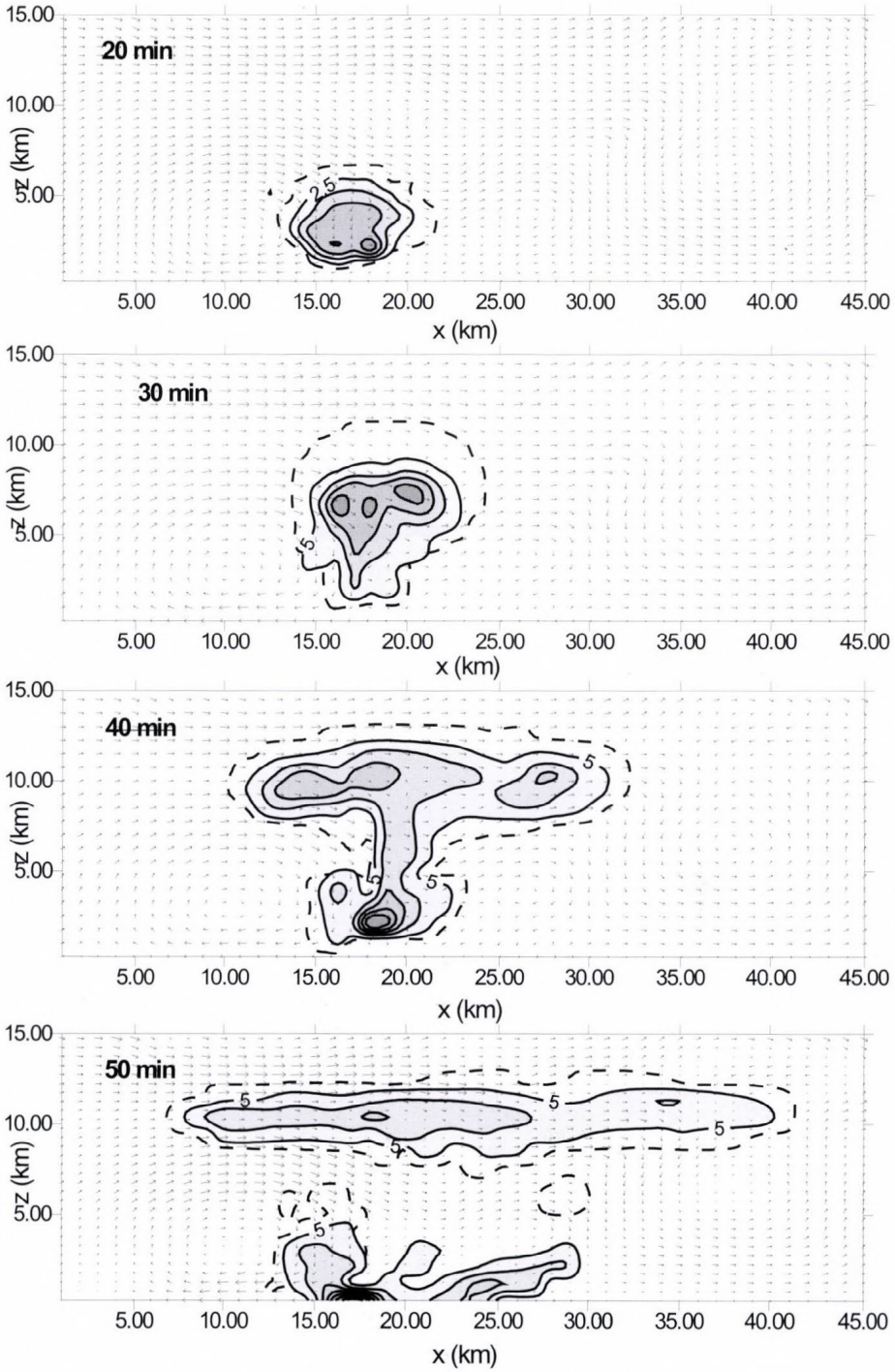

Fig. 5. Time evolution of sulfate concentration in the cloud (μg m^{-3}) in $x - z$ plane at $y = 8.0$ km in 10, 30, 40, and 50 min. of the simulated storm on July 6, 1995. Arrows denote wind fields.

Table 2. The comparison between simulated and observed parameters on July 6, 1995 (summer case)

Parameter	Cloud base (km)	Cloud top (km)	Max. vertical velocity ($m\ s^{-1}$)	Max. radar reflectivity (dBz)	Total acc. rain ($kg\ m^{-2}$)	Total acc. hail ($kg\ m^{-2}$)
Model	2.2	13.5	20.4	56	175	1.3
Observed	2.4	14.6	18.3	50	180	-

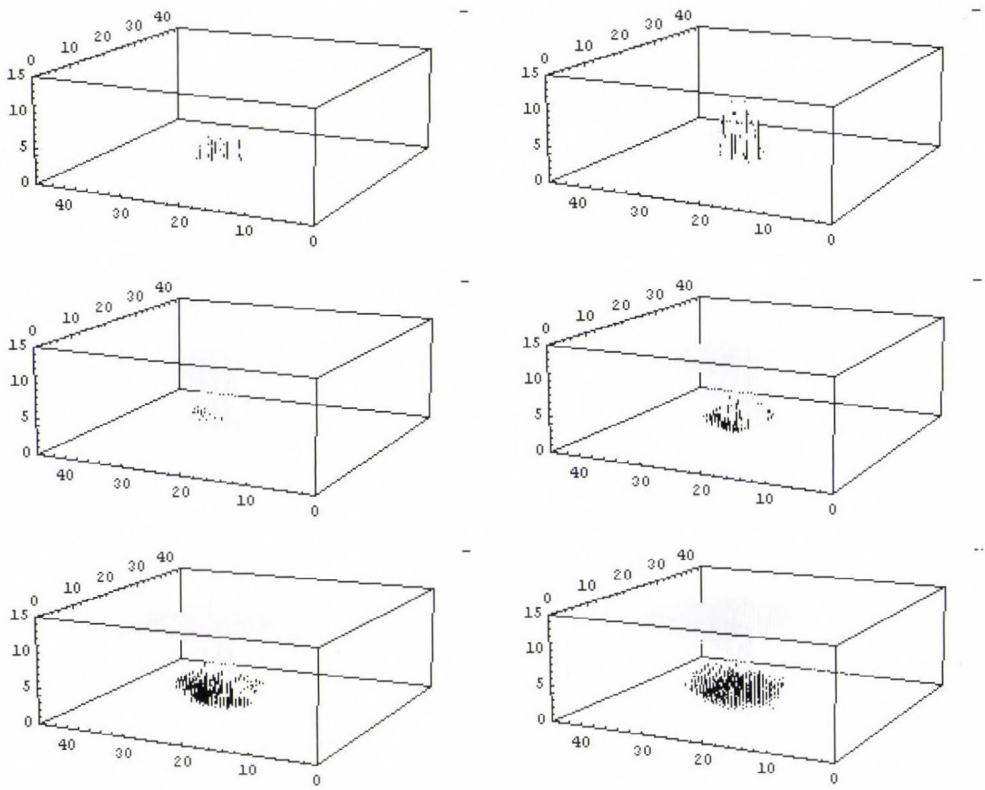

Fig. 6. Three-dimensional view of sulfate transport and redistribution, in 10, 20, 30, 40, 50, and 120 min. of time. The dark patterns delineate cloud water mixing ratio greater than 0.01 g kg^{-1}, the light fields are sulfate concentrations greater than 2.5 ($\mu g\ m^{-3}$).

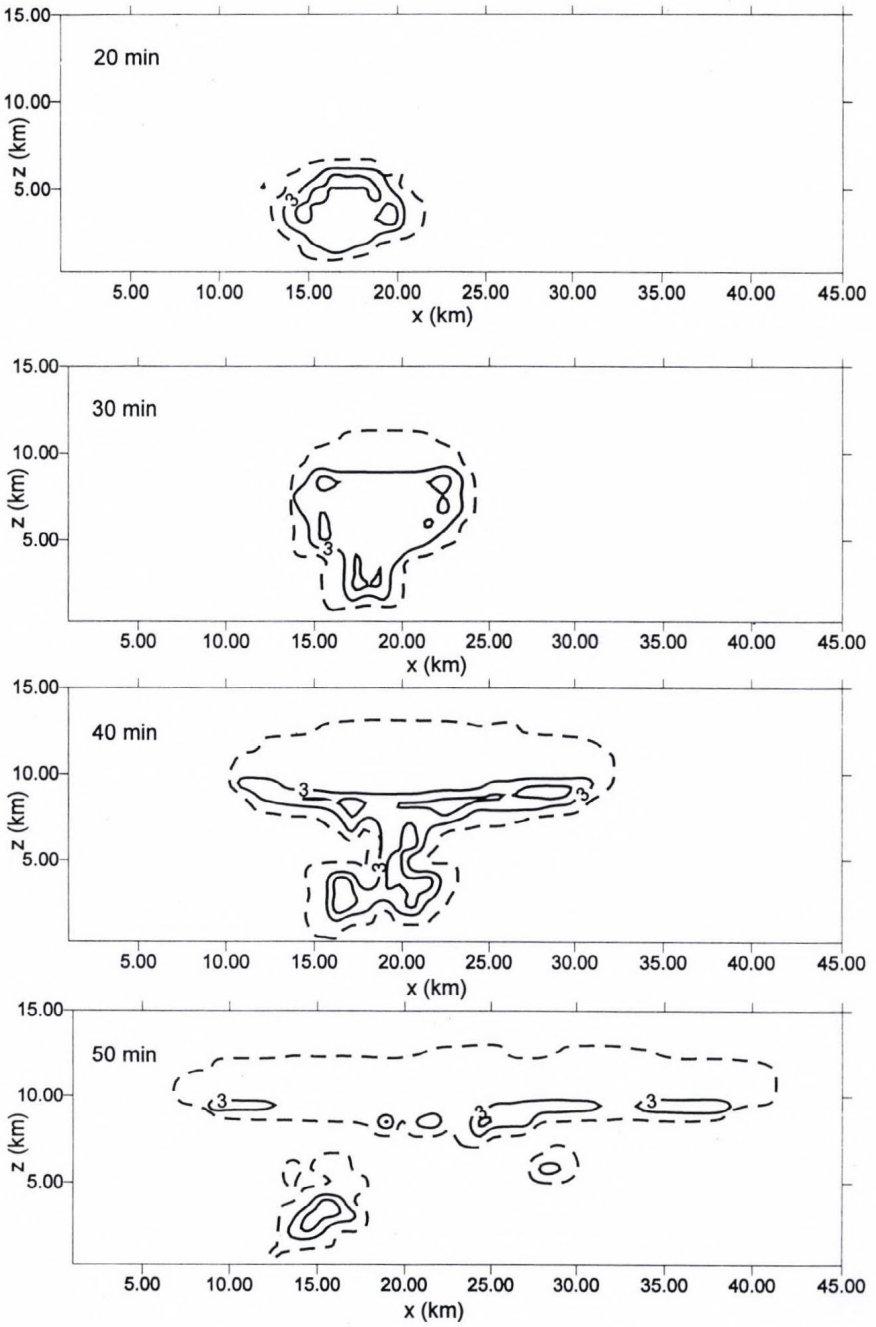

Fig. 7a. Time evolution of the pH values of cloud water in the $x-z$ plane at $y = 8.0$ km, in 20, 30, 40, and 50 min. of the simulation time.

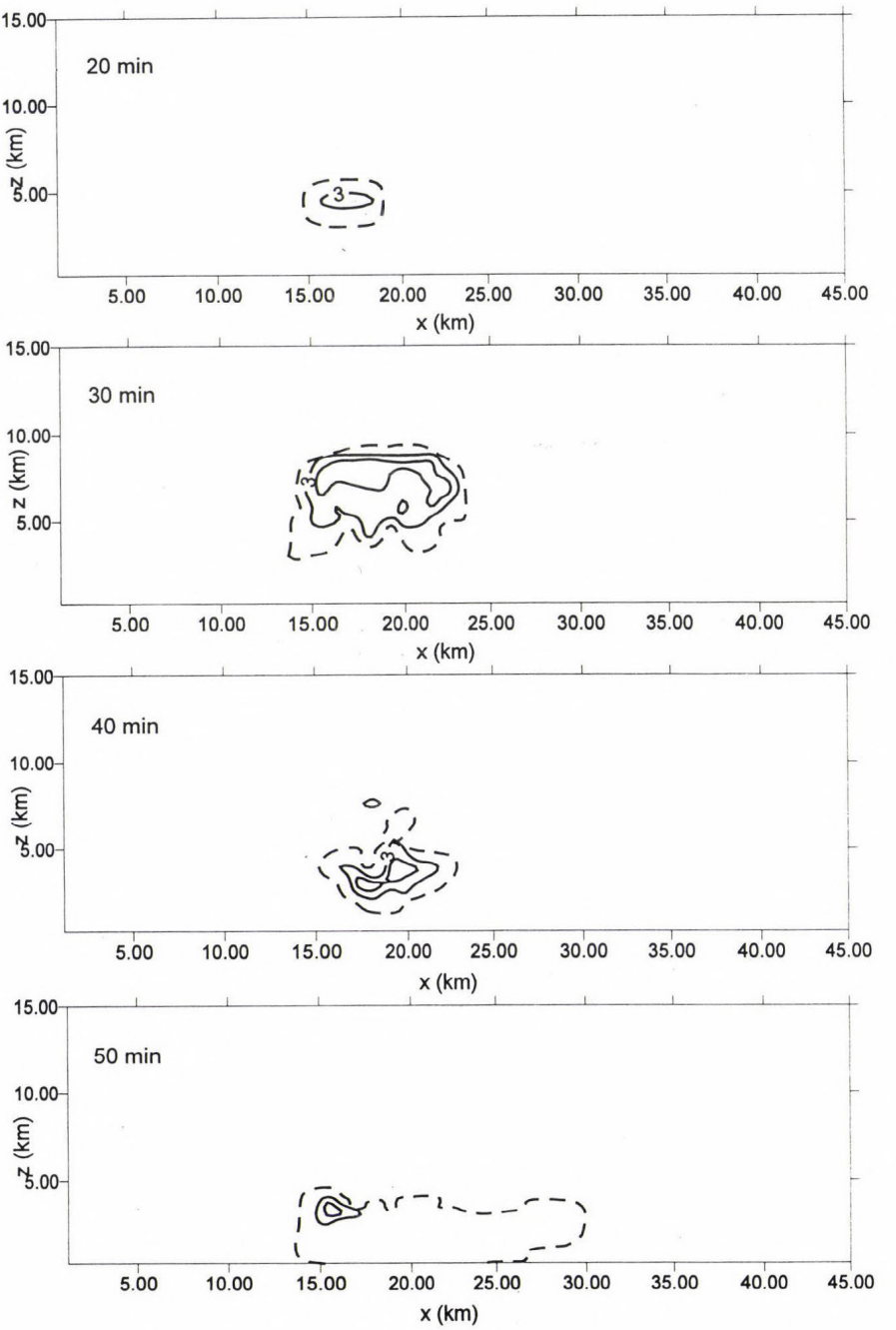

Fig. 7b. Time evolution of the pH values of rainwater in the x–z plane at $y = 8.0$ km, in 20, 30, 40, and 50 min. of the simulation time.

pH of rain near the ground is lower than 3.0 demonstrating the influence of increased nucleation and oxidation on the acidity of the rain. Similar results for the pH distribution, but for warm clouds are illustrated in the study by *Tremblay* and *Leighton* (1986) and for a one-dimensional case by *Taylor* (1989b). The higher pH in *Taylor* (1989b) is a result of the assumed Henry's law equilibrium and implicit treatment of gases taking part in sulfate production. The lower calculated rainwater pH in *Tremblay* and *Leighton* (1986) is mainly due to the cloud model limitation, the warm cumulus convection ignoring ice-phase processes.

3.2 The spring case simulation of April 3, 2000

Large amount of mineral dust can be mobilized over the Sahara and injected into the atmosphere under favorable atmospheric conditions. Even areas far away from the desert such as Macedonia are sometimes affected by dust transport and deposition, when dust behaves as a pollutant that significantly reduces the air quality. It also causes the increase of content of all chemical components, both anions, cations, and heavy metals (*Nickovic et al.*, 2000). Ambient SO_4^{2-} aerosol concentrations during such dust storms may considerably exceed international standards for allowable concentrations.

In order to understand the sulfate aerosol transport and transformation processes in such conditions and to investigate the modification of pollutant concentration in the local cloud environment, also fully three-dimensional simulation of the chemistry of a convective cloud have been performed.

The time evolution of the size-integrated SO_4^{2-} aerosol concentration distribution during the storm's life is depicted in *Fig. 8.* The numerical simulation has shown rapid vertical transport of sulfate in the cloud formation stage due to the mass transfer by nucleation of the sulfate particle matter. Subsequently, this cloud parcel is advected and dispersed by the turbulent flow field. Enhanced zonal flows at the upper level rapidly move the polluted cloud into the central part of the integration domain. Early formation of rain contributes to enhanced microphysical sulfate mass exchange among different water species. The much higher sulfate concentration value after 30 min. is mainly due to oxidation of SO_2 to SO_4^{2-} and scavenging processes. After this the updrafts are not sufficient to maintain sulfate mass at the cloud base, and washout by rain gradually reduces cloud dissolved sulfate. It is also seen, that rain-laden sulfate reaches the ground after 30 min., causing wet deposition at the surface. The short time cycle of the convective cloud does not allow continuation of the process, and cloud enters into dissipative stage.

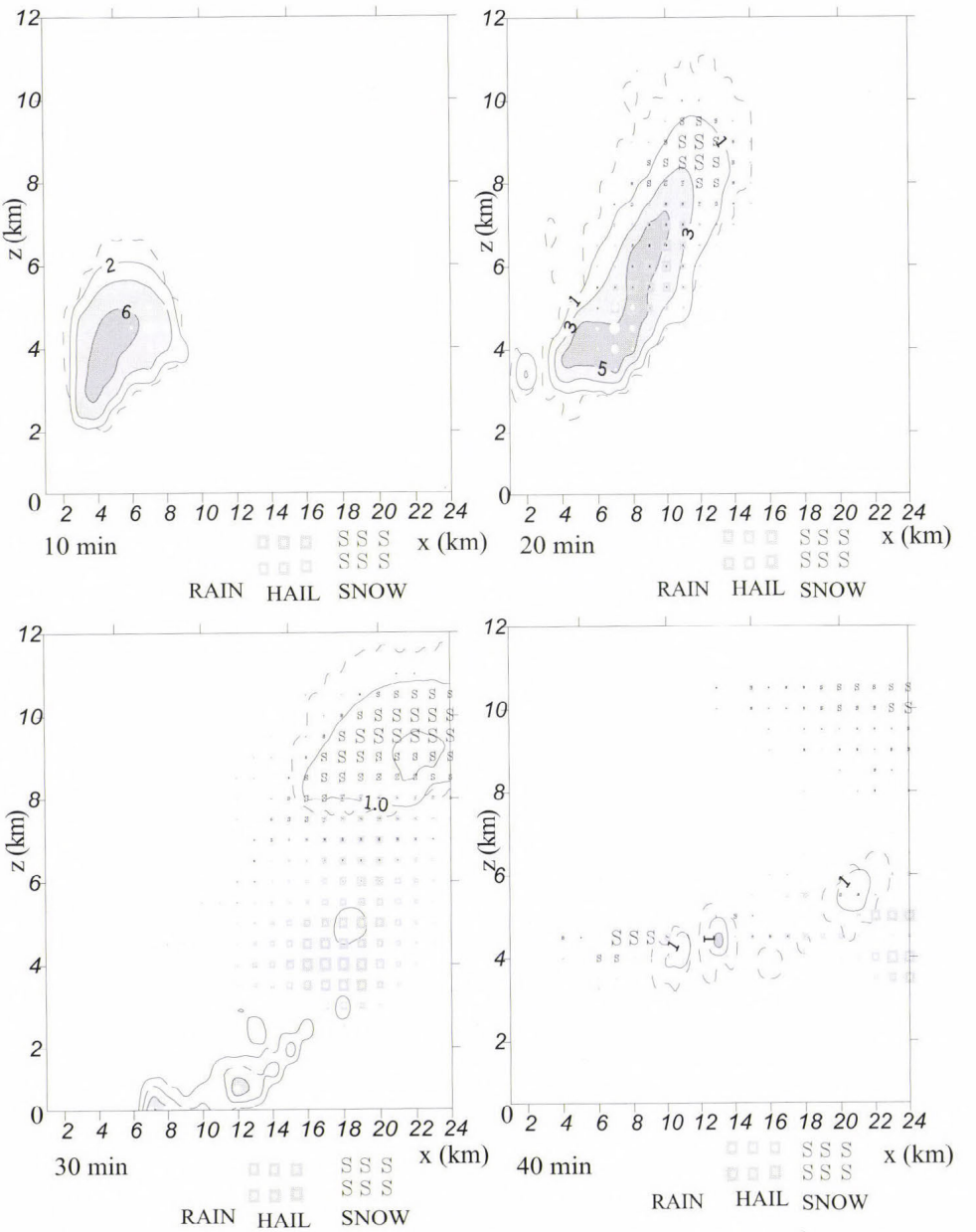

Fig. 8. Time evolution of sulfate (SO_4^{2-}) aerosol concentration (mg ℓ^{-1}) in 10, 20, 30, and 40 min., in the simulated cloud, in the x–z plane at $y=10$ km, on April 3, 2000. Cloudy areas are outlined by the dashed line with (cloud water + cloud ice) mixing ratio greater than 0.01 g kg^{-1}. Dots and asterisks indicate rain and hail mixing ratios greater than 0.5 g kg^{-1}, respectively. The symbol '*s*' denotes the snow mixing ratio greater than 0.5 g kg^{-1}. The solid curves represent isopleths of SO_4^{2-} fields in the simulated cloud.

Table 3 lists some parameters that characterized the numerical simulation performed here. Among others, maximum volume concentration of SO_4^{2-} (mg ℓ^{-1}), pH of cloud and rainwater, respectively, and total wet deposition (mg m^{-2}) for 60 min simulation were calculated.

Table 3. List of the model calculated parameters for the spring case simulation

Parameter	Time (minute)					
	10	**20**	**30**	**40**	**50**	**60**
Total rainfall (ℓ m^{-2})	0.0	0.0	5.6	19.5	24.3	27.8
pH – cloud water	5.0	6.0	6.5	6.0	5.0	5.5
pH – rain	3.0	4.5	7.0	3.6	4.5	5.5
Max. concentration $[SO_4^{2-} - S]$ (μg m^{-3})	4.3	6.5	8.0	10.5	8.0	5.5
Total wet deposition $[SO_4^{2-} - S]$ (mg m^{-2})	0.0	0.2	15.4	29.4	38.4	40.2
Max. ionic concentration $[NH_4^+]$ (μg m^{-3})	0.6	0.6	0.6	0.6	0.5	0.4
Mixing ratio of rain, q_R (g kg^{-1})	0.0	0.1	0.4	0.4	0.4	0.4
Mixing ratio of snow, q_S (g kg^{-1})	0.0	0.6	1.5	1.5	1.5	1.5
Max. vertical velocity, W_{max} (m s^{-1})	11.6	12.8	13.9	13.9	13.9	13.9

3.3 Comparison between simulated and measured of cloud chemical characteristics

Model results were compared to those observed and analyzed by standard laboratory methods. Precipitation samples from meteorological station Lazaropole (located in a rural representative area at 1333 meters a.s.l.) have been collected in every 24 hours with a wet only sampler ARS 1510. These measurements are continuously carried out in the framework of the European Monitoring and Evaluation Programme (EMEP). The chemical analysis of rainfall samples is performed using standard methods for anions (see, e.g., *Nickovic et al.*, 2000; *Andreevska et al.*, 2001).

The observed and measured parameters detected in precipitation samples for the period March–April 2000 are listed in *Table 4*. It is conspicuous, that

maximum amount of rainfall, pH, volume concentration of SO_4^{2-}, and wet deposition have really occurred on April 3 and 4. It is certain, that unstable conditions and convection contributed to the maximum rainfall and adequately higher concentration and deposition values in that period.

Table 4. Rainfall, pH, sulfate volume concentration and wet deposition, measured at the meteorological station Lazaropole during March–April, 2000

Date	Rain (ℓ m^{-2})	pH	SO_4–S (mg ℓ^{-1})	SO_4–S (mg m^{-2})
March 2–3, 2000	19.0	4.75	0.107	2.04
March 5–6, 2000	0.8	4.46	0.371	0.287
March 15–16, 2000	25.2	4.47	0.107	2.70
March 16–17, 2000	1.4	5.38		
March 17–18,2000	0.2	4.99		
March 18–19, 2000	0.1	4.53	0.270	0.027
March 26–27, 2000	1.7	5.36	0.964	1.64
March 27–28, 2000	8.1	5.05	0.321	2.60
April 1–2, 2000	6.2	6.10	1.070	6.63
April 3–4, 2000	**30.2**	**7.65**	**6.690**	**42.04**
April 4–5, 2000	**6.0**	**7.78**	**3.540**	**21.22**
April 5–6, 2000	6.1	6.26	0.910	5.54
April 6–7, 2000	2.7	4.70	0.320	0.87
April 7–8, 2000	2.4	5.68		
April 10–11, 2000	11.3	5.52	3.620	7.97
April 18–19, 2000	2.2	6.43		
April 19–20, 2000	2.6	6.04	0	0
April 20–21, 2000	4.0	4.11		
April 25–26, 2000	9.0	4.28	0.129	1.16
April 29–30, 2000	5.0	4.10	0.740	3.70
April 30–May 01, 2000	8.2	4.07	0.160	1.31

Note: On April 3 and 4, unstable conditions and strong convection led to the high concentration and deposition values.

The comparative analysis has shown good agreement between simulated and observed total accumulated precipitation. Higher measured pH values as compared to calculated pH = 5.5 are probably due to the fact, that dust is an alkaline compound that increases the pH value. There is also a fairly good agreement between measured and calculated total wet deposition of SO_4^{2-}. The latter was 40.16 mg m^{-2} for 120 min. simulation time. One of the reasons for higher simulated concentration value of SO_4^{2-} (10.50 mg ℓ^{-1}) is the result of using higher initial SO_4^{2-} concentration. The laboratory results and peaks have also shown good coincidence with the model-computed results.

These results have also been compared with the results of chemical analysis of precipitation at the main meteorological station (MMS) Lazaropole taken from the study on air pollution monitoring system in FYROM, published by the Japan International Cooperation Agency (*JICA*, 1999). Results shown in *Table 3* show quite reasonable values of pH in comparison to annual averaged pH value (6.22). There is also good agreement between calculated and measured SO_4^{2-} and NH_4^+ ionic concentrations.

Table 5. The relative contribution of the total sulfur and NH_4^+ mass removed by wet deposition for continental non-polluted and continental polluted background for a summer case simulation on July 6, 1995. The asterisk represents which chemical or physical parameterization is not involved in the simulation

3D Model run	Absorption		Nucleation and impact scavenging		Liquid-phase oxidation of SO_2 by H_2O_2 and O_3		Aqueous simulation of ice phase	Sulfur and NH_4^+ integrated precipitation mass (in kg)			
	Kinetic/Henry's Law		in-cloud/subcloud		in-cloud/subcloud			Continental clouds non-polluted / polluted			
								SO_4^{2-}	NH_4^+	SO_4^{2-}	NH_4^+
I	yes*	no	yes	yes	yes	yes	yes	8.12	3.42	26.20	6.84
II	no	yes*	yes	yes	yes	yes	yes	12.05	4.43	42.17	12.50
III	yes	no	no*	yes	yes	yes	yes	5.93	2.39	20.75	5.52
IV	yes	no	yes	no*	yes	yes	yes	5.20	2.00	17.51	5.06
V	yes	no	yes	yes	no*	yes	yes	5.05	3.42	16.95	6.84
VI	yes	no	yes	yes	yes	no*	yes	4.75	3.42	16.70	6.84
VII	yes	no	yes	yes	no*	yes	no*	11.30	4.78	39.79	11.43

4. The model sensitivity tests

The relative importance of absorption, scavenging, oxidation, and ice phase processes in the production and subsequent deposition of SO_4^{2-}, for mid-latitude moderate air mass thunderstorms have been determined from the cloud model generated microphysics and chemical fields. *Table 5* gives the parameters that distinguish among the seven numerical experiments carried out here. The first run that includes entire chemistry serves as a basis for comparison to each other. *Table 6* lists the sulfate source terms for the summer case simulation on July 6, 1995. As it can be seen from *Table 6*, the dominant production terms that control the sulfate chemical reactions are the SO_4^{2-} nucleation scavenging (PS3), oxidation of S(IV) in cloud water and rainwater by O_3 and H_2O_2 (PS2, PS9), SO_4^{2-} transfer from cloud water to cloud ice as

a result of depositional growth of cloud ice (PS14), and transfer of cloud water to SO_4^{2-} when cloud droplets evaporate (PS15).

Table 6. The sulfate production terms for the summer case simulation on July 6, 1995 (kg $kg^{-1}s^{-1}$). All terms are defined in Part I. Symbols in bold letter denote the dominant sulfate source terms

PSU1	$0.3 \cdot 10^{-12}$	**PSU2**	$0.1 \cdot 10^{-8}$	**PSU3**	$0.3 \cdot 10^{-9}$	PSU4	$0.1 \cdot 10^{-12}$	PSU5	$0.9 \cdot 10^{-11}$
PSU6	$0.4 \cdot 10^{-13}$	PSU7	$0.4 \cdot 10^{-11}$	PSU8	$0.9 \cdot 10^{-12}$	**PSU9**	$0.8 \cdot 10^{-8}$	PSU10	$-0.2 \cdot 10^{11}$
PSU11	$0.3 \cdot 10^{-11}$	PSU12	$0.2 \cdot 10^{-11}$	PSU13	$0.2 \cdot 10^{-11}$	**PSU14**	$0.3 \cdot 10^{-10}$	**PSU15**	$0.5 \cdot 10^{-10}$
PSU16	$0.7 \cdot 10^{-12}$	PSU17	$0.1 \cdot 10^{-11}$	PSU18	$-0.7 \cdot 10^{18}$	PSU19	$0.6 \cdot 10^{-19}$	PSU20	$0.2 \cdot 10^{-11}$
PSU21	$0.2 \cdot 10^{-12}$	PSU22	$0.3 \cdot 10^{-12}$	PSU23	$0.1 \cdot 10^{-13}$	PSU24	$0.2 \cdot 10^{-14}$	PSU25	$0.2 \cdot 10^{-12}$
PSU26	$0.5 \cdot 10^{-11}$								

4.1 The absorption of chemical species

The absorption of gas phase chemical species into cloud water and rainwater is determined by either Henry's law equilibrium or by explicit time-dependant calculation of gas transfer to droplets, using mass transfer limitation calculations.

Fig. 9a shows how the mixing ratios of gases included in sulfate production, dissolved in the cloud water and rainwater, are propagated and distributed within the simulated storm by applying the kinetic gas uptake method. Panels shown in *Fig. 9b* depict distributions of gases assuming Henry's law equilibrium. The difference is more emphasized for a more soluble gas as hydrogen peroxide.

The assumption of Henry's law equilibrium leads to about 148% higher value of the integrated sulfate mass removed by wet deposition for continental non-polluted clouds, and about 133% for continental polluted clouds. It suggests that models of mid-latitude continental storms, which neglect kinetic gas uptake limitations, will tend to over-predict the wet deposition.

4.2 The effects of in-cloud and sub-cloud scavenging for continental non-polluted and polluted clouds

Scavenging is found to be a very important process contributing to the redistribution of sulfate, which can cause decrease of concentrations of chemical species inside the cloud and in the near-to-cloud environment. The efficiency of scavenging processes in the production and subsequent deposition

of SO_4^{2-} for the continental non-polluted and polluted air mass thunderstorms were determined from the model generated microphysical and chemical fields.

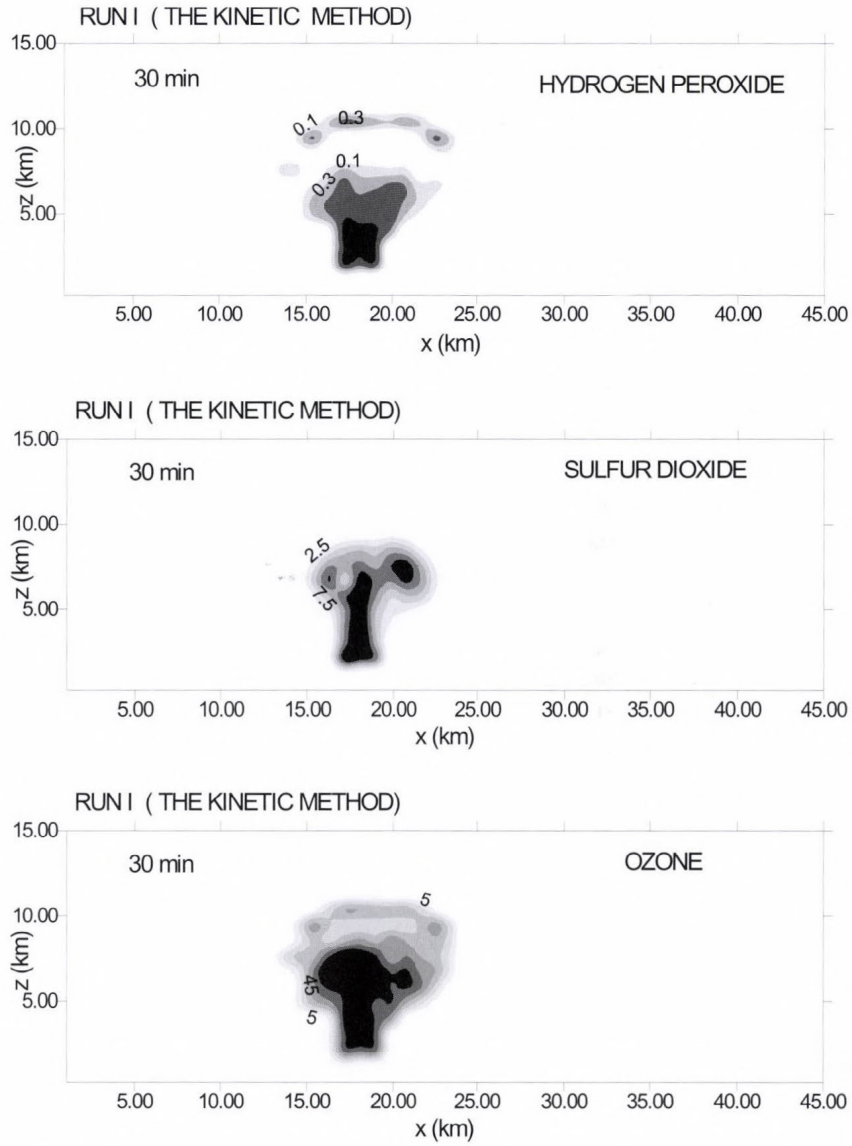

Fig. 9a. Time evolution of H_2O_2, SO_2, and O_3 concentrations in ($\mu g\ m^{-3}$) in x–z plane at $y = 8$ km, in 30 min. of the simulated cloud on July 6, 1995, by including method of kinetic gas limitations.

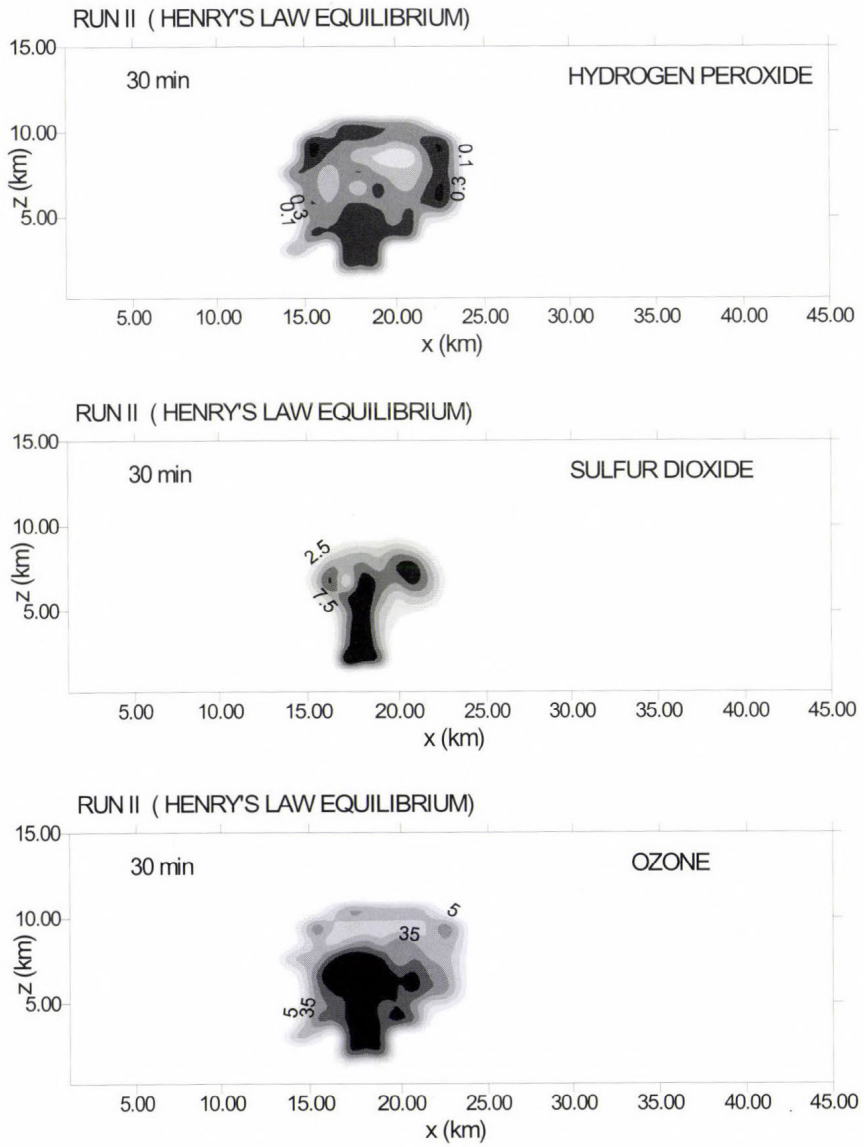

Fig. 9b. Time evolution of H_2O_2, SO_2, and O_3 concentrations in ($\mu g\ m^{-3}$) in x–z plane at $y=8$ km, in 30 min. of the simulated cloud on July 6, 1995, using Henry's Law assumption.

Examination of the SO_4^{2-} fields provides information about the integrated aerosol scavenging, i.e., nucleation scavenging, Brownian diffusion by cloud droplets, and dynamic-impact scavenging by falling hydrometeors. In-cloud

scavenging of SO_4^{2-} and NH_4^+ parallel, providing that the ratio SO_4^{2-}/NH_4^+ remains constant. Sub-cloud scavenging is also a linear function of the local aerosol concentration and non-linear function of precipitation rate. Since the NH_4^+ and SO_4^{2-} aerosol fields have identical collection efficiency (11.0), scavenging of SO_4^{2-} aerosol in the sub-cloud region will take place parallel with the NH_4^+ sub-cloud scavenging.

In-cloud scavenging for distributions in continental non-polluted and polluted cases is responsible for about 27% and 20% of the total production, respectively. Sub-cloud scavenging for those types of clouds contributes about 35% and 29%, respectively. Values in *Table 6* indicate that about 30% of the NH_4^+ in precipitation is from in-cloud scavenging, and that about 23% is from sub-cloud scavenging.

In-cloud scavenging processes in *Taylor* (1989b) accounted for 30–50%, while sub-cloud scavenging contributed for about 25%. These higher calculated percentage numbers, especially for in-cloud scavenging, are attributed to one-dimensionality of the model used, and to the assumed Henry's law equilibrium, which leads to strong scavenging of gases.

4.3 The relative importance of oxidation in sulfate production and wet deposition

Reactions, which evolve during oxidation of S (IV) to S (VI) by H_2O_2 and O_3, are of particular interest of cloud chemistry. In order to estimate the relative contribution of SO_2 oxidation, two experiments were set up. The first one was accomplished using the entire chemistry parameterization discussed in paper by *Spiridonov* and *Curic* (2003), while the second turned off all oxidation terms, i.e., PS2, PS9, PH20, OHP20, PH21, and OHP21. *Fig. 10a* shows time series of SO_4^{2-} aerosol distributions obtained by the oxidation off run, in the mature and heavy precipitation stages of the storm evolution. Plots shown in *Fig. 10b* represent distribution by oxidation off run. As it can be seen in *Fig. 10a*, inclusion of oxidation terms gives relatively higher in-cloud and sub-cloud SO_4^{2-} concentration values almost everywhere in the domain. It suggests that possible enhanced oxidation in convective clouds may act as an important source of sulfate in the air, as illustrated by the time evolution of the integrated sulfate concentration.

In-cloud oxidation of S (IV) to SO_4^{2-} is a function of aerosol composition and accounts for about 35% in the non-polluted clouds and about 32% in the polluted ones. Sub-cloud oxidation contributes to 40% and 35% of the total sulfur mass removed by wet deposition in the case of non-polluted and polluted

clouds, respectively. Oxidation of SO_2 accounts for about 15% of the in-cloud SO_4^{2-}. These results are in quite good agreement with those of *Wang* and *Prinn* (2000). Their calculations indicate that about 9.0% of dissolved SO_2 have been converted into aqueous sulfuric acid for 30 hours simulation. As a result, the aqueous processes only contribute 21% to the total sulfate production. A slightly higher estimated value of our study (15%) in light of *Wang* and *Prinn* (2000) is probably attributed to different model initializations and using low ozone (10 ppb) in the initial profile of O_3 mole fraction.

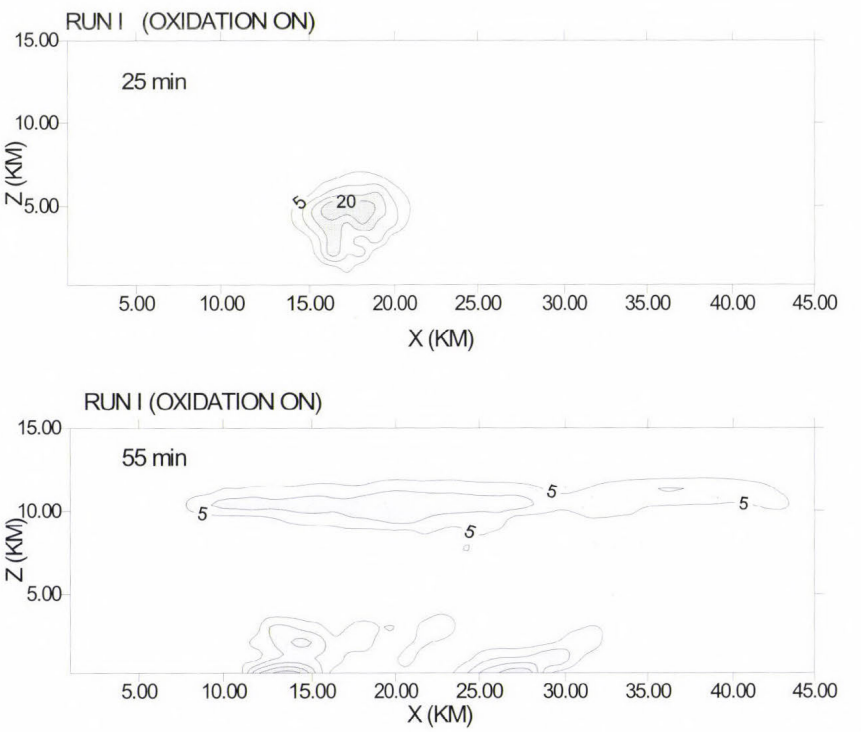

Fig. 10a. Time evolution of the sulfate concentration (μg m^{-3}) in the $x-z$ plane at $y = 8.0$ km, in 25 and 55 min. Panels represent sulfate distribution by oxidation on run.

It is also interesting to compare the results here to those in *Taylor* (1989b), where in-cloud oxidation of SO_2 contributed to 10% and 25% of the total sulfur mass deposited, while sub-cloud oxidation accounted for about

10% and 35% for continental non-polluted and continental polluted clouds, respectively. These values seem to be overestimated, as the result of implicit treatment of gases included in chemistry scheme and assumed Henry's law equilibrium. Finally, the integrated sulfur mass removed by wet deposition for continental non-polluted and continental polluted distributions of our study accounted for about 8.12 and 26.20 kg, respectively, and are similar to estimated values (7.35 and 24.35 kg) in *Taylor* (1989b).

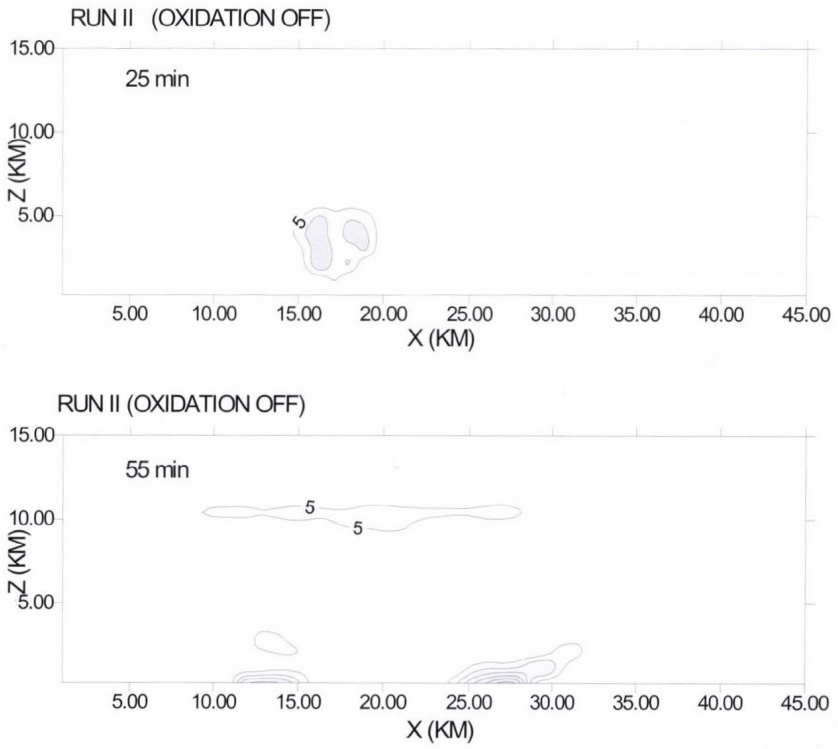

Fig. 10b. Time evolution of the sulfate concentration ($\mu g\ m^{-3}$) in the $x-z$ plane at $y = 8.0$ km, in 25 and 55 min. Panels represent sulfate distribution by oxidation off run.

4.4 The role of the ice phase processes

Table 7 lists the dominant production terms for rain, snow, and hail that control the microphysical processes for the summer case simulation of July 6, 1996. As it can be seen, most of the precipitation in the simulated convective

clouds came from the ice-phase processes. The key microphysical processes that transfer the dissolved species to the resultant frozen hydrometeor are the accretion of cloud water by snow (PSACW), accretion of cloud ice by snow (PSACI), depositional growth of snow (PSDEP), wet and dry growth of graupel (PGDRY, PGWET), accretion of cloud water by graupel (PGACW), and auto-conversion (aggregation) of snow (PGAUT). Conversion of cloud water to ice phase terminates the aqueous phase sulfate reactions. Collision of super-cooled droplets with solid ice and riming leads to the efficient retention of sulfate. In order to study the effects of ignoring the ice phase upon the chemistry, a series of test were made in which the cloud dynamics and microphysics were not changed, but the chemical reactions in the frozen hydrometeors were assumed to be identical to those in precipitation water. Neglecting liquid-ice phase leads to overestimation of the total sulfur mass removed by wet deposition of about 148% for continental non-polluted and around 133% for continental polluted distributions, relative to the base run.

Table 7. The dominant transfer rates for the microphysical processes for the summer case simulation on July 6, 1995

Rain ($g\,g^{-1}s^{-1}$)		Snow ($g\,g^{-1}s^{-1}$)		Hail ($g\,g^{-1}s^{-1}$)	
PRAUT	0.0	PSAUT	0.0	**PGAUT**	$0.6\cdot10^{-7}$
PRACW	0.0	**PSACI**	$0.2\cdot10^{-5}$	PGFR	$0.3\cdot10^{-9}$
PIACR	0.0	**PSACW**	$0.5\cdot10^{-5}$	**PGACW**	$0.3\cdot10^{-5}$
PSACR	$0.9\cdot10^{-6}$	PSACR	$0.3\cdot10^{-11}$	PSACR	$0.4\cdot10^{-11}$
PGARR	$-0.3\cdot10^{-14}$	PSFW	$0.4\cdot10^{-13}$	**PRACS**	$0.3\cdot10^{-5}$
PGFR	0.0	PSFI	$0.1\cdot10^{-12}$	PRACI	$0.2\cdot10^{-19}$
PSMLT	$-0.7\cdot10^{-10}$	PIACR	$0.6\cdot10^{-16}$	PGACR	$0.2\cdot10^{-11}$
PREVP	$-0.2\cdot10^{-5}$	**PSDEP**	$0.3\cdot10^{-6}$	PGACRP	$0.4\cdot10^{-10}$
PRAUT	0.0	PSMLT	0.0	PIACR	$0.1\cdot10^{-16}$
PRACW	0.0	PGACS	0.0	PGSUB	0.0
PSACW	0.0	PGAUT	$0.4\cdot10^{-7}$	PGACS	$0.2\cdot10^{-5}$
PGACW	0.0	**PRACS**	$0.8\cdot10^{-6}$	**PGDRY**	$0.3\cdot10^{-5}$
PGMLT	$-0.2\cdot10^{-5}$	PSSUB	$-0.2\cdot10^{-7}$	PGWET	$0.8\cdot10^{-4}$

5. Summary and conclusions

A three-dimensional interactive cloud dynamics, microphysics, and chemistry model has been used to simulate the sulfate transport and redistribution by deep convective clouds.

The summer case simulation has shown generation of strong vertical upward and downward air motions, intensive cloud evolution, microphysical transformations, and occurrence of extensive precipitation. The simulation demonstrated that the local air mass thunderstorm can significantly change the spatial distribution of sulfate aerosol concentrations. The formation of ice phase can greatly modify the relative efficiency of aqueous reactions, and thus modify the changes in chemical properties induced by deep convection. The early formation of precipitation and enhanced scavenging contributed to the build-up of approximately 2.5 times greater equivalent air concentration of sulfate in precipitation near the surface than that found in the air at this level. The key microphysical processes that transferred the dissolved matter to the resultant frozen hydrometeor were the accretion of cloud water by snow, accretion of cloud ice by snow and depositional growth of snow, wet and dry growth of graupel, accretion of cloud water by graupel, and auto-conversion (aggregation) of snow.

The spring case numerical experiment with chemical background taken from Macedonia provided insight into the potential influence on the long-range transport of atmospheric pollutants, and ascertained some semi-quantitative and semi-qualitative hypotheses about processes by which acidic species are incorporated into precipitation. The model computed sulfate concentration and wet deposition are in fairly good agreement with observations. The average equivalent cloud water pH and rainwater pH, when more acid precipitation occurs, are about 5.0 and 4.5, respectively.

The performed sensitivity tests have revealed that nucleation and aerosol in-cloud scavenging account for about 30% and 20% of the total sulfur mass removed by wet deposition, for continental non-polluted and polluted clouds, respectively. Sub-cloud scavenging contributed to 35% and 29% of the total sulfur mass deposited. Liquid-phase in-cloud oxidation contributes to about 35% and 32%. Sub-cloud oxidation in those types of clouds accounted for about 40% and 35%, respectively. Neglect of the ice phase when considering chemistry in continental non-polluted and continental polluted clouds may lead to overestimation by about 140% and 150% of the total sulfur mass removed by wet deposition. The assumption of Henry's law equilibrium for those types of clouds gives overestimation of about 148% and 133%, respectively.

Many questions related to the impact of deep convection on redistribution of atmospheric pollutants remain unanswered. Our next task is to improve the

model chemistry by including more detailed gaseous phase physics and chemistry, better initialization without random parts, parameterization of radiation, as well as surface chemical processes.

Acknowledgements—First of all we acknowledge to *Mr. Bosko Telenta* for his support, giving insights, and explanations concerning the technical aspects of his model. We also wish to express our gratitude to *Professor Dragan Markovic* of the University of Belgrade for his suggestions and advice during development of the chemistry part of the cloud model. The anonymous referees have made many substantial remarks that increased the completeness and clarity of the manuscript. We would like to express our special gratitude to *Dr. Tamás Práger* for his important contribution giving constructive comments during final revision of the paper.

References

Andreevska, M., Spiridonov, V., and *Cvetkovic, J.*, 2001: Dust transport and deposition in FYROM in April 2000. *J. Environmental Protection and Ecology 2,* 704-716.

Curic, M., Janc, D., and *Vuckovic, V.*, 1999: The effects of the hail suppression seeding simulated by the two-dimensional convective cloud model. Seventh WMO Scientific Conference on Weather Modification, Thailand, *WMO/TD-No. 936, Vol. II*, 515-518.

Durran, D.R., 1981: The effects of moisture on mountain lee waves. *Ph.D. Thesis*. Massachusetts Institute of Technology Boston, MA(NTIS PB 82126621).

Hsie, E.Y., Farley, R.D., and *Orville, H.D.*, 1980: Numerical simulation of ice-phase convective cloud seeding. *J. Appl. Meteor. 19*, 950-977.

JICA, 1999: The study on air pollution monitoring system in FYROM. Final report (draft).

Klemp, J.B. and *Durran, D.R.*, 1983: An upper boundary condition permitting internal gravity wave radiation in numerical mesoscale models. *Mon. Wea. Rev. 11*, 430-444.

Nickovic, S., Spiridonov, V., Andreevska, M., and *Music, S.*, 2000: Simulation and measurements of dust deposition in Macedonia. *Proc. 15th International Conference on Nucleation & Atmospheric Aerosols (AIP)*. Rolla, Missouri, Arizona, USA.

Spiridonov, V. and *Telenta, B.*, 2000: Numerical simulation of propagation of air pollution released from coal power plant during snowstorm. *Proc. 13th Int. Conf. on Clouds and Prec., Vol. I.* Reno, Nevada, USA, 902-905.

Spiridonov, V. and *Curic, M.*, 2003: Application of a cloud model in simulation of atmospheric sulfate transport and redistribution. Part I. Model description. *Időjárás 107,* 85-114.

Taylor, G.R., 1989b: Sulfate production and deposition in midlatitude continental cumulus clouds II, Chemistry model formulation and sensitivity analysis. *J. Atmos. Sci. 46,* 1991-2007.

Telenta, B. and *Aleksic, N.*, 1988: A three-dimensional simulation of the 17 June 1978 HIPLEX case with observed ice multiplication. *2nd Int. Cloud Modeling Workshop. WMO/TD,* No. 268, Toulouse, 277-285.

Tremblay, A. and *Leighton, H.*, 1986: A three-dimensional cloud chemistry model. *J. Climate Appl. Meteor. 25*, 652-671.

Wang, C. and *Prinn, R.G.*, 2000: On the roles of deep convective clouds in tropospheric chemistry. *J. Geophys. Res. 105,* 22,269-22,297.

IDŐJÁRÁS

Quarterly Journal of the Hungarian Meteorological Service
Vol. 108, No. 2, April–June 2004, pp. 123–140

An estimate of the influence of climate change on heating energy demand in regions of Hungary, Romania, and Finland

Andrea Vajda, Ari Venäläinen, Heikki Tuomenvirta and **Kirsti Jylhä**

Finnish Meteorological Institute, Meteorological Research,
P.O. Box 503, FIN-00101 Helsinki, Finland; E-mail: claudia.vajda@fmi.fi

(Manuscript received February 27, 2002; in final form July 1, 2003)

Abstract—In this study the impacts of predicted anthropogenic climate change on heating energy demand in some regions of three European countries are estimated. The countries studied are Hungary, Romania, and Finland. The estimate is obtained by examining the projected future values of the heating degree-days (HDD) index, a measure widely used for assessing heating energy consumption. Estimates of climate change are obtained from two coupled atmosphere-ocean general circulation model runs, conducted by the HadCM3 and the ECHAM4/OPYC3 models. The results suggest a 10–14% decrease in heating energy demand during the next 50 years in the three studied countries. Though there are still uncertainties related to the magnitude of climate warming, the negative trend in heating energy demand seems so evident, that it should be taken into account in the planning of future energy management.

Key-words: climate change, heating degree-days index, heating energy demand, energy and climate.

1. Introduction

The anticipated air temperature rise due to anthropogenic climate change will have several impacts on the energy sector (e.g., *Darmstadter*, 1993). Higher temperatures lead to reduced heating energy demand during the winter seasons, and in some regions to an increased cooling energy demand during summers, although, the estimate of the net effect is scenario- and location dependent. Some energy production and distribution systems may experience adverse impacts that would reduce supplies or system reliability, while other

energy systems may benefit. The availability of hydro-, wind-, and solar power may change if precipitation, evaporation, wind and cloudiness undergo changes. Changes in river flow regimes, greater probability of drought and less precipitation falling as snow may reduce the hydroelectric capacity of current powerhouses. Increased cloudiness can reduce solar energy production. Wind energy production would also be reduced if wind speeds increased above or fall below the acceptable operating range of available technology (*IPCC*, 2001a,b). Global warming may also affect the energy sector. For example, the efficiency of condensing power plants may decrease, the rise of the cooling water temperature (taken from oceans and continental waters: rivers, lakes) may produce this negative influence additionally. The amount of available bioenergy may increase as the speed of forest growth increases (e.g., *Kellomäki*, 1993).

The HDD index is the sum of the differences between daily mean outdoor temperature and indoor temperature. It has been found to be a good measure for estimating heating energy consumption (e.g., *Quayle* and *Diaz*, 1980). The HDD index has been used as an estimate for heating energy demand in several research projects. For example, *Cvitan* and *Poje* (1985) estimated the degree of coldness in Croatian winters using the number of heating days and the heating degree-days. *Hargy* (1997) constructed objective mapping of the spatial variation of degree-days for Ireland applying statistical models of spatial variation to a digital terrain model of Ireland. These maps were then used to identify areas with anomalous temperature regimes. *Kadioglu et al.* (1999) studied heating degree-days in Turkey and represented maps of spatial degree-days distribution; these were then related to various climatic, meteorological, and topographic features of Turkey. Studies on heating degree-days were conducted in Czech Republic by *Starostova* (1999). The study examined the heating period characteristics in south Bohemia for the period 1961–1997, when the annual sums of degree-days showed a slight regressive trend.

In North America, *Soule* and *Suckling* (1995) examined the temporal trends and spatial variability of heating and cooling degree-days in a region of south-eastern USA for the period 1960–1989 using time series analysis, regression analysis, and a climate departure index. Their results showed a weak downward trend for actual heating degree-days values across the region during the studied period. *Darmstadter* (1993) studied climate change impacts on the energy sector and energy supply in the MINK region (Missouri, Iowa, Nebraska, and Kansas states). He illustrated that a 0.65–0.90°C rise in temperature results in a 5–8% decline in heating degree-days and a 20–40% rise in cooling degree-days. In Canada, the HDD values during the period 1990–1998 showed a significant negative trend. Heating degree-days, as simulated by the first version of Canadian Global Coupled Model (CGCM1) in

the GHGA runs, may decrease by 25–50% over northern landmasses by the year 2100 (*Kharin* and *Zwiers*, 2000).

The scope of the present research is to estimate the possible future change in the heating energy demand for two regions, Finland in northern Europe and parts of Hungary (Great Hungarian Plain) and Romania (Transylvanian Basin) in Central and East Europe. Within the studied regions, *Tistea* (1974) has determined the monthly HDD values for Romania and identified the regions. In Hungary, *Ambrózy* and *Faragó* (1988) analyzed the effect of severe meteorological conditions, especially the unusually cold winter periods, on the energy supply and demand. They introduced some additional tasks which pertain to energy problems that might arise under severe meteorological conditions. *Faragó et al.* (1991) studied the global and regional changes of climate and impacts of these, as well as the climatic sensitivity of the energy demand and consumption. According to their results, the climatic change will have essential impact upon the energy demand and consumption: 1°C change in the mean winter temperature would cause a change of 6% of opposite sign in the domestic energy use for heating purposes.

In Finland, *Kuivalainen et al.* (1996) conducted a study of the impact of climate change on the energy production and consumption. Their results suggest a significant decrease in the need for heating energy (25% by 2100) and an increase in the energy-supply (5% for hydroenergy capacity by 2100). Their study was based on two climate scenarios: the Finnish Research Programme on Climate Change, SILMU (*Carter et al.*, 1995), and the Nordic project (*Jonsson et al.*, 1994). *Sælthun et al.* (1998) have also studied the climate change impacts on the energy consumption and hydropower production in Nordic countries. For Finland they determined a 2.4% reduction in the electricity demand by 2050. In the current study the estimates for the magnitude of climate warming are obtained from two transient climate change simulations, performed with coupled atmosphere-ocean general circulation models: HadCM3 (e.g., *Gordon et al.* (2000) and *Pope et al.* (2000)) and ECHAM4/OPYC3 (*Roeckner et al.*, 1999). The period studied is the first half of the 21st century (2000–2050). Measured data (1901–1999) were used to obtain an indication in the natural variation of the HDD index.

Population-weighted heating degree-days are often used, as they reflect the combined effects of climate fluctuations and population movements (*Downton et al.*, 1988; *Taylor*, 1981). Besides population, the heating energy consumption also depends on building construction. For example, new buildings may have better insolation, and thus energy consumption is less than in older buildings. The volume of building stock also affects the absolute heating energy demand; the increase in building stock during the study period causes more heating energy demand. However, this paper does not study how

the population will develop, how the volume of building stock will change, or how construction techniques will develop in the future. These issues are beyond the scope of the paper, we will concentrate on climate related aspects that also contain a number of uncertainties.

2. Data and methods

2.1 The calculation of heating degree-days

The heating degree-days index (HDD) is the sum of the differences between daily mean outside temperature (Tdaily) and inside temperature. There are different ways to calculate HDD index, for example, sometimes daily maximum and minimum outside air temperatures are used instead of daily mean temperature. The inside or base temperature is adopted according to historical convention, quite often 15°C is used (*Heerdegen*, 1988). In Scandinavian countries the inside temperature is estimated to be 17°C, and thus monthly HDD index can be calculated using Eq. (1),

$$HDD = \sum_{i=1}^{n} [-(Tdaily_i - 17)], \tag{1}$$

where n is the number of days per month. In the January–June period HDD values will not be zero if *Tdaily* is less than 10°C, while in July–December if *Tdaily* is less than 12°C. These limits are defined based on the assumption that during the first half of the year, the heating of buildings due to solar radiation is greater, as there are usually fewer clouds than in the second half of the year. The method explained here is found to give a good interpretation of the heating energy demand and used routinely by energy producers in Scandinavian countries.

The HDD index is conventionally calculated on the based of daily values. As only monthly data were available from Global Spectral Model (GSM) runs, we first studied if it would be possible to calculate HDD using only monthly mean temperatures. HDD values, calculated with monthly and daily data, are strongly correlated — for example, the correlation coefficient at two Finnish stations, Helsinki and Sodankylä (*Fig. 1*) was 0.993 and 0.995, at the Romanian station, Târgu-Mures it was 0.989 (*Fig. 1*). Due to the strong correlation, it was justified to use monthly mean temperatures for the calculation of the HDD index,

$$HDD = -(Tmonthly - 17)\, n, \tag{2}$$

where n is the number of days per month. Seasonal and annual HDD index values were calculated using monthly HDD index values. During the winter season, when temperatures are below cut-off limits, 10 and 12°C, the difference between values calculated using daily and monthly data is negligible, but during other seasons, the HDD index values obtained from monthly data may be somewhat smaller than if daily data were used (see *Table 1*). An apparent reason is that the period between spring and autumn includes months, when temperatures are over the cut-off limits (10–12°C). However, as most of the heating energy demand appears during the winter season, when the temperature is clearly below the cut-off limits, the difference between values calculated from monthly and daily data is insignificant.

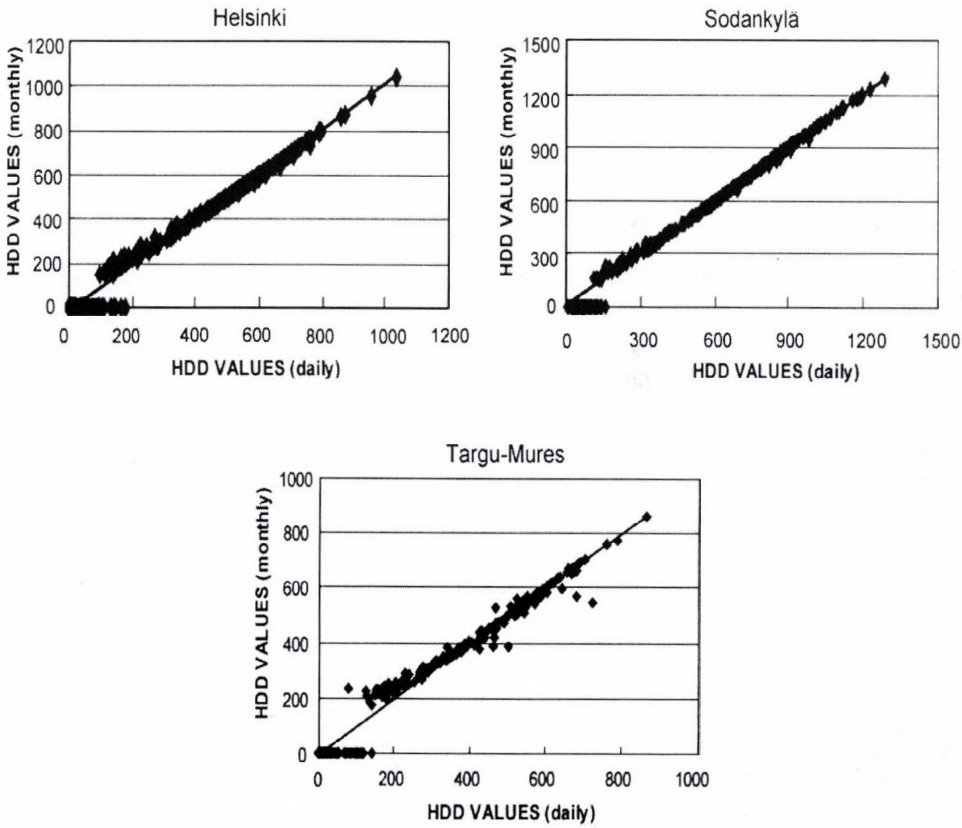

Fig. 1. Monthly HDD index calculated using daily (x-axis) and monthly (y-axis) mean temperatures in Helsinki, Sodankylä, and Târgu-Mures in 1970-1999.

Table 1. The mean seasonal and annual HDD index values calculated using all available (Fig. 3) monthly mean temperatures

Stations	Annual	Oct–Mar	Apr–Sep	Winter	Spring	Summer	Autumn
Jyväskylä	4727	3836	891	2213	1308	11	1195
Helsinki	4102	3347	755	1928	1211	0	962
Kuopio	4961	3994	967	2308	1390	11	1252
Vaasa	4623	3643	980	2069	1388	16	1150
Sodankylä	6256	4750	1506	2684	1753	213	1605
Békéscsaba	2498	2428	70	1563	430	0	505
Debrecen	2622	2534	88	1600	456	1	564
Túrkeve	2550	2481	69	1586	430	0	534
Cluj-Napoca	3028	2821	207	1756	606	0	666
Bistrita	3079	2855	224	1761	623	0	695
Dej	3021	2839	182	1762	593	0	666
Târgu-Mures	2931	2775	156	1740	546	2	642
Turda	3005	2811	194	1748	588	0	668

2.2 Estimation of heating degree-days applying general circulation models

Estimates of the magnitude of projected climate warming were obtained from two general circulation models: HadCM3 developed at the Hadley Centre (UK; see *Gordon et al.*, 2000; *Pope et al.*, 2000) and ECHAM4/OPYC3 developed at the Max-Planck-Institute for Meteorology and German Climate Computing Centre (DKRZ, Germany; see *Roeckner et al.*, 1999). In this present study we used an all-anthropogenic forcing integration (AA) by HadCM3 and a sulfate aerosol and greenhouse gas experiment (GSD) by ECHAM4/OPYC3. In addition to warming due to enhanced concentrations of greenhouse gases, both these simulations include an estimate of the cooling influence of anthropogenic sulphate aerosols due to backscattering of solar radiation in clear skies (direct effect). The HadCM3-AA simulation also estimates the impact of sulfate aerosols on cloud albedo (indirect effect), as well as radiative forcing due to anthropogenic changes in the tropospheric ozone. From 1860 to 1990, radiative forcing is calculated on the basis of observations. From 1990 onward, HadCM3-AA uses the IS95a emissions scenario, and ECHAM 4/OPYC3-GSD applies the IS92a emissions scenario.

A 90-year simulation starting from the year 1961 was used for both models. The 90-year period was divided into three 30-year periods. By comparing these 30-year periods, it was possible to obtain an estimate how the HDD index may change in the near future. The grid sizes of the global models

HadCM3 and ECHAM4/OPYC3 are 2.5×3.75° and 2.8×2.8° (latitude-longitude), respectively. These correspond roughly to 200–300 km at the latitudes studied (*Fig. 2*). For this study we selected 9 (4 from HadCM3 and 5 from ECHAM4) grid squares for Finland and 6 (3 from HadCM3 and 3 from ECHAM4) grid squares for Romania and Hungary, and examined how the HDD index would change in these grid squares.

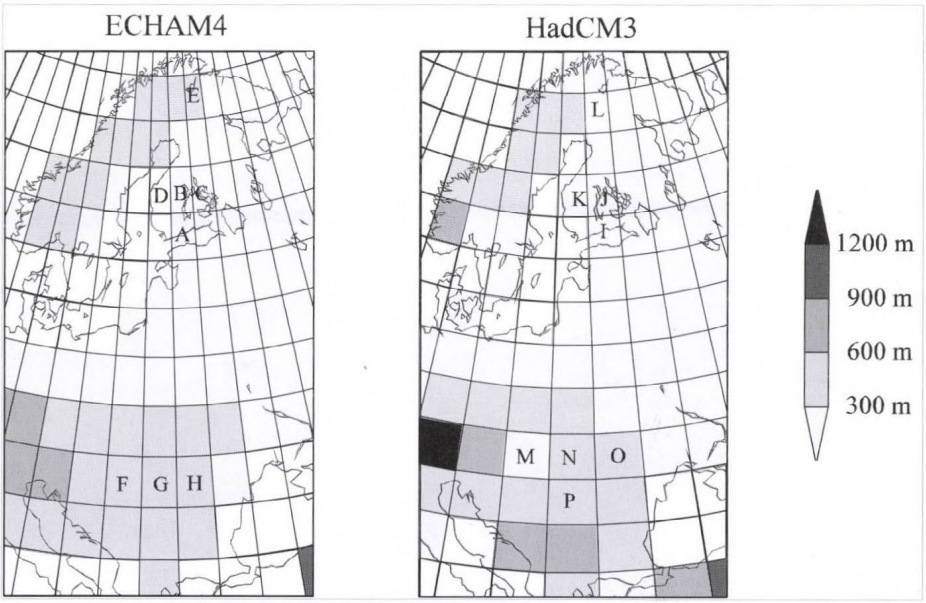

Fig. 2. The land-sea mask in the ECHAM4 and HadCM3 AOG models. The grid-squares used in the current study are named using letters A-H (ECHAM4) and I-P (HadCM3).

Grid values represent mean values over the whole grid box. To obtain an indication of how the HDD index varies naturally at certain locations, measured temperature values were studied first. Measured data covered the period 1901–1999 from 5 locations in Finland (Helsinki, Jyvaskylä, Vaasa, Kuopio, and Sodankylä), 3 locations in Hungary (Debrecen, Békéscsaba, Túrkeve), and 5 locations in Romania (Cluj-Napoca, Dej, Turda, Târgu-Mures, Bistrita) (*Fig. 3*). These weather stations belong to national meteorological networks and measurement data has been passed through quality control. The whole of Finland is represented by the stations used, while the data sources from the two other countries are located in western Romania (Transylvanian Basin) and eastern Hungary (Hungarian Plain on the left bank of Danube).

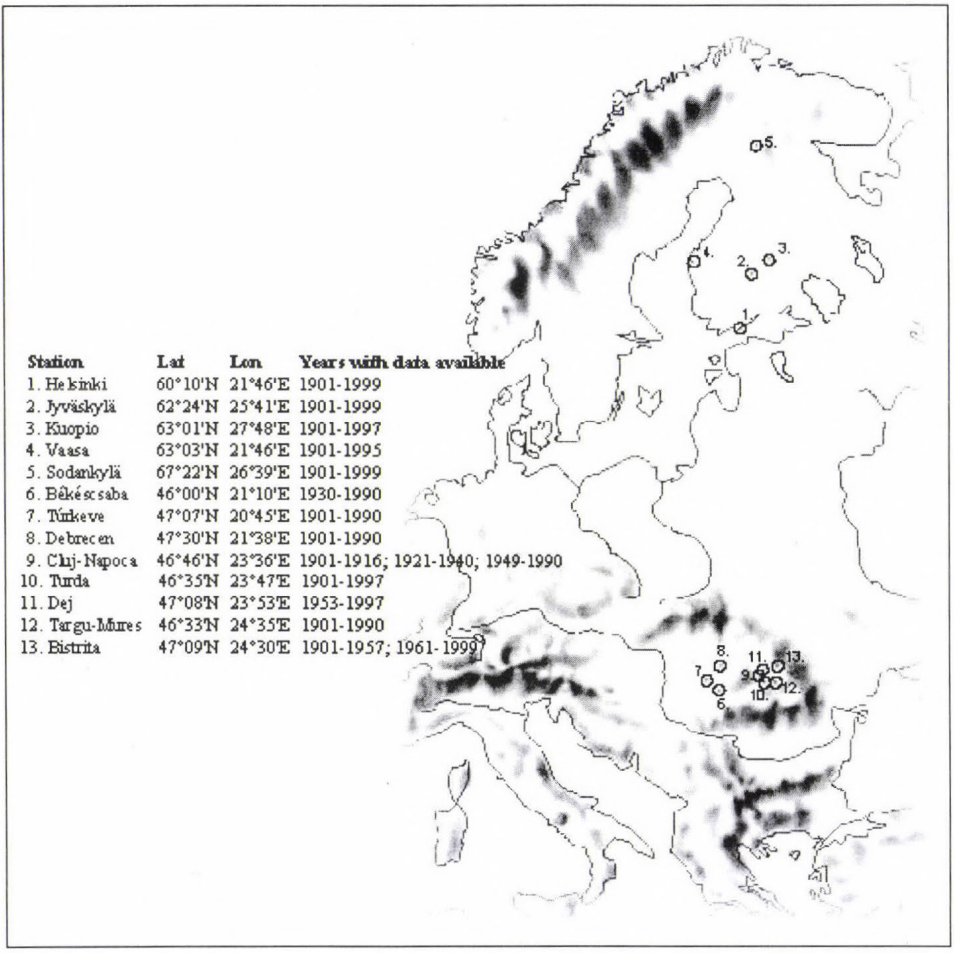

Fig. 3. Stations used in the study.

It is questionable how accurate an estimate of HDD can be, obtained using global model rather than more detailed data. If we were to examine how much the HDD index varies at certain locations, then use of global model grid square values is not a good alternative. However, in our study we are interested in how much the energy demand will change in a larger area, and in that sense the use of global model is justified, though the details of spatial variation are less well described by global models. A larger source of uncertainty than the grid size is related to the general accuracy of climate models as well as the uncertainty related to future emission scenarios.

In order to obtain an estimate of the uncertainty related to different scenarios and atmosphere-ocean general circulation model (AOGCMs) calculations, the mean wintertime (December–February) temperature changes, from 1961–1990 until 2021–2050, under the four preliminary SRES98 marker scenarios from the IPCC Special Report on Emissions Scenarios (*IPCC,* 2000; *Hulme* and *Carter*, 2000) and nine different AOGCMs model runs were determined. Based on these temperature values, the HDD index for Finland for the studied period 2021–2050 was calculated. The scenarios used give quantitative interpretations for four alternative storylines (A1, A2, B1, B2) representing possible futures with different driving force combinations. Further, a scaling method (*Hulme* and *Carter*, 2000) was used to estimate the range of regional climate projections arising from the uncertainties in emissions and climate system response. B1-low assumes low emissions and low climate sensitivity; A1-mid and B2-mid are based on central estimates; A2-high assumes high emissions and high climate sensitivity. The adopted AOGCMs were CGCM1 (*Flato et al.*, 2000), CSIRO-Mk2 (*Gordon* and *O'Farrell*, 1997), HadCM2 (four ensemble runs) (*Johns et al.*, 1997), HadCM3 (*Gordon et al.*, 2000; *Pope et al.*, 2000), NCAR DOE-PCM (*Washington et al.*, 2000), ECHAM4 (*Roeckner et al.*, 1999). The mean temperature of Finland (*TF*) was defined as the mean of temperatures in the grid squares (*Tsq)* covering the country.

$$TF = \frac{\sum_{i=1}^{nu} Tsq_i}{nu}, \tag{3}$$

where *nu* is the number of grid squares covering Finland. The mean HDD index for the Finnish locations in 2021–2050 ($HDD_{2021-2050}$) was calculated by rising the mean 1901–1999 temperature as indicated by different models and scenarios.

$$HDD_{2021-2050} = [17 - (TW_{1901-1999} + \Delta T)]\,90, \tag{4}$$

where $TW_{1901-1999}$ is the mean temperature for period 1901–1999, calculated as the mean of the five stations (Helsinki, Jyväskylä, Kuopio, Vaasa, and Sodankylä) used in this study, ΔT is the temperature rise predicted by the different scenarios and models, and 90 indicates the number of days during the three-month period (December–February). This estimate is cruder than that based on monthly data, but it still provides an estimate of the limits of uncertainty involved.

3. Results

3.1 The variation of monthly and seasonal heating degree-days index values

Let us first look at the HDD index values in present day climate. Due to the cooler climate, the HDD values calculated using the measurements of the past 100 years are higher in Finland. The annual value is 1000–2000°C higher than in the other study areas (*Table 1*, see also Fig. 6). The values at stations in Hungary and Romania are close to each other. In the Romanian locations they are about 10% higher, partly due to the geographic position and orography: the mean elevation is about 300–400 m higher in the Transylvanian Basin than in the Hungarian Plain.

When examining the season-based HDD values at the studied stations, it was found that in the winter half of the year (October–March) the highest value is 4750°C at Sodankylä, while the lowest in Finland, at Helsinki, is 3347°C. In Jyväskylä, Vaasa, and Kuopio, the values are within the 3640–3995°C range. In Hungary, the long term mean values for the winter half of the year are within the 2420–2540°C range, and in Romania the values are somewhat higher within the 2770–2850°C range (*Table 1*).

For the summer half of the year (April–September), the values are very low in Hungary (70–88°C), the dominant value is zero for the April–September period (some exceptions are recorded for April). In Romania, the HDD values follow the same pattern, but the zero-period is shorter (May–August). In Finland, extreme values are recorded again in Sodankylä (1506°C, the highest) and in Helsinki (755°C, the lowest) with values in the 890–980°C range at the other stations.

To depict how the HDD index values based on measurements are related to values obtained from climate scenarios, we divided the monthly HDD values obtained from the HadCM3 scenario (1961–2050 period) into three thirty-year periods (1961–1990, 1991–2020, and 2021–2050) and plotted them to the same figure with the values based on measurements. For the analyses we selected one station from each country: Jyväskylä from Finland, Debrecen from Hungary, and Cluj-Napoca from Romania (*Fig. 4*).

In the case of the Great Hungarian Plain and Transylvanian Basin, the HDD values based on the HadCM3 simulation for 1961–1990 period are relatively close to measurements. For Finland, the HadCM3 model predicts systematically lower temperatures than those indicated by the measurements. Due to the natural climate variation in the 1991–2020 or even 2021–2050 scenario periods, during a few months higher HDD index values are shown than in the 1961–1990 period, e.g., in January in Jyväskylä.

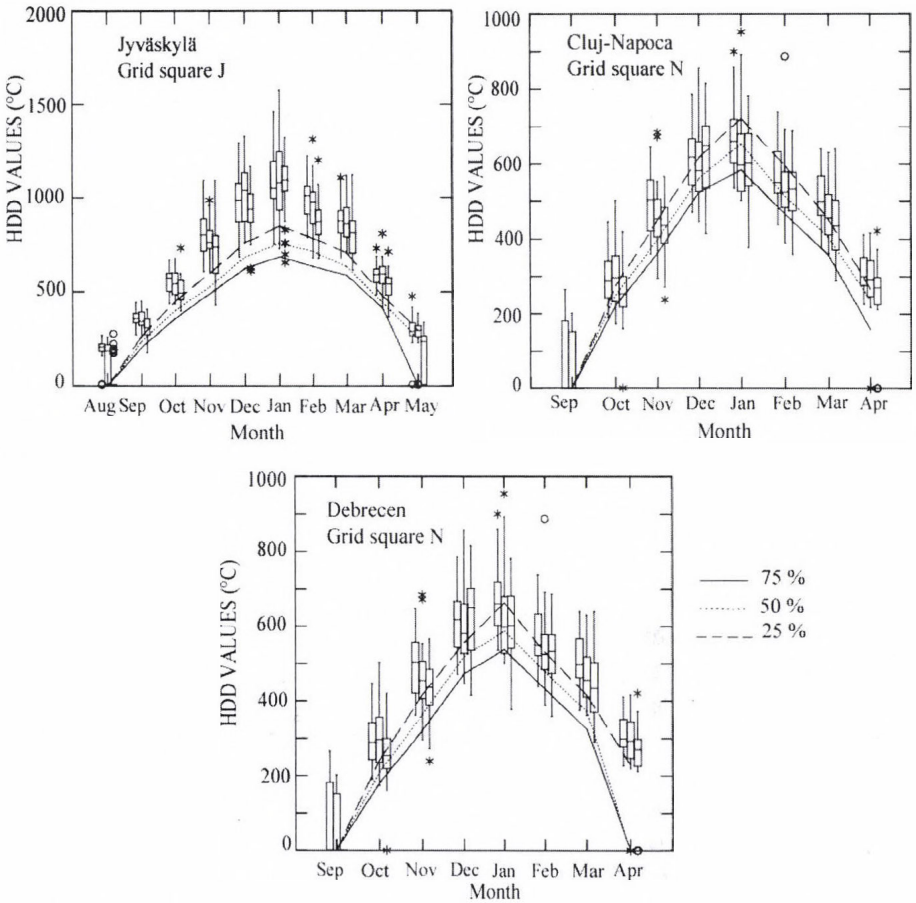

Fig. 4. Monthly HDD index values at Jyväskylä, Debrecen, and Cluj-Napoca. The line plots are 25%, 50%, and 75% percentiles based on 1901–1999 observations. The box-plots depict the variation based on the three thirty-year periods (1961–1990, 1991–2020, and 2021–2050) obtained from HadCM3 model for grid squares J and N. The horizontal line within the box corresponds to the median, the end of the box shows the interquartile range, the "whiskers" give extreme values within -1.5 and 1.5 times the interquartile range. Values outside these extreme ranges are indicated with an asterisk.

3.2 The variation in the annual heating degree-days index values

When we examine the 30-year periods of the annual HDD index (*Fig. 5*) we can see that in case of the ECHAM4 model the values are smaller than in the case of HadCM3. The latter model systematically indicates a colder climate. In Finland, the HDD indexes calculated on the base of the HadCM3 model are

approximately the same during the two periods 1961–1990 and 1991–2020, while the period 2021–2050 is clearly warmer than the two earlier periods. In the case of the ECHAM4 model, the warming of climate is slightly larger between the first and second thirty-year periods than during the second and third thirty-year periods. At all the Finnish locations, the studied HDD index values decrease on an average by 400–500°C when the 2021–2050 period is compared to the first thirty-year period 1961–1990.

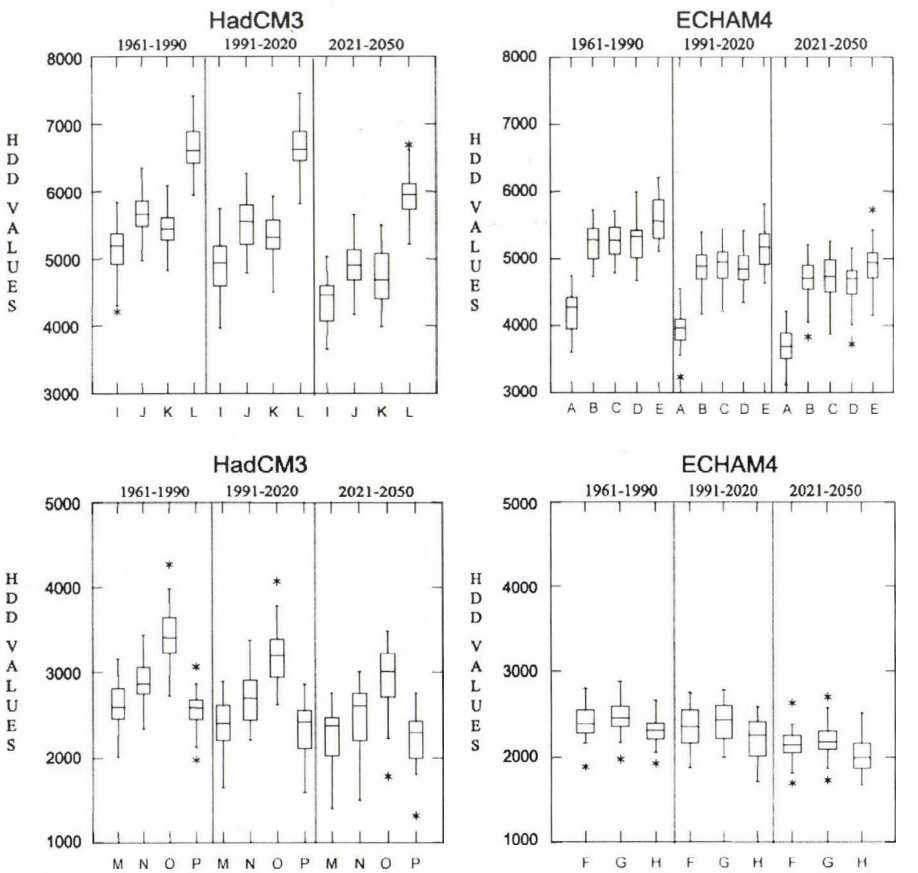

Fig. 5. The variation in annual HDD index values at grid square locations (Fig. 1) used in the study. The box-plots depict the variation based on the three thirty-year periods obtained from the HadCM3 and ECHAM4 models.

At the Romanian and Hungarian stations, the warming trend predicted by both of the models is linear. The decrease in the HDD index is about 300°C

when the 1961–1991 period is compared to the 2021–2050 period. The values in Romania are about 500–600°C higher than in Hungary, although, the stations are situated on the same latitude where the continental effect is detectable.

For the analyses of annual HDD index value changes, we have selected one reliable station from each country with long and complete data series: Jyväskylä from Finland, Túrkeve from Hungary, and Turda from Romania. Whilst examining the annual HDD index value changes during the past 100 years (*Fig. 6A*), there is a slight negative trend according to measurements (179°C in Jyväskylä). Correspondingly, the standard deviations according to measurements are 411°C (Jyväskylä), 271 (Túrkeve), and 264 (Turda).

When modeled data is examined, the negative trend in the corresponding grid squares according to ECHAM4 for the period 1950–2050 (*Fig. 6B*) is 1040, 494, 496°C in grid square B (Jyväskylä), grid square F (Túrkeve), and grid square G (Turda), respectively, and the corresponding standard deviations (trend removed from the data) are 293, 189, and 194. The natural variation of climate at the station is thus larger than the variation simulated by ECHAM4. When we examine the HadCM3 data (*Fig. 6C*), we find that in grid square J (Jyväskylä) there is no trend until 2000 and after that there is also a negative trend. The negative trend for the whole period is 1133, 593, 501°C in grid square J (Jyväskylä), grid square M (Túrkeve), and grid square P (Turda), respectively, and the corresponding standard deviations (trend removed from the data) are 390, 316, and 278. In Jyväskylä, the natural variation of climate is approximately the same in magnitude as the variation simulated by the HadCM3 model, while at other locations it is somewhat larger than the values indicated by the measurements.

3.3 The change in the heating energy demand

The change in the HDD index can be interpreted directly as a change in the heating energy demand per capita (e.g., *Quayle* and *Diaz*, 1980). According to ECHAM4, the heating energy need for the Finnish locations will decrease by 6–8% percent until the 1991–2020 period and by 10–13% until the 2021–2050 period. Using the HadCM3 values, the decrease until 2020 is only 1–4% and under 1% in northern Finland. For the latter period (after 2020), the decrease is about 10% in northern Finland and about 14% in the rest of the country (*Fig. 7*).

In the Romanian and Hungarian locations, the ECHAM4 scenario predicts a 2–4% decrease until 1991–2020 and 11–13% until 2021–2050. The HadCM3 model predicts 6–8% for the first period and 10–14% for the second period (*Fig. 7*).

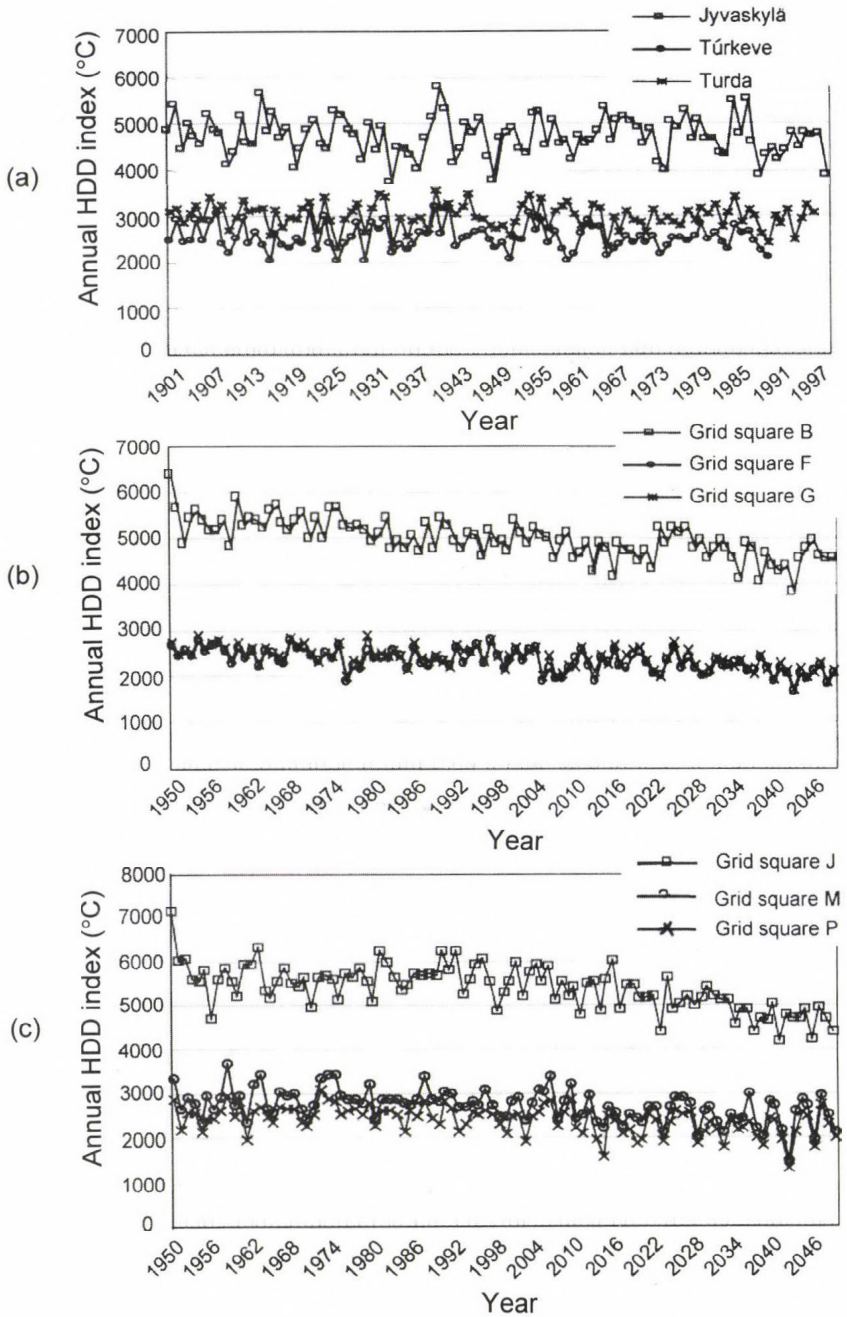

Fig. 6. Annual HDD index values calculated for three stations using: (*a*) measured monthly temperature values 1901–1999, (*b*) ECHAM4, and (*c*) HadCM3 simulations.

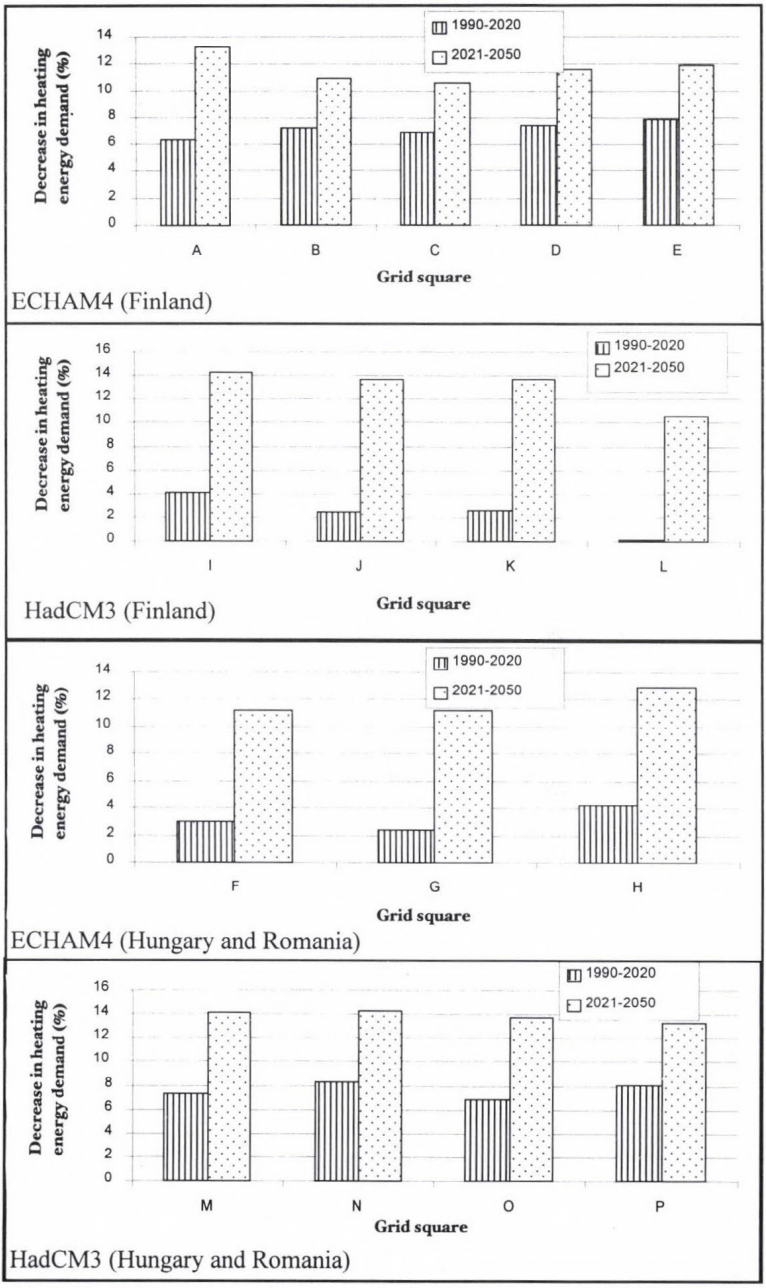

Fig. 7. The mean decrease in the heating energy demand (%) compared to the period 1961–1990, based on HadCM3 and ECHAM4 model simulations.

3.4 Estimated uncertainty

Based on the mean temperature change by 2021–2050 under the four SRES scenarios and nine different AOGCMs model runs, we determined the change in the wintertime (December–February) temperature and heating degree-days index for Finland for the studied period 2021–2050 (*Fig. 8*).

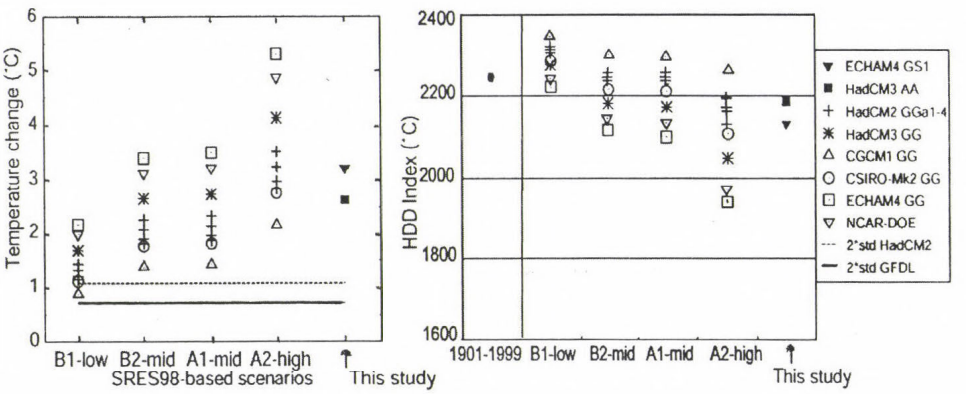

Fig. 8. The estimated climate warming from 1961–90 to 2021–2050 (*a*), and the HDD index (*b*) in Finland as obtained from nine different AOGC model simulations according to four SRES scenarios (*IPCC*, 2000; *Hulme* and *Carter*, 2000) for mid-winter months (December-February). The 2*std lines give the 2 times standard deviation values as obtained from the HadCM2 and GFDL multi-decadal simulations and depict natural climate variation. The HDD index was calculated by rising the mean 1901–1999 temperature as indicated by different simulations and scenarios (Eq. (4)). In (b) there are also HDD index values calculated on the base of the 1901–1999 mean winter temperatures included as well as the HadCM3 and ECHAM4 simulations used in the present study.

The model with the largest warming in this study was ECHAM4 and the coldest was GCCM1. The A1 and B2 scenarios showed roughly similar changes, while the decrease in the HDD index was between 100 and 300°C. The A2 scenario predicts the greatest warming with a decrease in the HDD index of between 200 and 450°C. The coldest climate would be obtained if B1-low conditions were to become true. In this case the decrease in HDD index is between 100 and 200°C.

The difference between the predicted greatest and smallest warming is still large, indicating the uncertainties related to local climate prediction and assessment studies. The HDD index change according to the results of this study corresponds to the A1-mid scenario changes, and the results are quite close to a type of predicted "average" of different models and scenarios.

4. Conclusions

The results of this study suggest that climate change will decrease the heating energy demand by 10–14% during the next 50 years. For the wintertime – when the heating energy demand is the highest – the scenarios predict a 10–12% decrease for Finland and 6–8% for the studied regions of Hungary and Romania. Though there are still uncertainties related to the magnitude of climate warming, the negative trend in heating energy demand seems so evident that it should be taken into account in the energy production scenarios.

An interesting subject to study in the future will be the probability of cold, relatively short 1-2-week periods, as the energy production capacity must be made to cover also these maximum consumption periods. Besides the heating energy demand, the climate change will inevitably also influence the cooling energy demand during summertime.

Acknowledgements—The authors wish to express sincere thanks to the reviewers of this article for their valuable comments.

References

Ambrózy, P. and *Faragó, T.*, 1988: Recent severe winters in Hungary: meteorological approach and some energy supply/demand aspects. In *Identifying and Coping with Extreme Meteorological Events* (eds: *E. Antal* and *M.H. Glantz*). Hungarian Meteorological Service, Budapest, 281-335.

Carter, T., Posch, M., and *Tuomenvirta, H.*, 1995: *SILMUSCEN and CLIGEN, Users guide*. The Finnish Research Programme on Climate Change SILMU. Publications of the Academy of Finland 5/1995.

Cvitan, L. and *Poje, D.*, 1985: Winter coldness on Croatia with regard to the number of heating days and the degree-days. *Hidrometeoroloski Zavod 20*, Rasprave, Zagreb, Yugoslavia, 65-71.

Darmstadter, J., 1993: Climate change impacts on the energy sector and possible adjustments in the MINK region. *Climatic Change 24(1-2)*, 117-129.

Downton, M.W., Stewart, T.R., and *Miller, K.A.*, 1988: Estimating historical heating and cooling needs: per capita degree-days. *J. Applied Meteorology 27(1)*, 84-90.

Faragó, T., Iványi, Zs., and *Szalai, S.* (eds.) 1991: *Climate Variability and Change, II*. Changes in composition of atmosphere and in the climatic characteristics, detection, modelling, scenarios and impacts of the regional changes (in Hungarian). Hungarian Ministry for Environment and Regional Policy — Hungarian Meteorological Service, Budapest.

Flato, G.M., Boer, G.J., Lee, W.G., Mcfarlane, N.A., Ramsden, D., Reader, M.C., and *Weaver, A.J.*, 2000: The Canadian Centre for Climate Modelling and Analysis global coupled model and its climate. *Climate Dynamics 16*, 451-467.

Gilbert, R.O., 1989: *Statistical Methods for Environmental Pollution Monitoring*. Van Nostrand Reinhold Company, New York.

Gordon, C., Cooper, C., Senior, C.A., Banks, H., Gregory, J.M., Johns, T.C., Mitchell, J.F.B., and *Wood, R.A.*, 2000: The simulation of SST, sea ice extents and ocean heat transports in a version of the Hadley Centre coupled model without flux adjustments. *Climate Dynamics 16*, 147-168.

Gordon, H.B. and *O'Farrell, S.P.*, 1997: Transient climate change in the CSIRO coupled model with dynamic sea ice. *Monthly Weather Review 125*, 875-907.

Hargy, V.T., 1997: Objectively mapping accumulated temperature for Ireland. *Int. J. Climatology 17*, 909-927.

Heerdegen, R.G., 1988: Evaluation of the heating degree-days index. *Weather and Climate 8(2)*, 69-75.

Hulme, M. and Carter, T.R., 2000: The Changing Climate of Europe. In *Assessment of Potential Effects and Adaptations for Climate Change in Europe* (ed.: *M. Parry*). Jackson Environment Institute, University of East Anglia, Norwich, UK, 47-84.

IPCC, 2000: *Special Report on Emissions Scenarios. Nakicenovic, N., Alcamo, J., Davis, G., De Vries, B., Fenhann, J., Gaffin, S., Gregory, K., Grübler, A., Jung, T.Y., Kram, T., LaRovere, E.L., Michaelis, L.*. http://www.grida.no/climate/ipcc/emission/index.htm.

IPCC, 2001a: *Climate Change-2001: The Scientific Bases*. Contribution of Working Group I. *Albritton, D.L., Allen, M.R., Baede, A.P.M., Church, J.A., Cubash, U., Xiaosu, D., Yihui, D., Ehhalt, D.H., Folland, C.K., Giorgi, F., Gregory, J.M., Griggs, D.J., Haywood, J.M.* http://ipcc-ddc.cru.uea.ac.uk/index.html

IPCC, 2001b: *Climate Change 2001: Impacts, Adaptation and Vulnerability*. Contribution of Working Group II. Eds.: *McCarthy, J.J., Canziani, O.F., Leary, N.A., Dokken D.J., White K.S.*. Cambridge University Press, London.

Johns, T.C., Carnell, R.E., Crossley, J.F., Gregory, J.M., Mitchell, J.F.B., Senior, C.A., Tett, S.F.B., and *Wood, R.A.*, 1997: The second Hadley Centre coupled ocean-atmosphere GCM: model description, spinup and validation. *Climate Dynamics 13*, 103-134.

Jonsson, T., Johannesson, T., and *Källen, E.*, 1994: *Climate Changes Scenario for the Nordic Countries. A Preliminary Report.* Vedurstofa Islands, Orkustofnun, Icelandic Meteorological Office, National Energy Authority, OS-94030/VOD-04B.

Kadioglu, M., Sen, Z., and *Gultekin, L.*, 1999: Spatial heating monthly degree-day features and climatologic patterns in Turkey. *Theoretical and Applied Climatology 64(3-4)*, 263-269.

Kellomäki, S., 1993: Computations on the influence of changing climate on the soil moisture and productivity in Scotsh pine stands in southern and northern Finland. *Climatic Change 29*, 35-51.

Kharin, V.V. and *Zwiers, F.W.*, 2000: Changes in the extremes in an ensemble of transient climate simulations with a coupled atmosphere-ocean GCM. *J. Climate 13*, 3760-3788.

Kuivalainen, P., Forsius, J., and *Mäkinen, P.*, 1996: *Effects of Climate Change on the Production and Consumption of Electricity in Finland.* Imatra Voima OY, Environmental Protection Division, Vantaa, Finland.

Pope, V.D., Gallani, M.L., Rowntree, P.R., and *Stratton, R.A.*, 2000: The impact of new physical parameterisations in the Hadley Centre Climate model-HadCM3. *Climate Dynamics 16*, 123-146.

Quayle, R.G. and *Diaz, H.F.*, 1980: Heating degree-day data applied to residential heating energy consumption. *J. Applied Meteorology 19(3)* 241-246.

Roeckner, E., Bengtsson, L., Feichter, J., Lelieveld, J., and *Rodhe, H.*, 1999: Transient climate change simulations with a coupled atmosphere-ocean GCM including the tropospheric sulfur cycle. *J. Climate 12*, 3004-3032.

Sælthun, N.R., Aittoniemi, P., Bergström, S., Einarsson, K., Johannesson, T., Lindström, G., Ohsson, P.E., Thomsen, T., Vehviläinen, B., and *Aamodt, K.O.*, 1998: *Climate Change Impacts on Runoff and Hydropower in the Nordic Countries. Final report from the project "Climate Change and Energy Production"*, Copenhagen.

Soule, P.F. and *Suckling, P.W.*, 1995: Variations in heating and cooling degree-days in the South-eastern USA, 1960-1989. *Int. J. Climatology 15*, 355-367.

Starostova, M., 1999: Air temperature and heating period characteristics in south Bohemia (in Czech). *Hydrometeorologicky Ustav*, Prague, Czech Republic, 57-66.

Taylor, B.L., 1981: Population-weighted heating degree-days for Canada. *Atmosphere-Ocean 19*, 261-268.

Tistea, D., 1974: Computation and zoning of annual heating period duration and heating degree-days sum corresponding to inside and outside temperatures (in Romanian). *Studii de Climatologie 2*, 131-155.

Washington, W.M., Weatherly, J.W., Meehl, G.A., Semtner, A.J. Jr, Bettge, T.W., Craig, A.P., Strand, W.G. Jr, Arblaster, J., Wayland, V.B., James, R., and *Zhang, Y.*, 2000: Parallel climate model (PCM) control and transient simulations. *Climate Dynamics 16*, 755-774.

IDŐJÁRÁS

Quarterly Journal of the Hungarian Meteorological Service
Vol. 108, No. 2, April–June 2004, pp. 141–153

Tendencies in variability of gridded temperature and precipitation in Hungary (during the period of instrumental record)

Louise Bodri

Research Group on Geophysics and Environmental Physics, Hungarian Academy of Sciences, c/o Geophysics Department of Eötvös Loránd University, Pázmány P. sétány 1/C, H-1117-Budapest, Hungary; E-mail: bodri@pangea.elte.hu

(Manuscript received August 15, 2002; in final form March 7, 2003)

Abstract—Analysis of monthly variability was performed on two 100–150 years long grid-point series of temperature anomalies and precipitation from Central Europe, near Hungary. Increasing temperature during the 19th and 20th centuries has been accompanied by a decrease in monthly variability. Thus, at present the temperature evolves towards to more stable climate, especially in spring and summer. Lower variability is linked to more rapid winter warming. Slow decrease of precipitation together with the noticeable increase in precipitation variability is characteristic for the 20th century. The increase in precipitation variability is more rapid in summer. Observed climatic variability near Hungary is generally consistent with the patterns found for other European mid-latitude locations as well as with those predicted by Global Circulation Models (GCMs).

Key-words: temperature, precipitation, variability trends.

1. Introduction

Climate is variable on all time scales. For better understanding of the nature of the climate changes, attention is to be focused not only to the evolution of mean climate characteristics, but also to the changes in the climate variability, and to climate extremes. The necessity of including of the variability characteristics in the climate change studies has been demonstrated in several works (*Katz* and *Brown*, 1992; *Rebetez*, 1996; *Wilks* and *Riha*, 1996; and the references therein). A detailed understanding of climate variability is important to the prediction of extreme climatic events. It can be demonstrated that the frequency of climatic

extremes is more sensitive to the changes in variability rather than to the mean climate state (*Katz* and *Brown*, 1992). *Rebetez* (1996) has shown that climate variability is one of the most important characteristics in the human perception of climate. The potential response of the socio-economic fabrics of the global community to the changes in climate variability may be stronger than to the changes in climatic averages (*Rebetez*, 1996; *Wilks* and *Riha*, 1996), while these changes are completely obscured when examining only the evolution of mean characteristics.

One of the important fields of application of the variability investigations is the detection of possible forced (e.g., anthropogenic) climate trends. For example, in the face of the climatic change from the increased greenhouse gas concentrations in the Earth atmosphere, there is strong evidence that changes will occur not only in climatic mean state but also in their higher order moments. General Circulation Models (GCMs) associated with the build-up of greenhouse gases predict not only increase in temperatures but also a possible decrease in temperature variability (*McGuffie et al.*, 1999; *Karl et al.*, 1999). While a global trend of 0.3–0.6°C during the last century has been widely recognized (*Nicholls et al.*, 1996; *Hansen et al.*, 2001), changes in the climate variability have been less well studied or understood. Recent investigations of the surface air temperature (SAT) variability in fact revealed definite decreasing variability trends in SAT records (*Karl et al.*, 1995; *Moberg et al.*, 2000; *Rebetez*, 2001; *Yan et al.*, 2001, *Bodri* and *Cermak*, 2003). These studies admitted also, that the climate changes differently from one region to another; thus, changes in the SAT variability can be confidently diagnosed only on the base of wide regional studies. Such investigations can be used for the validation of the simulated models for various scenarios of greenhouse-gas emission and land use.

The situation is more complex with other associated climatic variables, such as precipitation, that also can be affected by the global warming phenomenon. Most of the existing models, like, e.g., recent investigations by *Hulme et al.* (1998), are oriented towards the influence of the global warming on the precipitation means. Precipitation sensitivity to the global warming for the land areas simulated in the above work by a set of eight HadCM2 models with different forcings achieved 1.5 to 2.5%/K over the period 1900–1996. These values imply 3–15 mm precipitation growth for the last century, and coincide well with the global land precipitation growth of 9 mm/100 years, calculated by *New et al.* (2001), from precipitation gauge data. This growth is relatively small in comparison with considerable precipitation variability. According to *New et al.* (2001) on the decadal time scale range of the global land precipitation oscillations achieves ± 40 mm from the century mean of 950 mm.

The pioneering investigations concerning precipitation variability were performed by *Houghton et al.* (1992), who summarized model results for

conditions under doubled carbon dioxide concentration, and conclude that there is some indication of increase of the precipitation rate in selected regions, which could be accompanied by the simultaneous increase in the variability of the precipitation. The simulations of 21st century climate by *Kattenberg et al.* (1996) using GCMs forced with increasing atmospheric concentrations of greenhouse gases also indicated an increase in the intensity of the hydrological cycle as global temperature increases, implying increase in total precipitation, in the number of wet days and days with extreme precipitation, as well as revealed an area dependence of the changes. These conclusions were further specified in the study by *Mearns et al.* (1995). Investigations of $2 \times CO_2$ influence conducted with a regional climate model (RegCM) nested in a GCM indicated the possibility of significant regional increase in precipitation variability (with or without changes in median intensity). In vast regions there may be larger and more significant changes in variability rather than in medians. The possibility of detectable alterations in precipitation variability with no and/or imperceptible changes in its mean characteristics hints the necessity to include the higher order moments in precipitation change assessments.

In present work we analyze 100–150 years long surface air temperature (SAT) and precipitation time series from the territory of Hungary in order to better understand the pattern of their variability variations. This work can contribute to a few previous investigations of climatic variability and somewhat complete still insufficient information on the regional variability changes.

2. Data

To investigate the patterns of variability, we used the gridded time series of SAT anomalies and precipitation for the territory of Hungary. Gridded data accumulate the effects of individual stations. These time series appear more smoothed, thus, the range of variability variations may be more narrow, than in the measured data, and the "explosions" of variability resulting from the local extreme events may be missed. On the other hand, general trends revealed by these data are of the area importance, and can serve for verification of variability trends obtained from original station data. Traditionally, long-term climatic data in Europe have consisted of monthly mean values. Such scale of aggregation is more suitable for the regional investigation. As it was mentioned by *Yan et al.* (2001), at the shorter time scale, e.g., daily, variability is quite local in character. This makes it relatively sensitive to any changes in local conditions, thus, it may serve as a good indicator of inhomogeneity in climatic series, rather than the real variability changes.

Data sets of SAT anomalies and precipitation were provided by the Climate Research Unit, University of East Anglia, Norwich UK (www.cru.uea.ac.uk).

The SAT data is a combination of land air temperature anomalies (*Jones*, 1994) and sea surface temperature anomalies (*Parker et al.*, 1995) on a 5° × 5° grid-box basis. This size is as best as possible merging the effect of the temperature gradients and data availability. The merging of the two datasets is discussed in *Parker et al.* (1994). Both components of the dataset are expressed as anomalies from 1961–90. The monthly data from the grid-box 45–50°N, 15–20°E embracing the period of 1856–1998 were used for the calculations. All stations were actively assessed for the homogeneity. Some of these corrections are site specific relating to moves of the instruments and exposure changes (one of the important errors is connected to urbanization effect around the sites), and some are nationally specific arising from observation time and methods used to calculate monthly means. The elaboration of the homogenized long-term climate data for Hungary was performed by *Szentimrey* (1997, 1999; see also http://omsz.met.hu/ismeretterjesztes/rendezvenyek/rendezveny_hu.html).

The most informative homogenized precipitation series for the 20th century are presented by *Hulme et al.* (1998) (see also updated version on www.cru.uea.ac.uk) as land precipitation amounts from 1900 to 1998, gridded at 2.5° latitude by 3.75° longitude resolution. Because of stronger spatial variability of the precipitation, a smaller box size would be preferable. The present size is stipulated by the data availability. The grid box with the center at 47.5°N, 18.75°E was used for calculations. The station data were corrected to exclude gauge biases due to changing place and gauge design. Data have been also subjected to additional homogeneity procedure reported by *Hulme* (1992). For example, they were screened for gross outliers and typographical errors. Both time series are presented in *Figs. 1* and *2* (top), respectively.

Temperature anomalies record contains definite linear warming trend of 0.65 ± 0.11 K/100 yr (*Fig. 1*). The amount of the 20th century warming is comparable with the values of 0.3–0.6 K/100 yr obtained for the global warming trend (*Nicholls et al.*, 1996; *Hansen et al.*, 2001). In order to perform seasonal analyses, original monthly temperature anomalies were stratified into four commonly defined seasons. Linear trends for the seasonalized data are shown in *Table 1*. Obtained slopes indicate far the largest warming in the winter season. Warming trends in spring and autumn are approx. two times lower than in winter, while the summer warming is very light. Such distribution indicates that the warming process happens through the loss of the coldest part of the year. The monthly precipitation contains a general decreasing linear trend of -5.9 ± 2.7 mm/100 yr (possibility of slightly drier conditions in future) existing at least from the beginning of the 20th century (*Fig. 2*). Decreasing trend is observable for all seasons, though, very slightly in summer. However, neither of these trends is statistically significant (*Table 1*).

3. Temperature and precipitation variability

The measure of variability used in the present study is based on the work by *Karl et al.* (1995) and is defined by the absolute value of the difference in precipitation between two adjacent periods of time. For the time series of T_1, T_2, T_3, ..., T_i, ... the measure of variability ΔT_N (N-point change) is defined as the absolute difference between the average of a sequence of measured values for N points that begins at point i and the average for the N-point long sequence beginning at point $(i+N-k)$

$$\Delta T_N = abs\left(\overline{T_i} - \overline{T_{i-k}}\right), \tag{1}$$

where

$$\overline{T_i} = \frac{1}{N}\sum_{m=i}^{i+N-1} T_m\,; \quad \overline{T_{i-k}} = \frac{1}{N}\sum_{m=i+N-k}^{i+2N-k-1} T_m\,. \tag{2}$$

For the time lag $k > 0$ there are partly overlapping running differences. The method above is free of some disadvantages of more conventional methods, such as the standard deviation, thus, e.g., prevents a confounding of high- and low-frequency variability (*Karl et al.,* 1995). Similarly to other measures of variability, N-point change characterizes the range of climatic variations. Low variability value means approx. the same conditions in the next time interval as in the previous one, while high variability corresponds to significant differences between the neighboring intervals. For example, high value of monthly precipitation variability means that, e.g., a dry month was immediately followed by an extremely wet month.

The measure of variability was calculated successively for the whole time series to obtain variability measure. The value of N was chosen as one, corresponding to the monthly averaging intervals. *Figs. 1* and *2* (bottom) show the monthly variability curves for the SAT anomalies and precipitation, respectively. As it can be seen, climate warming during the 20th century has been accompanied by the reduction in monthly variability, predicted by the most of GCMs. Time series of SAT variability exhibits general decreasing trend of -0.20 ± 0.06 K/100 yr that implies approx. 15% present decrease in SAT variability in comparison with the beginning of the 20th century. Observed decrease in temperature variability can be explained by the more rapid winter warming in comparison with the summer period. While the summer period shows practically no long-term warming trend, the winter warming is approx. two times higher than the estimated global value. A larger increase in the winter temperatures than in the summer temperatures results in a substantial decline in

the annual temperature range (difference between summer and winter temperatures), thus, in the corresponding decrease in variability. An analysis of variability trends for different seasons shows, that the SAT variability decreases during the warmest part of the year from spring to autumn and is insignificant in the winter season (*Table 1*).

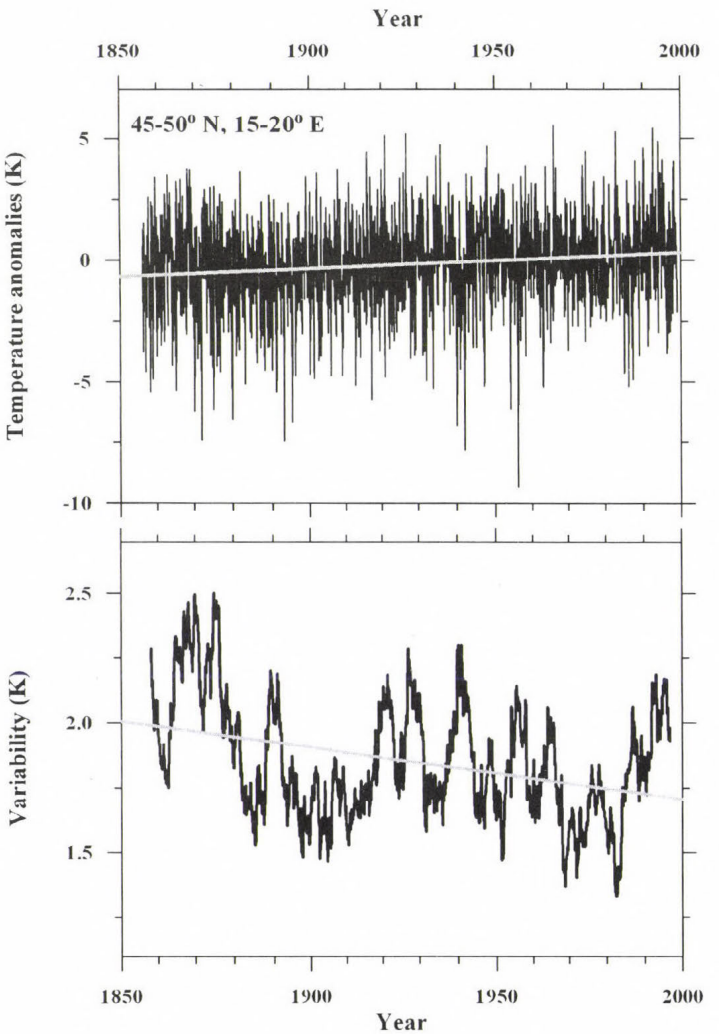

Fig. 1. Top: Time series of monthly SAT anomalies for the historical data set grid box centered at 47.5°N, 17.5°E (*Jones*, 1994). *Bottom:* Variability pattern for monthly SAT series. Low frequency changes are highlighted by a Gaussian filter corresponding roughly to 4-year moving averages. Thick lines represent the linear trends.

Time series of precipitation variability (*Fig. 2*, bottom) exhibits general increasing trend of 5.1 ± 0.9 mm/100 yr. The variability of precipitation increases for all seasons, but most rapidly in the summer period (*Table 1*). This hints at more variable summer precipitation in the future, and because of existing strong coupling of extreme and monthly precipitation, when the wettest day of the month

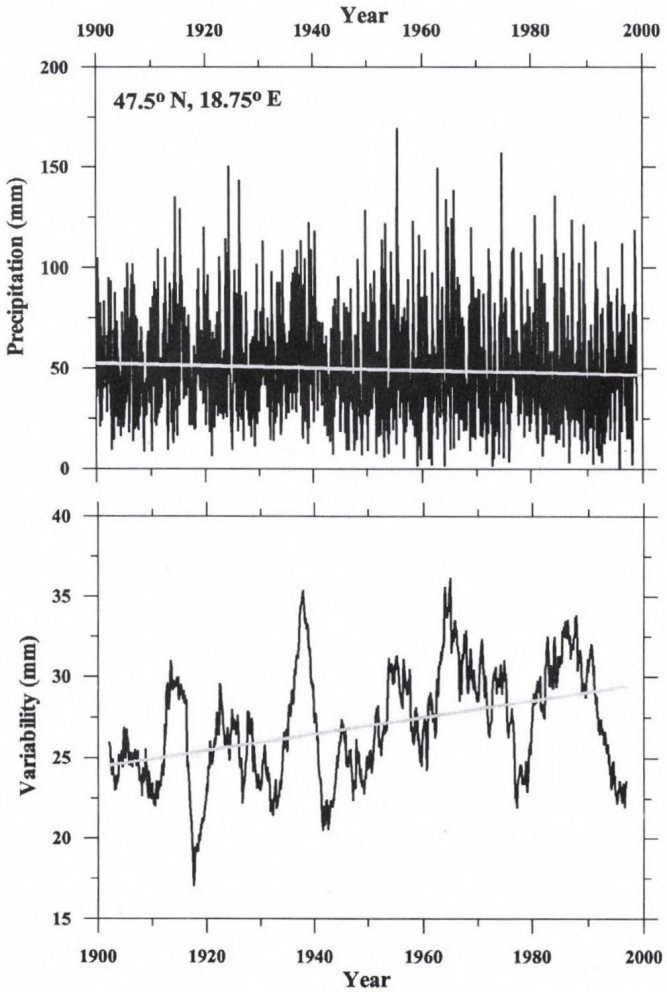

Fig. 2. Top: Time series of monthly precipitation for the historical monthly precipitation data set grid box centered at 47.5°N, 18.75°E (*Hulme et al.*, 1998). *Bottom:* Variability pattern for monthly precipitation. A Gaussian filter corresponding roughly to 4-year moving averages highlights low frequency changes.

contributes considerably to the total sum (see e.g., *Heino et al.*, 1999), at increasing probability of precipitation extremes in the summer period. Similar intensification of the hydrological cycle was obtained in several early works. *Karl et al.* (1995) analyzed daily precipitation data from the U.S. for the period 1910–1996, and found approx. 10% increase in annual precipitation, that occurred in most cases, because of a greater number of rainy days, with the greatest contribution arising from an increase in the number of extreme precipitation events, indicating an increased precipitation variability. The most recent investigations of precipitation trends in the 20th century by *New et al.* (2001) based on the gridded data sets revealed secular increasing trends in different domains, e.g., 8.9 and 41.6 mm/100 yr for global data set and in the mid-latitudes (40–60°N) of the Northern Hemisphere, respectively, in many regions accompanied by the increase of the wet spells frequency. They concluded that over much of the global land area (including also Europe) there was an increase in the intensity of precipitation events on the scales from 1 day to 3 months.

Table 1. Linear trends in monthly SAT anomalies (1856–1998) and precipitation (1900–1998) and their variability. (Trends are given in K/yr for SAT anomalies and/or for their variability and in mm/yr for precipitation and its variability, respectively.)

Period	Winter	Spring	Summer	Autumn	Year
SAT	0.013±0.003	0.006±0.002	0.002±0.002	0.005±0.002	0.006±0.001
SAT variability	0.0001± 0.0012	-0.0034± 0.0015	-0.0030± 0.0012	-0.0020± 0.0017	-0.0020± 0.0006
Precipitation	-0.038±0.041	-0.098±0.049	-0.018±0.054	-0.083±0.061	-0.059±0.027
Precipitation variability	0.020±0.012	0.028±0.013	0.107±0.022	0.019±0.019	0.051±0.009

Variability calculations above were completed by spectral analysis. Traditional Fourier analysis picks up signals changing in both frequency and time, features that are more closely related to real patterns of climate change. While the monthly precipitation itself does not possess any significant periodicity except for the ordinary 1 and 1/2 year waves (see results of the spectral analysis of precipitation time series; *Fig. 3*, top), the variability pattern exhibits definite quasi-cyclicity. Part of these oscillations can be attributed to the large scale forcing mechanisms, such as the NAO and AO (*Bodri et al.*, 2004). "Explosions" of variability generally coincide with the enhanced monthly precipitation; thus, imply an increased risk of extreme precipitation. However, in the present case an observed quasi-cyclicity does not contain any predictive possibility. As it can be seen in *Fig. 3* (bottom), the power spectrum of precipitation variability obeys a

power law form over a given frequency range of $E(f) \sim f^{-b}$, where f is the frequency, characteristic for the scale invariant (fractal) behavior. Spectral exponent b equals to -1.97 ± 0.08, thus, practically coincides with 2. Series with $b = 2$ represent ordinary Brownian noise, which is known as a purely random process. Thus, the observed cycles are quite far from periodic; for example, they cannot be extrapolated as the sample lengthens, cannot be related to the temporal periodicity of the precipitation forming process, etc.

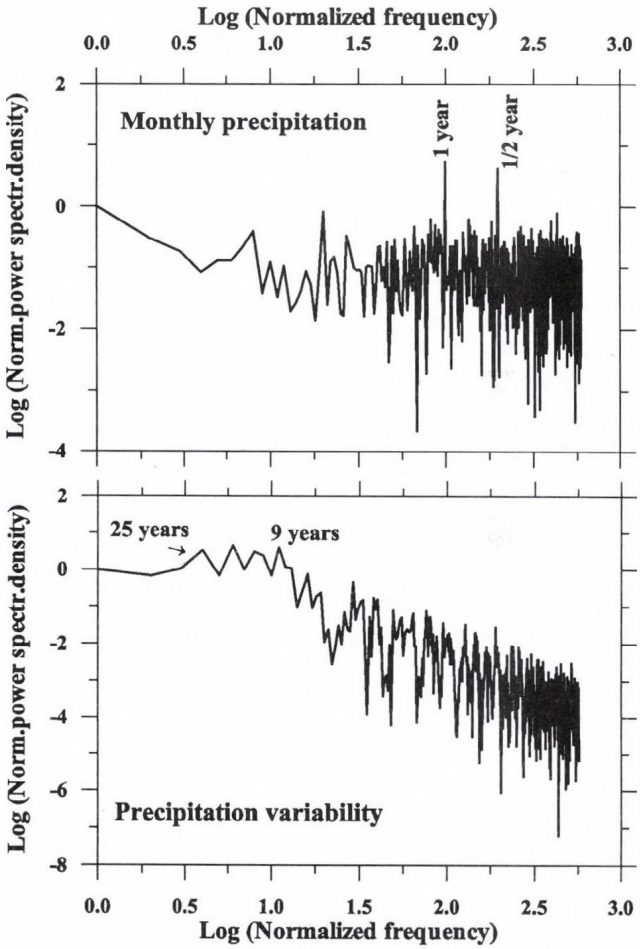

Fig. 3. Top: Power spectrum of the precipitation time series. The values are relative: the frequencies are normalized to the lowest frequency in the spectrum, the power spectral density to that at the lowest frequency. *Bottom:* Power spectrum of the precipitation variability time series.

4. Conclusions

As it was shown in several works, the quantities that are to be used to describe climate change scenarios are not only the mean characteristics of the climate but also higher order statistical moments, such as variability. The study of climate variability gives a more comprehensive summary of climate than conventional climate averages. Results of variability-related studies have many practical applications, since the impact of the variability changes on the environmental and associated socio-economic systems may be more perceptible than the slow changes in the mean characteristics. The investigations of variability, likewise the investigation of general trends, can be further used for the validation of the simulated models for various scenarios of greenhouse-gas emission and land use. The GCMs, that have been applied to the problem of the effect of increasing CO_2 levels combined with aerosol increases, predict not only global increase of surface air temperature, but also changes in the precipitation rate, however, they do not give an unequivocal picture of how the higher moments might be expected to change. Variability changes, especially, the changes in the hydrological cycle, are likely depending on the investigated spatial domain. In present work, two climatic data sets were collected for Hungary in order to characterize the variability of temperature and precipitation over the period of historical records. Analyses presented in this work lead to the following conclusions.

- Since the middle of the 19th century, monthly SAT temperatures in Hungary have warmed by 0.9°C (in comparison with the 0.3–0.6°C global value; *Nicholls et al.*, 1996; *Hansen et al.*, 2001). Simultaneously, the temperature variability decreased by approx. 15%. The decrease in temperature variability occurred due to the fact, that on a seasonal basis, the bulk of the warming in Hungary has taken place in the colder periods of the year (fall-spring); only very light warming was observed in summer.

- On monthly scale, precipitation slightly decreased over the 20th century. For the same period there was approx. 20% increase in precipitation variability, which occurred because of the less rapid decrease in the summer precipitation amounts, than in the winter amounts. On seasonal scale, variability increase is far more pronounced in summer. If this tendency will further continue, the summer may become far more variable season than the rest of the year, including the possibility of heavy precipitation extremes and increased risk of summer floods. It should be mentioned, however, that the situation in Hungary is far less marginal, than in some other regions of Europe. *Fig. 4* shows time series of monthly precipitation together with the calculated variability pattern for the grid box with the center at 50°N and 15°E, which coincides approximately with the position of Prague (the Czech

Republic). Variability shows general increasing trend of 6.0±0.3 mm/100 yr since at least the beginning of the 20th century. Except for this general increasing trend, the range of variability variations also increased significantly, that can be attributed to the more rapid growth of the variability maxima than the minimum values (14.8 and 4.2 mm/100 yr, respectively). Rapid growth of variability maxima implies the corresponding

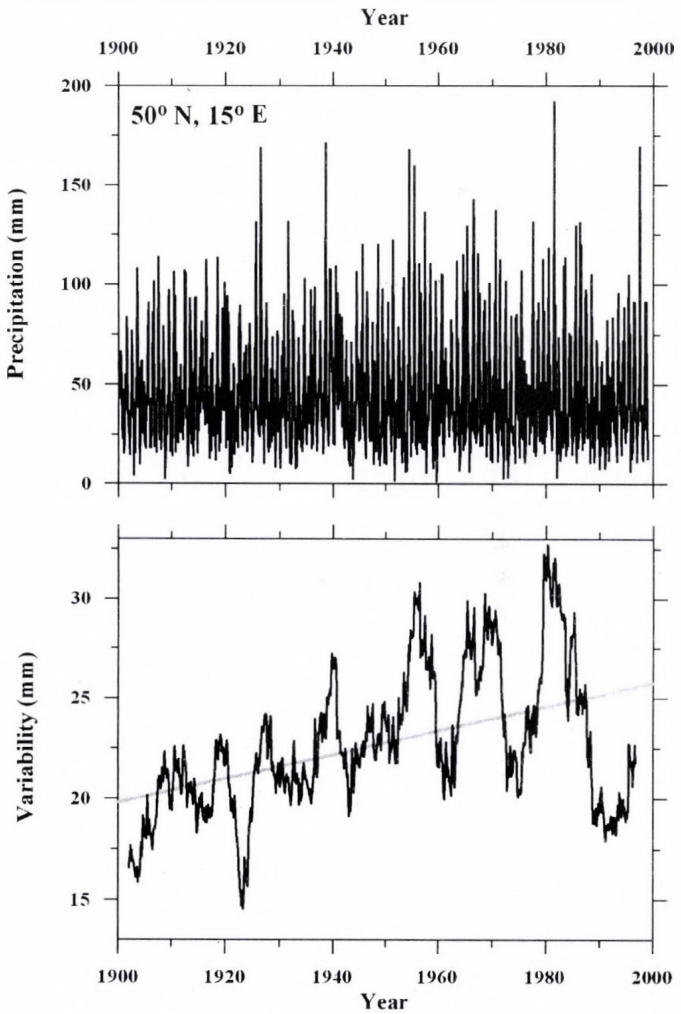

Fig. 4. Top: Time series of monthly precipitation for the historical monthly precipitation data set grid box centered at 50°N, 15°E (*Hulme et al.*, 1998). *Bottom:* Variability pattern for monthly precipitation.

increase of occurrence and intensity of extreme precipitation events. The oscillations of variability have become more pronounced after the year 1950. At least for the last 50 years, interdependence between extreme precipitations, increased range of precipitation variability, and the summer floods at the river Vltava can be traced (e.g., events of Julies 1954, 1981 and 1997; *Kakos*, 1997; as well as the recent floods of August 2002). On the contrary, with the precipitation record from the Czech Republic, the range of precipitation variability oscillations in Hungary even somewhat decreased for the last 50 years.

- As with many other areas of the world, the findings of the present study are broadly consistent with the projections made by $2 \times CO_2$ models of global warming.

Acknowledgements—Author thanks the Climatic Research Unit, University of East Anglia, Norwich, UK, for kindly providing the data used in this study.

References

Bodri, L. and *Cermak, V.*, 2003: High frequency variability in recent climate and the North Atlantic Oscillation. *Theor. Appl. Climatol. 74*, 33-40.

Bodri, L., Cermak, V., and *Kresl, M.*, 2004: Trends in precipitation variability: Prague (the Czech Republic). *Climate Change* (in press).

Hansen J., Ruedy, R., Sato, M., Imhoff, M., Lawrence, W., Easterling, D., Peterson, T., and *Karl, T.*, 2001: A closer look at United States and global surface temperature change. *J. Geophys. Res. 106*, 23947-23963.

Heino, R., Brazdil, R., Forland, E., Tuomenvirta, H., Alexandersson, H., Beniston, M., Pfister, C., Rebetez, M., Rosenhagen, G., Rösner, S., and *Wibig, J.*, 1999: Progress in the study of climatic extremes in Northern and Central Europe. *Climatic Change 42*, 151-181.

Houghton, J.T., Callander, B.A., and *Varney, S.K.* (eds.), 1992: *Climate Change 1992.* The Supplementary Report to Climate Change: The IPCC Scientific Assessment. Report prepared for the IPCC Working Group I. Cambridge Univ. Press, Cambridge.

Hulme, M., 1992: A 1951-80 global land precipitation climatology for the evaluation of GCMs. *Climate Dynamics 7*, 57-72.

Hulme, M., Osborn, T.J., and *Johns, T.C.*, 1998: Precipitation sensitivity to global warming. Comparison to observations with HadCM2 simulations. *Geophys. Res. Lett. 25*, 3379-3382.

Jones, P.D., 1994: Hemispheric surface air temperature variations: a reanalysis and an update to 1993. *J. Climate 7*, 1794-1802.

Kakos, V., 1997: Hydrometeorological analysis of historical flood in the year 1897 in connection with the catastrophic floods in the Czech Lands in the beginning of September 1890 and in Morava River in July 1997 (in Czech). *Meteorologicke zpravy 50*, 191-196.

*Karl, T.R., Knight, R.*W., and *Plummer, N.*, 1995: Trends in high frequency climate variability in the twentieth century. *Nature 377*, 217-220.

Karl, T.R., Nicholls, N., and *Ghazi, A.*, 1999: CLIVAR/GCOS/WMO workshop on indices and indicators for climate extremes. Workshop summary. *Climatic Change 42*, 3-7.

Kattenberg, A., Giorgi, F., Grassl, H., Meehl, G.A., Mitchell, J.F.B., Stouffer, R.J., Tokioka, T., Weaver, A.J., and *Wigley, T.M.L.*, 1996: Climate models: projections of future climate. In *Climate Change 1995: The Science of Climate Change* (eds.: *J.T. Houghton, L.G. MeiroFilho, B.A. Callendar, A. Kattenberg*, and *K. Maskell*). Cambridge Univ. Press, Cambridge, UK, 285-357.

Katz, R.W. and *Brown, B.G.*, 1992: Extreme events in a changing climate: variability is more important than averages. *Climatic Change 21*, 289-302.

McGuffie, K., Henderson-Sellers, A., Holbrook, N., Kothavala, Z., Balachova, O., and *Hoekstra, J.*, 1999: Assessing simulations of daily temperatures and precipitation variability with global climate models for present and enhanced greenhouse climates. *Int. J. Climatol. 19*, 1-26.

Mearns, L.O., Giorgi, F., McDaniel, L., and *Shields, C.*, 1995: Analysis of daily variability of precipitation in a nested regional climate model: comparison with observations and doubled CO_2 results. *Global Planet. Change 10*, 55-78.

Moberg, A., Jones, P.D., Barriendos, M., Bergström, H., Camuffo, D., Cocheo, C., Davies, T.D., Demareé, C., Martin-Vide, J., Mangeri, M., Rodriguez, R., and *Verhoeve, T.*, 2000: Day-to-day temperature variability trends in 160- to 275-year-long European instrumental records. *J. Geophys. Res. 105*, 22849-22868.

New, M., Todd, M., Hulme, M., and *Jones, P.*, 2001: Precipitation measurements and trends in the twentieth century. *Int. J. Clim. 21*, 1899-1922.

Nicholls, N., Gruza, G.V., Jousel, J., Karl, T.R., Ogallo, L.A., and *Parker, D.E.*, 1996: Observed climate variability and change. In *Climate Change 1995: The Science of Climate Change* (eds.: *J.T. Houghton, L.G. MeiroFilho, B.A. Callendar, A. Kattenberg*, and *K. Maskell*). Cambridge Univ. Press, Cambridge, UK, 133-192.

Parker, D.E., Jones, P.D., Bevan, A., and *Folland, C.K.*, 1994: Interdecadal changes of surface temperature since the late 19th century. *J. Geophys. Res. 99*, 14373-14399.

Parker, D.E., Folland, C.K., and *Jackson, M.*, 1995: Marine surface temperature: observed variations and data requirements. *Climatic Change 31*, 559-600.

Rebetez, M., 1996: Public expectation as an element of human perception of climate change. *Climatic Change 32*, 495-509.

Rebetez, M., 2001: Changes in daily and nightly day-to-day temperature variability during the twentieth century for two stations in Switzerland. *Theor. Appl. Climatol. 69*, 13-21.

Szentimrey, T., 1997: Statistical procedure for joint homogenization of climatic time series. *Proc. Seminar for Homogenization of Surface Climatological Data,* Budapest, Hungary, 47-62.

Szentimrey, T., 1999: Multiple analysis of series for homogenizaton (MASH). *Proc. Second Seminar for Homogenization of Surface Climatological Data,* Budapest, Hungary; WMO, WCDMP-No.41, 27-46.

Wilks, D.S. and *Riha, S.J.*, 1996: High-frequency climatic variability and crop yields. *Climatic Change 32*, 231-235.

Yan, Z., Jones, P.D., Moberg, A., Bergström, H., Davies, T.D., and *Yang, C.*, 2001: Recent trends in weather and seasonal cycles: An analysis of daily data from Europe and China. *J. Geophys. Res. 106*, 5123-5138.

GUIDE FOR AUTHORS OF *IDŐJÁRÁS*

The purpose of the journal is to publish papers in any field of meteorology and atmosphere related scientific areas. These may be

- research papers on new results of scientific investigations,
- critical review articles summarizing the current state of art of a certain topic,
- short contributions dealing with a particular question.

Some issues contain "News" and "Book review", therefore, such contributions are also welcome. The papers must be in American English and should be checked by a native speaker if necessary.

Authors are requested to send their manuscripts to

Editor-in Chief of IDŐJÁRÁS
P.O. Box 39, H-1675 Budapest, Hungary

in three identical printed copies including all illustrations. Papers will then be reviewed normally by two independent referees, who remain unidentified for the author(s). The Editor-in-Chief will inform the author(s) whether or not the paper is acceptable for publication, and what modifications, if any, are necessary.

Please, follow the order given below when typing manuscripts.

Title part: should consist of the title, the name(s) of the author(s), their affiliation(s) including full postal and E-mail address(es). In case of more than one author, the corresponding author must be identified.

Abstract: should contain the purpose, the applied data and methods as well as the basic conclusion(s) of the paper.

Key-words: must be included (from 5 to 10) to help to classify the topic.

Text: has to be typed in double spacing with wide margins on one side of an A4 size white paper. Use of S.I. units are expected, and the use of negative exponent is preferred to fractional sign. Mathematical formulae are expected to be as simple as possible and numbered in parentheses at the right margin.

All publications cited in the text should be presented in a *list of references*, arranged in alphabetical order. For an article: name(s) of author(s) in Italics, year, title of article, name of journal, volume, number (the latter two in Italics) and pages. E.g., *Nathan, K.K.,* 1986: A note on the relationship between photo-synthetically active radiation and cloud amount. *Időjárás 90,* 10-13. For a book: name(s) of author(s), year, title of the book (all in Italics except the year), publisher and place of publication. E.g., *Junge, C. E.,* 1963: *Air Chemistry and Radioactivity.* Academic Press, New York and London. Reference in the text should contain the name(s) of the author(s) in Italics and year of publication. E.g., in the case of one author: *Miller* (1989); in the case of two authors: *Gamov* and *Cleveland* (1973); and if there are more than two authors: *Smith et al.* (1990). If the name of the author cannot be fitted into the text: *(Miller,* 1989); etc. When referring papers published in the same year by the same author, letters a, b, c, etc. should follow the year of publication.

Tables should be marked by Arabic numbers and printed in separate sheets with their numbers and legends given below them. Avoid too lengthy or complicated tables, or tables duplicating results given in other form in the manuscript (e.g., graphs)

Figures should also be marked with Arabic numbers and printed in black and white in camera-ready form in separate sheets with their numbers and captions given below them. Good quality laser printings are preferred.

The text should be submitted both in manuscript and in electronic form, the latter on diskette or in E-mail. Use standard 3.5" MS-DOS formatted diskette or CD for this purpose. MS Word format is preferred.

Reprints: authors receive 30 reprints free of charge. Additional reprints may be ordered at the authors' expense when sending back the proofs to the Editorial Office.

More information for authors is available: antal.e@met.hu

Information on the last issues: http://omsz.met.hu/irodalom/firat_ido/ido_hu.html

Published by the Hungarian Meteorological Service

Budapest, Hungary

INDEX: 26 361

HU ISSN 0324-6329

IDŐJÁRÁS

QUARTERLY JOURNAL
OF THE HUNGARIAN METEOROLOGICAL SERVICE

CONTENTS

****

http://omsz.met.hu/english/ref/jurido/jurido_en.html

VOL. 108 * NO. 3 * JULY – SEPTEMBER 2004

IDŐJÁRÁS

Quarterly Journal of the Hungarian Meteorological Service

Editor-in-Chief
LÁSZLÓ BOZÓ

Executive Editor
MARGIT ANTAL

Editorial Office: P.O. Box 39, H-1675 Budapest, Hungary or
Gilice tér 39, H-1181 Budapest, Hungary
E-mail: bozo.l@met.hu or *antal.e@met.hu*
Fax: (36-1) 346-4809

Subscription by

mail: IDŐJÁRÁS, P.O. Box 39, H-1675 Budapest, Hungary;
E-mail: bozo.l@met.hu or *antal.e@met.hu*; *Fax: (36-1) 346-4809*

IDŐJÁRÁS

Quarterly Journal of the Hungarian Meteorological Service

Editorial

I have been nominated as the Editor-in-Chief of IDŐJÁRÁS by the President of the Hungarian Meteorological Service, for the period of 2004–2008, starting with this issue of our Journal.

I graduated in meteorology from the Eötvös Loránd University in Budapest in 1986. Currently I am leading the Environmental Division of the Hungarian Meteorological Service, involved in several research issues of air pollutants' transport and dispersion modeling. I have been a member of the Editorial Board of IDŐJÁRÁS since 1997. I am taking part in the activities of international scientific communities as a member of Working Group on Environmental Pollution and Atmospheric Chemistry of WMO CAS, as a national expert of the Steering Committee of the EU Harmonization within Atmospheric Dispersion Modelling for Regulatory Purposes, and as national secretary of the International Union of Geodesy and Geophysics.

I have been principal investigator of several national, bi-lateral, and multi-lateral international scientific projects in the field of meteorology and environmental sciences for the past 15 years.

It is great honour to me to have been selected for this prestigious position at IDŐJÁRÁS, the fifth oldest meteorological journal in the world, which has now 108 years long history. It is very exciting and challenging task to follow excellent Hungarian meteorologists in this position. The scope and policy of the Journal should not be changed: to publish high quality peer reviewed papers from any parts of the world in the field of meteorology and atmosphere related scientific areas. Most of the members of the Editorial Board will continue their valuable work in realizing this goal, altogether with new experts which have recently joined the Board.

László Bozó D.Sc.

IDŐJÁRÁS

Quarterly Journal of the Hungarian Meteorological Service
Vol. 108, No. 3, July–September 2004, pp. 155–162

Estimation of the nitrogen loading from the atmospheric dry deposition of ammonium and nitrate aerosol particles to Lake Balaton

Szilvia Kugler[1]* and **László Horváth[2]**

[1]*Department of Meteorology, Eötvös Loránd University,*
P.O. Box 32, H-1518 Budapest, Hungary; E-mail: kuglersz@ludens.elte.hu

[2]*Hungarian Meteorological Service,*
P.O. Box 39, H-1675 Budapest, Hungary; E-mail: horvath.l@met.hu

(Manuscript received July 30, 2003; in final form September 17, 2003)

Abstract—The N-loading to Lake Balaton is an important cause for the observed eutrophycation. One of the most important sources of nitrogen compounds is atmospheric deposition. In this paper, the N-loading due to the dry deposition of atmospheric particles is determined. Concentrations of ammonium and nitrate ions in the particulate phase were determined on the basis of one-year bulk concentration measurements. Mean deposition velocities were estimated on the basis of *Slinn* and *Slinn* (1980) for ammonium and nitrate using the mean mass diameter of particles determined by *Mészáros et al.* (1997). From the measured concentrations and dry deposition velocities derived, a total of 11.2 ± 1.1 and 7.7 ± 0.8 mg N m^{-2} yr^{-1} N-loading were calculated for ammonium and nitrate particles, respectively. This amount is negligible in comparison with the other N-sources from the atmosphere.

Key-words: dry deposition, aerosol particles, ammonium and nitrate particles, nitrogen loading.

1. Introduction

The observed eutrophycation of Lake Balaton in the second half of the last century was the consequence of the increased nutrient (N, P) loading from various sources. Among them, the atmospheric input of the nitrogen is one of the most important factors. Since the mid-1970's numerous experiments have

*Correspondig author

been carried out to determine the rate of nutrient flux by atmospheric dry and wet deposition to the surface of Lake Balaton (e.g., *Dobolyi* and *Horváth,* 1978; *Mészáros et al.,* 1980; *Horváth et al.*, 1981; *Horváth,* 1982; *Horváth,* 1984; *Horváth,* 1990).

Investigations described in these papers have determined wet deposition based on a sampling network installed around the lake. The wet deposition rate of phosphorus and nitrogen compounds was derived from the chemical composition (concentration of N- and P-forms) and the amount of precipitation.

The estimation of the dry deposition flux is more complicated compared to the determination of the wet deposition flux. Previous studies did not take into account two important nitrogen compounds (N_2O, HNO_3). Furthermore, there are some other compounds (e.g., N_2O and NH_3) that have bi-directional flux, i.e., as a function of the physico-chemical conditions the net flux can be positive (emission) or negative (deposition). Since the rate of exchange processes controlling the nitrogen balance between the water and atmosphere strongly depends on the nitrogen loading of the water, in extreme cases the lake would be a net emitter for nitrogen compounds. In other words, a negative feed-back mechanism which results in self-cleaning of the lake can not be excluded.

In addition to the problems of gaseous N-compounds, estimation of the dry deposition of particle-phase ammonium and nitrate ions is one of the most uncertain term in the estimation of N-loading. In the earlier estimations (e.g., *Horváth et al.*, 1981) the dry deposition velocities for these particles were considered on the basis of laboratory measurements. However, there is evidence that deposition mechanism of particles onto a natural water surface with waves present is quite different (*Zufall et al.*, 1999a,b).

In summary: the nutrients carried by precipitation (wet deposition) can be easily determined. However, the prediction of the rate of dry deposition is much more difficult. According to the above mentioned reasons, even the direction of the flux of gaseous N-compounds is uncertain. On theoretical grounds, the possibility that more nitrogen compounds are released from the lake than deposited from the atmosphere cannot be excluded. Conversely, the rate of dry deposition could be higher than expected, and in extreme cases it may exceed the rate of wet deposition by orders of magnitude. The ratio of dry to wet deposition cannot be determined from the data presently available.

For the above reasons it is necessary to re-evaluate the nitrogen balance between the atmosphere and Lake Balaton on the basis of new considerations for modeling and measurement strategies. The present work aims to determine the nitrogen loading by the dry deposition of atmospheric nitrate and ammonium particles.

2. *Methods and measurements*

Dry deposition of aerosol particles is calculated with the aid of a simple model. If the flux of the particles is one-directional, i.e., the upward flux can be neglected, then the deposition model is more simple than for gases. The deposition velocity of particles strongly depends on their size distribution. The deposition rate for particles (D_d) with a diameter of d can be described by the formula: $D_d = v_d\, c_d$, where v_d is the deposition velocity, and c_d is the atmospheric concentration. In order to determine the mean deposition flux of the particles, the size distribution, the mean deposition velocity of a certain size fraction, and the concentration in the given size fraction must be known. The goal of our work is to determine these parameters. Theoretically, the integral of D_d for the whole size distribution of the aerosol particles containing nitrogen gives the total deposition. In practice, however, an average size of the particles is derived from size distribution curves. A certain dry deposition velocity value is related to a given average particle size by a function that strongly depends on the size of the particle. The product of the deposition velocity and the concentration of the particulate ammonium or nitrate in a given size range gives the rate of the dry deposition.

2.1 Measurement of nitrate and ammonium concentrations in particle phase

Ammonium and nitrate concentration in the aerosol particles was measured in samples taken at Siófok station (southern shore of Lake Balaton) at a height of 12.3 m above the water surface. Sampling period ranged from March, 2002 to February, 2003. During the sampling, total suspended aerosol particles were collected on a Teflon filter on the basis of bulk aerosol sampling in the entire size range. A NILU EK-type sequential (two-channel) sampler was used and combined with three-stage filter packs. Ammonium and nitrate particles were determined from the first (Teflon) filter. After extracting the filters, the nitrate and ammonium concentrations in the solution were analyzed by ion chromatography and spectrophotometric method. For details of sampling and analysis see: *EMEP* (1996).

Monthly averages calculated from the daily concentrations measured at the station are presented in *Table 1*. It should be mentioned here that in case of nitrate an expressed concentration minimum can be observed during summer months as a consequence of the higher volatilization rate of nitrate with the increase of temperature. It would result in parallel increase of nitric acid concentration in the atmosphere.

Table 1. The measured mean monthly ammonium and nitrate in particle phase at Lake Balaton

2002–2003	Monthly mean concentrations ($\mu g\ m^{-3}$)	
	Ammonium	**Nitrate**
March	1.97	4.11
April	1.89	2.43
May	1.00	1.16
June	0.91	0.60
July	0.80	0.54
August	1.11	0.73
September	1.34	1.58
October	1.49	2.20
November	1.55	2.18
December	2.76	2.73
January	2.68	3.02
February	4.61	6.19
Yearly mean	**1.84**	**2.29**

2.2 *Size distribution of aerosol particles*

Only a few data are available for the particle size distribution. According to observation of *Mészáros et al.* (1997), the mean mass diameter of the nitrate particles for summer and winter are 1.5 and 0.80 μm, while for ammonium these values are 0.6 and 0.8 μm, respectively. The latter experiment was carried out over a less polluted area of the town Veszprém, situated approximately 8 km north of Lake Balaton. According to the experimental results for background aerosol particles (*Horváth et al.*, 2001, 2003), the majority of the nitrate particles is in the coarse particle fraction ($d > 2.5$ μm), while the ammonium particles are in the fine particle fraction ($d < 2.5$ μm). The experimental results of different time and location are quite different, the only similarity between them is that nitrate can usually be found in the particle fraction with larger diameter. In order to calculate the dry deposition rates it is necessary to use the values resulting from the calculations of the measurements near the lake (*Mészáros et al.*, 1997). In *Table 2* the results of these measurements are compiled.

2.3 *Dry deposition velocity of particles*

There are large uncertainties in the estimation of the dry deposition velocity of aerosol particles. Most of the existing measurements, wind tunnel experiments, and theoretical calculations relate to deposition on solid surfaces. The values for deposition velocity obtained from the different methods vary with orders of

magnitude. *Ruijgork et al.* (1993); *Borrell et al.* (1997) have pointed out that the deposition velocity determined theoretically or on the basis of laboratory measurements are much lower than those obtained from field measurements. It is evident that deposition velocities determined for the areas covered with vegetation are different from those over water surfaces. The deposition rates are different due to differences in the roughness parameter and the relative humidity above the water surfaces. The paper of *Slinn* and *Slinn* (1980) demonstrates that the deposition velocity above water surfaces depends mainly on the characteristics of the particle especially their hygroscopic or non-hygroscopic nature. In our calculations the values given by the above authors for hygroscopic particles were used at 5 m s^{-1} wind speed and 99% relative humidity above the water surface. The deposition velocities used for Lake Balaton are presented in *Table 2*, indicating the strong dependence on average particle diameter.

Table 2. Mean concentration, particle diameter, dry deposition velocity, and dry deposition of ammonium and nitrate particles (summer half year: April–September; winter half year: October–March)

Ammonium				
Period	**Concentration** ($\mu g\ m^{-3}$)	**Mean particle diameter** (μm)	**Deposition velocity** ($cm\ s^{-1}$)	**Dry deposition** ($mg\ N\ m^{-2}$)
Summer half	1.18	0.6	0.016	2.3
Winter half	2.51	0.8	0.029	8.9
Year	**1.84**	–	–	**11.2**

Nitrate				
Period	**Concentration** ($\mu g\ m^{-3}$)	**Mean particle diameter** (μm)	**Deposition velocity** ($cm\ s^{-1}$)	**Dry deposition** ($mg\ N\ m^{-2}$)
Summer half	1.17	1.5	0.1	4.2
Winter half	3.41	0.8	0.029	3.5
Year	**2.29**	–	–	**7.7**

3. Results: estimation of the dry deposition rate for nitrate and ammonium particles

The most important data concerning the deposition rate of the ammonium and nitrate particles are presented in *Table 2*. The second column gives the mean concentrations that were determined as described in paragraph 2.1. The third column shows the average particle diameters determined as described in

paragraph 2.2, while the fourth column gives the values determined from *Slinn* and *Slinn* (1980). From these data, dry deposition values were calculated as given in the last column. The uncertainty of these figures can be estimated as the bulk error of sampling and analysis of nitrate and ammonium concentrations. The estimated bulk relative error for filter pack sampling and analysis is between 5–10% (*Horváth et al.*, 2003).

Taking into account these uncertainties, the ammonium and nitrate particle deposition onto Lake Balaton are 11.2 ± 1.1 and 7.7 ± 0.8 mg N m^{-2} yr^{-1}. The total N-deposition from atmospheric particles is 18.9 ± 1.9 mg N m^{-2} yr^{-1}. The ammonium and nitrate loading for the whole surface of the lake is 11.2 ± 1.1 t N yr^{-1} assuming a surface area of 595 km^2. This rate is likely negligible in comparison with the total nitrogen loading determined on the basis of previous measurements (*Horváth et al.*, 1981). In that paper a total of 590 t N yr^{-1} for the nitrogen loading to Lake Balaton was reported, that is higher by two orders of magnitude than the dry deposition of ammonium and nitrate particles estimated here. The difference is obviously due to wet deposition of nitrate and ammonium ions. It is difficult to give an estimation for the total N-budget between the lake and the atmosphere in the lack of knowledge of ammonia, nitrous oxide, and nitric acid dry fluxes. Investigation of these processes will be a task for the future, but dry flux of nitrogen compounds in particle phase probably does not play an important role in nitrogen loading.

The probability of a long-term variation in N-loading by aerosol particles can be estimated from the long-term variation of concentrations. Long term concentration data from the nearest background air pollution monitoring station (K-puszta, 150 km east of Siófok) shows the large variation between the years (*Fig. 1*). During the last 15–20 years, changes in ammonium and nitrate concentration have been within a factor of about two. It is difficult to predict future variability, but it is likely that considerable changes can not be expected in concentrations and, therefore, in the deposition of N-containing particles.

3. Conclusion

According to the experiments, theoretical considerations, and literature data, we can conclude that the dry flux of ammonium and nitrate aerosol particles to the lake surface are 11.2 ± 1.1 and 7.7 ± 0.8 mg N m^{-2} yr^{-1}. According to the long term changes of concentrations, these rates are not expected to change considerably in the near future. The ammonium and nitrate load for the whole lake is 11.2±1.1 t N yr^{-1}. This amount of load is likely negligible in comparison to the total nitrogen flux determined on the basis of previous

measurements (*Horváth et al.*, 1981). In the future, when the balance of gases (ammonia, nitrous oxide, nitric acid) will be better known, the yearly loading of N-compounds is subject to changes, but it is probable that deposition of aerosol particles does not carry nitrogen to the lake in substantial quantity.

Acknowledgements—Investigations has been sponsored by the Ministry of the Environment, Hungary. We wish to thank the personnel of Siófok observatory for their help in sampling.

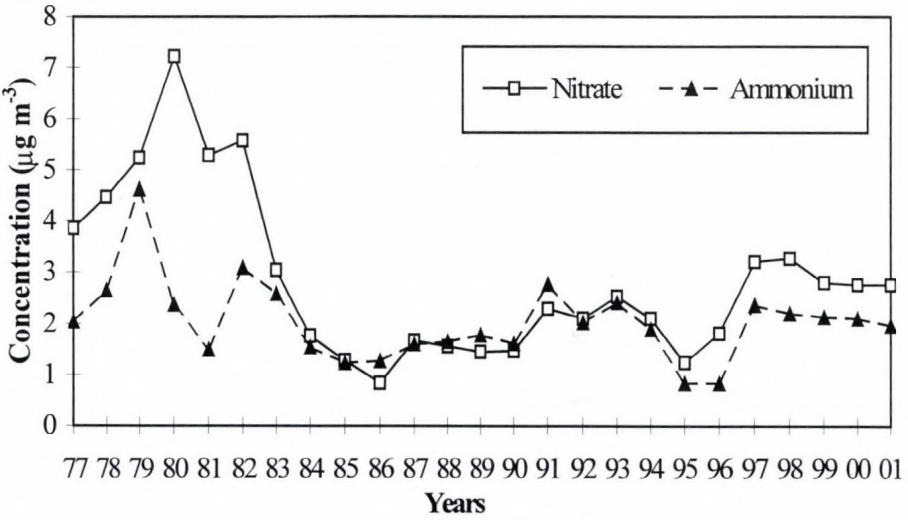

Fig. 1. Long term variation of nitrate and ammonium concentration in particles, K-puszta station.

References

Borrell, P., Builtjes, J.H., Grennfelt, P., and *Hov, O.* (eds.), 1997: *Transport and Chemical Transformation of Pollutants in the Troposphere, 10. Photo-Oxidants, Acidification and Tools: Policy Applications of EUROTRAC Results*. Springer-Verlag, Berlin, Heidelberg, 116 pp.

Dobolyi, E. and *Horváth, L.*, 1978: Investigation of the amount of direct nutrient (P, N) loading from the atmosphere to Lake Balaton (in Hungarian). *Hidrológiai Közlöny 12*, 547-552.

EMEP, 1996: EMEP co-operative program for monitoring and evaluation of the long-range transmission of air pollutants in Europe. EMEP Manual for sampling and chemical analysis. *EMEP/CCC-Report 1/95*, NILU, Kjeller, Norway.

Horváth, L., 1982: On the vertical flux of gaseous ammonia above water and soil surfaces. In *Deposition of Atmospheric Pollutants*. D. Reidel Publishing Company, Dodrecht, pp. 17-22.

Horváth L., 1984: Effect of the air pollution on the water quality of Lake Balaton (in Hungarian). OKKFT A/12 "Regional environmental protection research of Lake Balaton". *OKTH Környezet- és természetvédelmi kutatások* 3, 161-162.

Horváth L., 1990: Concentration and deposition of airborne pollutants in the catchment of Lake Balaton (in Hungarian). *Vízügyi Közlemények 77*, 204-208.

Horváth, L., Mészáros, Á., Mészáros, E., and *Várhelyi, G.*, 1981: On the atmospheric deposition of nitrogen and phosphorus into Lake Balaton. *Időjárás 85*, 194-200.

Horváth, L., Mészáros, R., Pinto, J.P., and *Weidinger, T.*, 2001: Estimate of the dry deposition of atmospheric nitrogen and sulfur species to Spruce forest. In *Proc. of EUROTRAC Symposium 2000* (eds.: *P.M. Midgley, M. Reuther*, and *M. Williams*). *Garmish-Partenkirchen, Germany*, 27-31 March 2000. Springer-Verlag, Berlin, Heidelberg.

Horváth, L., Pinto, J., and *Weidinger, T.*, 2003: Estimate of the dry deposition of atmospheric nitrogen and sulfur species to spruce forest. *Időjárás 105*, 249-255.

Mészáros, E., Horváth, L., Mészáros, Á., and *Várhelyi, G.*, 1980: Effect of the air pollution on the water quality of Lake Balaton (in Hungarian). *MTA/VEAB Monográfiái 6*, 87-101.

Mészáros, E., Barcza, T., Gelencsér, A., Hlavay, J., Kiss, Gy., Krivácsi, Z., Molnár, Á. and *Polyák, K.*, 1997: Size distributions of inorganic and organic species in the atmospheric aerosol in Hungary. *J. Aerosol Sci. 28*, 1163-1175.

Ruijgork, W., Nicholson, K.W., and *Davidson, C.I.*, 1993: Dry deposition of particles. In *Models and Methods for the Quantification of Atmospheric Input to Ecosystems*. Nordiske Seminar og Arbejdsrapporter 1993: 573. Nordic Council of Ministers, Copenhagen, 145-161.

Slinn, S.A. and *Slinn, W.G.N.*, 1980: Prediction for particle deposition on natural waters. *Atmos. Environ. 14*, 1013-1016.

Zufall, M.J., Dai, W., Davidson, C.I. and *Etyemezian, V.*, 1999a: Dry deposition of particles to wave surfaces: I. Mathematical modeling. *Atmos. Environ. 33*, 4273-4281.

Zufall, M.J., Dai, W., and *Davidson, C.I.*, 1999b: Dry deposition of particles to wave surfaces: II. Wind tunnel experiments. *Atmos. Environ. 33*, 4283-4290.

IDŐJÁRÁS

Quarterly Journal of the Hungarian Meteorological Service
Vol. 108, No. 3, July–September 2004, pp. 163–171

Analysis of the extremity of precipitation intensity using the POT method

Mónika Lakatos[1]* and **István Matyasovszky**[2]

[1]*Hungarian Meteorological Service,*
P.O. Box, 38, H-1525 Budapest, Hungary; E-mail: lakatos.m@met.hu

[2]*Department of Meteorology, Eötvös Loránd University,*
P.O. Box 32, H-1518 Budapest, Hungary; E-mail: matya@ludens.elte.hu

(Manuscript received March 16, 2004; in final form July 16, 2004)

Abstract—The paper presents a procedure going beyond the classical extreme value analysis of data sets considering only one extreme value per year. The main advantage of the Peaks Over Threshold (POT) method is to use every data exceeding a specified high, or staying under a specified low threshold. The methodology is used to estimate return levels. A return level is defined as a level, which is exceeded in average one time during a specified period. The procedure is applied to a data set consisting of 10-minute precipitation amounts at Baja-Csávoly, Hungary, for the period from 1997 to 2003.

Key-words: short-term precipitation, extremes, POT method, generalized Pareto distribution, return levels.

1. Introduction

The measuring practice of short-term precipitation has completely changed with installing automatic climate stations. In the period preceding the automatization, ombrographs registered the quantity of precipitation. Evaluation of the rain register paper was carried out by selecting the largest precipitation amounts during 5, 10, 20, 30, 60, 180 min periods within a wet event, considering the slope of the curve of accumulated precipitation and registering these partial amounts. In the national observing network *Váradi* and *Nemes* (1992) performed a statistical analysis of data registered by

* Corresponding author

ombrographs for 26 stations in Hungary for the period from 1967 to 1991. Besides frequency histograms, extreme value analysis was also made for the maxima of different time intervals using a procedure developed by *Faragó* (1990). This program fits the GEV distribution to maxima and results in the return levels for different return periods.

Automatic stations replaced the ombrographs in many places in Hungary making the short term sampling possible. At the Hungarian Meteorological Service the amount of precipitation is registered every ten minutes forming a data set for further analysis. This paper reports an examination of extreme large ten minutes precipitation amounts. Section 2 presents the methodology based on the so-called POT technique. Section 3 summarizes the main results. Finally, a section is provided for conclusions.

2. POT method

Extreme value analysis is generally based on asymptotic formulae. Under general conditions, the maximum of a sample is described by the Jenkinson distribution, which includes the three possible types of the probability distribution of maxima, namely the Gumbel, Fréchet and Weibull distributions. This is a successful way, when a quite large sample is available for the maximum. However, the method cannot be applied when the maximum of an N length period is in question, and observations cover an n length period, where n is not much larger than N. Also, even an appropriate sample size is available there is a chance that the largest value from an n length period is smaller than the second largest value from an other period.

Therefore, it looks promising to use every observation representing large values. The concept includes a specification of a high threshold and peaks over threshold (POT), i.e., threshold excesses are used in the analysis. Modeling of threshold excesses has been first applied to hydrological problems. Statistical properties of this approach are detailed in *Davison* and *Smith* (1990). Description of the POT method and other techniques to analyze extreme values is summarized in *Coles* (2001). Results obtained with the POT method and GEV model are compared for Palmer Drought Severity Index for several Hungarian meteorological stations (*Zempléni et al.*, 1999).

2.1 Generalized Pareto distribution

Let X be a random variable with probability distribution function F. Taking a threshold w, the conditional probability

$$P(X > w + y \mid X > w) = \frac{1 - F(w+y)}{1 - F(w)}, \qquad y > 0, \tag{1}$$

could be easily calculated if F were known. Because the distribution function is not known as accurately as required for using Eq. (1), an asymptotic approximation is used in practice. Under general conditions (*Leadbetter et al.*, 1983), the Eq. (2) approximates Eq. (1) for high thresholds:

$$P(X > w + y \mid X > w) = \frac{1 - F(w+y)}{1 - F(w)} = \left[1 + \frac{\xi y}{\sigma}\right]^{-1/\xi} = 1 - H(y), \tag{2}$$

where $H(y)$ is the generalized Pareto distribution function

$$H(y) = 1 - (1 + \frac{\xi y}{\sigma})^{-1/\xi}, \qquad y > 0, \qquad (1 + \xi y/\sigma) > 0. \tag{3}$$

When the shape parameter ξ is zero, the Pareto distribution becomes exponential distribution with parameter $1/\sigma$:

$$H(y) = 1 - \exp(-\frac{y}{\sigma}), \qquad y > 0. \tag{4}$$

Note that ξ does not depend on w but the scale parameter σ does.

Choice of the threshold has a crucial role in application. When taking a too low threshold, the Pareto distribution is a poor approximation to Eq. (1), and thus the model is biased. Also, even observations X_i, $i = 1,...n$, are not independent, the excesses $X_i - w > 0$ tend to be independent as w tends to infinity. However, a too high threshold delivers a small number of observations exceeding this threshold and results in a large variance of the estimated parameters. Therefore, the threshold must not be too high.

There are two ways of the threshold selection. The first is to estimate the threshold too, while the second way is to fit Pareto distributions with different thresholds and analyze the stability of estimated parameters. In the first case, it is utilized that $\mathrm{E}[X - w \mid X > w]$ is a linear function of w. Thus, substituting the conditional expected values by corresponding means, the threshold is chosen as the minimum of candidate values of w, which satisfies the linear dependence of means on w. In the second case, the threshold is chosen such that estimates of ξ under different values of w fluctuate around a constant.

2.2 *Parameter estimation*

With $y_i = X_i - w$, $X_i > w$, $i = 1,...,k$ the log-likelihood function

$$l(\sigma,\xi) = -k\log\sigma - (1+1/\xi)\sum_{i=1}^{k}\log(1+\xi_i/\sigma), \quad 1+\xi_i y_i/\sigma > 0, \tag{5}$$

has to be maximized with respect to σ and ξ. Numerical techniques are required for the purpose taking care to avoid numerical instabilities when $\xi \approx 0$. In the case of $\xi = 0$, the log-likelihood is

$$l(\sigma) = -k\log\sigma - \sigma^{-1}\sum_{i=1}^{k} y_i .$$

2.3 *Return levels*

The degree of extremity can be characterized by return levels. A return level x_m is defined as a level, which is exceeded in average one time during an m length period. Due to this definition and considering Eq. (3),

$$P(X > x_m) = p_w\left(1+\xi\left(\frac{x_m - w}{\sigma}\right)\right)^{-1/\xi} = 1/m \tag{6}$$

is solved for x_m, where $p_w = P(X > w)$. In the solution:

$$x_m = w + \frac{\sigma}{\xi}\left[(mp_w)^{\xi} - 1\right], \tag{7}$$

the parameters are substituted by their maximum likelihood estimates, $\tilde{\xi},\tilde{\sigma}$, and $\tilde{p}_w = k/n$.

In the case of $\xi \approx 0$, Eq. (4) leads to $x_m = w + \sigma\log(mp_w)$.

2.4 *Model verification*

Graphical methods are generally used to check suitability of the fitted Pareto distributions. Having an ordered sample $y_{(1)} \le ..... \le y_{(k)}$ used to fit a Pareto model, the relative frequencies $\{i/(k+1); i = 1,...,k\}$ and model-generated $\{\tilde{H}(y_{(i)}); i = 1,...,k\}$ estimates of probabilities $\{P(X - w \mid X > w) < y_i; i = 1,...,k\}$

should be close to each other. Therefore, the points $\{(i/(k+1), \widetilde{H}(y_{(i)})); i = 1,\ldots,k\}$ will fluctuate around a line when the model is appropriate (probability plot).

Another approach, the quantile plot, considers the points $\{(\widetilde{H}^{-1}(i/(k+1)), y_{(i)}); i = 1,\ldots,k\}$, because they will scatter around a line when the model is appropriate.

3. Example

The data set consists of 10-minute precipitation amounts for Baja-Csávoly (φ=46°11', λ=19°01'), for the period from 1997 to 2003. The automatic rain gauge was installed earlier, but reliable and continuous data are available since 1997. Months of the year were analyzed separately due to the strong annual cycle. Thus, Pareto distributions were fit for each month using an Splus program of *Coles* (2001).

The first and very important step of the model building is the selection of suitable thresholds as it was mentioned in Section 2. A properly selected threshold considers two requirements. Namely, the threshold w is enough high to satisfy the statistical independence of threshold excesses, but enough low to have a satisfactory amount of threshold excesses to estimate model parameters with moderate variances. This procedure is demonstrated with July, because this is a typical period of short and intensive rainfall events in Hungary.

A diagnostic procedure using the modified scale parameter, $\sigma^* = \sigma_w - \xi w$, and shape parameter ξ can help in the threshold selection. *Fig. 1* shows these parameters with their confidence intervals of 95% against the threshold. The lowest threshold w has to be chosen, which satisfies that the above-mentioned parameters may be considered constants for higher values of w. Note that both σ^* and ξ show an apparent change around w = 1 mm, but stabilize over 1.2 mm. As it is crucial that enough number of threshold excesses are available for the estimation procedure, a threshold larger than 1 mm does not seem a good choice. Because at w = 1 mm the number of excesses is 97, and a considerably higher threshold delivers drastically smaller number of such cases (see *Fig. 2*), our final choice is 1 mm in July. Excesses corresponding to this choice have been tested for statistical independence using a test based on the sign of neighboring sample elements (*Kendall* and *Stuart,* 1966). The independence is acceptable at least at 0.01 significance level. This procedure was applied for each month, and the selected thresholds are shown in *Table 1*. These values are obviously larger for summer than winter, due to the more intensive precipitation in the warm season. However, the low thresholds in winter appear quite, high because considerably fewer excesses are available than in

summer. This is because relatively high thresholds had to be chosen to satisfy the statistical independence of excesses.

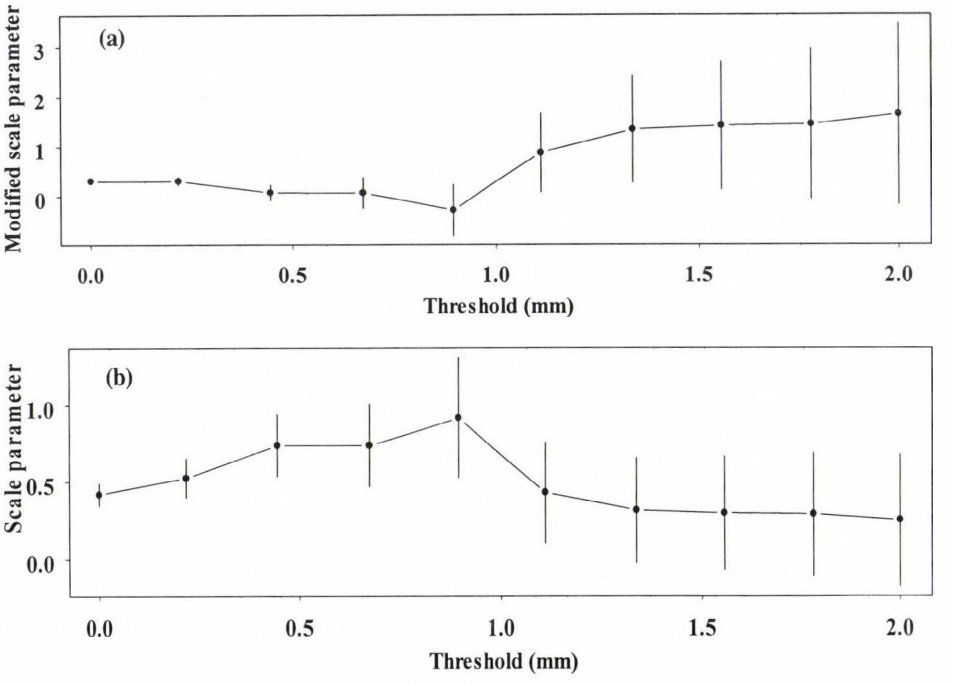

Fig. 1. Modified scale ($\sigma^* = \sigma_u - \xi$) (*a*) and scale parameter ξ (*b*) against w of the Pareto distribution fitted to July data.

Having the thresholds, the scale and shape parameters are estimated by maximizing Eq. (5). In the case of July, the estimated parameters of the Pareto fitting are $\sigma = 1.405$ and $\xi = 0.383$. Return levels obtained from Eq. (7) are also shown in *Table 1*, for 2, 5, 10, 50, and 100 years return periods. As it is expected, the highest values are in summer and lowest ones are in winter. Comparing the 5 and 10 years return levels with the observed 7-year maximum, the values estimated by Eq. (7) look underestimated. For instance, the observed 7-year maximum in January is 1.9 mm corresponding to the 50-year return level. Such underestimation does not appear in summer suggesting the effect of few threshold excesses in winter. For December the Pareto fitting leads to $\xi = 0.01$, so the exponential distribution seemed to be a good approximation of Eq. (4).

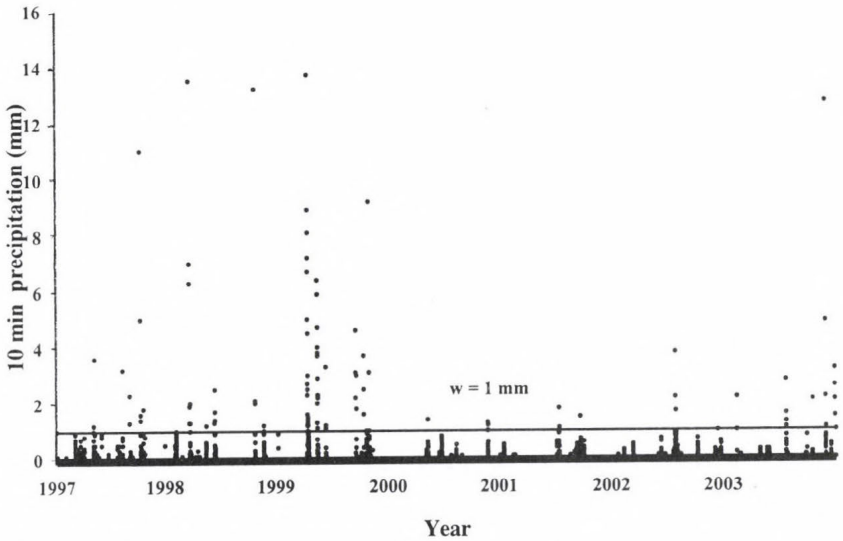

Fig. 2. 10 min precipitation sums and the selected $w = 1$ mm threshold for July, in the period 1997–2003.

Table 1. Selected thresholds and return levels for each month

Month	Threshold w (mm)	Return period (year)					
		2	5	10	50	100	
January	0.5	1.2	1.4	1.6	1.9	2.0	
February	0.5	1.5	1.9	2.4	3.5	4.1	
March	0.6	1.4	1.6	1.7	1.8	1.8	
April	0.7	1.8	2.0	2.2	2.5	2.6	
May	0.7	3.3	4.5	5.7	9.1	11.0	
June	0.9	6.5	9.4	12.3	22.0	28.0	
July	1.0	10.6	16.2	22.0	43.5	57.7	
August	0.6	6.7	11.0	15.7	35.1	49.5	
September	0.7	4.0	5.7	7.3	12.7	16.0	
October	0.6	3.5	5.1	6.8	13.0	17.2	
November	0.7	1.8	2.3	2.8	4.1	4.8	
December	0.6	1.1	1.3	1.5	1.9	2.0	

Return level (mm)

Return levels with confidence intervals of 95% are presented on a logarithmic scale for July in *Fig. 3.* Empirical estimates of the sample elements are also shown in the return level plots. Evidently, the confidence interval

becomes wider as return period increases. Because the observed 7-year maximum in July is 13.7 mm, the values shown in *Table 1* probably overestimate the return levels in this month.

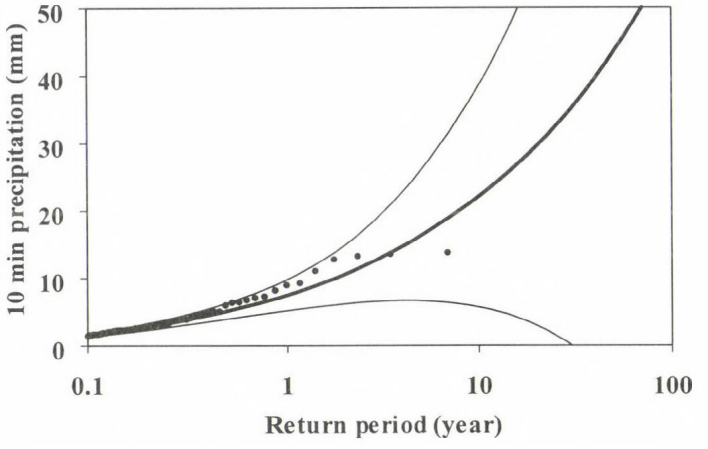

Fig. 3. Return levels and 95% confidence intervals to the different return period for July.

Diagnostic plots for the fitted generalized Pareto distribution are shown in *Fig. 4a* and *b*. The probability plot (*Fig. 4a*) for July data is approximately linear, while the goodness-of-fit considering the quantile plot (*Fig. 4b*) seems less convincing, because there are very large uncertainties at high levels.

4. Conclusions

The purpose of this paper was to present a procedure going beyond the classical extreme value analysis of data sets, taking into account only one extreme value per year. The main advantage of POT method is to use every data exceeding a specified threshold. This threshold, however, has a crucial role, and its choice is a trade-off between the bias and variance of the model. Also, statistical independence of threshold excesses should be satisfied by the choice. This problem is reflected by underestimated return levels in winter.

It may be useful to analyze short-term precipitation extremes for further intervals, e.g., for 20 min and 30 min. Also, there is a need to develop a procedure establishing a relationship between data registered with the former practice and data measured with automatic instruments.

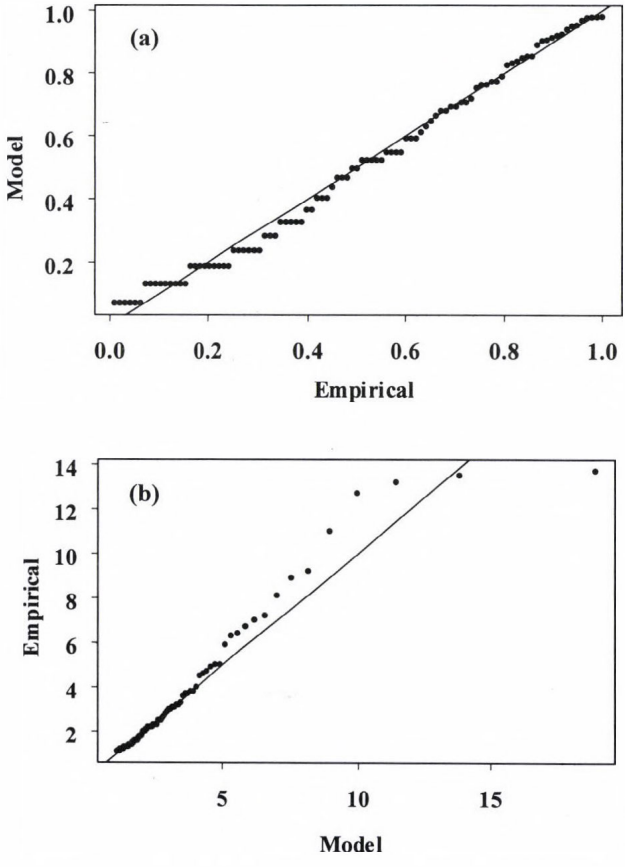

Fig. 4. Probability plot (*a*) and quantile plot (*b*) of July data.

References

Coles, S.G., 2001: *An Introduction to Statistical Modeling of Extreme Value*. Springer-Verlag, New York .

Davison, A.C. and *Smith, R.L.*, 1990: Models for exceedances over high thresholds. *J. Roy. Stat. Soc. B 52*, 393-442

Faragó, T. and *Katz, R.W.*, 1990: Extremes and design values in climatology. *WMO, TD-No. 386*, Geneva.

Leadbetter, M.R., Lindgren, G., and *Rootzen, H.*, 1983: *Extremes and Related Properties of Random Sequences and Processes*. Springer-Verlag, New York.

Váradi, F. and *Nemes, Cs.*, 1992: Frequencies of short-term precipitation in Hugary (in Hungarian). *Légkör XXXVII* (3), 8-13.

Zempléni, A.Z., Bermundez, P., and *Csiszár, V.*, 1999: Applying extreme value models for PDSI drought severity index series in Hungary (in Hungarian). *Meteorológiai Tudományos Napok*. Országos Meteorológiai Szolgálat, Budapest, 57-69.

IDŐJÁRÁS

Quarterly Journal of the Hungarian Meteorological Service
Vol. 108, No. 3, July–September 2004, pp. 173–194

Connections between urban heat island and surface parameters: measurements and modeling

János Unger[1], Zsolt Bottyán[2], Zoltán Sümeghy[1] and Ágnes Gulyás[1]

[1]*Department of Climatology and Landscape Ecology, University of Szeged, P.O. Box 653, H-6701 Szeged, Hungary*

E-mail: unger@geo.u-szeged.hu; sumeghy@geo.u-szeged.hu; agulyas@geo.u-szeged.hu

[2]*Department of Resource Economy, University of Debrecen, P.O. Box 10, H-4015 Debrecen, Hungary, E-mail: zbottyan@helios.date.hu*

(Manuscript received May 5, 2003; in final form September 26, 2003)

Abstract—This study deals with the influence of urban surface factors on the air temperature patterns, using mobile measurements under different weather conditions in the periods of March 1999 – February 2000 and April – October 2002. The studied city (Szeged, Hungary) is located on a plain with a population of 160,000. Investigations concentrated on the urban heat island (UHI) at its strongest development during the diurnal cycle. Tasks included: (1) Determination of spatial distribution of UHI intensity and some urban surface parameters (built-up and water surface ratios, sky view factor, building height). (2) Development of statistical models in the heating and non-heating seasons using the above mentioned parameters and their areal extensions. (3) Identification of similarities or differences in the seasonal spatial patterns of UHI along an urban cross-section and explanation these features using land-use and climatological parameters.

In both seasons the spatial distribution of UHI intensity fields has a concentric shape with some local irregularities. The intensity reaches more than 2°C (heating season) and 3°C (non-heating season) in the centre. According to the model equations determined by stepwise multiple linear regression analysis, there are clear connections between the spatial distribution of the urban excess temperature and the examined land-use parameters. Among these parameters sky view factor and building height are the most determining factors, which are in line with the urban surface energy balance. Along the cross-section the UHI intensity has a seasonal change, as a consequence of the prevailing weather conditions. The role of cloudiness and wind speed is clearly recognized during most of the time in the studied period. Utilization of normalized values shows that the form of the seasonal UHI profile is independent of the seasonal climatological conditions, and is determined by urban surface factors to a high degree.

Key-words: urban heat island, spatial and seasonal patterns, statistical model equations, urban cross-section, seasonal profiles.

1. Introduction

Urbanization modify materials, structure, and energy balance of the surface and air composition compared to the natural surroundings. As a consequence of the effects of these artificial factors, a distinguished local climate (urban climate) develops in the cities, which manifests itself by the excess temperature (urban heat island – UHI) most obviously. The magnitude of this excess is the UHI intensity (namely ΔT, the temperature difference between urban and rural areas). Generally, in its diurnal cycle the strongest development occurs 3–5 hours after sunset.

Simulation of real factors and physical processes generating the urban climate is difficult because of the complicated urban terrain with regard to surface geometry and materials, as well as artificial production of heat and air pollution. The detection of these factors and processes demands complex and expensive instruments, and sophisticated numerical and physical models. Despite these difficulties, several models have been developed for small-scale climate variations within the city. Some of these models are based on advective (*Oke*, 1976), energy balance (*Tapper et al.*, 1981; *Johnson et al.*, 1991; *Myrup et al.*, 1993; *Ruffieux*, 1995), radiation (*Voogt* and *Oke*, 1991), heat storage (*Grimmond et al.*, 1991), water balance (*Grimmond* and *Oke*, 1991), and surface sensible heat flux (*Voogt* and *Grimmond*, 2000) approaches. In order to study microclimate alterations within the city, utilization of statistical modeling may provide useful quantitative information about the urban temperature excess by employing different surface parameters (e.g. *Outcalt,* 1972; *Oke*, 1981, 1988; *Park*, 1986, 1987; *Kuttler et al.*, 1996; *Matzarakis et al.*, 1998).

Our objective is to investigate the seasonal effects and interactions inside the city on the air temperature, a few hours after sunset, when the UHI effect is generally most pronounced. To achieve this aim, we construct horizontal isotherm maps to show the average spatial distribution of the UHI intensity in the investigated periods and present some obvious relationships between temperature patterns and urban factors. Then we examine the quantitative effects of the relevant surface factors and their combinations on the patterns of the urban-rural temperature differences. The selection of these parameters, namely built-up ratio, water surface ratio, sky view factor, and building height, is based on their role in small-scale climate variations (*Oke*, 1987; *Golany*, 1996). Finally, we identify similarities or differences in the spatial distributions of ΔT by seasons along an urban cross-section and explain these features using land-use and climatological parameters.

2. Environmental conditions

The studied city, Szeged, is located in the south-eastern part of Hungary (46°N, 20°E) at 79 m above sea level on a flat flood plain. River Tisza passes through the city, otherwise, there are no large water bodies nearby. The river is relatively narrow and, according to our earlier investigation, its influence is negligible (*Unger et al.* 2000, 2001). These environmental conditions make Szeged a suitable place for studying an almost undisturbed urban climate.

Most of Hungary belongs to Köppen's climatic region Cf (temperate warm climate with a fairly uniform annual distribution of precipitation). Climatic subregions are distinguished using the mean temperature of vegetative season (t_{VS} in °C) and the aridity index ($H = Q^*/L_V P$ where Q^* is the annual mean net radiation in MJ m^{-2}, L_V is the latent heat of evaporation in MJ kg^{-1} and P is the annual mean precipitation in kg m^{-2}). The climate is arid or humid, according to whether the dimensionless H is bigger or less than 1, respectively. Szeged is in the *warm-dry* subregion by this classification, which is characterized by $t_{VS} > 17.5$°C and $H > 1.15$ (*Unger*, 1999). Two half years can be distinguished from the point of view of city dwellers: the heating (from October until April) and the non-heating (from April until October) seasons.

Szeged has an administration district of 281 km^2 with a population of 160,000. The base of the street network is a circuit-avenue system. Different land-use types are present including a densely-built centre with medium-wide streets and large housing estates of high concrete buildings set in wide green spaces. There are zones used for industry and warehousing, areas occupied by detached houses, considerable open spaces along the riverbanks, in parks, and around the city's outskirts (*Unger et al.*, 2000).

3. Parameters and methods

3.1 Grid network

Our efforts were focused on the urbanized part of the administration district. The area of investigation was divided into two sectors and subdivided further into 0.5 km × 0.5 km square cells (*Fig. 1*). The same grid size was employed, for example, in an investigation of UHI in Seoul, Korea (*Park*, 1986). The original study area consists of 107 cells covering the urban and suburban parts of Szeged, mainly inside of the circle dike that protects the city from river floods. The outlying parts, characterized by mostly rural features, are not included in the network except for four cells on the western side of the area, which are necessary to determine the temperature contrast between urban and

rural areas. The grid was established by quartering the 1 km × 1 km square network of 1:10,000 scale maps of the Unified National Mapping System developed for the topographical maps of Hungary (*Unger et al.*, 2000, 2001).

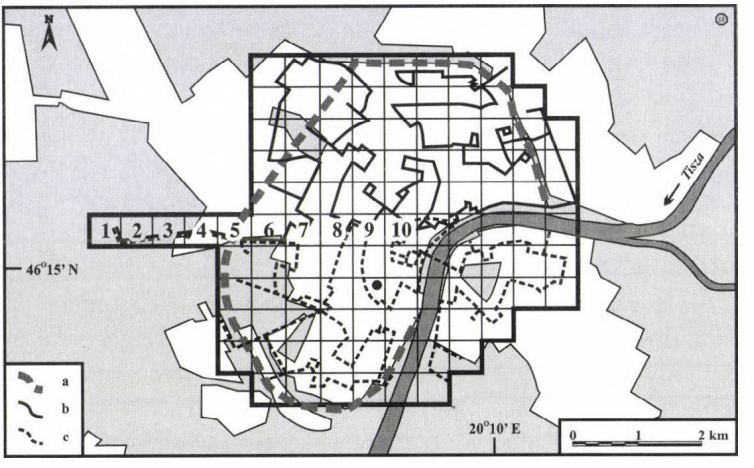

Fig. 1. Division of the area of study into 0.5 km × 0.5 km grid cells. The dashed line (*a*) denotes the circle dike, (*b*) and (*c*) are the measurement routes in the northern and southern sectors, respectively. The permanent measurement site of the University of Szeged is indicated as •, and the cells of cross-section are numbered from 1 to 10.

In the present research, six southern and four western cells of the original study area are omitted because of the lack of one parameter in the data set (building height, see Section 3.5). Therefore, we employ altogether 97 cells covering an area of 24.25 km^2.

3.2 Temperature (maximum UHI intensity)

In order to collect data on ΔT for every cell, mobile measurements were performed on fixed return routes once a week during the period of March 1999–February 2000 (*Fig. 1*). In case of surface and near-surface air UHI measurements, vehicle-based observation (car, tram, helicopter, airplane, satellite) is a common process (e.g., *Conrads* and *van der Hage*, 1971; *Oke* and *Fuggle*, 1972; *Johnson*, 1985; *Moreno-Garcia*, 1994; *Yamashita*, 1996; *Voogt* and *Oke*, 1997; *Klysik* and *Fortuniak*, 1999). Altogether 48 car traverses were taken, 24 in the northern, and another 24 in the southern sector. The frequency of traverses provided sufficient information under different weather conditions, except for rain.

Division of the area of the study into two sectors was necessary because of the large number of cells. The 75 km and 68 km long return routes in the northern and southern sectors, respectively, were needed to make time-based corrections, since measurements took about 3 hours. Temperature readings were obtained using a radiation-shielded resistance sensor connected to a data logger for digital sampling. Data were collected every 16 sec, so at an average car speed of 20–30 km h^{-1}, the average distance between measuring points was 89–133 m. In order to avoid the influence of engine and exhaust heat, the sensor was mounted 0.60 m in front of the car at 1.45 m above the ground. The speed was sufficient to provide adequate ventilation for the sensor to measure the ambient air temperature. The traffic density in the late hours of measurements was rather low. The logged values at forced stops (e.g., at traffic lamps) were rejected from the data set.

Having averaged the measurement values by cells, time adjustments to a reference time were applied assuming linear air temperature change with time. This change was monitored by the continuous records of the automatic weather station of the University of Szeged (*Fig. 1*). The linear adjustment appears to be correct for data collected a few hours after sunset in urban areas. However, because of the different time variations of cooling rates, it is only approximately correct for suburban and rural areas (*Oke* and *Maxwell*, 1975). The reference time, namely the likely time of the occurrence of the strongest UHI in the diurnal course, was 4 hours after sunset, a value based on earlier measurements. Consequently, we can assign one temperature value to every cell in the northern sector or in the southern sector at a given measuring night. These values refer to the centre of each cell.

UHI intensities were determined by cells referring to the temperature of the westernmost cell (1) of the original area of the study ($T_{cell} - T_{(1)}$), which was regarded as a rural cell because of its location outside of the city (*Fig. 1*). Moreover, the weather station of the Hungarian Meteorological Service is located there, and its records were used as rural (reference) data in the earlier studies on the urban climate of Szeged (e.g., *Unger*, 1996, 1999).

The 97 points (the above mentioned cell centerpoints) covering the urban parts of Szeged provide an appropriate basis to interpolate isolines (temperature and other parameters) using a geostatistical gridding method, the standard Kriging procedure.

3.3 Built-up and water surface ratio

Ratios of the built-up (covered surface – building, street, pavement, parking lot, etc.) (*B*) and water surface (*W*) by cells were determined by a vector and raster-based GIS database combined with remote sensing analysis of SPOT XS

images. The digital satellite image was rectified to the Unified National Mapping System using 1:10,000 scale maps. The nearest-neighbour method of resampling was employed, resulting in a root mean square value of less than 1 pixel. The geometric resolution of the image was 20 m × 20 m.

Normalized Difference Vegetation Index was calculated from the pixel values, using visible (0.58–0.68 μm) and near infrared (0.72–1.1 μm) bands (*Gallo* and *Owen*, 1999). They are between −1 to +1 indicating the effect of green space in the given spatial unit. Using these values, built-up, water, and vegetated surfaces were distinguished and their ratios (to total cell area) for each grid square were determined using cross-tabulation (*Unger et al.*, 2000). In the Szeged region the occurrence of non-vegetated (bare) areas is negligible, namely, each non-built-up place is covered by some vegetation (e.g., garden and cultivated plants, trees, grass, bushes, weeds).

3.4 Sky view factor

The built-up ratio does not describe completely the characteristics of an artificial urban surface. Streets and buildings create canyons, and this 3D geometry plays an important role in the development of UHI. Namely, heat transport and outgoing long wave radiation decrease because of the moderated turbulence and increased obstruction of the sky.

To estimate the openness of the cell surfaces quantitatively, we applied the sky view factor (*SVF*, now marked shortly by *S*). It is a dimensionless measure (between 0 and 1) of the degree to which sky is obscured by the surroundings for a given point (*Oke*, 1981, 1988). Commonly, *S* is determined using either analytical or photographic methods, employing theodolite, fish-eye lens (digital) camera, or automatic canopy analyzer (*Oke*, 1981; *Bärring et al.*, 1985; *Park*, 1987; *Grimmond et al.*, 2001).

In our analytical method we have measured two elevation angles to the top of the buildings (α_1 and α_2) perpendicularly to the axis of streets in both directions, using an 1.5 m high theodolite. From these data, wall view factors can be calculated to the left (WVF_{W1}) and right (WVF_{W2}) sides (*Oke*, 1981). The measuring points are not always coincident with the midpoint of the distance between buildings on both sides (*Fig. 2*). The calculation of *S* is based on *Oke's* (1988) results (for explanation of symbols see *Fig. 2*):

$$WVF_{W1} = (1 - \cos\alpha_1)/2 \qquad \text{where } \alpha_1 = \tan^{-1}(H_1/W_1), \tag{1}$$

$$WVF_{W2} = (1 - \cos\alpha_2)/2 \qquad \text{where } \alpha_2 = \tan^{-1}(H_2/W_2), \tag{2}$$

$$S = 1 - (WVF_{W1} + WVF_{W2}). \tag{3}$$

In order to determine *S* values, the same long canyons (measuring routes) were used as for temperature sampling. 532 points were surveyed by theodolite, and the values of *S* were also averaged by cells. In line with the temperature sampling, the distance between the points was 125 m on average. Angle measurements taken higher within a canyon (1.5 m) excluded more of the terrain (non-sky) and resulted in an over-estimate of *S* after the calculation. This effect is more pronounced in canyons with low *H/W* ratios (*Grimmond et al.*, 2001). Due to technical difficulties, we did not have any measurement points at the intersections of roads, so the calculated *S* values are probably a bit smaller than the real ones. Furthermore, if there were parks, forests, or water surface in a particular direction, we assigned 0° as an angle value, because it is difficult to determine *S* values modified by the vegetation, and the results are not unambiguous (*Yamashita et al.*, 1986).

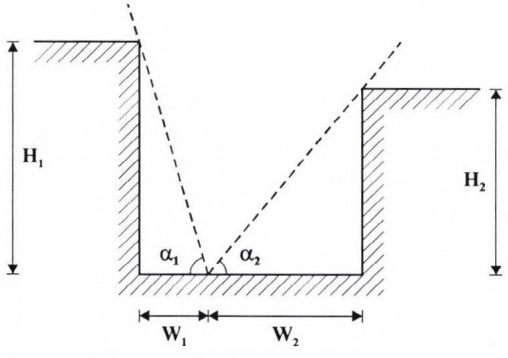

Fig. 2. Geometry of a non-symmetric canyon flanked by buildings with a measuring point not at the centre of the floor (modified after *Oke*, 1988).

While earlier investigations were limited to the centre or only some parts of the cities and used far smaller numbers of measurements (*Oke*, 1981, 1988; *Johnson*, 1985; *Yamashita et al.*, 1986; *Park*, 1987; *Eliasson*, 1996; *Grimmond et al.*, 2001), the obtained data set represents almost the total urban area.

3.5 Building height

Since some areas with different land-use features can produce almost equal *S* data (narrow street with low buildings versus broad street with high buildings), *S* values alone do not describe sufficiently the vertical geometry of cities. It is important to have quantitative information on the vertical size of a canyon, because it plays significant role in the energy budget.

To determine the vertical dimension of a canyon, we applied a combined procedure. The above mentioned elevation angles (α_1 and α_2) are available at each point. If we have the distances to the walls from the measuring point (W_1 and W_2, see *Fig. 2*), there is a simple formula to calculate wall heights (H_1 and H_2), taking the instrument height of 1.5 m into account:

$$H_1 = \tan \alpha_1 \, W_1 + 1.5 \text{ m}, \tag{4}$$

$$H_2 = \tan \alpha_2 \, W_2 + 1.5 \text{ m}. \tag{5}$$

The width of the streets was determined by means of aerial photographs concerning any part of the street. After digitizing these images, we made an orthophoto of Szeged using the Ortho Base tool of the ERDAS IMAGINE GIS software, and marked the measurement points. This orthophoto is already suitable to determine distances of the walls (W_1 and W_2) from the measurement points. As the aerial photographs do not cover completely the area of the study, these distances are not available for six and four cells in the southern and western parts of Szeged, respectively.

3.6 The applied statistical model

In order to assess the extent of the relationships between the mean maximum UHI intensity (ΔT) and various urban surface factors, multiple correlation and regression analyses were applied. Some examples of the modeled variables and employed variable parameters of earlier studies are in *Table 1*.

In the course of determination of model equations we used ΔT as predictant (dependent variable) in both seasons and the afore-mentioned parameters as predictors: ratios of built-up surface (B) and water surface (W) as a percentage, mean sky view factor (S), mean building height (H) in m by cells. Searching for statistical relationships, we have to take into account that our parameters are variables (spatially) and constants (temporally) at the same time. Since these parameters change rapidly with the increasing distance from the city center, we applied the exponentially distance-weighted spatial means of the mentioned land-use parameters for our model. The distance scale of the weight should be derived from the transport scale of the heat in the urban canopy. Our statistical model determined this scale from the measured parameter values. A set of predictors concerning all four basic urban parameters were originated as areal extensions and grouped in the following way:

Group 1: parameter values (S, H, B, W) in the cell with $\Delta i^2 + \Delta j^2 = 0$.

Group 2: mean parameter values ($S1$, $H1$, $B1$, $W1$) of all cells with $0 < \Delta i^2 + \Delta j^2 < 2^2$.

Group 3: mean parameter values ($S2$, $H2$, $B2$, $W2$) of all cells with $2^2 < \Delta i^2 + \Delta j^2 < 4^2$.

Here i and j are cell indices in the two dimensions, while Δi and Δj are the differences of cell indices with respect to a given cell. These zones cover the entire investigated model area of Szeged.

Table 1. Survey of some studies using statistical models for prediction of UHI (extended after *Unger et al.*, 2000)

Predicted variable	**Employed parameters**	**Reference**
UHI intensity	Wind speed, cloudiness	*Sundborg* (1950)
UHI intensity	Population, wind speed	*Oke* (1973)
Max. UHI intensity	Population	
UHI intensity	Wind speed, cloudiness, atmospheric stability, traffic flow, energy consumption, temperature	*Nkemdirim* (1978)
UHI intensity at four different air levels	Lapse rate, wind speed, ratio of lapse rate to wind speed	*Nkemdirim* (1980)
UHI intensity	Wind speed, land-use type ratios	*Park* (1986)
Max. UHI intensity	Impermeable surface, population	
UHI intensity	Wind speed, cloudiness, temperature, humidity mixing ratio	*Goldreich* (1992)
UHI intensity	Wind speed, cloudiness, air pressure	*Moreno-Garcia* (1994)
Surface UHI intensity	Solar radiation, wind speed, cloudiness	*Chow et al.* (1994)
UHI intensity	Built-up area, height, wind speed, time, temperature amplitude	*Kuttler et al.* (1996)
UHI intensity for T_{avg}, T_{max}, T_{min}	NDVI, surface temperature (satellite-based)	*Gallo* and *Owen* (1999)
UHI intensity	Distance from the city centre, built-up ratio	*Unger et al.* (2000)
UHI intensity	Wind speed, cloudiness	*Morris et al.* (2001)

With these areal extensions we have 12 predictors to construct the linear statistical model. However, there could be some multi-colinearity among these parameters. In order to eliminate these multi-colinearities, the set of parameters have to be selected. Using the cross-correlation matrix of these predictors we can find the highest correlation coefficients, which means strong connections among them. To avoid the unreasonable reduction of the number of predictors, only the parameter with maximum absolute mean of its correlation coefficients was taken out of each group.

The method for the construction of model equations is the stepwise multiple linear regression. The applied implementation of this procedure is part of the SPSS 9 statistical software. A comprehensive discussion of the mathematical background of this method is found in *Miller* (2002). Predictors were entered or removed from the model depending on the significance of the F value of 0.01 and 0.05, respectively. Since there is a well noticeable difference between the magnitudes of ΔT fields in these seasons, under these conditions two linear statistical model equations were determined: one for the heating and one for the non-heating season.

3.7 Cross-section investigation

A small but representative part of the original area of the study (altogether 10 cells) is examined seasonally in detail. This is an overlapping part between the northern and southern sectors (*Fig. 1*), namely a cross-section in the urban area, which consists of cells stretching from the rural area (cell 1) to the city core (cell 10) with a distance of 4.5 km.

The profiles of the UHI intensity along the cross-section were investigated by comparison of absolute and normalized seasonal means taking land-use and climatological features into consideration. The normalized values by cells are the ratios of the absolute means of a given cell and cell 10 (where ΔT is the highest in all seasons). Since meteorological conditions (first of all wind speed and cloudiness) influence the absolute values (in °C) of the UHI intensity (e.g., *Landsberg*, 1981; *Park*, 1986; *Yagüe et al.*, 1991; *Unger*, 1996), the seasonal comparison of spatial variation of ΔT is more effective using normalized values. Namely, the profile of the normalized seasonal mean UHI intensity is expected to be independent of the prevailing weather conditions in the studied period; nevertheless, it is expected to be dependent on the surface factors (e.g., land-use features, distance from the city centre, etc.).

4. Results and discussion

4.1 Spatial characteristics of the urban parameters and UHI

The spatial distribution of the built-up ratio in the city has almost a concentric shape decreasing from the central areas to outwards (*Fig. 3a*). The densely built-up areas are concentrated in the middle and north-eastern parts of the city with maximum values more than 96%. River Tisza with its environment has a low built-up ratio and, of course, a high water surface ratio which can be clearly recognized with its east-to-south curve (*Fig. 3b*). Apart from this, the

extension of water surfaces is negligible, except for some small and shallow recreational lakes in the western part of the city.

Due to the significant variability of the building height and width of the streets, the sky view factor pattern is very complicated (*Fig. 3c*). This field does not form a circular structure and its extreme values are not located only in the centre. There are three parts of the city where S is low (with values of lower than 0.8), and in the centre it is lower than 0.7. The highest buildings are concentrated in the north-eastern part of the city with maximum values of about 20 m (*Fig. 3d*). There is an other area in the southern central region, where the buildings are higher than 15 m. Generally, the average building height is more than 10 m in the studied area.

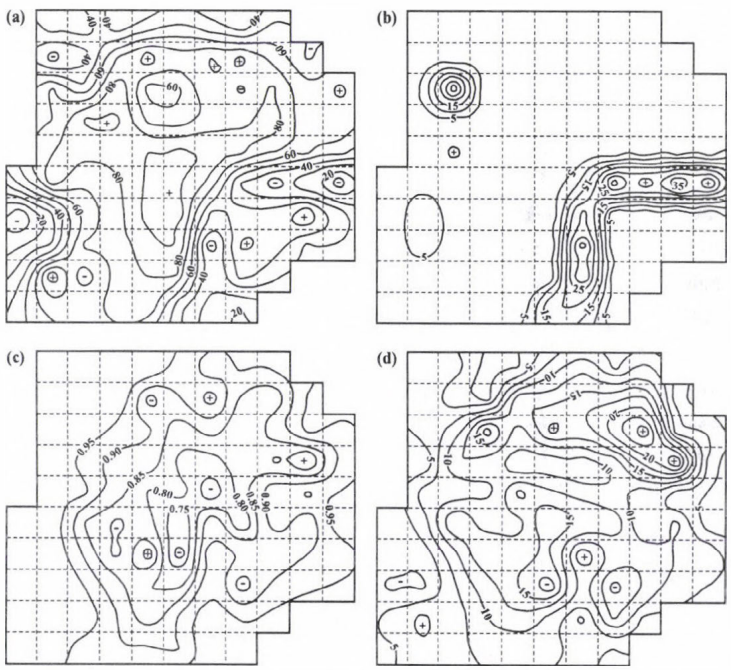

Fig. 3. Spatial distribution of (*a*) the ratio of the built-up area, (*b*) the ratio of the water surface to the total area (in percent), (*c*) the average sky view factor values and (*d*) the average building heights (in m) by cells in Szeged.

In the non-heating season (*Fig. 4a*), the greatest mean UHI intensity (3.18 C) is found in the central cell, and the ΔT of higher than 2 C – indicating significant thermal modification caused by urbanization – covers about 37% of the investigated area. In the heating season (*Fig. 4b*), the highest value of the

UHI intensity (2.12°C) occurs in the central cell, too, but the area of considerable differences (>2°C) covers only about 2% of the total area (*Unger et al.*, 2000).

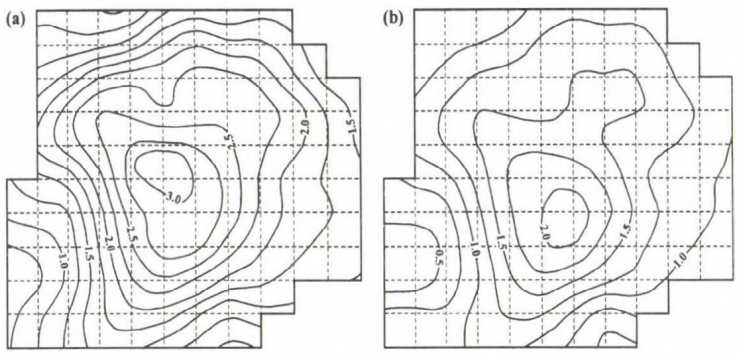

Fig. 4. Spatial distribution of the measured mean maximum UHI intensity (°C) during (*a*) the non-heating season (April 16 – October 15: 26 measurements) and (*b*) the heating season (October 16 – April 15: 22 measurements) in Szeged.

The most obvious common features of the UHI patterns are that the isotherms show almost concentric shapes in both seasons (*Fig. 4*). A deviation from this shape occurs in the north-eastern part of the city, where the isotherms stretch towards the suburbs. This anomaly can be explained by the effect of the large housing estates with high concrete buildings located mainly in the north-eastern part of the city with a built-up ratio higher than 75% (*Fig. 3a*), a sky view factor less than 0.85 (*Fig. 3c*), and a building height more than 15 m (*Fig. 3d*). The second irregularity is caused by the cooling influence of River Tisza, because along the river the isotherms are a bit drawn back towards the centre. The third area of anomaly can be found in the western part of the city, where the surface geometry changes abruptly along a westbound transect (which starts at the centre). This region is characterized by S values higher than 0.95, building heights lower than 7 m, and built-up ratio of about 25%.

The seasonal differences in the spatial distribution of ΔT (in °C) may be formed rather as a consequence of different weather characteristics of the two seasons than as a consequence of heating or non-heating of dwellings. In the Szeged region the climate conditions in winter, conducing to the formation of UHI, are less common (*Table 2*). Thus, in the warmer (non-heating) season, the role of the weather conditions (stronger solar radiation, more frequent clear sky, and weak wind) and the reduced latent heat transport, due to the more impermeable and guttered urban terrain, is more pronounced in the

development of UHI than the anthropogenic heat emission by heating in the colder season (*Unger et al.*, 2000).

Table 2. Monthly and seasonal means of the selected meteorological parameters in Szeged (March 1999 – February 2000)

Period	M	A	M	J	J	A	S	O	N	D	J	F	Spr.	Sum.	Aut.	Win.
Wind speed ($m\ s^{-1}$)	3.5	3.5	2.6	2.5	2.6	2.1	2.7	2.9	2.6	3.4	3.5	3.4	3.2	2.4	2.7	3.4
Cloudiness (okta)	4.7	4.9	4.3	4.6	3.8	3.6	3.6	4.5	5.9	5.6	6.1	3.7	4.6	4.0	4.7	5.1

4.2 Statistical model equations

Table 3 contains the cross-correlation matrix of the predictors and maximum absolute means of the correlation coefficients by lines. As a result of the selection procedure to reduce the multi-colinearities, three parameters (*S*, *H*1, and *S*2) were taken out of the original parameter-set. Thus, for the construction of the model equations, nine predictors remained.

Table 3. Cross-correlation matrix of the parameters and absolute means of the correlation coefficients by lines. Parameters are taken out of the models, and their absolute means are marked with bold setting (see Section 3.3–3.6 for explanation)

Parameter	B	S	W	H	B1	S1	W1	H1	B2	S2	H2	W2	Abs. mean
B	-	-0.50	-0.48	0.52	0.62	-0.50	-0.24	0.45	0.11	-0.12	0.01	-0.12	0.33
S	-0.50	-	0.13	-0.72	-0.52	0.64	0.09	-0.55	-0.05	0.41	-0.33	0.02	**0.36**
W	-0.48	0.13	-	-0.16	-0.13	0.02	0.29	-0.10	0.04	-0.22	0.18	0.16	0.17
H	0.52	-0.72	-0.16	-	0.43	-0.50	-0.16	0.57	-0.01	-0.42	0.23	-0.11	0.34
B1	0.62	-0.52	-0.13	0.43	-	-0.64	-0.49	0.57	0.15	-0.14	0.06	-0.21	0.36
S1	-0.50	0.64	0.02	-0.50	-0.64	-	0.04	-0.84	-0.04	0.56	-0.49	0.08	0.39
W1	-0.24	0.09	0.29	-0.16	-0.49	-0.04	-	-0.14	-0.08	-0.27	0.17	0.24	0.20
H1	0.45	-0.55	-0.10	0.57	0.57	-0.84	-0.14	-	-0.03	-0.63	0.48	-0.08	**0.40**
B2	0.11	-0.05	0.04	-0.01	0.15	-0.04	-0.08	-0.03	-	-0.10	0.21	0.02	0.08
S2	-0.12	0.41	-0.22	-0.42	-0.14	0.56	-0.27	-0.63	-0.10	-	-0.85	-0.10	**0.35**
H2	0.01	-0.33	0.18	0.23	0.06	-0.49	0.17	0.48	0.21	-0.85	-	0.13	0.28
W2	-0.12	0.02	0.16	0.23	-0.21	0.08	0.24	-0.08	0.02	-0.10	0.13	-	0.12

In both seasons the order of significance of the applied parameters is the same, but in the heating season the role of them is more pronounced than in the non-heating season. The model equations have four predictors, among them the *S*1 predictor is the most important, but *H* and *B*1 factors also play important role in both seasons (*Table 4*).

Table 4. Values of the stepwise correlation of mean maximum UHI intensity (ΔT) and urban surface parameters, and their significance levels in the studied periods in Szeged (n = 97) (see Section 3.3–3.6 for explanation)

Period	Parameter entered	Multiple |r|	Multiple r^2	Δr^2	Significance level (%)
April 16 - October 15 (non-heating season)	S1	0.806	0.649	0.000	0.1
	S1, H	0.845	0.714	0.065	0.1
	S1, H, B1	0.863	0.744	0.030	0.1
	S1, H, B1, W1	0.902	0.814	0.070	0.1
October 16 - April 15 (heating season)	S1	0.791	0.626	0.000	0.1
	S1, H	0.834	0.696	0.070	0.1
	S1, H, B1	0.852	0.726	0.030	0.1
	S1, H, B1, W1	0.873	0.762	0.036	0.1

The four-variable models for the non-heating (*nh*) and heating (*h*) seasons indicate strong linear relation between the mean maximum UHI intensity and the applied land-use parameters (*Table 4*). The model equations for ΔT_{nh} and ΔT_h (in °C) are the next (*Table 5*):

$$\Delta T_{nh} = -4.291S1 + 0.035H + 0.023B1 + 0.042W1 + 3.824, \quad (6)$$

$$\Delta T_h = -3.242S1 + 0.025H + 0.014B1 + 0.021W1 + 3.036. \quad (7)$$

The absolute values of the multiple correlation coefficients (r) between ΔT and the studied parameters are 0.902 and 0.873 in the non-heating and heating seasons; both are significant at 0.1% level. This means that with these four parameters we are able to explain 81.4% and 76.2% of the above mentioned relationships in the studied periods (*Table 4*). The standard errors of the estimates are 0.272 and 0.218 in the non-heating and heating half year, respectively.

We used these two model equations ((6) and (7)) to determine the spatial distribution of ΔT patterns in the studied area (*Fig. 5*). There is a considerable similarity between the measured and predicted UHI intensity fields in both seasons, namely, they have the same irregularities, however, some differences can be detected (*Fig. 4* and *Fig. 5*).

Table 5. Values of significance, coefficients, and standard errors of the applied urban surface parameters of the models in the studied periods in Szeged (n = 97) (see Section 3.3–3.6 for explanation)

Period	Parameter	Significance	Coefficient	Standard error
April 16 – October 15 (non-heating season)	S1	0.000	**-4.291**	0.787
	H	0.000	**0.035**	0.006
	B1	0.000	**0.023**	0.003
	W1	0.000	**0.042**	0.007
	Const.	0.000	**3.824**	0.897
October 16 – April 15 (heating season)	S1	0.000	**-3.242**	0.631
	H	0.017	**-0.025**	0.005
	B1	0.006	**0.014**	0.003
	W1	0.022	**0.021**	0.006
	Const.	0.000	**3.036**	0.718

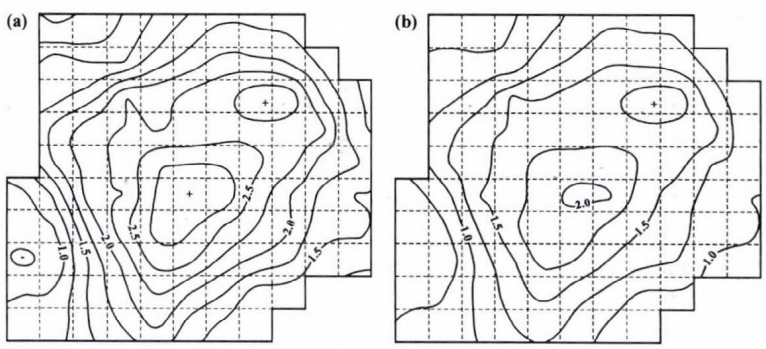

Fig. 5. Spatial distribution of the predicted mean max. UHI intensity (°C) during the (*a*) non-heating season and (*b*) the heating season in Szeged.

We compared the results of the model to an independent UHI intensity data set measured during the non-heating half year in 2002. The studied area and the mobile sampling method were the same as in the earlier cases, except that we used two cars to take temperature measurements at the same time in the two sectors, altogether 18 times. According to *Fig. 6a*, the measured independent UHI intensity pattern is similar to the one mentioned above (*Fig. 5a*), though the largest ΔT value is smaller by about 0.5°C. After that we calculated the spatial distribution of the difference between the predicted and measured independent UHI intensities (*Fig. 6b*). We can find only two small areas where the absolute UHI intensity anomaly is between 0.4°C and 0.6°C.

In the north-eastern part of the city, the predicted values are lower than the measured ones (negative anomaly). At the western border of the investigated area the predicted values are higher than the measured ones (positive anomaly). However, these areas occupy only a minor part of the area of the study (about 3.9 cells, 1 km^2, 4% of the total area). The areas characterized by the differences lower than 0.2°C are significantly larger, covering altogether 73 cells (about 18,2 km^2, 75%).

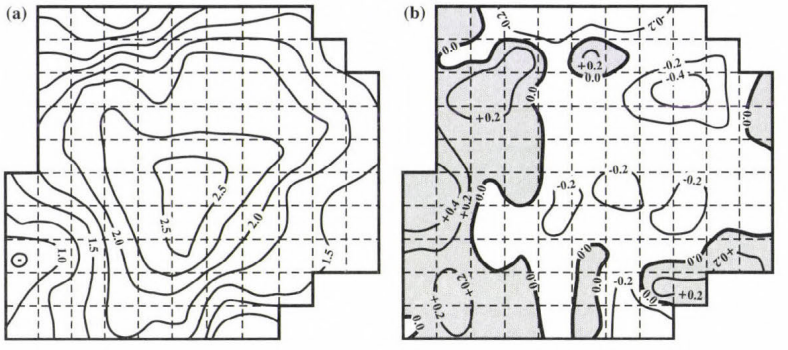

Fig. 6. (*a*) Spatial distribution of the measured mean max. UHI intensity (°C) during the independent non-heating season in 2002 and (*b*) spatial distribution of the difference of measured and predicted mean max. UHI intensity (°C) during the same season in Szeged.

It can be established that our model described the spatial distribution of the real UHI intensity field in the investigated area rather correctly. On the basis of our results, we may apply this model-construction procedure to predict the ΔT for other cities of different size and even non-concentric shape.

4.3 Cross-section profiles of UHI by seasons

Table 6 contains the areal ratios (%) of the main land-use types by cells along the selected cross-section. The largest built-up density (more than 90%) can be found around the centre (see cells 9 and 10 in *Fig. 1*), but the variation from the urban edge to the core is not uniform. The proportion of the water surface is rather negligible.

According to *Fig. 7a,* the profiles in every season show a marked increase from a rural level after reaching the edge of built-up areas (cell 3, see *Table 6*), and the highest values are in the city centre (cell 10). The absolute values of the seasonal profiles are almost the same in every cell, with the exception of winter. The values of the winter profile (with the largest seasonal

mean UHI intensity of 1.44°C) do not reach even the half of the values of other seasons. Because of the low winter values, the mean annual profile is a bit moderate compared to the ones of the first three seasons (the largest ΔT is 2.58°C).

Table 6. Land-use types by cells along the urban cross-section in Szeged

Land-use type (%)	Cell number									
	1	**2**	**3**	**4**	**5**	**6**	**7**	**8**	**9**	**10**
Built-up	0	0	18.9	70.4	54.2	85.6	71.7	77.8	91.4	90.5
Open	100	100	81.1	23.5	45.3	11.1	28.3	22.2	8.6	9.1
Water	0	0	0	6.1	0.5	3.3	0	0	0	0.4

Using normalized values, the differences among the seasonal profiles tend to disappear (*Fig. 7b*). These patterns follow remarkably well the general cross-section profile of the typical UHI described by *Oke* (1987): the 'cliff' is a steep temperature gradient at the rural/urban boundary, and much of the rest of the urban area appears as a 'plateau' of warm air with a steady but weaker horizontal gradient of increasing temperature towards the city centre. The urban core shows a final 'peak', where the largest temperature difference is observed (*Fig. 7c*).

In Szeged, the normalized ΔT values varied together along the cross-section with the largest deviation of only 0.13, in all seasons and in the whole one-year period (*Fig. 7b*). The 'cliff' with the large temperature gradient is located between cells 2 and 4 (the distance is 1 km). The profile shows a 1.5 km long thermal 'plateau' which is characterized by a very low temperature increment through its four cells (from 4 to 7). Then there is a second, very steep 'cliff' between the cells 7 and 8 (0.5 km), which indicates the onset of the 'peak' region. The areal extent of the largest values are rather wide (three cells, 1 km), so the steepness at the 'peak' value is relatively less sharp. This is explicable by the extent and homogeneity of the central urban part, which is dominated by 3–5 storey buildings built around the turn of the 19th and 20th centuries after the so called 'Great Flood' in 1879, which destroyed the city.

The seasonal variation of the urban temperature anomaly along the cross-section is attributed mainly to differences in weather conditions (*Table 2*). Winter months have the highest wind speed and cloudiness: at this time the UHI intensity is the weakest. In summer, when the above mentioned parameters have the smallest values, the extent of ΔT is not the largest in every point along the cross-section: it is slightly under or over the ΔT values in spring and autumn. These facts suggests that the effects of the climatological

parameters are fairly complex, and the investigation of their influence on the UHI cannot be restricted to only two, although important, parameters.

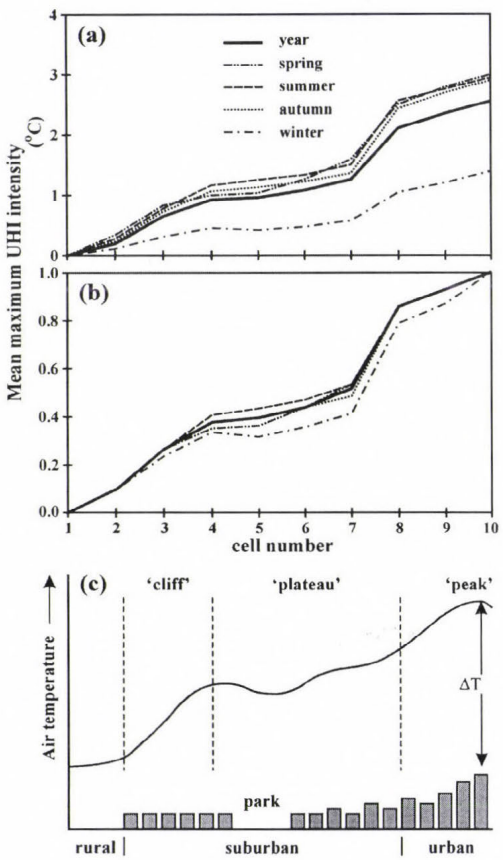

Fig. 7. Seasonal and annual profiles of (*a*) the absolute and (*b*) the normalized mean maximum UHI intensity across Szeged. (*c*) Generalized cross-section of the typical UHI after sunset (modified after *Oke*, 1987).

The use of the normalized values proved that the form of seasonal mean UHI profile depends only on surface factors. Among these factors, the built-up ratio may not be the most important one, because the steady, but not uniform increment of temperature towards the city core does not follow exactly the built-up density variation by cells (*Table 6*). However, an another parameter, however, the distance from the city centre seems to be more dominant in this general increasing tendency of urban temperature (*Unger et al.*, 2000).

5. Conclusions

In this paper the spatial and temporal features of the UHI effect was investigated in Szeged, Hungary. The following conclusions can be drawn from the analysis presented:

- The heat island phenomenon always appeared in the studied area, even though the UHI intensity changed during the year, as a consequence of the prevailing weather conditions, which vary by seasons in the temperate climatic region.
- The results on the seasonal spatial distribution of mean UHI indicate that:
  (i) The spatial patterns of the UHI intensity have almost concentric shapes with the values decreasing from the central areas towards the outskirts. The anomalies are caused by the alterations in the urban surface factors.
  (ii) There are significant differences in the magnitudes of the seasonal patterns. The area of the mean UHI intensity higher than 2°C is far larger in the non-heating than in the heating season.
- The statistical estimation of the spatial distribution of mean UHI intensity by the aid of surface parameters indicates that:
  (i) On the basis of the statistical analysis there is a strong linear relationship between the mean UHI intensity and the studied urban parameters, such as sky view factor, building height, built-up ratio, water surface ratio, and their areal extensions in both seasons.
  (ii) Generally, our model described the spatial distribution of the real UHI intensity field in the area of the study rather correctly, because the areas characterized by the differences lower than 0.2°C cover the larger parts of the city (75%). Nevertheless, there are small differences between the predicted and measured UHI fields, which are caused by some possible errors in the temperature samplings, the low number of studied parameters, and the considerable irregularities of the surface geometry.
  (iii) This procedure, used to predict the UHI intensity, may be applicable for other cities of different size and even non-concentric shape, but for the true validation it is necessary to have complete databases of measured intensities for those cities.
- The profile of mean UHI and its seasonal variation along a cross-section indicates that:
  (i) The seasonal profiles follow remarkably well the general cross-section of the typical UHI.

(ii) The role of cloudiness and wind speed on the seasonal variation of the UHI is clearly recognized throughout the one-year period.

(iii) The usefulness of the normalized values in the investigaton of the cross-section temperature distribution has been proved. It came to light, that the shape of the seasonal mean UHI profile is independent of the seasonal weather conditions, and it is determined mainly by the surface factors.

- Consequently, our preliminary results prove that the statistical approach on estimation of the UHI intensity in Szeged is promising. We are planning to extend this project by modeling urban thermal patterns as they are affected by weather conditions with a time lag. We intend to employ the same parameters used in this study, as well as additional urban and meteorological parameters, to predict the magnitude and spatial distribution of the UHI intensity on the days characterized by any kind of weather conditions (apart from precipitation), at any time of the year, without having recourse to extra mobile measurements. Although, adding meteorological predictors increase the complexity of the model, it may give us a useful tool for the prediction of the temperature field for several hours in advance.

Acknowledgements—The authors wish to give special thanks to *P. Purnhauser, E. Robotka,* and *Z. Zboray* who took part in the measurement campaigns and data pre-processing, and to the reviewers for their helpful suggestions. This research was supported by the grant of the Hungarian Scientific Research Fund (OTKA T/034161). The work of the first author was also supported by the Széchenyi István Grant of the Ministry of Education.

References

Bärring, L., Mattsson, J.O., and *Lindqvist, S.*, 1985: Canyon geometry, street temperatures and urban heat island in Malmö, Sweden. *Int. J. Climatol. 5*, 433-444.

Chow, S.D., Zheng, J., and *Wu, L.*, 1994: Solar radiation and surface temperature in Shangai City and their relation to urban heat island intensity. *Atmos. Environ. 28*, 2119-2127.

Conrads, L.A. and *van der Hage, J.C.H.*, 1971: A new method of air-temperature measurement in urban climatological studies. *Atmos. Environ. 5*, 629-635.

Eliasson, I., 1996: Urban nocturnal temperatures, street geometry and land use. *Atmos. Environ. 30*, 379-392.

Gallo, K.P. and *Owen, T.W.*, 1999: Satellite-based adjusments for the urban heat island temperature bias. *J. Appl. Meteorol. 38*, 806-813.

Golany, G.S., 1996: Urban design morphology and thermal performance. *Atmos. Environ. 30*, 455-465.

Goldreich, Y., 1992: Urban climate studies in Johannesburg, a sub-tropical city located on a ridge – A review. *Atmos. Environ. 26B*, 407-420.

Grimmond, C.S.B. and *Oke, T.R.*, 1991: An evapotranspiration-interception model for urban areas. *Water Resour. Res. 27*, 1739-1755.

Grimmond, C.S.B., Cleugh, H.A., and *Oke, T.R.*, 1991: An objective urban heat storage model and its comparison with other schemes. *Atmos. Environ. 25B*, 311-326.

Grimmond, C.S.B., Potter, S.K., Zutter, H.N., and *Souch, C.*, 2001: Rapid methods of estimate sky-view factors applied to urban areas. *Int. J. Climatol. 21*, 903-913.

Johnson, D.B., 1985: Urban modification of diurnal temperature cycles in Birmingham. *J. Climatol. 5*, 221-225.

Johnson, G.T., Oke, T.R., Lyons, T.J., Steyn, D.G., Watson, I.D., and *Voogt, J.A.*, 1991: Simulation of surface urban heat islands under 'ideal' conditions at night, I: Theory and tests against field data. *Bound.-Lay. Meteorol. 56*, 275-294.

Klysik, K. and *Fortuniak, K.*, 1999: Temporal and spatial characteristics of the urban heat island of Lódz, Poland. *Atmos. Environ. 33*, 3885-3895.

Kuttler, W., Barlag, A.-B., and *Roßmann, F.*, 1996: Study of the thermal structure of a town in a narrow valley. *Atmos. Environ. 30*, 365-378.

Landsberg, H.E., 1981: *The Urban Climate*. Academic Press, New York.

Matzarakis, A., Beckröge, W., and *Mayer, H.*, 1998: Future perspectives in applied urban climatology. *Proceed. The Second Japanese-German Meeting*. RCUSS, Kobe University, 109-122.

Miller, A.J., 2002: *Subset Selection in Regression*. Chapman&Hall/CRC, Boca Raton.

Moreno-Garcia, M.C., 1994: Intensity and form of the urban heat island in Barcelona. *Int. J. Climatol. 14*, 705-710.

Morris, C.J.G., Simmonds, I., and *Plummer, N.*, 2001: Quantification of the influences of wind and cloud on the nocturnal urban heat island of a large city. *J. Appl. Meteorol. 40*, 169-182.

Myrup, L.O., McGinn, C.E., and *Flocchini, R.G.*, 1993: An analysis of microclimatic variation in a suburban environment. *Atmos. Environ. 27B*, 129-156.

Nkemdirim, L.C., 1978: Variability of temperature fields in Calgary, Alberta. *Atmos. Environ. 12*, 809-822.

Nkemdirim, L.C., 1980: A test of lapse rate/wind speed model for estimating heat island magnitude in an urban airshed. *J. Appl. Meteorol. 19*, 748-756.

Oke, T.R., 1973: City size and the urban heat island. *Atmos. Environ. 7*, 769-779.

Oke, T.R., 1976: The distinction between canopy and boundary layer urban heat islands. *Atmosphere 14*, 268-277.

Oke, T.R., 1981: Canyon geometry and the nocturnal urban heat island: comparison of scale model and field observations. *J. Climatol. 1*, 237-254.

Oke, T.R., 1987: *Boundary Layer Climates*. Routledge. London and New York, 405 pp.

Oke, T.R., 1988: Street design and urban canopy layer climate. *Energ. Buildings 11*, 103-113.

Oke, T.R. and *Fuggle, R.F.*, 1972: Comparison of urban/rural counter and net radiation at night. *Bound.-Lay. Meteorol. 2*, 290-308.

Oke, T.R. and *Maxwell, G.B.*, 1975: Urban heat island dinamics in Montreal and Vancouver. *Atmos. Environ. 9*, 191-200.

Outcalt, S.I., 1972: A synthetic analysis of seasonal influences in the effects of land use on the urban thermal regime. *Arch. Meteor. Geophy. B 20*, 253-260.

Park, H.-S., 1986: Features of the heat island in Seoul and its surrounding cities. *Atmos. Environ. 20*, 1859-1866.

Park, H.-S., 1987: Variations in the urban heat island intensity affected by geographical environments. *Environmental Research Center Papers 11*. The University of Tsukuba, Ibaraki, Japan, 79 pp.

Ruffieux, D., 1995: Winter surface energy budget in Denver, Colorado. *Atmos. Environ. 29*, 1579-1587.

Sundborg, A., 1950: Local climatological studies of the temperature conditions in an urban area. *Tellus 2*, 222-232.

Tapper, P.D., Tyson, P.D., Owens, I.F., and *Hastie, W.J.*, 1981: Modeling the winter urban heat island over Christchurch. *J. Appl. Meteorol. 20*, 365-367.

Unger, J., 1996: Heat island intensity with different meteorological conditions in a medium-sized town: Szeged, Hungary. *Theor. Appl. Climatol. 54*, 147-151.

Unger, J., 1999: Urban-rural air humidity diferences in Szeged, Hungary. *Int. J. Climatol. 19*, 1509-1515.

Unger, J., Bottyán, Z., Sümeghy, Z., and *Gulyás, A.*, 2000: Urban heat island development affected by urban surface factors. *Időjárás 104*, 253-268.

Unger, J., Sümeghy, Z., and *Zoboki, J.*, 2001: Temperature cross-section features in an urban area. *Atmos. Res. 58*, 117-127.

Voogt, J.A. and *Oke, T.R.*, 1991: Validation of an urban canyon radiation model for nocturnal long-wave radiative fluxes. *Bound.-Lay. Meteorol. 54*, 347-361.

Voogt, J.A. and *Oke, T.R.*, 1997: Complete urban surface temperatures. *J. Appl. Meteorol. 36*, 1117-1132.

Voogt, J.A. and *Grimmond, C.S.B.*, 2000: Modeling surface sensible heat flux using surface radiative temperatures in a simple urban area. *J. Appl. Meteorol. 39*, 1679–1699.

Yagüe, C., Zurita, E., and *Martinez, A.*, 1991: Statistical analysis of the Madrid urban heat island. *Atmos. Environ. 25B*, 327-332.

Yamashita, S., 1996: Detailed structure of heat island phenomena from moving observations from electric tram-cars in metropolitan Tokyo. *Atmos. Environ. 30*, 429-435.

Yamashita, S., Sekine, K., Shoda, M., Yamashita, K., and *Hara, Y.*, 1986: On the relationships between heat island and sky view factor in the cities of Tama River Basin, Japan. *Atmos. Environ. 20*, 681-686.

IDŐJÁRÁS

Quarterly Journal of the Hungarian Meteorological Service
Vol. 108, No. 3, July–September 2004, pp. 195–208

Radiation maps of Hungary

Anikó Rimóczi-Paál

Hungarian Meteorological Service
P.O. Box 39, H-1675 Budapest, Hungary

(Manuscript received June 18, 2003; in final form August 4, 2003)

Abstract—The meteorologist always considered the mapping of solar energy reaching the surface as main object to supply useful information for engineers and scientists working in the agriculture, designing buildings, and other spheres of the economy, where the solar energy plays an important role. In Hungary, the first radiation maps were already constructed in the time of the publication of the first radiation maps in the world. First, in the present paper, traditional radiation maps of Hungary are reviewed.

Meteorological satellite data represent proper input information for estimating surface radiation balance at high spatial resolution. In this study a method of mapping the radiation balance components, i.e., global radiation, downward longwave radiation, shortwave and longwave radiation balance, and net radiation of the surface, is presented and illustrated for the territory of Hungary (93,000 km^2). The radiation balance components were calculated by a relatively simple model developed at the Satellite Research Laboratory of the Hungarian Meteorological Service. Digital images from the METEOSAT satellite and radiosonde observations for the period of 1992–1996 were used for this purpose. The methodology was validated for all components by using 10×10 km^2 area around the BSRN (Baseline Surface Radiation Network) station at Budapest-Lőrinc. Stratified sampling, according to a macrosynoptic classification, is applied before processing the monthly radiation maps to make the 5-year satellite samples more representative for the 1961–1990 climate period. For example, maps of global radiation in July and net radiation in January are shown.

Key-words: radiation map, global radiation, net radiation, satellite data, solar energy.

1. Introduction

The first radiation maps of Hungary (*Dobosi* and *Takács*, 1959) were already constructed simultaneously with the publication of the first radiation maps in developed countries. From the measurements of the Robitzsch and later of the thermo-electrical instruments new and new radiation maps were derived in

Hungary. The traditional radiation network did not make possible to derive radiation maps with a good spatial resolution. Meteorological satellites have given a new opportunity for estimation of much more detailed radiation maps than those constructed by using only traditional surface radiation measurements, not always having long-term spatial representativity and backward quality assurance. Different methods were elaborated in the world to determine radiation maps from satellite data. Hence, a relatively simple model has been developed at Satellite Research Laboratory of the Hungarian Meteorological Service to derive components of the radiation budget with a spatial resolution of 10×10 km^2 using data of METEOSAT satellite, empirical formulae, and a radiative transfer model.

2. Traditional radiation maps of Hungary

First map of incoming solar radiation – the global radiation – for region of Hungary and for the period 1901–1950 was derived by *Dobosi* and *Takács* (1959). They calculated the global radiation by using different modified Ångström formulae for 14 regions of Hungary from sunshine duration of 45 stations. The Ångström formulae were determined from the measurements of the International Geophysical Year (1957). Spatial distribution of the global radiation in July obtained by them is shown in *Fig. 1*.

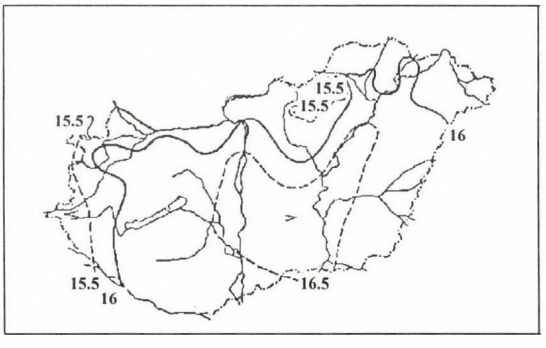

Fig. 1. Global radiation in July for the period 1901–1950 (kcal cm^{-2}) (after *Dobosi* and *Takács*, 1959).

Continuous recording of the solar irradiation of the horizontal plane began in 1936 using bimetallic pyranographs. Since that time as many as 38 radiation stations have been established in Hungary, most of them in the International

Geophysical Year (1957). Of these stations only 15 Robitzsch instruments recorded the global radiation in Hungary for at least 15 years. *Takács* (1974) published the first map of spatial distribution of the global radiation on the basis of direct radiation measurements in Hungary.

From the measurements of Robitzsch instruments the Radiation Division of the Hungarian Meteorological Service published the first measured climatological dataset of the solar radiation edited by *Major* (1976). The global radiation maps were constructed from the measurements of 13 Robitzsch instruments and by empirical formulae from the sunshine duration of maximum 33 stations. The net radiation was calculated by empirical formulae from the global radiation. To illustrate these calculations *Fig. 2* shows the spatial distribution of global radiation in July, while in *Fig. 3* spatial distribution of net radiation in January can be seen.

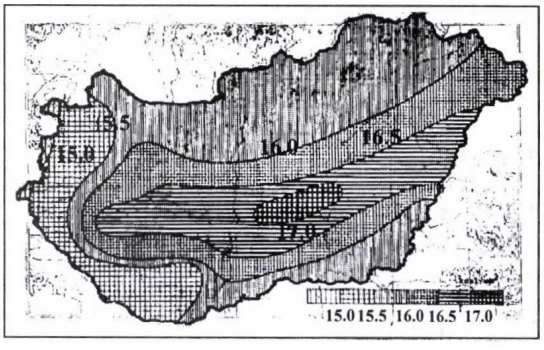

Fig. 2. Global radiation in July for the period 1958–1972 (kcal cm^{-2}) (after *Major*, 1976).

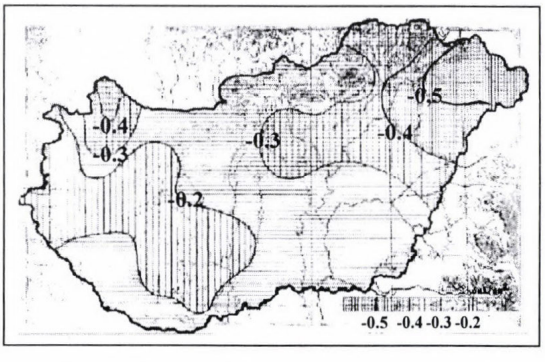

Fig. 3. Net radiation in January for the period 1958–1972 (kcal cm^{-2}) (after *Major*, 1976).

Later the Robitzsch instruments were changed to modern thermoelectric pyranometers, and 6 stations measured continuously the global radiation and one station (Budapest-Lőrinc) registered all components of the radiation balance. *Major* and *Takács* (1985) constructed 25-year global radiation maps using measurements in the period 1958–1982. *Dávid et al.* (1990) published the 30-year (1951–1980) maps of global radiation, surface albedo, short-wave radiation balance, and net radiation. These radiation maps have had the best spatial resolution before maps derived using satellite information. The region of Hungary was separated into 44 polygons providing spatial resolution approximately 80 × 80 km^2. Every polygon contained one or more stations measuring either global radiation or sunshine duration. The global radiation maps were calculated partly from surface measurements and partly from sunshine duration by using empirical formulae. Ångström formulae improved by *Dobosi* and *Takács* (1959) were also applied for the estimation of the global radiation from the sunshine duration. Maps of short-wave radiation balance and net radiation were derived from the global radiation using empirical formulae. Maps of the long-wave components of radiation balance could not be constructed because of absence of measurements. In *Fig. 4* spatial distribution of the global radiation in July, while in *Fig. 5* that of the net radiation in January can be seen after *Dávid et al.* (1990).

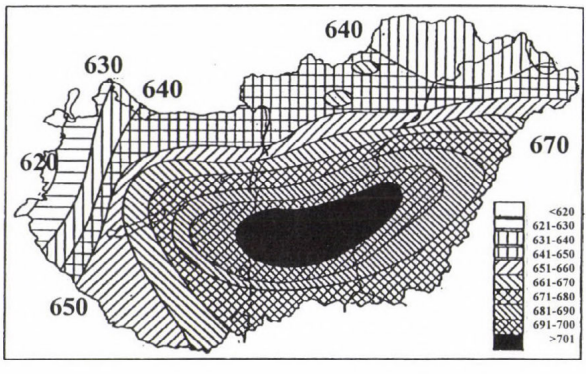

Fig. 4. Global radiation in July for the period 1951–1980 (MJ m^{-2}) (after *Dávid et al.*, 1990).

Since 1994, 13 automatic meteorological stations have been measuring the global radiation in Hungary, but only one station (Budapest-Lőrinc) measures all components of the radiation balance. Satellite Research Laboratory of the Hungarian Meteorological Service has received and archived data of METEOSAT and NOAA satellites since 1992. The new information gave good

opportunity to map both short-wave and long-wave components of the radiation balance with a very good spatial resolution.

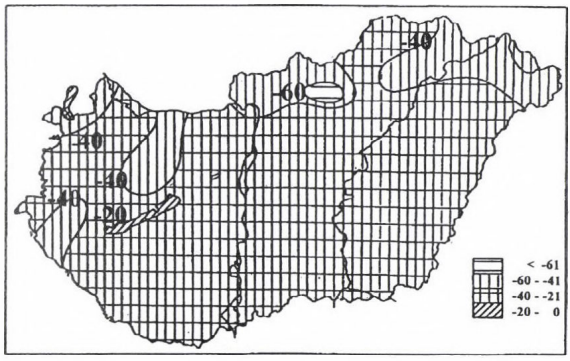

Fig. 5. Net radiation in January for the period 1951–1980 (MJ m^{-2}) (after *Dávid et al.*, 1990).

3. Methodology

Schmetz (1989), *Sellers et al.* (1990), and *Eymard* and *Taconet* (1995) reviewed a large number of methods using satellite data developed in the last 30 years to estimate surface radiation budget components. The algorithms can be classified as empirical and physical methods, and into a combined use of satellite data and numerical weather forecast models (*Brisson et al.*, 1994). The empirical methods are based on regression between co-located simultaneous satellite radiances and measured insolation at surface (*Fritz* and *Rao*, 1967; *Tarpley*, 1979; *Klink* and *Dollhoph*, 1986).

Since the early '80s, physical methods have been developed (*Gautier et al.*, 1980; *Möser* and *Raschke*, 1984). These methods use radiances measured by instruments onboard satellites and related fluxes considering optical cloud properties, obtained by radiative transfer calculations. At present, surface flux components can be described by more complex methods, like the one by *Laszlo* and *Pinker* (1993).

Concerning the longwave (LW) component of the radiation budget, no simple relations like in the shortwave part are possible. Nevertheless, these methods are sensitive to the individual cloud types, their height and optical thickness, and temperature and humidity profiles in the atmosphere. All these methods are based on physical assumptions and have been applied to different data sets, like TOVS (*Gupta*, 1989), METEOSAT data combined with

meteorological measurements (*Schmetz*, 1984), or METEOSAT and ERBE data (*Stuhlmann*, 1993).

Three satellite-based radiation budget dataset are available on world wide web (*Bess et al.*, 2000). The dataset for ERBE is a 5-year monthly average time series from February 1985 through December 1989. The SRB dataset from July 1983 through June 1991 includes surface downward shortwave fluxes, surface downward longwave fluxes, surface albedos, and cloud coverage.

A relatively simple method to determine radiation budget components at the surface was developed at the Satellite Research Laboratory of the Hungarian Meteorological Service. Visible digital images of METEOSAT 4 or 5 satellite received in the morning hours (8 or 9 UTC), around noon (11 or 12 UTC), and in the afternoon (14 or 15 UTC) at the Hungarian Meteorological Service were used to characterize the daytime cloudiness, and the night-time cloudiness was taken from infrared images received at 21, 24, and 03 UTC. The region of Hungary has been covered by a grid (53 × 35 grid points), and pixels of 10 × 10 km^2 areas have been averaged for computation of the radiation balance components.

Methodology of radiation computations has already been described elsewhere (*Rimóczi-Paál et al.*, 1997a,b, 1999), here we give just a brief introduction and also a remark on the only step which differs from the steps previously applied in the process.

The radiation balance at the surface was calculated as

$$RB = G\,(1 - RS) + (LD - LU), \tag{1}$$

where *RB* is the radiation balance of the surface; *G* is the global radiation, *RS* is the surface albedo; *LD* is the longwave radiation reaching the surface; *LU* is the longwave radiation emitted by the surface.

The global radiation was calculated by a revised empirical equation from the relative brightness:

$$G = G_0 - 3.4 - 8.15\,B, \tag{2}$$

where *G* (%) is the global radiation given in percents of the solar radiation at the top of the atmosphere, G_0 is the clear sky global radiation. The definition of the relative brightness, *B*, is published in *Rimóczi-Paál* (1985). The clear-sky global radiation and longwave radiation reaching the surface were calculated by the radiative transfer model adapted from Main Geophysical Observatory of St. Petersburg (*Karol* and *Frolkis*, 1984; *Práger* and *Kovács*, 1988). Temperature and humidity profiles are taken from radiosonde observations

of 8 nearby radiosonde stations, by inverse quadratic distance interpolation for the 53 × 35 grid points. The emission of the surface could be estimated using the Stefan-Boltzmann law. Monthly surface albedo was taken from *Dávid et al.* (1990).

Effect of the clouds on the longwave radiation was approximated by a modified multi-layer parameterization. Vertical air humidity profiles are investigated to identify break-points. If there is one single break-point, then longwave estimations consider one cloud-layer at that level. We have assumed that the cloudiness of this layer produces the relative brightness of the corresponding pixel. If there is more than one breakpoint of the humidity profile, cloudiness is evenly distributed between the 2 or 3 most significant break-points.

First, the observations from each month of the 1992–1996 period are averaged for each selected hours, and these more regularly varying values are, then, numerically integrated over the whole month. In this manner, mean daily components of the radiation balance are determined for each month. Multiplicating these values by the number of days in a month, we have the monthly sum of the calculated radiation balance components.

Our purpose is to derive climatically representative radiation maps, obtained from a larger number of years (e.g., 30). In satellite meteorology only a very few series can even approximate this period. Hence, stratified sampling considering the frequency of macrosynoptic types defined for the study area is applied (*Mika et al.*, 1994). Skill of stratification depends on the selected weather categories, therefore, instead of the original macrosynoptic types by *Péczely* (1957), which defined 13 classes from the sea-level pressure patterns in Central Europe, later a set of new weather types was derived from the macrotypes with respect to their cloudiness (C) and temperature (T) conditions (*Rimóczi-Paál et al.*, 1997b). In this modified version, each macrotype had been selected into one of the 3 × 3 weather types, defined according to their negative, average, or positive long-term mean conditional anomalies considered in areal average for Hungary.

The climatically representative mean M^* has been calculated by Eq. (3):

$$M^* = \sum_{i=1}^{K} M_i(x) p(i), \tag{3}$$

where M^* is the climatically representative mean, $M_i(x)$ is the conditional mean value in the sample, for macrotype i (not perfectly equal to m_i, not known in general), the a priori probabilities (i.e., climatically determined relative frequencies) of these macrotypes are p_i ($i=1,\ldots,K$).

4. Verification

For testing our computations, satellite derived radiation balance terms of the corresponding 10 × 10 km^2 area were compared to the observed 10-minute averages at the BSRN station Budapest-Lőrinc. This BSRN station has been measuring the components of the radiation balance continuously with the same instrument since 1994. Thus, the verification has been carried out for the period 1994–1996. Results of this comparison are presented in *Tables 1* and *2*.

This investigation shows that correlations between traditional measurements and satellite-based estimations are generally fairly good. Characteristic values of the correlation coefficient are 0.6–0.9 as demonstrated in *Tables 1* and *2*. The correlation is generally higher in the cloudless situations, but this behavior is not clearly reflected in the annual cycles. Sample size is 94–1052 in case of global radiation and 510–1509 for the net radiation.

Mean systematic differences (biases) are almost always positive – that is the estimated values are higher than the measured ones – in all components of the radiation balance (including also those which are not displayed in *Tables 1* and *2*). Characteristic values of the bias are 10–20 J cm^{-2} for the global radiation demonstrated in *Table 1*. In case of high cloud coverage, defined by relative brightness values between 6 and 10, there is a strong under-estimation of the global radiation. In the case of net radiation, this bias is comparable to the observed averages.

Table 1. Results of the verification of the global radiation of point-wise surface observations at the Budapest-Lőrinc BSRN station and the corresponding METEOSAT-based 10 × 10 km^2 estimations (1994–1996). Seasonal subsamples and those according to the cloud amount (relative brightness) are presented. N – number of observations; Mean – observed average at the station (J cm^{-2}); SD – standard deviation (J cm^{-2}); Bias – average difference (J cm^{-2}); RMS – root mean square error (J cm^{-2}); Corr – correlation

	Global radiation					
	N	**Mean**	**SD**	**Bias**	**RMS**	**Corr**
			Cloud categories			
0–2	1052	183.3	87.7	14.9	45.5	0.87
2–4	312	117.2	81.0	17.5	60.2	0.70
4–6	179	98.1	70.5	2.1	57.1	0.58
6–10	94	82.9	67.5	-28.9	61.6	0.60
			Seasons			
Winter	237	80.5	49.3	7.1	28.9	0.85
Spring	541	158.4	88.2	11.4	50.3	0.83
Summer	660	199.8	86.4	10.8	22.7	0.75
Autumn	199	91.2	56.4	19.3	44.0	0.72
			Whole sample			
All	1637	155.6	91.8	11.5	51.0	0.84

Table 2. Results of the verification of the net radiation of point-wise surface observations at the Budapest-Lőrinc BSRN station and the corresponding METEOSAT-based 10 × 10 km^2 estimations (1994–1996). Seasonal subsamples and those according to the cloud amount (relative brightness) are presented. N – number of observations; Mean – observed average at the station (J cm^{-2}); SD – standard deviation (J cm^{-2}); Bias – average difference (J cm^{-2}); RMS – root mean square error (J cm^{-2}); Corr – correlation

	Net radiation					
	N	**Mean**	**SD**	**Bias**	**RMS**	**Corr**
Cloud categories						
0–2	1569	58.8	71.3	25.6	40.9	0.93
2–4	685	19.5	52.0	18.4	33.9	0.86
4–6	510	9.6	43.6	11.2	27.3	0.82
6–10	679	-1.9	27.0	11.2	22.1	0.73
Seasons						
Winter	564	4.6	28.1	16.8	23.2	0.82
Spring	965	40.6	65.6	22.6	37.6	0.92
Summer	1220	50.4	74.1	20.1	40.5	0.91
Autumn	694	8.9	37.9	15.0	25.8	0.87
Whole sample						
All	3443	31.8	62.7	19.2	34.6	0.82

Characteristic values of the RMS error of global radiation are between 23 and 60 J cm^{-2}. Net radiation is estimated by 22–40 J cm^{-2} RMS errors exhibiting annual cycle parallel to the mean value. Root-mean square errors for the net radiation (*Table 2*) are also comparable with the observed averages, which means that our algorithm can not be considered as the final approximation. As concerns the 5-year averages, either arithmetic or stratified, the substantial number of sample elements supporting the hourly estimations, the random error can already be just a minor part of its (unknown) real value.

Monthly totals were calculated by numerical integration for the period 1994–1996 and they were compared to measurements of BSRN station of Budapest. Both surface and satellite data were available in 33 months in this period. Using results of the validation at the calculation of the monthly total radiation matrices, the hourly values were corrected by the mean bias error for the actual month before the numerical integration, thus, significant over-estimation could not occur.

The comparison of the satellite-derived and measured monthly totals of the radiation balance components is presented in *Table 3*. Very good agreement could not be expected because of the integration approximation from the 4–8 hourly matrices per day. Inspite of this fact, it seems from *Table 3* that the Bias and RMS errors became much more lower than in the case of the hourly values. It can be concluded, that our method is suitable for the calculation of the monthly sums of the radiation balance components.

Table 3. Verification of monthly sums of the radiation budget components of point-wise surface observations at the Budapest-Lőrinc BSRN station and the corresponding METEOSAT-based 10 × 10 km^2 estimations (1994–1996). Seasonal subsamples and those according to the cloud amount (relative brightness) are presented. N – number of observations; Mean – observed average at the station (MJ m^{-2} month^{-1}); SD – standard deviation (MJ m^{-2} month^{-1}); Bias – average difference (MJ m^{-2} month^{-1}); RMS – root mean square error (MJ m^{-2} month^{-1}); Corr – correlation

Monthly amounts of the radiation budget components						
Component	**N**	**Mean**	**SD**	**Bias**	**RMS**	**Corr**
Global radiation	33	363.2	205.6	6.9	69.3	0.97
SW balance	33	279.3	166.6	12.1	58.8	0.96
Down longwave	33	786.0	161.8	20.4	66.9	0.92
LW balance	33	-149.1	77.3	-35.7	78.5	0.62
Net radiation	33	118.3	124.9	40.8	57.3	0.95

5. Results of monthly mapping

The above computations were performed for all months and radiation balance components by applying both schemes of averaging. In both cases first means of each hour were calculated, then the monthly sums were derived by numerical integration. In the case of climatically representative means, the individual hourly values were weighted by the relative frequency of the actual macro-synoptic type. There is no place and also no motivation to show all the digital maps, so we limit ourselves to the two main components, the global and net radiation. In consistency with the previous figures, maps of the global radiation in July (*Fig. 6*) and net radiation in January (*Fig. 7*) are presented in this paper. In the new National Climatic Atlas of Hungary (2001) normal average sums of the global radiation and net radiation in central months of the four seasons are published. Let us remind the reader that the resolution of the estimations is 10 × 10 km^2.

Comparing the maps prepared by the two different ways of averaging, one can establish a general similarity between the patterns in both pairs of demonstrated maps. This can be explained either by the inefficiency of the applied macrosynoptic classification or by the sufficient duration of the five years for climatic mapping. Since the macrotypes are grouped with respect to the conditional averages of cloudiness and near-surface temperature, we consider the second interpretation to be more likely. There are numerical differences between the two maps in July and January, too. Of course this is just a casual feature of the circulation anomalies in the particular period as compared to the 1961–1990 climate normal period. Among the presented pair

of maps, the net radiation patterns differ the most, as their magnitudes have the smallest absolute value, accompanied by relatively high RMS deviations, considered by the two averaging processes differently.

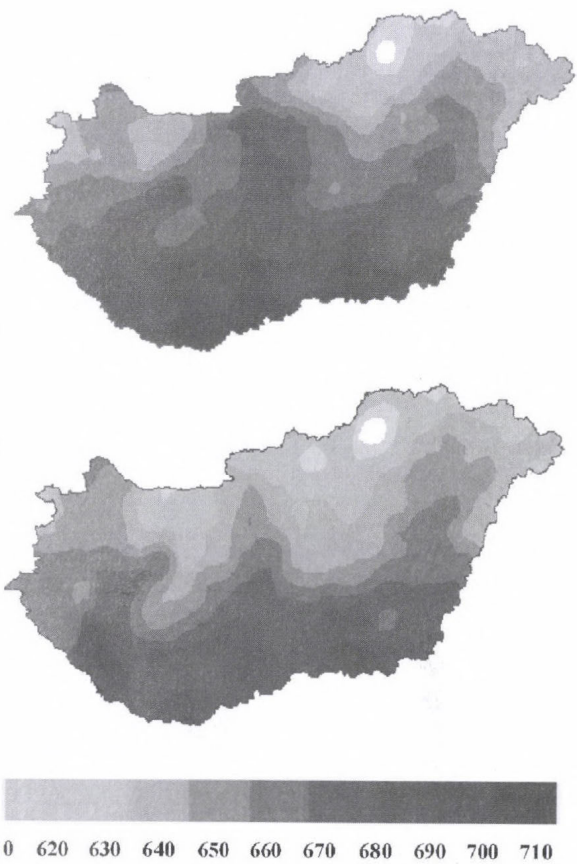

Fig. 6. Global radiation in July using METEOSAT data (MJ m^{-2}).
Top: 1992-1996. Bottom: climatically representative mean.

Comparing the new satellite-based radiation maps to the traditional maps one can establish that the "basin feature" in the global radiation does not appear as clearly in the new maps as one can be seen in the previous maps. The reason of this difference can be the circulation anomalies in the particular period. The new maps of the net radiation are much more detailed than the traditional maps.

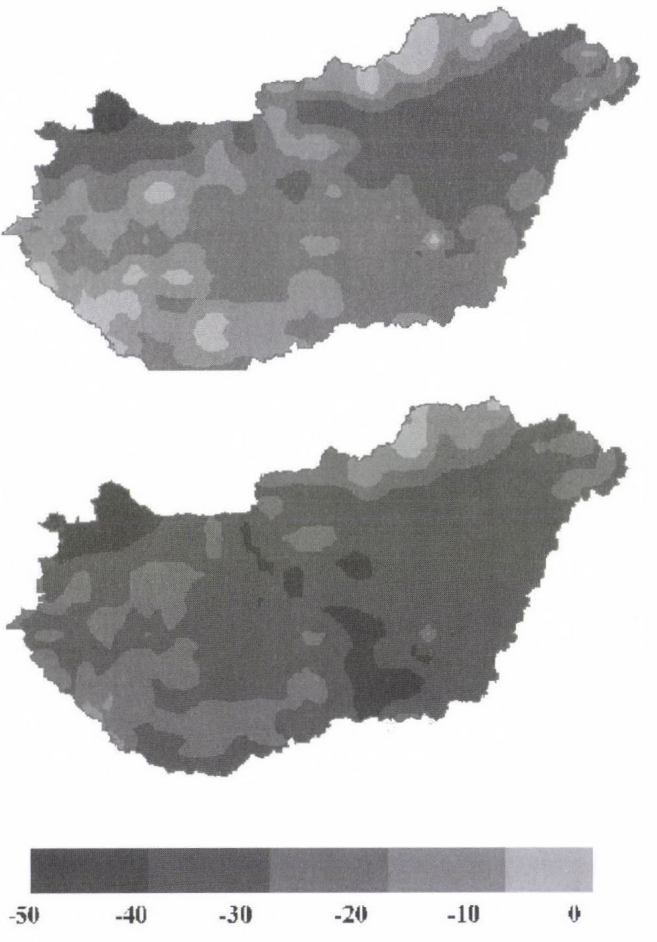

Fig. 7. Net radiation in January using METEOSAT data (MJ m^{-2}).
Top: 1992–1996. Bottom: climatically representative mean.

6. Summary

- Traditional radiation maps of Hungary are summarized.
- Our method to determine satellite-based radiation maps is shortly reviewed.
- Results of the validation are listed.
- Spatial distribution of the global radiation in July and that of the net radiation in January are presented by using two kinds of averaging.

- The new satellite-based radiation maps are much more detailed than the previous traditional radiation maps, and the "basin feature" can not be found as significantly as in the case of the previous maps.
- New operational method has been producing eight radiation matrices every day since the beginning of 2003.

Acknowledgements—The study was supported by the National Long-Term Research Fund (OTKA-T014933 and T025543) and Hungarian Space Agency (TP 088/2001-2002). Great thanks *Dr. János Mika* for the idea and determination of the climatically representative hourly radiation matrices, and *Dr. Roger Randriamampianina* for the Fortran program for the spatial interpolation of the humidity and temperature profiles.

References

Bess, T.D., Carlson, A.B., Mackey, C., Denn, F.M., Wilber, A., and *Rithley, N.*, 2000: World wide web access to radiation dataset for environmental and climate change studies. *B. Am. Meteorol. Soc. 81*, 2645-2652.

Brisson, A., Le Borgne, P., Marsoiun, A.,and *Moreaau, T.*, 1994: Surface irradiances calculated from Meteosat sensor data during SOFIA-STEX. *Int. J. Remote Sens. 15*, 197-205.

Dávid, A., Takács, O., and *Tiringer, Cs.*, 1990: *Distribution of the Radiation Balance in Hungary in the Period of 1951-1980* (in Hungarian). Országos Meteorológiai Szolgálat Kisebb Kiadványai, No. 66., Budapest.

Dobosi, Z. and *Takács, L.*, 1959: Spatial distribution of the global radiation in Hungary (in Hungarian). *Időjárás 63*, 82-84.

Eymard, L. and *Taconet, O.*, 1995: The methods inferring surface fluxes from satellite data, and their use for atmosphere model validation. *Int. J. Remote Sens. 16*, 1907-7930.

Fritz, S. and *Rao, K.P.*, 1967: On the infrared transmission through cirrus clouds and the estimation of relative humidity from satellites. *J. Appl. Meteorol. 6*, 1088-1096.

Gautier, C., Diak, G., and *Masse, S.*, 1980: Simple physical model to estimate incident solar radiation from GOES satellite data. *J. Clim. Appl. Meteorol. 19*, 1005-1012.

Gupta, S.K, 1989: A parameterization for longwave surface radiation from Sun-synchronous satellite data. *J. Climate 2*, 302-315.

Karol, I.L. and *Frolkis, A.A.*, 1984: Energy-balance type radiative-convective model of global climate (in Russian). *Meteorology and Hydrology*, No. 8, 59-68.

Klink, J.C. and *Dollhopf, K.J.*, 1986: An evaluation of satellite-based insolation estimates for Ohio. *J. Clim. Appl. Meteorol. 25*, 1741-1751.

Laszlo, I. and *Pinker, R.T.*, 1993: Shortwave cloud-radiative forcing at the top of the atmosphere, at the surface and of the atmospheric column as determined from ISCCP C1 data. *J. Geophys. Res. 98(D2)*, 2703-2713.

Major, Gy., (ed.), 1976: *The Solar Radiation in Hungary, 1958-1972* (in Hungarian). Orsz. Meteorológiai Szolgálat Hivatalos Kiadványa. Magyarország éghajlata, No. 10, Budapest.

Major, G. and *Takács, O.*, 1985: Main characteristics of solar irradiation in Hungary. *Int. Agrophysics 1*, 67-73.

Mika, J., Szentimrey, T., Domonkos, P., Rimóczi-Paál, A., and *Károssy, C.*, 1994: Approximating climatic representativity for satellite samples of limited length. *Adv. Space Res. 14*, 125-128.

Möser, W. and *Raschke, E.*, 1984: Incident solar radiation over Europe from METEOSAT data. *J. Clim. Appl. Meteorol. 23*, 166-170.

Péczely, G., 1957: *Grosswetterlagen in Ungarn.* Kleinere Veröffentlichungen der Zentralanstalt für Meteorologie. Nr. 30, Budapest.

Práger, T. and *Kovács, E.*, 1988: Estimation of climate forcing effects of atmospheric gases and aerosols by radiative-convective model (in Hungarian). *Időjárás 92*, 153-162.

Rimóczi-Paál, A., 1985: Determination of surface global radiation using relative brightness as new parameter to characterize the cloudiness. *Adv. Space Res. 5*, No. 6., 329-333.

Rimóczi-Paál, A., Randriamampianina, R., and *Gyarmati, Gy.*, 1997a: Radiation balance investigations using METEOSAT data. In *International Radiation Symposium*. Fairbanks, Alaska, 19-24 August, 1996, 1049-1052.

Rimóczi-Paál, A., Mika, J., Szentimrey, T., Csiszár, I., Gyarmati, G., Domonkos, P., and *Károssy, C.*, 1997b: Estimation of surface radiation balance components from METEOSAT images: Five years statistics. *Adv. Space Res. 19*, 473-476.

Rimóczi-Paál, A., Kerényi, J., Mika, J., Randriamampianina, R., Dobi, I., Imecs, Z., and *Szentimrey, T.*, 1999: Mapping daily and monthly radiation components using METEOSAT data. *Adv. Space Res. 24*, 967-970.

Schmetz, J., 1984: On the parameterisation of the radiative properties of broken cloud. *Tellus 36A*, 417-432.

Schmetz, J., 1989: Towards a surface radiation climatology: Retrieval of downward irradiances from satellite. *Atmos. Res. 23*, 287-321.

Sellers, P.J., Rasool, S.I., and *Bolle, H.-J.*, 1990: A Review of Satellite Data Algorithms for Studies of the Land Surface. *B. Am. Meteorol. Soc. 71*, 1429-1447.

Stuhlmann, R., 1993: Feasibility study for calculating the cloud-generated radiative flux divergence from METEOSAT imagery data. *Technical Report*. Institut für Physik II/PC, GKSS-Forschungszentrum. Geesthacht, Germany.

Takács, O., 1974: Spatial distribution of the global radiation using measured data in Hungary (in Hungarian). *Beszámolók az 1971-ben végzett tudományos kutatásokról*. Országos Meteorológiai Szolgálat, Budapest, 251-256.

Tarpley, J., 1979: Estimating incident solar radiation at the surface from geostationary satellite data. *J. Appl. Meteorol. 18*, 1172-1181.

GUIDE FOR AUTHORS OF *IDŐJÁRÁS*

The purpose of the journal is to publish papers in any field of meteorology and atmosphere related scientific areas. These may be

- research papers on new results of scientific investigations,
- critical review articles summarizing the current state of art of a certain topic,
- short contributions dealing with a particular question.

Some issues contain "News" and "Book review", therefore, such contributions are also welcome. The papers must be in American English and should be checked by a native speaker if necessary.

Authors are requested to send their manuscripts to

Editor-in Chief of IDŐJÁRÁS
P.O. Box 39, H-1675 Budapest, Hungary

in three identical printed copies including all illustrations. Papers will then be reviewed normally by two independent referees, who remain unidentified for the author(s). The Editor-in-Chief will inform the author(s) whether or not the paper is acceptable for publication, and what modifications, if any, are necessary.

Please, follow the order given below when typing manuscripts.

Title part: should consist of the title, the name(s) of the author(s), their affiliation(s) including full postal and E-mail address(es). In case of more than one author, the corresponding author must be identified.

Abstract: should contain the purpose, the applied data and methods as well as the basic conclusion(s) of the paper.

Key-words: must be included (from 5 to 10) to help to classify the topic.

Text: has to be typed in double spacing with wide margins on one side of an A4 size white paper. Use of S.I. units are expected, and the use of negative exponent is preferred to fractional sign. Mathematical formulae are expected to be as simple as possible and numbered in parentheses at the right margin.

All publications cited in the text should be presented in a *list of references*, arranged in alphabetical order. For an article: name(s) of author(s) in Italics, year, title of article, name of journal, volume, number (the latter two in Italics) and pages. E.g., *Nathan, K.K.,* 1986: A note on the relationship between photo-synthetically active radiation and cloud amount. *Időjárás 90,* 10-13. For a book: name(s) of author(s), year, title of the book (all in Italics except the year), publisher and place of publication. E.g., *Junge, C. E.,* 1963: *Air Chemistry and Radioactivity.* Academic Press, New York and London. Reference in the text should contain the name(s) of the author(s) in Italics and year of publication. E.g., in the case of one author: *Miller* (1989); in the case of two authors: *Gamov* and *Cleveland* (1973); and if there are more than two authors: *Smith et al.* (1990). If the name of the author cannot be fitted into the text: *(Miller,* 1989); etc. When referring papers published in the same year by the same author, letters a, b, c, etc. should follow the year of publication.

Tables should be marked by Arabic numbers and printed in separate sheets with their numbers and legends given below them. Avoid too lengthy or complicated tables, or tables duplicating results given in other form in the manuscript (e.g., graphs)

Figures should also be marked with Arabic numbers and printed in black and white in camera-ready form in separate sheets with their numbers and captions given below them. Good quality laser printings are preferred.

The text should be submitted both in manuscript and in electronic form, the latter on diskette or in E-mail. Use standard 3.5" MS-DOS formatted diskette or CD for this purpose. MS Word format is preferred.

Reprints: authors receive 30 reprints free of charge. Additional reprints may be ordered at the authors' expense when sending back the proofs to the Editorial Office.

More information for authors is available: antal.e@met.hu

Information on the last issues: http://omsz.met.hu/irodalom/firat_ido/ido_hu.html

Published by the Hungarian Meteorological Service

Budapest, Hungary

INDEX: 26 361

HU ISSN 0324-6329

IDŐJÁRÁS

QUARTERLY JOURNAL
OF THE HUNGARIAN METEOROLOGICAL SERVICE

CONTENTS

****

http://omsz.met.hu/english/ref/jurido/jurido_en.html

VOL. 108 * NO. 4 * OCTOBER – DECEMBER 2004

IDŐJÁRÁS

Quarterly Journal of the Hungarian Meteorological Service

Editorial Office: P.O. Box 39, H-1675 Budapest, Hungary or
Gilice tér 39, H-1181 Budapest, Hungary
E-mail: bozo.l@met.hu or *antal.e@met.hu*
Fax: (36-1) 346-4809

Subscription by

mail: IDŐJÁRÁS, P.O. Box 39, H-1675 Budapest, Hungary;
E-mail: bozo.l@met.hu or *antal.e@met.hu*; *Fax: (36-1) 346-4809*

IDŐJÁRÁS

Quarterly Journal of the Hungarian Meteorological Service
Vol. 108, No. 4, October–December 2004, pp. 209–251

The greenhouse effect and the spectral decomposition of the clear-sky terrestrial radiation

Ferenc M. Miskolczi[*1] and **Martin G. Mlynczak**[2]

[1]*Analytical Services & Materials Inc.,*
One Enterprise Parkway, Suite 300 Hampton, VA 23666, U.S.A.
E-mail: f.m.miskolczi@larc.nasa.gov

[2]*NASA Langley Research Center, Mail Stop 420, Hampton, VA 23681-2199, U.S.A.*
E-mail: m.g.mlynczak@larc.nasa.gov

(Manuscript received March 8, 2004; in final form November 1, 2004)

Abstract—In this paper the clear-sky infrared radiation field of the Earth-atmosphere system is characterized by the spectral decomposition of the simulated upward and downward flux density components into three distinct wave number regions. The relative contributions of the far infrared, middle infrared, and windows spectral regions to the total longwave flux densities have been established. The approximate qualitative description of the meridional distributions of the zonal averages gave us a detailed insight into the role of the less explored far infrared spectral region. We demonstrate that on a global scale, the far infrared contribution to the clear-sky normalized greenhouse factor is significantly increasing toward the polar regions. Accurate computation of the transmitted and re-emitted part of the outgoing longwave radiation showed that in the far infrared the normalized upward atmospheric emittance increases poleward. This phenomenon is the direct consequence of the downward shift of the peak of the weighting functions in the strongly absorbing opaque spectral regions. The clear-sky total longwave terrestrial flux transmittance seems to be well correlated with the far infrared flux transmittance, which implies the possibility of inferring total longwave flux densities solely from far infrared observations. The zonal averages of the total normalized atmospheric upward emittances are almost independent of the water vapor column amount, they have no meridional variation, and they are constantly about fifty percent of the surface upward flux density, an indication, that the gray atmosphere in the IR is in radiative equilibrium. The meridional distribution of the greenhouse temperature change and its dependence on the atmospheric water vapor content were also evaluated. Solving the Schwarzschild-Milne equations for the bounded atmosphere the infrared atmospheric transfer and greenhouse functions were derived. The theoretically predicted greenhouse effect in the clear atmosphere are in perfect agreement with simulation results and measurements.

Key-words: greenhouse effect, radiative equilibrium, far infrared.

* Corresponding author

1. Introduction

Terrestrial radiation or outgoing longwave radiation (*OLR*) are terms which refer to the emitted infrared (IR) radiation field of the Earth-atmosphere system. An accurate knowledge of the spatial and temporal distribution of this radiation field is fundamental in climate research. When long-term radiative equilibrium between the solar and terrestrial radiation exists monitoring the *OLR* one can identify the changes in the shortwave net input into the Earth-atmosphere system. From the satellite observation of the Earth's radiation budget (*ERBE*, 2004) we estimated that the five years average effective planetary temperature is about 253.8 K. When using the observed albedo and a solar constant of 1365 W m^{-2}, this results in an effective temperature of 253.0 K. Despite the fact that the average net radiation is off by about 5 W m^{-2}, these results support the idea of the long-term radiative equilibrium.

The knowledge of the spectral characteristic of the *OLR* is equally important. Keeping the *OLR* constant, climate change might occur by changing the concentration of the greenhouse gases. Any change in the longwave atmospheric transparency will alter the contribution of the different spectral intervals to the *OLR*. For example, increased spectral *OLR* in the window regions coupled with constant total *OLR* and surface emissivity will point to an amplified greenhouse effect due to increased greenhouse gas concentration.

In principle, the classification of the spectral intervals of the terrestrial radiation must be based on observations of the spectral characteristics of the *OLR* or the downward atmospheric emittance (E_D). So far the spectral boundaries of the far infrared (FIR), middle infrared (MIR), and windows (WIN) spectral regions are not exactly defined and there is no convention accepted by the scientific community regarding these boundaries. This is primarily because in the highly variable atmosphere, the exact wavelength of the complete absorption is changing. Sometimes, due to technical or engineering constraints, the spectral sensitivity of a detector or instrument design sets the spectral boundaries. However, focusing on the spectral aspects of the Earth's radiation budget or climate change, such definitions sooner or later will be necessary. Until then, meaningful quantitative comparisons of FIR, MIR, and WIN flux densities, cooling rates, greenhouse factors, or other spectrally resolved quantities from different authors will be difficult.

On a purely physical basis, one may set the FIR upper wave number limit before or after the CO_2 15 μ fundamental absorption band. Although the separate treatment of the 15 μ CO_2 band, (620–720 cm^{-1}), is popular in broad band spectral radiative transfer models, to emphasize that the atmosphere is mostly opaque in the 1–720 cm^{-1} spectral region, in this work we have adopted the next definitions: total: 1–3000 cm^{-1}; FIR: 1–720 cm^{-1}; WIN: 720–1260 cm^{-1}; MIR: 1260–3000 cm^{-1}.

As a reference, in *Fig. 1* the positions of the FIR, WIN, and MIR spectral regions are presented together with the spectral *OLR* which was computed with 1 cm^{-1} spectral resolution for the USST 76 atmosphere. The surface upward radiation (S_U) as the blackbody emittance of the surface is also shown. In *Table 1* the numerical values of the integrated totals and averages are displayed. The first section of the table contains the quantities obtained directly from a line-by-line (LBL) simulation. The second section of the table contains some definitions of the derived quantities, and in the third part the commonly used greenhouse parameters are summarized.

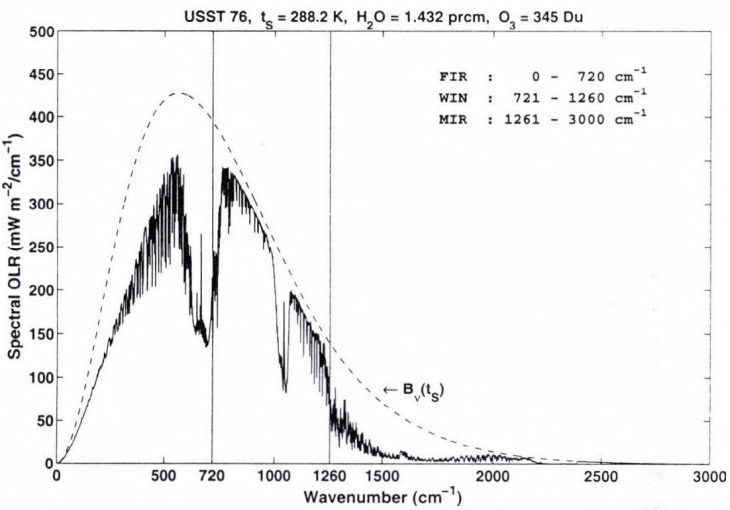

Fig. 1. Spectral *OLR* and $S_U = B_\nu(t_S)$, computed for the USST 76 atmosphere. The FIR spectral range contains the whole 15 μ CO_2 band.

In *Fig. 2* we present the basic flux density components of our simplified Earth-atmosphere radiative transfer model. As it is evident in our scheme, the shortwave atmospheric absorption and scattering together with all reflection related processes (both shortwave and longwave) are ignored.

We performed some test calculations using the tropical and subarctic winter standard atmospheres and the definitions of spectral boundaries given above. The total greenhouse forcing (G), as the difference of the S_U and *OLR* fluxes, are compared to similar results by *Brindley* and *Harries* (1997). The numerical values are summarized in *Table 2*. The large differences between the two computations are very unusual, considering, that the atmospheric profiles were fixed. The explanation is the use of different definitions for the FIR spectral limits. The dependence of the greenhouse forcing on the

wavenumber for the tropical and subarctic winter atmospheres are presented in *Fig. 3*. This figure clearly indicates the necessity of the exact definition of FIR spectral boundaries in FIR related publications. Notice the relatively large differences caused mainly by the differences in the H_2O profiles.

Table 1. Flux density components computed for the USST 76 atmosphere (W m^{-2})

	Components	Spectral intervals			
		Total	**FIR**	**MIR**	**WIN**
1	Surface upward radiation, S_U	391.2	203.1	45.9	142.2
2	Downward atmospheric emittance, E_D	290.1	199.9	42.5	47.6
3	Upward atmospheric emittance, E_U	168.9	121.2	11.3	36.3
4	Atmospheric flux transmittance, $Tr_A=1-A$	0.2162	0.0064	0.0392	0.573
5	Transmitted radiation, $S_T=S_U*Tr_A$	84.6	1.3	1.8	81.5
6	Outgoing longwave radiation, $OLR=S_T+E_U$	253.5	122.5	13.1	117.8
7	Absorbed radiation, $A_A=S_U-S_T$	306.6	201.8	44.0	60.8
8	Net atmosphere, $N_A=S_U-E_D-OLR$	-152.4	-119.3	-9.7	-23.2
9	Net surface, $N_S=E_D-S_U$	-101.1	-3.2	-3.3	-94.6
10	Terrestrial flux transmittance, $Tr_T=OLR/S_U$	0.648	0.603	0.285	0.828
11	Greenhouse factor, $G=S_U-OLR$	137.7	80.6	32.8	24.4
12	Normalized greenhouse factor, $G_N=1-Tr_T$	0.352	0.397	0.715	0.172
13	Inverse Tr_T, $I_T=1/Tr_T$	1.54	1.658	3.509	1.208

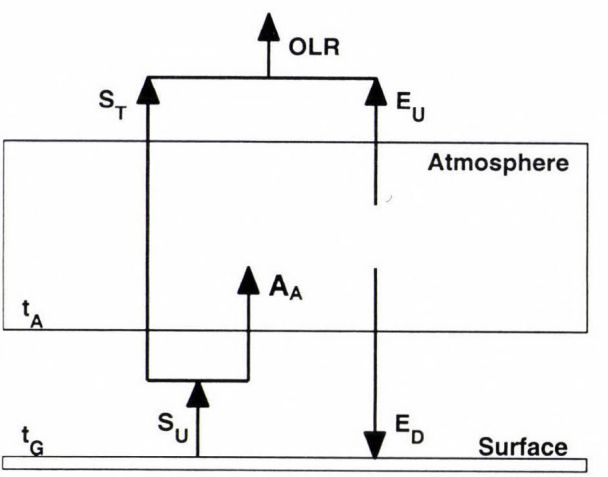

Fig. 2. IR rdiative transfer model of the atmosphere. The definitions of the flux density components are included in Table 1. t_A is the surface air temperature, t_G is the surface temperature. In the simulation t_A and t_G was set to be equal, $t_S = t_A = t_G$, where t_S is the thermal equilibrium temperature.

It has been recognized for a long time, that the far infrared part of the OLR plays an important role in the Earth radiation budget. However, due to the lack of the operational observation of the FIR spectral range, the global picture of the terrestrial radiation field is not yet complete. With our recent work we will try to fill up this gap with high accuracy LBL computations of the FIR, MIR, and WIN flux density components for a set of carefully selected atmospheric profiles from around the globe. In the next section the details of the input database and the parameters of the simulation are discussed.

Table 2. Comparisons of the FIR part of total greenhouse forcing (%)

Atmosphere	**This calculation**			***Brindley* and *Harries* (1997)**
	FIR: 1–560 cm^{-1}	**FIR: 1–660 cm^{-1}**	**FIR: 1–720 cm^{-1}**	
Tropical	36	43	54	25
Subarctic winter	43	53	68	33

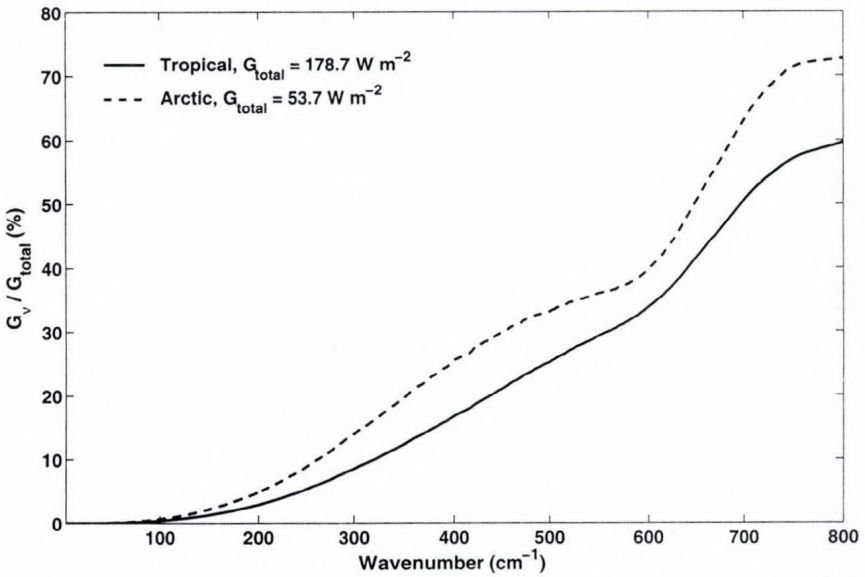

Fig. 3. The dependence of relative FIR spectral greenhouse factor on wave number. This figure demonstrates the importance of the definitions of the spectral boundaries.

2. *Global data set and LBL simulation*

Our qualitative estimates of the meridional distributions of the FIR, MIR, and WIN flux density components were based on a representative subset of the TIROS Initial Guess Retrieval (TIGR), global radiosonde archive (*Chedin* and *Scott*, 1983). From the TIGR archive, about 230 atmospheric profiles were extracted in a way that the temporal and spatial statistical characteristics of the original data set were preserved. The profiles were chosen regardless of the surface type. The surface emissivity was set to unity and the temperature of the emitting surface (t_G) was set to the temperature of the lowest atmospheric level (t_A): $t_S = t_A = t_G$, where t_S is the common temperature. The global average surface temperature and water vapor column amount (w) are 285.3 K and 2.53 precipitable cm (prcm), respectively. Further on we shall use the term "global avareage" to indicate that the average value is computed from zonal mean values weighted with the cosine of the latitude. It is usually hard to tell how representative a data set for global and annual climatology research is. We believe, that our data set contains sufficient information to characterize the contributions of different spectral ranges to the meridional distributions of the total and spectral clear-sky flux density components. Here we note, that the temperature profile set represents real equilibrium situations, where all kind of energy sources and sinks in the layered atmosphere are balanced by IR radiative cooling or heating. More details on the profile selection strategy can be found in *Miskolczi* and *Rizzi* (1998).

For the radiative transfer computations we used the High-resolution Atmospheric Radiative Transfer Code (HARTCODE), (*Miskolczi et al.*, 1990). More results on the validation of HARTCODE may be found in *Rizzi et al.* (2002) and *Kratz et al.* (2005). Here we shall not go into the full details of an LBL simulation, but summarize only a few important basic features. This work partly uses the results of a previous study performed to evaluate the temperature and water vapor sounding capabilities of the Advanced Earth Observing Satellite (ADEOS2) Global Imager (GLI) instrument, and therefore, particulars of the LBL simulations were already reported in *Miskolczi* and *Rizzi* (1998).

A large data set of directional radiances and transmittances computed for the TIGR profiles and GLI spectral range, (800–2800 cm^{-1}), with 1.0 cm^{-1} spectral resolution were already available. To obtain the total flux densities, additional radiance computations were done for the spectral ranges not covered by the GLI instrument. The directional radiances were determined in nine streams, and assuming cylindrical symmetry, a simple code was developed to facilitate the integration over the solid angle.

For the spectral range covered by the GLI instrument the GEISA (*Husson et al.*, 1994), absorption line compilation were used and for the remaining part of the spectra we used the HITRAN2K line catalog (*Rothman et al.*, 1998; *HITRAN2K*, 2002).

The atmosphere was stratified using 32 exponentially placed layers with about 100 m and 10 km layer thickness at the bottom and the top, respectively. The full altitude range was set to 61 km and the slant path was determined by spherical refractive geometry. The upward and downward slant path were identical, which assured that the directional spectral transmittances for the reverse trajectories were equal. Altogether eleven absorbing molecular species were involved: H_2O, CO_2, O_3, N_2O, CH_4, NO, SO_2, NO_2, CCl_4, F11, and F12.

The H_2O continuum absorption parameterization was similar to the CKD2.4 without the slight recent adjustments made in some part of the far infrared range (*Tobin et al.*, 1999). In the most affected spectral ranges of the CO_2 Q bands, the line-mixing effects were considered using a recent line-mixing parameterization by *Rodriguez et al.* (1999). No adjustments were implemented for the non-local thermodynamic effects and the effects of the aerosols were also ignored.

The direct output from HARTCODE were the spectral atmospheric upward emittance ($E_{\nu,U}$), downward emittance ($E_{\nu,D}$), surface upward flux density ($S_{\nu,U}$), and the atmospheric flux transmittance ($Tr_{\nu,A}$). The atmospheric spectral flux transmittance, by definition, is the ratio of the transmitted flux density ($S_{\nu,T}$) to the surface upward flux density: $Tr_{\nu,A} = 1 - A_\nu = S_{\nu,T} / S_{\nu,U}$, where A_ν is the spectral flux absorptance. The spectral outgoing longwave radiation is taken as the sum of the transmitted flux density and atmospheric upward emittance, $OLR_\nu = S_{\nu,T} + E_{\nu,U}$. The spectrally integrated and/or averaged quantities are indicated by omitting the subscript ν. The definitions of other derived quantities are given in *Fig. 2* and *Table 1*.

The ratio of the *OLR* to the surface upward flux density is sometimes called flux transmittance or total flux transmittance (Tr_T). To distinguish this quantity from the atmospheric flux transmittance, further on we shall call this quantity terrestrial flux transmittance: $Tr_T = OLR/S_U$. We use the term "total" to indicate integration over the 1–3000 cm^{-1} spectral range. In *Table 3* we present the basic statistics and global averages of the computed S_U, E_D, OLR, S_T, and G parameters.

Throughout this paper we frequently refer to figures with one or more parameterized functions. To make the reference to those parameterized functions easier, we supplied their serial number with a prefix character (#)

and included them into *Table 4*. When referencing to them only their special serial numbers are quoted.

Table 3. Basic statistics and global averages of the flux density components (W m^{-2})

Spectral regions	Parameters	S_U	E_D	*OLR*	S_T	*G*
Total	Minimum	165	103	150	22	5.9
	Maximum	521	429	297	112	223
	Mean	313	235	223	69	89
	Standard	82	82	34	13	49
	Global	382	309	250	61	132
FIR	Minimum	112	89	100	0.0	4.2
	Maximum	244	241	140	29	120
	Mean	173	166	119	7.0	54
	Standard	31	37	8.0	7.2	25
	Global	199	195	123	2.6	75
MIR	Minimum	7.4	6.6	6.0	0.7	0.4
	Maximum	79	73	21	2.8	63
	Mean	31	29	11	1.4	20
	Standard	16	16	3.0	0.3	14
	Global	45	43	14	1.3	31
WIN	Minimum	46	8.0	44	21	1.3
	Maximum	198	139	157	108	47
	Mean	109	40	93	61	16
	Standard	35	32	25	13	11
	Global	138	71	113	57	25

3. Results and discussion

3.1 Outgoing logwave radiation

One may not expect that a limited data set of 230 profiles will reproduce accurately the detailed meridional picture, especially around the highly variable ITC zone. However, it is possible to characterize the average behavior and tendency of the meridional variation by the zonal means or by a smooth curve - usually a low order polynomial or spline - fitted to the zonal means. This is clearly demonstrated in *Fig. 4,* where the simulated zonal mean *OLR* from the TIGR data set are compared to the mean clear-sky and all-sky meridional distributions obtained from the ERBE measurements.

Table 4. Parameterized functions in the Figures, (u=ln(w))

Fig.	X	Y	Curve	Function Y = f(X)	r	No.
7	u	Tr_A	Total	$\exp(-1.461 - 0.2819\,x - (1231\,x^2 + 541.9\,x^3 + 84.66\,x^4)/10^4)$	0.993	#1
			FIR	$\exp(-4.292 - 2.255\,x - 0.8324\,x^2 - 0.1781\,x^3 - 0.01521\,x^4)$	0.998	#2
			MIR	$\exp(-3.190 - 0.5659\,x + 0.02778\,x^2 + 0.01022\,x^3 - 0.0007153\,x^4)$	0.998	#3
			WIN	$\exp(-0.2249 - 0.2543\,x + 0.01545\,x^2 - 0.007840\,x^3 + 0.0007537\,x^4)$	0.994	#4
8	u	τ_A	Total	$\exp(0.3833 + 0.1908\,x + 0.05183\,x^2 + 0.01988\,x^3 + 0.002399\,x^4)$	0.992	#5
			FIR	$\exp(1.45 + 0.523\,x + (744\,x^2 - 43.1\,x^3 - 86.2\,x^4 - 19.14\,x^5 - 0.776\,x^6)/10^4)$	0.996	#6
			MIR	$\exp(1.161 + 0.1765\,x - 0.02598\,x^2 + 0.0004931\,x^3 + 0.0008610\,x^4)$	0.997	#7
	w		WIN	$0.2214 + 0.2611\,x$	0.992	#8
9	u	τ_T	Total	$\exp(-1.098 + 0.3055\,x)$	0.896	#9
			FIR	$\exp(-0.9682 + 0.3\,x)$	0.884	#10
			MIR	$\exp(-0.009824 + 0.2281\,x)$	0.834	#11
			WIN	$\exp(-1.912 + 0.3473\,x)$	0.903	#12
10	Tr_F	Tr_T		$0.09922 + 0.9043\,x$	0.997	#13
14	w	R_U	Total	$0.4961 + 0.0009681\,x$	0.028	#14
			FIR	$0.7026 - .04167\,x + 0.002596\,x^2$	0.658	#15
	u		MIR	$\exp(-1.1101 - 0.216\,x)$	0.738	#16
	w		WIN	$0.1311 + 0.1276\,x - 0.008184\,x^2$	0.975	#17
17	u	R_D	Total	$0.7371 + 0.06411\,x + 0.0156\,x^2 + 0.003123\,x^3$	0.947	#18
	w		FIR	$1 - 0.52071\exp(-3.213\,x^{0.4555})$	0.965	#19
			MIR	$1 - 0.6766\exp(-2.293\,x^{0.1656})$	0.842	#20
			WIN	$-1.518 + 1.67\exp(0.09220\,x - 0.006403\,x^2)$	0.987	#21
30	u	dt_G	Total	$22.32 + 7.921\,x + 0.86\,x^2$	0.913	#22
			FIR	$11.59 + 3.177\,x + 0.22\,x^2$	0.892	#23
			MIR	$1.163 + 0.4868\,x + 0.06251\,x^2$	0.931	#24
			WIN	$9.566 + 4.256\,x + 0.5768\,x^2$	0.917	#25
		dt_E	Total	$23.46 + 7.376\,x + 0.6058\,x^2$	0.886	#26
32	u	dt_A	Total	$17.43 - 4.552\,x - 1.178\,x^2 - 0.1971\,x^3 + 0.02624\,x^4$	0.982	#27
			FIR	$12.28 - 4.614\,x - 0.6769\,x^2 - 0.01734\,x^3 + 0.03412\,x^4$	0.994	#28
	w		MIR	$2.023 + 0.2647 - 0.1893\,x + 0.01746\,x^2$	0.727	#29
			WIN	$2.254 + 1.089 - 0.3753\,x + 0.02855\,x^2$	0.795	#30
	dt_A	t_S	Total	$302.7 - 0.08994\,x - 0.08778\,x^2$	0.869	#31

The correlation coefficient (r) is defined as: $r = (1 - \sigma^2_R / \sigma^2_Y)^{0.5}$, where σ_R is the residuum standard deviation.

The top and bottom curves in this plot were obtained by fitting a third order polynomial to the zonal averages of about 70,000 all-sky and 40,000 clear-sky annual average *OLR* measurements from the ERBS, NOAA9, and NOAA10 satellites. The markers in this figure are the TIGR OLR fluxes averaged over latitudinal belts of 5-degree widths.

The total *OLR* curve from the TIGR data set is between the clear-sky and all-sky *OLR* curves from the ERBE, and the shape of the curves are very similar.

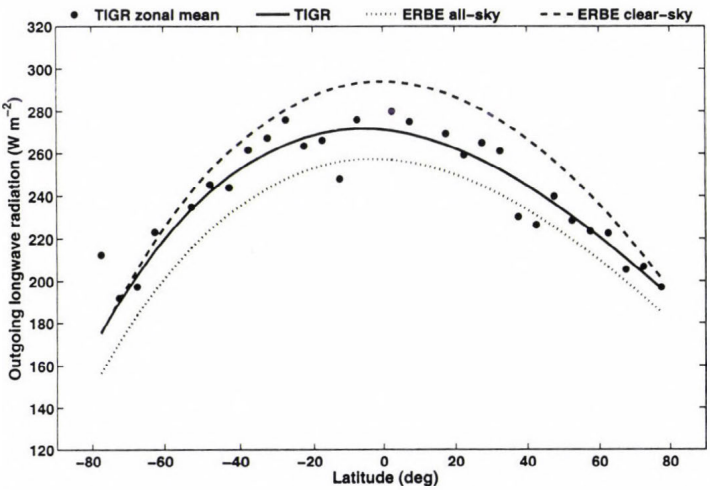

Fig. 4. Computed and measured *OLR*. The dotted and dashed curves are third order polynomials fitted to the ERBE clear-sky and ERBE all-sky zonal mean data points (ERBE, 2004).

Considering the surface temperature and emissivity settings in this simulation, this figure shows a remarkable agreement with the ERBE data set. The global averages of the *OLR*s are 250, 268, and 236 W m^{-2} for this simulation, the ERBE clear-sky and ERBE all-sky cases, respectively.

Fig. 5 shows the spectral decomposition of the *OLR*. The decreasing total *OLR* toward the poles are mainly due to the reduced upward fluxes in the WIN region. To a somewhat lesser extent, the FIR and MIR spectral regions also contribute to the poleward reduction of the total *OLR*. This is an indication of the presence of relatively small amounts of transmitted surface fluxes. Compared to the total *OLR*, the poleward variation in the FIR part is surprisingly small, not exceeding 5–7%.

The total *OLR* contains the FIR *OLR* and, therefore, theoretically there should be a strong correlation between the two quantities. According to our

data set, a linear relationship exists between the total and FIR *OLR* with a 0.88 correlation coefficient. Utilizing this relationship, we estimated the FIR component of the ERBE clear-sky *OLR*, and plotted it in *Fig. 5* as dots. In the plot, due to the large number of data points, the dots are organized into short vertical "bars". The vertical extensions of the bars indicate the variability of the ERBE FIR *OLR*s at a given latitude. The distances between the bars are 2.5 degrees, corresponding to the latitudinal resolution of the ERBE archive.

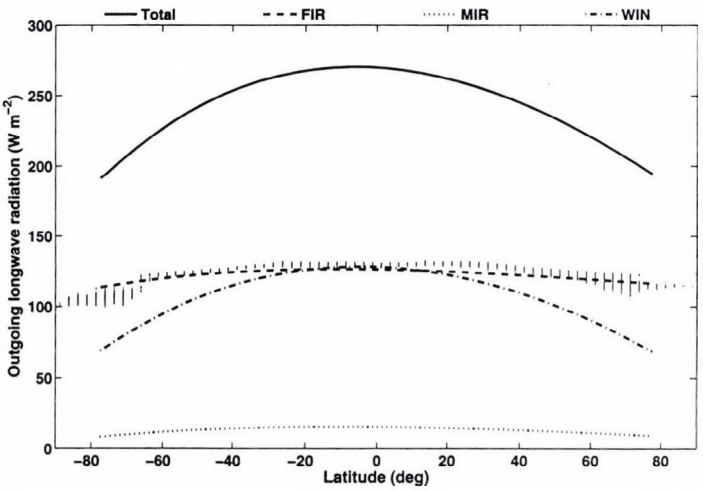

Fig. 5. Latitudinal distributions of the total and spectral components of the outgoing longwave radiation. The FIR and MIR components have very small latitudinal variation. The short vertical 'bars' are the estimated five year average ERBE FIR *OLR*.

Since it is known a-priori, that the surface and atmospheric temperatures are significantly decreasing poleward, the more or less constant meridional TIGR and ERBE FIR *OLR* must be the result of a delicate compensation mechanism. The interesting question is how the surface temperature, temperature and humidity profiles, and the atmospheric spectral transparency are linked together to produce the above phenomenon.

3.2 Flux transmittance and graybody optical thickness

The atmospheric transparency is increasing with decreasing absorber amount. In the Earth's atmosphere water vapor is the major absorber, therefore, the meridional distribution of Tr_A must obey the poleward decrease of the water vapor column amount. As it is evident from *Fig. 6*, the total, MIR, and WIN

components of Tr_A are increasing poleward, while the FIR part is effectively zero in the equatorial regions, reaching only 10% at the poles. The MIR Tr_A behaves similarly, except, it is always larger than zero because of the presence of larger transparent regions within the MIR spectral range.

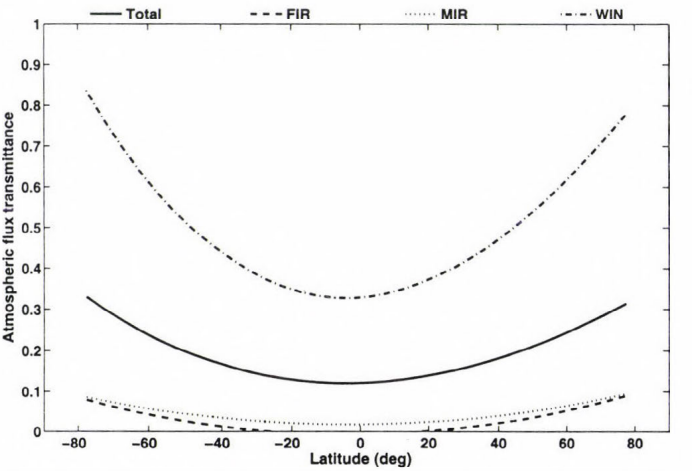

Fig. 6. Latitudinal distributions of the total and spectral components of the atmospheric flux transmittance, $Tr_A = S_T/S_U$.

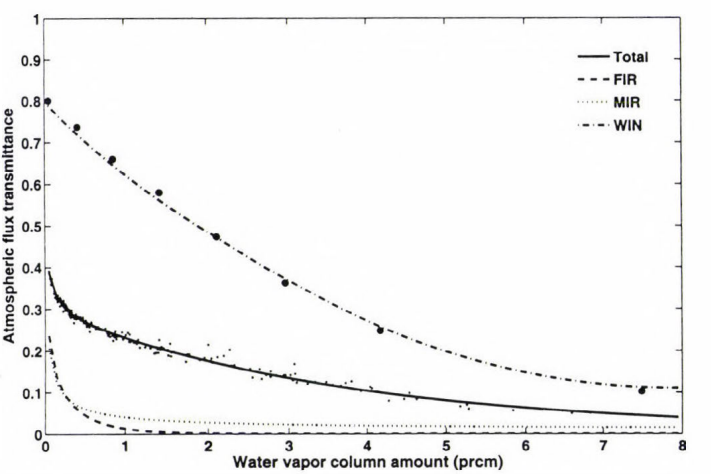

Fig. 7. Dependence of total and spectral atmospheric flux transmittance components on water vapor column amount. The large dots are the parameterized WIN Tr_A functions tested with an independent set of eight profiles.

In *Fig. 7* the total and spectral components of the Tr_A are plotted as the function of w. The small dots are for the total Tr_A. The parametrization of Tr_A with the water vapor column amount is of common interest. Eqs. #1 – #4 are the appropriate functions that reproduce Tr_A with a residuum correlation coefficient better than 0.995. The validity of Eq. #4 was tested with an independent profile set consisting of five climatological average profiles, the USST 76 atmosphere, and two extreme TIGR profiles. The computed window transmittances are marked by larger dots. Obviously, Eq. #4 is valid for the full range of w in the Earth's atmosphere.

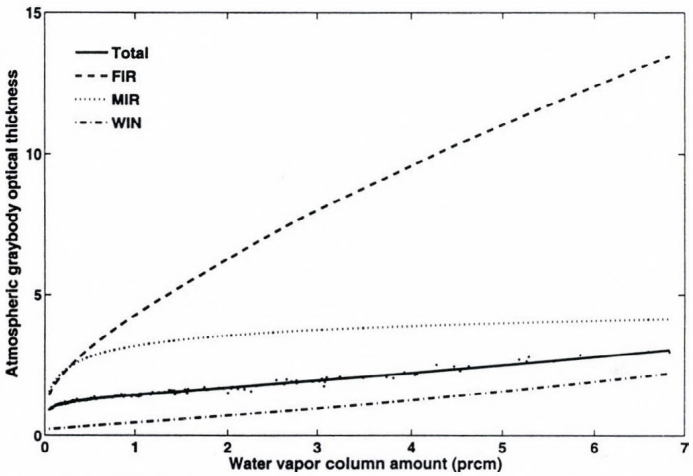

Fig. 8. Dependence of total and spectral atmospheric graybody optical thickness, $\tau_A = -\ln(S_T / S_U)$, on water vapor column amount.

By definition, the atmospheric graybody optical thickness (τ_A) is expressed as: $\tau_A = -\ln(Tr_A)$. The dependence of the total and spectral τ_A on w is displayed in *Fig. 8*, and the relevant parameterized formulas are given by Eqs. #5 – #8. For the total τ_A the original data points are also plotted. The important message of this figure is the fact, that due to the saturation tendency of the FIR and MIR Tr_A, above 1 prcm water vapor column amount (see also *Fig. 7*), the total atmospheric optical thickness is increasing according to the increase in the WIN component. We have a pretty good linear relationship for the WIN τ_A and, in the 0.5–7 prcm range of w, the linear relationship for the total τ_A is also a good approximation.

Using the terrestrial flux transmittance, it is also possible to define an effective terrestrial graybody optical thickness (τ_T): $\tau_T = -\ln(Tr_T)$. The

dependence of τ_T on w is shown in *Fig. 9*. The parameterized functions are Eqs. #9 - #12. The scattered dots belong to the total τ_T. Apparently, the scatter of the data is larger than in the case of τ_A, and there is a very limited range of w where a linear relationship would hold. The practical importance of this parameter is related to the fact that the *OLR* and S_U are readily available from satellite observations, therefore, Tr_T and τ_T can easily be derived on a global scale.

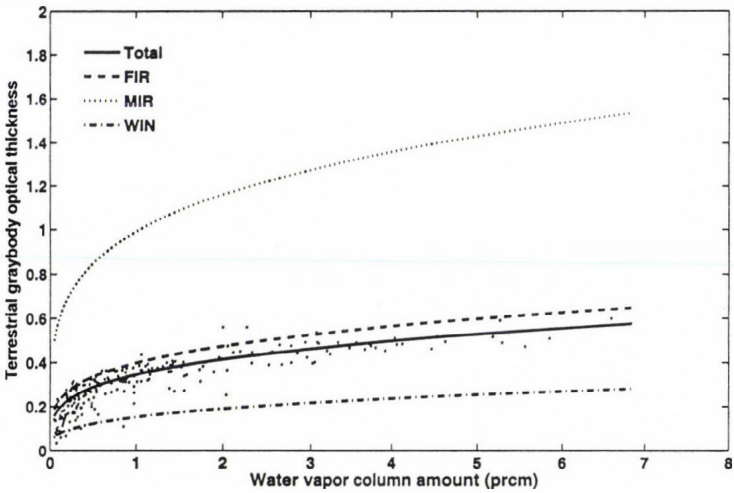

Fig. 9. Dependence of total and spectral terrestrial graybody optical thickness, $\tau_T = -\ln(OLR / S_U)$, on water vapor column amount.

The spectral components of Tr_T were also studied. The total Tr_T and its spectral components are presented in *Fig. 10*. The strong correlation of the total with the FIR Tr_T could be very useful for practical purposes. Probably this relationship could be improved by adjusting the FIR spectral limits. Based on this strong linear dependence, it is possible to derive the total *OLR* from observations of the FIR *OLR* alone and, perhaps, the surface temperature. This relationship could also work in the opposite direction, and the FIR flux density may be derived from the total *OLR*. Although Tr_T has not much physical meaning (as transmittance), later we shall see that Tr_T is closely related to the IR atmospheric transfer function. Generally speaking, the atmosphere modulates the surface upward flux density by absorption and emission. In radiative equilibrium, theoretically, the transfer function fully accounts for the combined absorption/emission effects and, therefore, Tr_T could be used for the large scale global estimate of the graybody optical thickness.

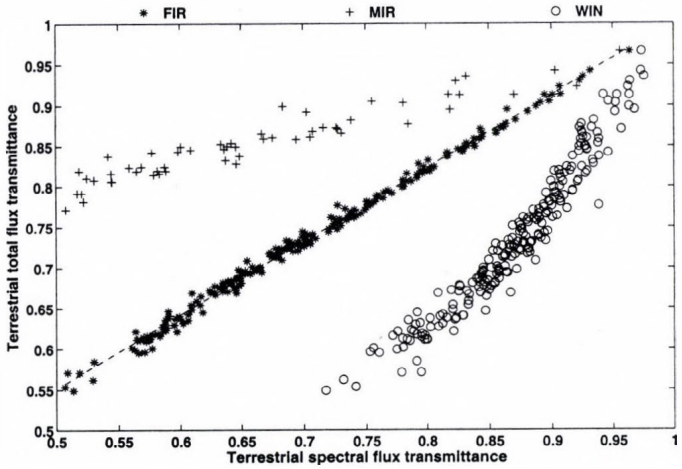

Fig. 10. Terrestrial total flux transmittance and its spectral components. The relatively larger scatter of the MIR and WIN data points are indication of increased S_T in those spectral ranges.

3.3 Transmitted surface radiation and atmospheric emittance

While the *OLR* can easily be measured with sufficient accuracy by satellite radiometers, the transmitted flux density and the upward atmospheric emittance can only be derived by lengthy computations of the accurate spectral flux transmittance.

The transmitted spectral flux density from the surface and the atmospheric upward emissivity may be written as $S_T = S_U Tr_A$ and $E_U = OLR - S_T$, respectively. The meridional distribution of the total S_T and its spectral components are presented in *Fig. 11*. It is not a surprise that the total S_T is governed by the WIN component, however, the latitudinal distribution of the WIN and the total S_T is very interesting. From the equatorial regions to about +/- 60° latitudes, S_T is increasing despite the large poleward decrease in the surface temperature. Proceeding toward the arctic regions, S_T will drop again considerably. The explanation for this unique behavior lies in the relative rate of the poleward decrease of the surface temperature and poleward increase of atmospheric transparency. After about +/- 60° latitudes, the temperature decrease will be the dominant factor.

This latitudinal dependence of S_T has an implication on its temperature dependence. Namely, the transmitted surface radiation is not increasing monotonously with the surface temperature, but must have a maximum value at around 270 K, representing the +/- 60° latitudes, see *Fig. 12*. Further on, this also implies that from +/- 60° latitudes toward the equator the surface net

radiation (atmospheric downward minus surface upward) will increase with increasing t_S. The above phenomenon is called "super-greenhouse effect" (*Vonder Haar*, 1986), and it is controlled by the strong H_2O continuum absorption in the windows region and the meridional distributions of w. At the polar regions or beyond +/– 60° latitudes, the longwave total net surface flux density is decreasing with increasing t_S, meaning, that the rate of warming of the surface by the downward atmospheric emittance is less efficient than the rate of energy loss of the surface.

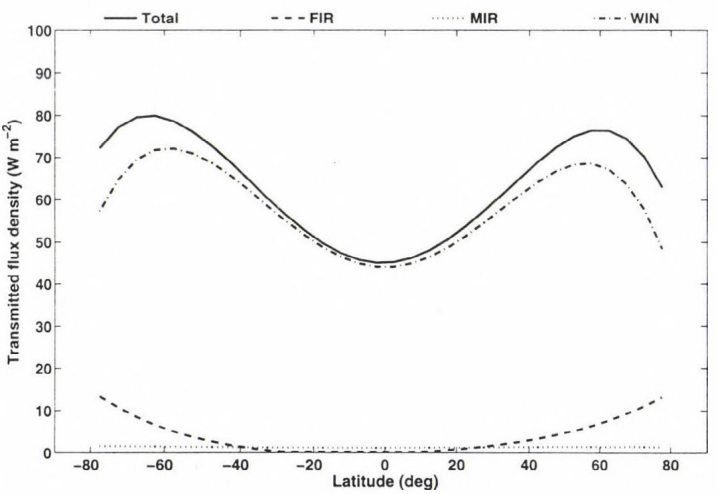

Fig. 11. Latitudinal distributions of the total and spectral components of the transmitted flux densities.

In *Fig. 11* the FIR component has a steady rise toward the poles from about +/– 20–30° latitudes. The little asymmetry in the region of the total absorption around the equator is related to the asymmetry in the latitudinal distribution of w. The contribution to the total S_T from the MIR spectral range is not significant (1–2 W m^{-2}) and does not change much along the latitudes.

The latitudinal variation of the FIR and WIN E_U are displayed together with the FIR and WIN *OLR* in *Fig. 13*. The FIR *OLR* is largely made up by the FIR E_U. In the polar regions the transmitted surface flux contributions may reach 15–20%. The WIN E_U contributions to the WIN *OLR* is decreasing poleward, up to +/– 65° latitudes. At higher latitudes there is a small increase in the WIN E_U, which could be the consequence of relatively higher temperatures in the lower troposphere due to frequent temperature profile inversions.

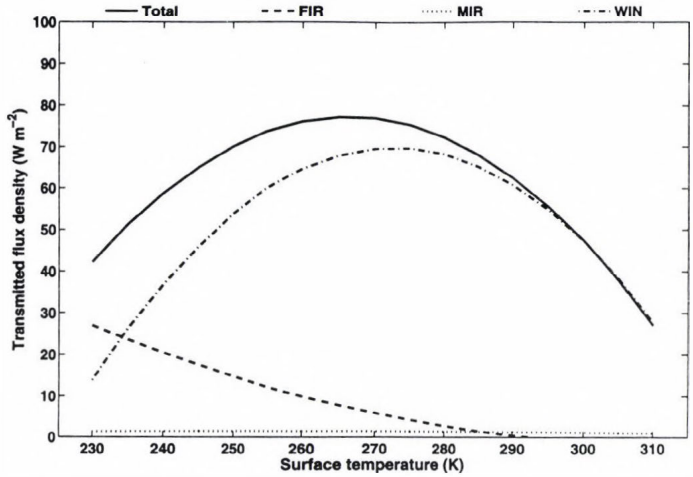

Fig. 12. Dependence of transmitted flux density on surface temperature. As a consequence of the peaks in the transmitted flux densities around +/–60° latitudes in Fig. 11, the total and WIN Tr_A functions have maximums at around t_S = 270 K.

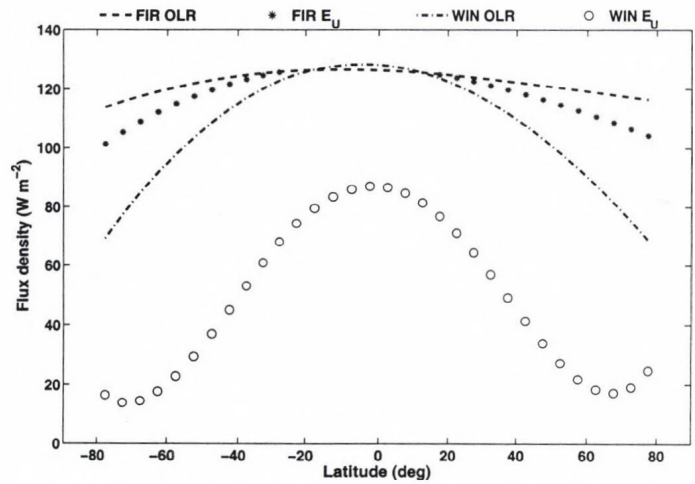

Fig. 13. Latitudinal distributions of the total, FIR, and WIN *OLR*s and the FIR and WIN upward atmospheric emittance.

The normalized atmospheric upward emittance (R_U) is an excellent parameter for studying the role of the atmospheric absorption in the different spectral regions: $R_U = E_U / S_U = Tr_T - Tr_A$. In *Fig. 14* the total and spectral

components of R_U are displayed as the function of w. The dots in this figure indicate the original FIR data points. The smooth curves are the plots of Eqs. #14 - #17. As is evident, the total zonal mean R_U is almost independent of w, see the low regression coefficient of Eq. #14. This figure actually suggests that, the zonal averages of the total upward atmospheric emittances are practically independent of w, and they may be taken as half of the surface upward flux densities. This is a clear indication that for zonal means, the assumption of radiadiative equilibrium approximately holds. Computed from the local S_U and E_U data, the global average E_U/S_U ratio is 0.495. Using the emissivity approximation, it can easily be shown, that the trivial solution for homogeneous atmosphere is 0.5 (see for example *Goody* and *Yung*, 1989). It can also be shown that in case the surface temperature and surface air temperature is equal, the theoretical ratio (R'_U) depends only on the graybody optical thickness: $R'_U = \hat{f} - Tr_A = A - \hat{g}$, where A is the flux absorptance and by definition, $\hat{f} = 2/(1 + \tau_A + Tr_A)$ is the atmospheric transfer function and $\hat{g} = 1 - \hat{f}$ is the greenhouse function. In *Fig. 15* the theoretical and some simulated ratios are compared. The global average of the R'_U factor is 0.496, which is in excellent agreement with the average R_U. The good agreement in the global averages is not a surprise, because of the planetary radiative equilibrium requirement. However, the existence of the radiative equilibrium for the zonal means is more interesting.

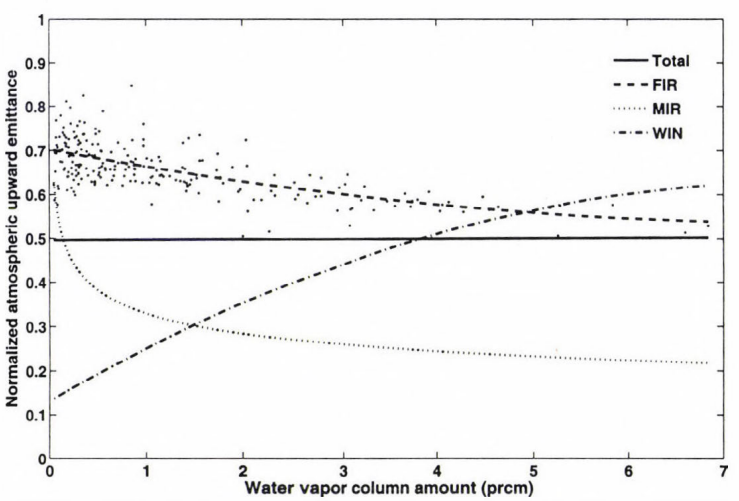

Fig. 14. Dependence of normalized atmospheric upward emittance on water vapor column amount.

In *Fig. 14* the FIR, MIR, and WIN part of R_U are varying significantly with w. The FIR and MIR components are decreasing with increasing w, while the WIN component shows the opposite effect. The physical explanation of these facts are very simple. In case of the opaque spectral regions like FIR and MIR, increasing w results in decreasing atmospheric transparency. This must be coupled with the upward shift of the weighting functions, and therefore, assuming a negative vertical temperature gradient, the effective atmospheric emittance will be shifted to colder atmospheric layers. This process will also explain the unusually small meridional variation in the FIR and MIR *OLR*s.

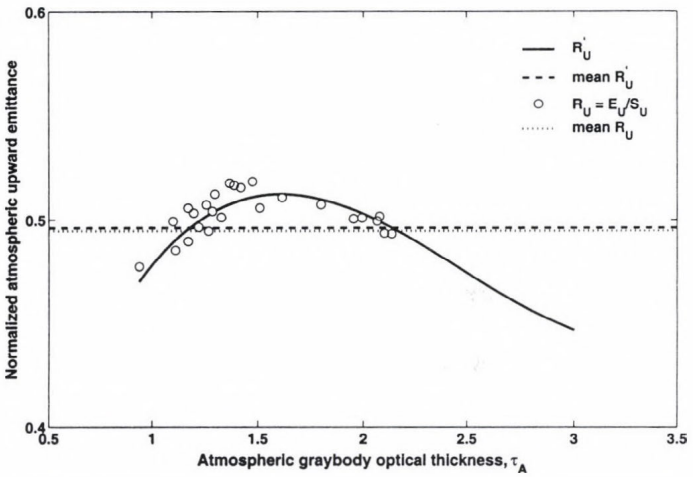

Fig. 15. Theoretical and simulated normalized upward emittance. The horizontal lines are global averages.

To make this point more clear and to quantify the process, test calculations were performed for the tropical and subarctic winter atmospheres. We have computed the weighting functions in the strongly absorbing part of the FIR region with the spectral resolution of 0.25 cm^{-1}. In plot A of *Fig. 16* the differences in the altitudes of the peak values (arctic-tropical) are shown as the function of the wave number. On average, there is about 2.5 km down-shift in the FIR spectral region. At some narrow spectral interval, the opposite effect may also be observed. In plot B the spectrally averaged weighting functions are presented, again showing the down-shift. The slightly different H_2O continuum coefficients in the FIR region, (CKD 0 and CKD 2.4) have no effect on the conclusions of the qualitative picture. The average peak positions were moving from about 7.7 km, in the case of the tropical atmosphere to about 5.2 km in the case of the arctic winter atmosphere. Apparently, the peaks are always above a possible low level inversion and below the stratospheric temperature

rise, even if we consider the lowering of the height of the tropopause toward the poles. The thermal structure of the atmosphere between the 5 and 10 km altitude range or up to the tropopause is usually characterized with a negative temperature gradient explaining the increasing FIR and MIR R_U with decreasing w (in *Fig. 14*). As an indirect evidence of the above process, by the simulation of the response of the *OLR* of the arctic winter atmosphere to the decrease in the H_2O continuum absorption coefficient in the FIR spectral range, it was shown in *Tobin et al.* (1999) that the top of the atmosphere flux density increases.

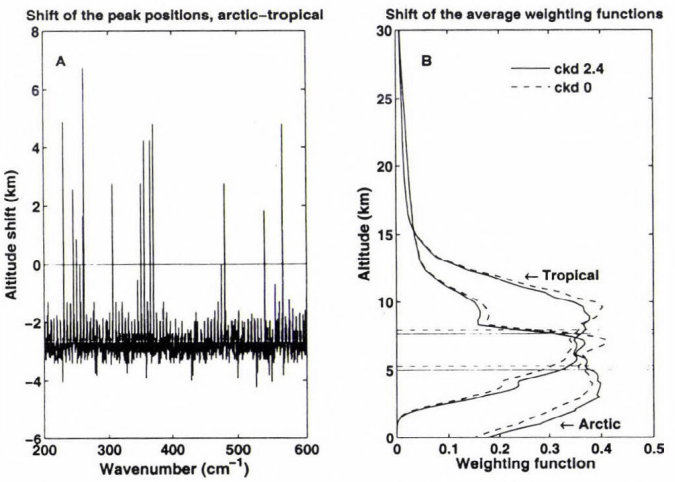

Fig. 16. Relative position of the peak of the FIR spectral weighting functions (plot A) and the average FIR weighting functions (plot B). Note the relatively small effect of the changes in the H_2O continuum parameterization in plot B.

The explanation of the behavior of the WIN R_U is also simple. Since the whole vertical atmosphere contributes to the E_U, its increasing value with increasing w indicates, that larger w is usually associated with warmer atmosphere, and the fractional amount of the upward re-emitted radiation is roughly proportional to the absorbed radiation. The WIN Tr_T does not change very much; the global average is 0.8544 and the standard deviation is about 6%. Consequently, the relationship $R_U \sim 0.8544 - Tr_A$ means, that the relative upward atmospheric windows emittance depends only on the total absorption.

Just for completeness, in *Fig. 17* the total and spectral normalized atmospheric downward emittances (R_D) are presented as the function of w, see also Eqs. #18 – #21. R_D is computed similarly to R_U, but using the atmospheric downward emittance : $R_D = E_D / S_U$. According to the Kirchoff's law, R_D may be identified as the clear-sky total graybody absorptance: $R_D = 1 - Tr_A = A$. For

the recent TIGR profile set - which contains some very cold and dry as well as very warm and humid profiles - R_D varies between 0.63 and 0.93. The only interesting feature of this figure is the saturation of the FIR R_D at around 2 prcm water vapor column amount. The sharp decrease in R_D with decreasing water vapor content is the result of the opening up of the so called "micro windows" in the FIR spectral region as it was also evidenced by the Surface Heat Budget of the Arctic Ocean, SHEBA, experiment (*Tobin et al.*, 1999). The FIR and MIR R_D may exceed one, which is the indication of cases with strong close to surface temperature profile inversions. The total R_D may be parameterized with quite a high accuracy using a third order polynomial of u, Eq. #18: $R'_D = f(u)$, where $u = \ln(w)$.

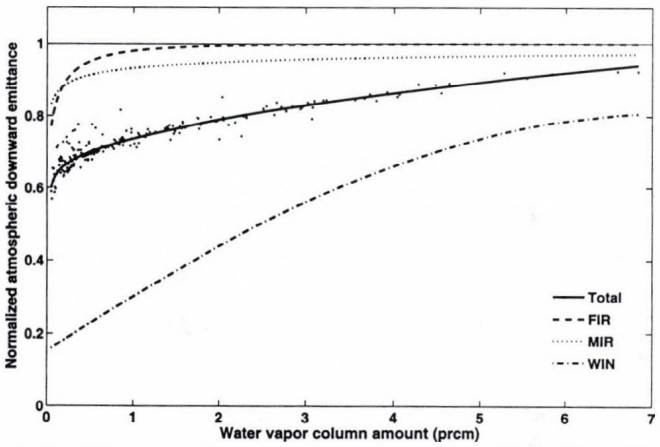

Fig. 17. Dependence of normalized atmospheric downward emittance on water vapor column amount.

E_D is an important term in the equation of the surface energy balance, and lots of efforts were devoted for its parameterization (*Brutsaert*, 1975; *Idso*, 1981; *Tuzet*, 1990). Using satellite observations of the air temperature at the surface and the water vapor column amount, together with the parameterized value of the clear-sky R_D by Eq. #18, the estimated downward emittance (E'_D) can easily be derived: $E'_D = \sigma t_A^4 R'_D$. The correlation coefficient between the true E_D and the parameterized E'_D is 0.998. There is some positive bias of 0.1%, and the 1 σ residuum standard deviation is 2.7%. While most of the commonly used empirical formulas fail at low temperatures and low water vapor content, and in the rare cases of very warm and dry profiles, the above parameterization gives pretty good fluxes even at extreme temperatures and water contents, see *Fig. 18* A and B.

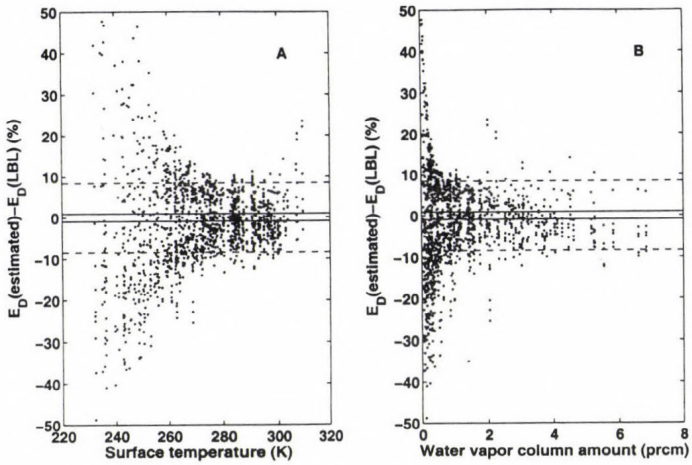

Fig. 18. Accuracy of the estimated downward atmospheric emittance calculated by bulk formulas and LBL simulations. Plot A shows the dependence on the surface temperature and plot B shows the dependence on the water vapor column amount. In both plots the dots represent the values computed by formulas of *Brutsaert* (1975) and *Idso* (1981). The dashed and solid lines are the standard deviations corresponding to the bulk formulas and LBL simulations, respectively.

In plot A of *Fig. 19* we have compared our parameterization with the highly sophisticated model of Gupta (*Gupta et al.*, 1992; *Gupta*, 1989). As it can be seen, the two parameterization compares very well. For further improvements we have developed a linear correction term to handle the temperature dependence. In case the information on the temperature and humidity profiles are available, one may calculate the effective temperature of the water vapor (t_H). Using t_A and t_H, our corrected formula may be written as: $E_D'' = E_D' - 32 + 0.857 t_A + t_H$. In plot B of *Fig. 19* E_D' and E_D'' are compared. The residuum correlation coefficient between E_D and E_D'' goes beyond 0.999, and probably sets the limit for the accuracy of simple parameterizations. The correction term seems to take care of almost all cases where the source of the differences were due to the low level temperature profile inversions. Further improvements seem to be difficult without building in more detailed temperature, water vapor, and ozone profile related information and breaking up the task for several shorter spectral intervals.

Such an increase of complexity is out of the scope of the recent paper. We have devoted much attention to the E_D parameter, but we shall see later, that through the $\tau_A \approx -\ln(1 - E_D / S_U)$ relationship we have the key for the large scale surface observation of the greenhouse effect or the IR equilibrium state of the atmosphere. For example, based on the CERES Ocean Validation

Experiment, (COVE), year 2002 time synchronized one minute archive of the E_D and S_U fluxes (*COVE*, 2003) we have estimated the local annual average all-sky atmospheric graybody optical thickness. For the April, 2002–March, 2003 time period, the annual average all-sky τ_A is 2.06 with a 1 σ standard deviation of 40%.

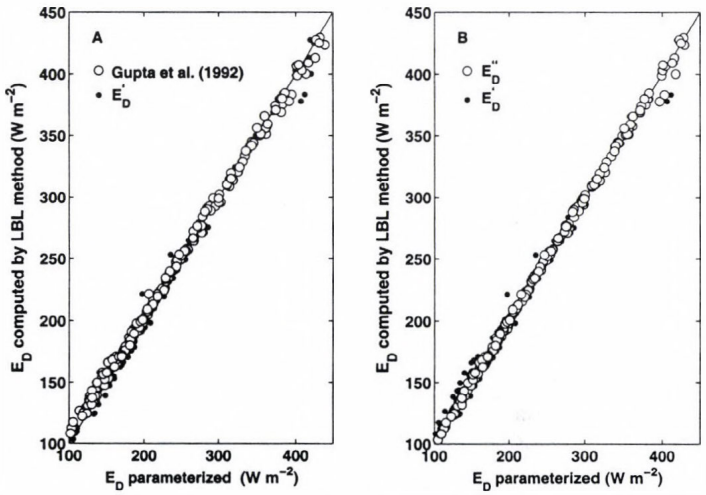

Fig. 19. Plot A is a comparison of E_D parametrizations by *Gupta* (1992) and the $E'_D = \sigma t_A^4 R'_D$ formula, where R'_D is a third order polynomial of $\ln(w)$, see Eq. #18 in Table 4. Plot B shows the effect of the temperature correction: $E''_D = E'_D + t_H - 0.857 * t_S - 32$, where t_H is the effective water vapor temperature.

Finally, in *Fig. 20* we summarize the two most important characteristics of the upward and downward emittances in the Earth's atmosphere:

- In the average sense the atmosphere is very close to the radiative equilibrium, and, as a consequence, the zonal and global average upward emittance is about half of the average surface upward flux density. This fact is supported by the recent assessment of the Earth's annual global mean energy budget by *Kiehl* and *Trenberth* (1997). Their estimates of S_U and E_U are 390 and 195 W m^{-2}, respectively.

- As a consequence of the Kirchoff's law, within the clear atmosphere the downward emittance is approximately equal to the absorbed flux density. Based on our data set, the global average clear-sky downward atmospheric emittance is 311.4 W m^{-2}, while the global average of the absorbed radiation by the clear-sky is 311.9 W m^{-2}. This equivalence – for

the highly variable atmospheric emission spectra and for global scale – was not shown before with such a high numerical accuracy. Utilizing the above two facts one may estimate the global (or zonal) average *OLR* with the simple expression: $OLR = 3E_U - E_D$.

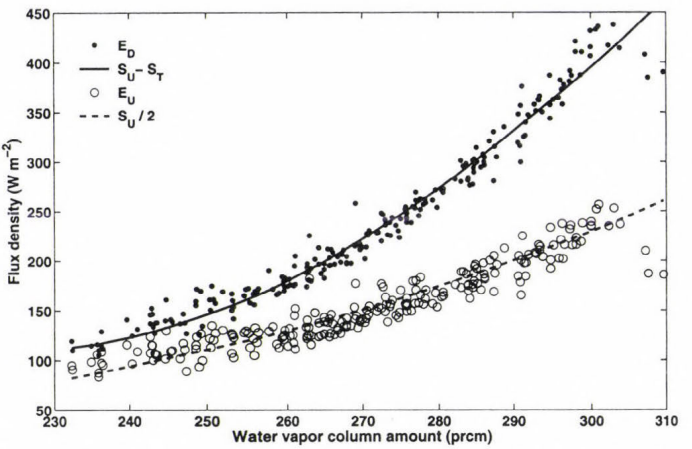

Fig. 20. Dependence of E_D and E_U fluxes on surface temperature. The solid line is a parabolic fit to the absorbed fluxes and the dashed line is the fit to the half of the surface upward fluxes.

4. Greenhouse effect

4.1 Overview

Regarding the planetary greenhouse effect we must relate the amount of the atmospheric absorbers to the surface temperature. Assuming monochromatic radiative equilibrium, isotropy in both hemispheres and a semi-infinite plane-parallel gray atmosphere, the predicted air temperature at the surface (t'_A) and the surface temperature (t'_G) are given by the next two equations (*Goody* and *Yung*, 1989; *Paltridge* and *Platt*, 1976):

$$t'_A = \left[\frac{OLR}{2\sigma}(1+\tau_A)\right]^{\frac{1}{4}}, \tag{1}$$

and

$$t'_G = \left[\frac{OLR}{2\sigma}(2+\tau_A)\right]^{\frac{1}{4}}. \tag{2}$$

In the above equations τ_A is the total graybody atmospheric optical thickness, as usually defined in two stream approximations, $\tau_A = (3/2)\tau$, where τ is measured vertically. The atmospheric skin temperature (t_0') and the characteristic graybody optical thickness which defines the IR optical surface of the planet (τ_C') are:

$$t_0' = \left[\frac{OLR}{2\sigma}\right]^{\frac{1}{4}}, \tag{3}$$

$$\tau_C' = 1. \tag{4}$$

Eqs. (1)–(4) are usually referred as the solutions of the Schwarzschild-Milne equations, see more details in *Rozanov* (2001), *Rutten* (2000), or in *Collins II* (2003). We should note, that the terrestrial graybody optical thickness is not an accurate measure of the atmospheric absorption and can not be used in Eqs. (1) and (2). These equations are frequently quoted in the meteorological literature and even in textbooks, however, it is a mistake to use them to study the radiative equilibrium and greenhouse effect in the Earth's atmosphere.

For the real atmosphere, the semi-infinite solutions must be replaced with the solutions valid for the bounded atmosphere. With relatively simple computation (we do not present it here) it can be shown, that for a given *OLR* or E_U the surface air temperature and surface temperature are mutually dependent on each other: $OLR = \hat{f}(S_A A + S_G Tr_A)$ or $E_U = \hat{f} S_A A - \hat{g} S_G Tr_A$, where S_G and S_A are the surface upward flux densities at t_G and t_A temperatures, respectively. The *IR atmospheric transfer* and the *greenhouse* functions ($\hat{f}$ and $\hat{g}$) play fundamental role in the planetary greenhouse effect.

In our simulation, for having no surface temperature data, and making the definition of the greenhouse effect simpler, we set the equilibrium surface temperatures to the surface air temperatures, $t_G = t_A = t_S$. Note, that in the boundary layer the principle of energy minimum (or maximum entropy) works toward the thermal equilibrium. In this case the theoretical dependence of t_S on the transfer function $\hat{f}$ is:

$$t_S'' = \left[\frac{OLR}{\sigma \hat{f}}\right]^{\frac{1}{4}} = \left[\frac{OLR(1+\tau_A + e^{-\tau_A})}{2\sigma}\right]^{\frac{1}{4}} \tag{5}$$

In case the lower boundary condition is explicitly set by t_G, the atmospheric skin temperature will also depend on the surface temperature and total optical thickness:

$$t_0'' = \left[\frac{OLR\,(1+e^{-\tau_A}(1+\tau_A)) - 2e^{-\tau_A}\sigma t_G^4}{2\sigma(1-e^{-\tau_A})} \right]^{\frac{1}{4}}. \tag{6}$$

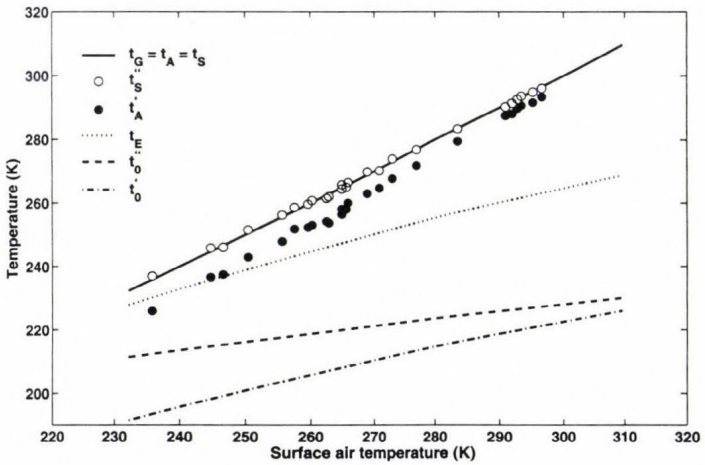

Fig. 21. Surface air, skin, and effective temperatures predicted by Eqs. (1), (3), (5), and (6). The dotted line is the effective temperature, $t_E = (OLR/\sigma)^{0.25}$. The symbols represent selected profiles with *OLR*s closest to the theoretical values.

In *Figs. 21* and *22* we compare the surface air and surface temperatures obtained by the different formulas. For reference, in *Fig. 21* the effective temperatures, $t_E = (OLR/\sigma)^{0.25}$, and the atmospheric skin temperatures are also plotted. Apparently, t_A' underestimates and t_G' badly overestimates the corresponding equilibrium surface and surface air temperatures. The error in t_A' decreases with increasing temperatures because of the increasing w (at higher temperatures). The atmospheric skin temperatures are also underestimated, and for the same reason the errors decrease with increasing temperatures.

The data points in these figures represent only about 10% of the total 230 profiles. Only those cases were selected for these plots, where the simulated and theoretically predicted *OLR*s agreed within less than 0.5%. Note, that (according to *Fig. 14*), for the zonal and global averages the radiative

equilibrium condition holds, but the individual profiles could be quite far from the radiative equilibrium. For example, it is obvious that profiles with temperature inversions will not fit into the theoretical picture which expects increasing temperatures with increasing optical thickness.

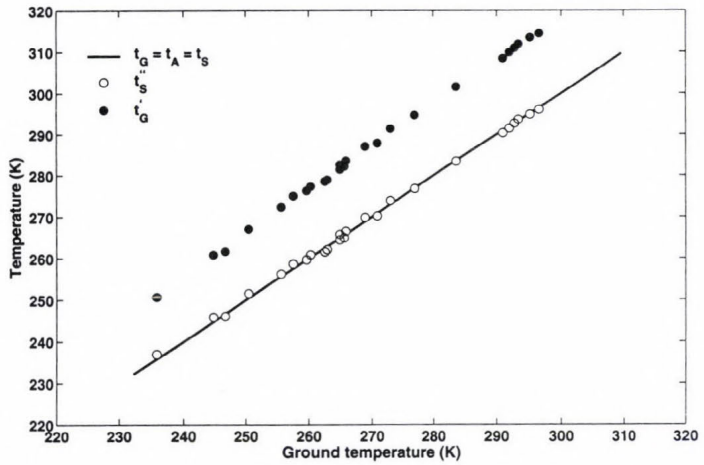

Fig. 22. Surface temperatures predicted by Eqs. (2) and (5). The symbols represent selected profiles with *OLR*s closest to the theoretical values.

In the bounded atmosphere the characteristic graybody optical thickness (τ_C'') becomes also dependent on the total optical thickness and surface temperature:

$$\tau_C'' = 1 - \frac{\tau_A - 2\left[\dfrac{\sigma t_G^4}{OLR} - 1\right]}{e^{\tau_A} - 1}. \tag{7}$$

In *Fig. 23* the τ_C'' and the simulated and theoretical atmospheric clear-sky graybody optical thicknesses are shown as the function of the surface temperature. The theoretical values (τ_A'') are the solutions of the transcendent equation for τ_A on the left hand side of Eq. (5). The τ_A'' and τ_A curves show excess optical thickness (water vapor) at very cold (arctic) and very warm (tropical) areas, while, there are optical thickness deficits at medium surface temperatures. With increasing temperature - or w -, τ_C'' tends toward the semi-infinite solution of 1.0. Sometimes τ_C'' is associated with an atmospheric altitude or pressure level of effective emission, see for example *Schneider et*

al. (1999). Since part of the *OLR* is, in fact, transmitted flux density from the surface, the physical meaning of such an atmospheric level is confusing. According to *Schneider et al.* (1999), the effective pressure level is between 540 and 600 hPa. Our computation shows a global average effective pressure level of 507 hPa. The global average effective pressure levels for the upward and downward atmospheric emissions are 339 and 666 hPa, subsequently.

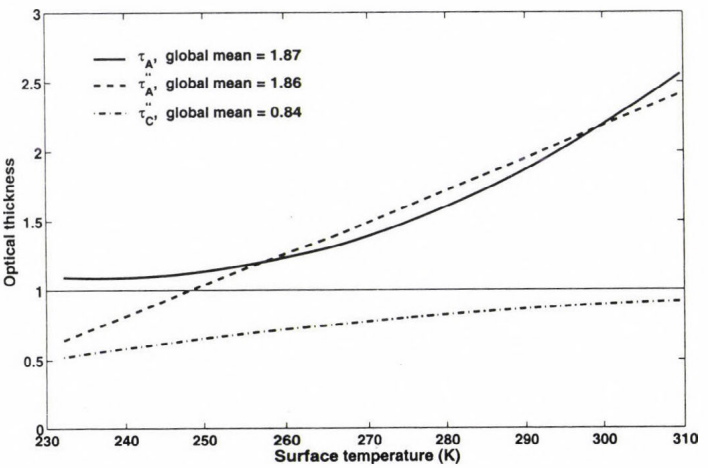

Fig. 23. Dependence of simulated and theoretical graybody optical thickness on surface temperature. The dash-dot line is the theoretical characteristic optical thickness, τ''_C, computed by Eq. (7).

The theoretical and simulated global average graybody optical thicknesses are in pretty good agreement: they are 1.87 and 1.86, and they correspond to a vertical optical thickness of about $\tau = 1.23$. These values are also the indication that the clear atmosphere loses its thermal energy close to the peak efficiency, see *Fig. 15*. Using Eq. (1) with the same data would result in about 9% higher optical thickness, and using Eq. (2) would result in an unrealistic low value of 0.67. Just for reference, if we use a global average surface and surface air temperature of 288 K and the ERBE global average clear-sky *OLR* of 268.0 W m^{-2}, the theoretically estimated vertical optical thickness would be 1.17, which is reasonably close to our global clear-sky average.

The atmospheric greenhouse effect is bounded to the absorption and emission of the IR radiation and controlled by the IR atmospheric graybody optical thickness. The keys to this parameter are the accurate (measured or modeled) atmospheric upward and downward flux densities, the correct computation of the atmospheric flux transmittances, and an adequate radiative

transfer model which relates the fluxes and flux transmittances. In the next section we shall shortly review the most commonly used greenhouse parameters and their relation to the atmospheric graybody optical thickness.

4.2 Greenhouse factor and normalized greenhouse factor

The most common measure of the greenhouse effect, which is also adopted by the global warming community, is the difference between the S_U and the *OLR*: $G = S_U - OLR$ (*Raval* and *Ramanathan*, 1989). The classical approach to the greenhouse effect is via the long-term energy balance equation of the solar radiation input and the IR radiation loss of the Earth surface. The difference between the effective planetary temperature – computed from the *OLR* or the solar input – and the global average surface temperature is the measure of the planetary greenhouse effect. In fact, the G factor is the application of the classical approach for the local flux densities without converting them to temperature differences. As we have seen in *Fig. 20*, the atmospheric absorption and the downward atmospheric emittance are approximately equal, therefore, the G factor can easily be related to the atmospheric upward and downward emittances: $G = S_U(1 - Tr_A) - E_U = E_D - E_U$. In case the surface air temperature and the surface temperature are equal, theoretically, the G factor is proportional to the product of S_U and the greenhouse function, which is only dependent on τ_A: $G = G(S_U, \tau_A) = S_U\, \hat{g}(\tau_A)$. The $\hat{g}(\tau_A)$ function may be expressed as:

$$\hat{g}(\tau_A) = \frac{\tau_A - 1 + e^{-\tau_A}}{\tau_A + 1 + e^{-\tau_A}}. \tag{8}$$

Eq. (8) shows the real physical meaning of the $g = G/S_U$ factor in *Raval* and *Ramanathan* (1989). The normalized greenhouse factor and the total atmospheric graybody optical thickness are uniquely related by the theory. For fixed absorber amounts the temperature sensitivity of $\hat{g}(\tau_A)$ – via the temperature dependence of the absorption coefficient – is very small due to the compensation effect through the τ_A and $\exp(-\tau_A)$ terms. In case of the standard tropical and arctic winter profiles, these sensitivities are –0.005 and –0.01% of $\hat{g}(\tau_A)$ per 1 K increase in the profile temperature. Obviously, these changes are negligible compared with the thermodynamic temperature dependence of the water vapor column amount on the temperature profile via the Clausius-Clapeyron equation, which has nothing to do with the temperature dependence of the greenhouse effect.

In *Fig. 24* we present comparisons of greenhouse factors obtained from the TIGR profile set and the ERBE data. The three versions of the G factor, $S_U - OLR$, $E_D - E_U$, and $S_U\,\hat{g}(\tau_A)$ are plotted as the function of surface temperature t_S. The ERBE annual averages were taken from *Raval* and *Ramanathan*, (1989) and they are plotted as open circles. Although we have some deviations at very large and small temperatures, this figure is actually an experimental proof of the validity of the theoretical $\hat{g}(\tau_A)$ function. The dependence of G on S_U also explains the high correlation with the surface temperature which was reported in *Raval* and *Ramanathan* (1989). For the sake of numerical comparisons, within the range of the ERBE data points, we calculated the regression lines of the $G_N(t_S)$, $u(t_S)$, and $G_N(u)$ linear functions. In *Table 5* the regression parameters are compared with similar ones in *Raval* and *Ramanathan* (1989). *Fig. 24* and *Table 5* show a very good overall agreement.

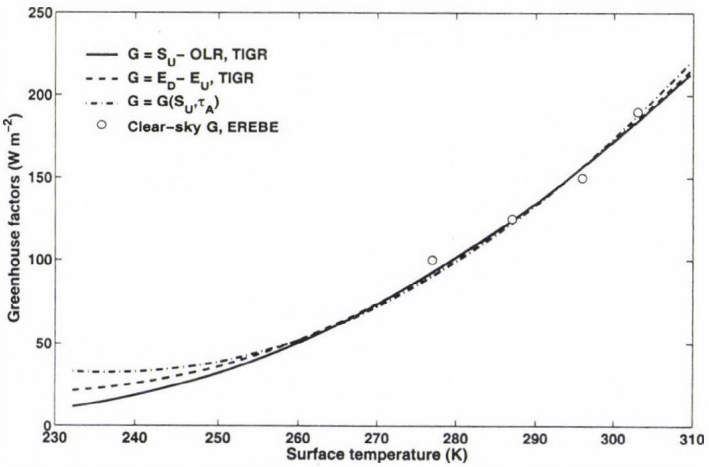

Fig. 24. Dependence of various greenhouse factors on surface temperature.

Table 5. Comparisons with *Raval* and *Ramanathan* (1989)

Parameter and equation	*Raval* and *Ramanathan*		This simulation		Correlation
	a	*b*	*a*	*b*	
$G_N = a * t_S + b$	0.00342	0.658	0.00465	-1.00	0.955
$u = a * t_S + b$	0.0553	-13.0	0.0588	-13.96	0.937
$G_N = a * u + b$	0.0576	0.155	0.0693	0.127	0.894

According to Eq. (8), the normalized greenhouse factor depends only on the total graybody atmospheric optical thickness. In *Fig. 25* we compare the $\hat{g}(\tau_A)$ function (solid line) with the G_N values (dots) obtained from our simulation. To show the general tendency of the simulated G_N, a smooth curve was fitted (dashed line) to the dots. Those cases which we marked as the closest ones to the state of radiative equilibrium are indicated with open circles. The global average $\hat{g}(\tau_A)$ and G_N are practically equal, $\overline{\hat{g}}(\tau_A) = \overline{G}_N = 0.33$, as it is expected from *Fig. 23*. We have seen already in *Fig. 8*, that the atmospheric graybody optical thickness grows almost linearly with the water vapor column amount. We have also shown a strong linear relationship between G_N and t_S in *Table 5*.

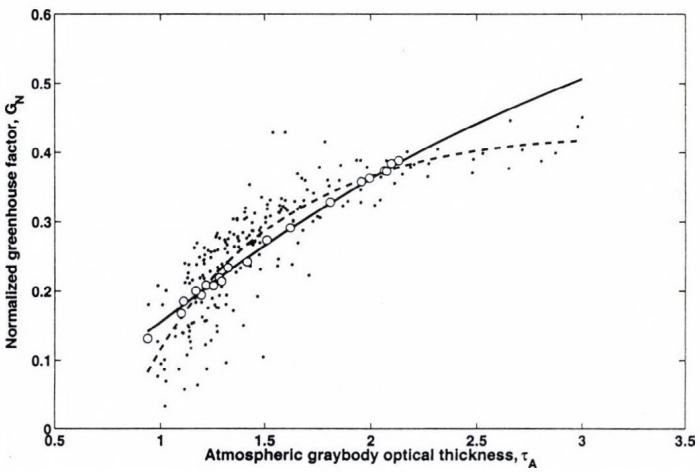

Fig. 25. Dependence of theoretical (solid line) and simulated (dots) normalized greenhouse factors on atmospheric graybody optical thickness. Open circles are the profiles closest to the radiative equilibrium. The dashed line was obtained by a second order polynomial fit to the dots.

These two facts imply that the dependence of G_N on the optical depth is a simple linear mapping of the $t_S(w)$ function. In other words, the local greenhouse effect does not follow the theoretical curve predicted by the radiative equilibrium, instead, it is controlled by thermodynamic and transport processes. However, the radiative equilibrium curve sets the global constraints. In case of an increase in the global average graybody optical thickness, the whole pattern will be shifted to the right along the equilibrium curve in a way that the new global average and the new radiative equilibrium optical thickness will be equal, assuring that the global radiative equilibrium

will hold. Perhaps, the structure of the pattern may change because of optical thickness perturbations have different relative effect at different latitudes. The magnitude of the shift (i.e., the new equilibrium optical thickness and surface temperature) is the function of the planetary albedo, solar constant, and the general dynamics of the system as well.

The derivative of Eq. (8) gives the sensitivity of the $\hat{g}$ parameter to the total optical thickness:

$$\hat{g}_S(\tau_A) = \frac{d\hat{g}(\tau_A)}{d\tau_A} = \frac{2\,(1-e^{-\tau_A})}{(e^{-\tau_A}+\tau_A+1)^2} = \hat{f}^2 A/2\,. \tag{9}$$

The variations of $\hat{g}(\tau_A)$ and $\hat{g}_S(\tau_A)$ functions for a wide range of τ_A are shown in *Fig. 26.* The values, corresponding to the global average optical thickness, $\tilde{\tau}_A = 1.86$, are marked with open and full circles.

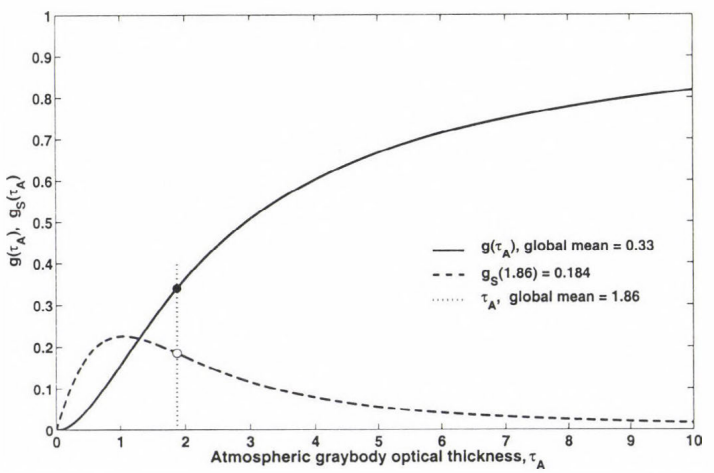

Fig. 26. Dependence of theoretical normalized greenhouse factor, Eq. (8), and its derivative, Eq. (9), on graybody optical thickness.

Using Eq. (9) one may easily estimate the initial tendency of the greenhouse temperature change due to greenhouse gas perturbations. To do this we need the value of $\hat{g}_S(\tilde{\tau}_A)$. From Eq. (9) the sensitivity is $\hat{g}_S(\tilde{\tau}_A) = 0.185$ per unit optical thickness. For example, a hypothetical CO_2 doubling would result in an increase of the global average $\tilde{\tau}_A$. To compute the increase in $\tilde{\tau}_A$ without much effort, global and zonal average atmospheric

profiles are needed. We computed the global average profile from the full TIGR dataset. To estimate the minimum and maximum expected temperature changes in cold and warm areas we also computed three zonal averages for the southern, tropical and northern latitudinal belts. The zonal belts were bounded by the following latitudes: -90, -42.2, 36.8 and 90 degrees (south is negative). The product of the optical depth perturbations with the sensitivity will give the expected changes in $\hat{g}$, from which, using the (unperturbed) *OLRs,* the surface temperature changes may be evaluated.

According to our estimate, a CO_2 doubling would rise the global average surface temperature by 0.48 K, corresponding to a global average primary greenhouse forcing of 2.53 W m^{-2}. The detailed results are included in *Table 6.*

Table 6. Effect of CO_2 volume mixing ratio perturbations. Current value is 366 ppmv

CO_2 perturbation	Change in τ_A (%)				Change in t_S (K)			
	Global	South	Tropic	North	Global	South	Tropic	North
0.0	-6.71	-19.4	-3.940	-16.90	-2.500	-5.070	-1.700	-4.720
0.5	-1.06	-2.17	-0.793	-1.93	-0.396	-0.579	-0.341	-0.547
2.0	1.29	2.25	1.060	2.02	0.482	0.601	0.455	0.573
10.0	6.16	9.14	5.350	8.29	2.290	2.450	2.290	2.360
100.0	22.30	30.00	20.00	27.50	8.200	8.100	8.430	7.840

We note, that the direct estimate using the right hand side of Eq. (5): $\Delta S_U = (dS_U / d\tau)\Delta\tau = A\,(\Delta\tau/2)\,OLR$ will give the same greenhouse forcing. For reference, our estimate is about 1.7 W m^{-2} (35%) less than the one published by Hansen (Table 1 on page 12754 in *Hansen et al.*, 1998). *Hansen et al.* (1998) used the correlated k-distribution method for the optical thickness calculations which compares well with LBL results. The reason of the relatively large differences in the greenhouse forcing must be the different method of relating the changes in the total optical thickness to the changes in the fluxes. Regarding the zonal temperature change estimates (in *Table 7*), once again we have to emphasize that keeping the zonal *OLR* as a constant (while changing the optical thickness) is not realistic. There exists only one overall constraint, and that is for the global average *OLR.*

An increase of 0.08 prcm in the global average w would result in the same temperature rise – or a decrease by the same amount could completely hide the greenhouse effect of the CO_2 doubling. Since the local and global variability of the water vapor column amount is more than a magnitude larger

on almost any practical time scale, the detection of the changes in the global and zonal greenhouse effect could be extremely difficult, and on local scale it is almost impossible. It is also obvious, that on a global scale, a strong direct $t_S \rightarrow \tau_A \rightarrow t_S$ feedback loop is not in effect in the Earth-atmosphere system.

The role of the water vapor in the Earth's atmosphere is very complex and is probably controlled by two major processes: the greenhouse effect and the redistribution of the system's heat energy by general circulation. As a result of these processes there are unique equilibrium meridional distributions for t_S and w. Obviously, the general circulation models (GCMs) are the adequate tools to predict those details. In any case, the decreasing tendency of the $\hat{g}_S(\tau_A)$curve above the unit optical thickness in *Fig. 26* and the negative temperature sensitivity of the $\hat{g}(\tau_A)$ function works against large positive feedback. It is interesting to note that in the clear atmosphere the CO_2 contribution to the total greenhouse effect is only about 9%, and an average atmosphere without CO_2 would be about 2.5 K colder. The above estimates are consistent with the wide range of predicted changes that can be found in the global warming literature.

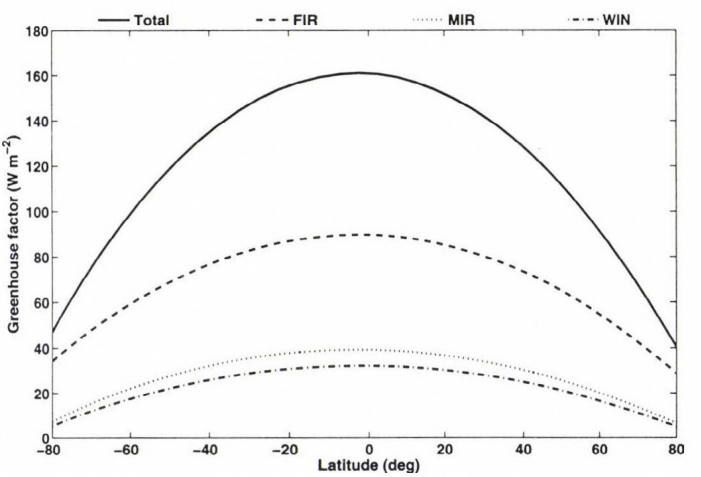

Fig. 27. Latitudinal dependence of the total and spectral greenhouse factors.

In *Fig. 27* the meridional variation of G is presented. Because of the direct dependence of G on the large meridional gradient in the surface temperature via S_U, and the larger sensitivity of the $\hat{g}_S(\tau_A)$ function at the polar regions, probably the first detection of the planetary greenhouse effect will be possible by the observations of the changes in the meridional gradient of the G factor. This is especially true for the FIR G component. Our data set

shows that the global average greenhouse factor is 131.8 W m^{-2}. The FIR contribution is 57%, and the shares of the MIR and WIN spectral ranges are 24% and 19%, respectively.

In *Fig. 28* the meridional distribution of the total and spectral G_N and the $\hat{g}(\tau_A)$ functions are plotted. The spectral G_N curves show the relative contributions to G_N from the FIR, MIR, and WIN regions. According to this figure, the total G_N is decreasing poleward from about 38% at the equatorial regions to about 15–20% at high latitudes. This behavior is obvious since decreasing water vapor content will increase the atmospheric infrared transparency almost everywhere in the longwave spectrum. The remarkably good agreement between the theoretically predicted greenhouse function and the simulated total normalized greenhouse factors further emphasize our earlier result, i.e., for zonal and global means the radiative equilibrium condition approximately holds.

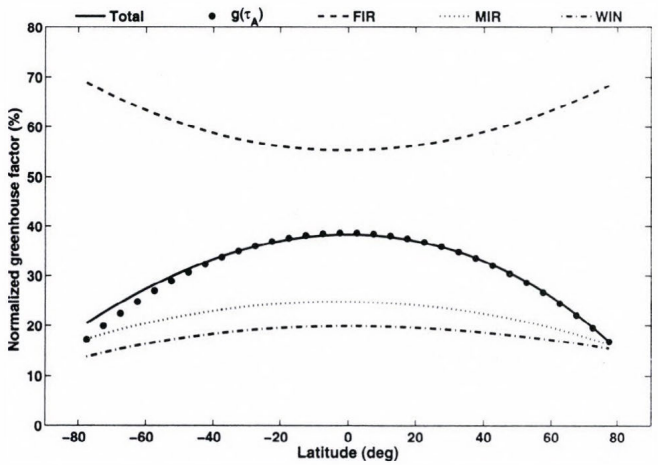

Fig. 28. Latitudinal distributions of the total and spectral normalized greenhouse factors. The full circles are computed by Eq. (8).

While the total G_N decreases poleward by about fifty percent, the far infrared contribution will increase from about 55% (of the total G_N) at the equatorial regions to 70% at +/–80 degrees latitudes. This increase, and the decrease of the MIR and WIN components, are due to the shift of the peak of the blackbody function toward the far infrared with decreasing temperature. The WIN G_N must also be affected by the ozone absorption, and theoretically, it should reflect the global average meridional distribution of the total ozone amount and the effective height of the ozone layer. Unfortunately, our data set does not contain sufficient information to explore these details.

4.3 Inverse terrestrial flux transmittance

The inverse terrestrial flux transmittance as another greenhouse parameter was introduced by *Stephens* and *Greenwald* (1991). Based on the functional relationship between I_T and G_N, this parameter does not contain any more information about the greenhouse effect than G_N and can not be related to the graybody atmospheric optical thickness in a simple way either. Theoretically I_T has a nonlinear relationship with the atmospheric graybody optical thickness:

$$I_T''(\tau_A) = \hat{f}^{-1} = \frac{1 + \tau_A + e^{-\tau_A}}{2}. \tag{10}$$

In *Fig. 29* the total I_T as the function of w is plotted with dots. According to *Stephens* and *Greenwald* (1991), the inverse terrestrial flux transmittance (I_T) may be related to the terrestrial graybody optical thickness of the atmosphere, and consequently, it is directly related to the atmospheric water vapor content. In *Stephens et al.* (1993) a linear relationship in the form of $I_T' = a + c * w$ was also assumed, where a and c are regression constants.

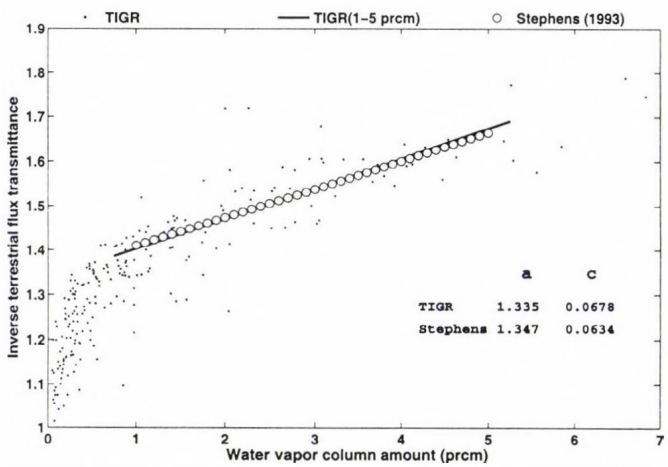

Fig. 29. Dependence of inverse terrestrial flux transmittance on water vapor column amount.

Based on satellite observations of *OLR*, w, and sea surface temperature, Stephens obtained the global annual mean distribution of I_T and computed the regression coefficients a and c for the year of 1989. His results are also displayed in *Fig. 29* as open circles. The thin solid line in the plot, which is representing the total simulated I_T, was obtained by a linear fit using the points

falling within the 1.0–5.0 prcm range. Regarding all the assumptions we made, and the accuracy of the satellite derived quantities in *Stephens et al.* (1993), this agreement is excellent, and at least in the 1–5 prcm range of w, the linear parameterization of the global greenhouse effect by the I'_T quantity looks adequate. However, the simple two-parameter characterization of the planetary greenhouse effect by I'_T for the full range of variability of w is not sufficient. Note, that Stephens curve fails to converge properly to 1.0 at low optical thickness, which is expected by the theoretical value I''_T. This tendency is reproduced pretty well by the simulated values.

4.4 Greenhouse temperature changes

The clear indication of the presence of the planetary greenhouse effect is the fact, that the global average surface temperature is much higher than the effective planetary temperature which is computed from the global average *OLR*. As we have shown in the introduction, using the ERBE data one may easily estimate the effective planetary temperature. The temperature difference, using an estimated 288 K global average surface temperature will result in an all-sky planetary greenhouse effect of 35 K. This corresponds to a global average $\hat{g}$ factor of 0.4.

In our data set t_E equals to 257.7 K, and t_G equals to 285.3 K. The temperature difference – we may call it clear-sky greenhouse temperature rise – is $dt_G = t_G - t_E = 27.91$ K, which is consistent with the theoretically predicted value: $dt_G = [OLR/(1-\hat{g})/\sigma]^{0.25} - t_G = 27.5$ K, and $\hat{g}$ is obtained from Eq. (8). The dependence of the local dt_G – computed as the difference of the local surface temperatures and effective temperatures – on the water vapor column amount is given in *Fig. 30.*

There are several possibilities to partition the dt_G function into the FIR, MIR, and WIN spectral regions. Here the dt_G components are weighted values with the corresponding spectral components of A_A. The dt_G dependence on w is non-linear, and at higher w, dt_G exhibits some saturation tendency, obviously related to the thermodynamic control of the column water amount. The greenhouse effect can be parameterized with sufficient accuracy via w, t_S, and O_3. If one insists on using simple formulas, Eq. (22) in *Table 4* reproduces the total greenhouse temperature rise with a correlation coefficient of 0.913. In this case the dependence on t_S and O_3 was ignored. The temperature differences computed from the downward and upward atmospheric emittances would produce practically the same results, therefore, we did not plot it in this figure.

The latitudinal variation of dt_G is presented in *Fig. 31*. The markers are the three degree zonal averages of the total dt_G. The major contributions to dt_G come from the FIR and WIN components, and the relatively sharp peak at the tropical area is caused by the WIN component. The much smaller latitudinal changes in the FIR and MIR components could be related to the same compensation mechanism affecting the FIR and MIR *OLR*s.

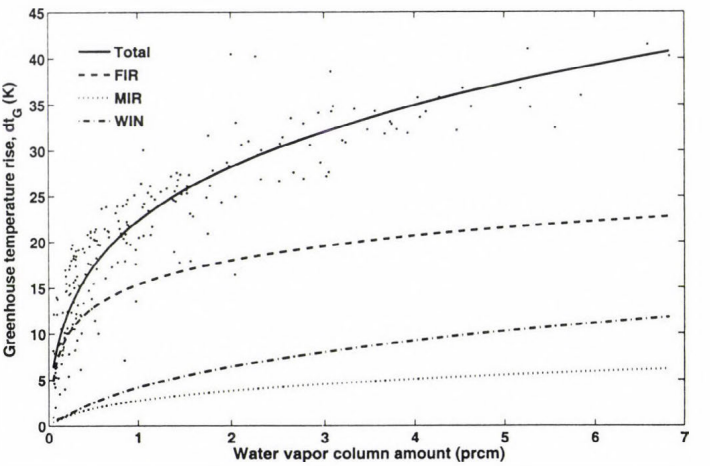

Fig. 30. Dependence of greenhouse temperature rise on water vapor column amount.

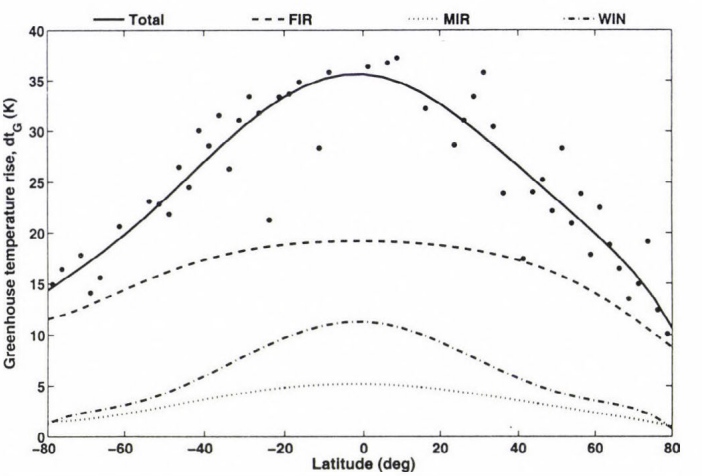

Fig. 31. Latitudinal variation of the greenhouse temperature rise, dt_G.

There are further possibilities to express the magnitude of the greenhouse effect for example, via the total absorbed flux density of the atmosphere, $A_A = S_U - S_T = S_U\ A$, or the downward atmospheric emittance E_D, see *Fig. 20*. In *Fig. 32*, we plot the quantity of $dt_A = t_S - \hat{t}_A$, as the function of w. Here $\hat{t}_A$ may be called as the clear-sky brightness temperature, computed from the total absorbed flux density using the Stefan-Boltzmann law. This figure expresses the fact that with increasing w the surface is getting closer to the radiative equilibrium with the atmosphere. All over the range of w the FIR spectral range is the major contributor to the total dt_A.

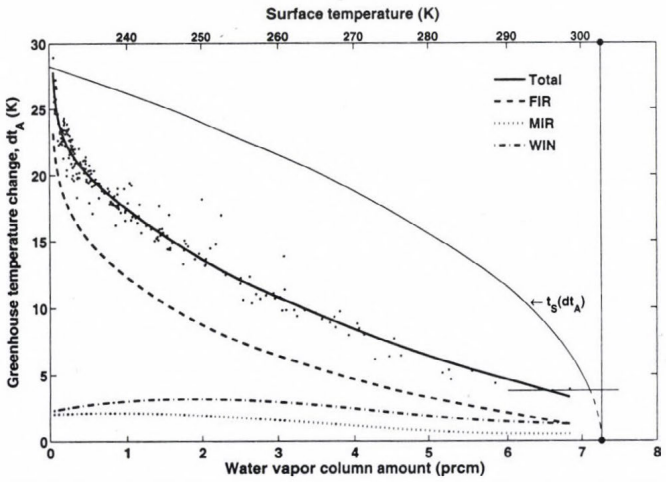

Fig. 32. Dependence of greenhouse temperature change, dt_A, on water vapor column amount and surface temperature.

Just like in the case of the dt_G, these curves are also showing some tendency for saturation at larger w. This tendency, as we mentioned already, is related to the direct thermodynamic control of the water vapor column amount. In *Fig. 32* the $t_S(dt_A)$ function is also plotted with a thin line. The extrapolation of this curve toward the dt_A = 0 line (dashed part of the curve) will point to the critical values of t_S and w, where the radiative cooling of the surface stops. Based on our data set, these values are 303.8 K and 7.38 prcm, respectively. According to the minimum value of dt_A – which is 3.77 K, and marked with a short horizontal line – such situation in the Earth's atmosphere is not likely to happen. Before reaching the above limits, the more efficient thermodynamic and transport processes will take over the re-distribution of the local surface heat energy and the water vapor amount.

None of the above discussed greenhouse parameters are better than the other. Which one to use largely depends on the available data and the nature of the radiative transfer problem at hand. It must be clear, that the greenhouse effect is a large scale phenomenon which requires the existence of the radiative equilibrium as a constraint, both for the temperature profile and the *OLR*. Eqs. (1)–(10) are only valid under the radiative equilibrium condition. Our results show that for global and zonal averages this condition approximately holds. The chances are very little to randomly select an individual vertical air column with its temperature profile in IR radiative equilibrium and measure the greenhouse effect.

Unfortunately, within the frame of this paper we could not go into the full mathematical details of the solution of the Schwazschild-Milne equations and the mathematical proofs of the new equations.

5. Conclusions

Besides the number of interesting details, the most significant result of this research was to establish a qualitative picture of the clear-sky spectral radiative properties of the Earth-atmosphere system in the three most important spectral regions. Several simple and accurate formulas of different physical quantities have been developed for direct use in practical applications. The basic tendency of the meridional variations of the FIR, MIR, and WIN spectral components were derived. We derived fundamental theoretical relationships that strongly supported the simulation results on the H_2O and CO_2 greenhouse effects. These results could be valuable contributions to the general global picture given by *Hansen* (1998), *Paltridge* and *Platt* (1976), or *Peixoto* and *Oort* (1992), or by several others who were not mentioned here. The application of our transfer and greenhouse functions in GCM climate simulations may also improve our understanding of the greenhouse effect in the Earth's atmosphere.

Equations related to the semi-infinite atmospheric model were replaced with new relationships valid for the semi-transparent atmosphere. With the help of the newly introduced transfer and greenhouse functions we established the connection between the theoretical and empirical greenhouse parameters. Probably the most important consequence of the semi-transparent atmospheric model is the significant reduction in the expected response in the surface upward flux density to greenhouse gas perturbations.

Obviously, the presented results have their limitations. The most significant one is related to the temperature profile data base. In some latitudinal belts we had rather few soundings, therefore, it is difficult to set up

selection procedures to obtain statistically consistent data sets for each latitudinal belts. There are virtually unlimited possibilities in increasing the complexity of such simulations by involving more atmospheric and surface parameters. The scientific community dealing with the present and future of the greenhouse effect of the Earth's atmosphere would certainly welcome such extensions of this kind of research. A similar study which deals with the cloud effect is also desirable.

Using an LBL code for the radiative transfer computations was also crucial. The fine details of the transitions of the flux transmittances from the opaque to the transparent spectral regions, especially at higher altitudes, can only be traced with correct mathematical representation of the infrared radiative transfer. Although the speed of computers are improving, the computational burden of doing such simulations on much larger data sets could be a concern.

The presented results in the FIR spectral range are awaiting the confirmation by direct observations. Apparently in the FIR region there is a kind of spectral compensation in effect which prevents the FIR *OLR* to dramatically respond to the poleward temperature decrease. However, statements on the variability of the FIR *OLR* must be supported by a solid FIR climatology, which is based on direct observations. The predicted meridional variation in the total and spectral transmitted flux densities should also be supported by observations. The role of the FIR and WIN spectral regions in forming the greenhouse temperature rise is obvious. One should not forget that the boundaries of the spectral ranges are unique, and changing these boundaries will alter the contributions of the different spectral components. The most critical wave number is the one which separates FIR and WIN regions.

In general, the qualitative picture given above must be validated against direct satellite measurements especially in the FIR spectral range. The first opportunity to gather satellite measured fluxes in the FIR spectral range has just arrived. The utilization of the differences of the coincidental flux measurements from the Terra and Aqua satellites will give us the first measured global radiative fluxes in this important spectral region.

Acknowledgements—This research was supported by the NASA Science Mission Directorate through the EOS project, (contract No. NAS1-02058). Support was also received from *M. Kurylo, D. Anderson,* and *H. Maring* at NASA HQ. We are very grateful to *S. Gupta* at AS&M for his helpful discussions regarding the scientific and technical details of the manuscript.

References

Brindley, H.E. and *Harries, J.E.*, 1997: The impact of far infra-red absorption on greenhouse forcing: sensitivity studies at high spectral resolution. In *IRS'96 Current Problems in Atmospheric Radiative Transfer*. Deepak pub., 981-984.

Brutsaert, W., 1975: On a derivable formula for longwave radiation from clear skies. *Water Resour. Res. 11*, 742-744.

Chedin, A. and *Scott, N. A.*, 1983: *The Improved Initialization Inversion Procedure*. Laboratoire de meteorologie dynamique. Centre National de la Recherche Scientifique, No. 117.

Collins, II, G.W., 2003: The *Fundamentals of Stellar Astrophysics. Part II. Stellar Atmospheres*. WEB edition.

COVE, 2003: COVE Time Synchronized Monthly Archive Files, http://www-svg.larc.nasa.gov.

ERBE, 2004: ERBE Monthly Scanner Data Product. NASA Langley Research Center, Langley DAAC User and Data Services, userserv@eosdis.larc.nasa.gov.

Goody, R.M. and *Yung, Y.L.*, 1989: *Atmospheric Radiation. Theoretical Basis*. Oxford University Press, Inc.

Gupta, S.K., 1989: A parameterization for longwave surface radiation from Sun-synchronous satellite data. *J. Climate 2*, 305-319.

Gupta, S.K., Darnell, W.L., and *Wilber, A.C.*, 1992: A parameterization for longwave surface radiation from satellite data: recent improvements. *J. Appl. Meteorol. 31*, 1361-1367.

Hansen, J.E., Sato, M., Lacis, A., Ruedy, R., Tegen, I., and *Matthews, E.*, 1998: Climate forcings in the industrial era. *Proc. Natl. Acad. Sci. USA, Vol. 95*, 12753-12758.

HITRAN2K, 2002; http://cfa-www.Harvard.edu/HITRAN/hitrandata.

Husson, N., Bonnet, B., Chedin, A., Scott, N., Chursin, A.A., Golovko, V.F., and *Tyuterev, V.G.*, 1994: The GEISA databank in 1993: a PC/AT compatible computers' new version. *J. Quant. Spectrosc. Ra. 52*, 425-438.

Idso, S.B., 1981: A set of equations for full spectrum and 8-14 μ and 10.5-12.5 μ thermal radiation from cloudless skies. *Water Resour. Res. 17*, 295-304.

Kiehl, J.T. and *Trenberth, K.E.*, 1997: Earth's annual global mean energy budget. *B. Am. Meteorol. Soc. 78*, 197-208.

Kratz, D.P., Mlynczak, M.G., Mertens, C.J., Brindley, H., Gordley, L.L., Martin-Torres, J., Miskolczi, F.M., and *Turner, D.D.*, 2005: An inter-comparison of far-infrared line-by-line radiative transfer models. *J. Quant. Spectrosc. Ra. 90*, 323-341.

Miskolczi, F., Bonzagni, M., and *Guzzi, R.*, 1990: High-resolution atmospheric radiance-transmittance code (HARTCODE). In *Meteorology and Evironmental Sciences: Proc. of the Course on Physical Climatology and Meteorology for Environmental Application*. World Scientific Publ. Co. Inc., Singapore, 743-790.

Miskolczi, F. and *Rizzi, R.*, 1998: High accuracy skin temperature retrieval using spectral measurements of multi-channel imagers. *International Radiation Symposium 1998*, Madison, Wisconsin, USA.

Paltridge, G.W. and *Platt, C.M.*, 1976: *Radiative Processes in Meteorology and Climatology*. Elsevier Scientific Publishing Company.

Peixoto, J.P. and *Oort, A.H.*, 1992: *Physics of Climate*. American Institute of Physics, NewYork.

Raval, A. and *Ramanathan, V.*, 1989: Observational determination of the greenhouse effect. *Nature 342*.

Rizzi, R., Matricardi, M., and *Miskolczi, F.*, 2002: On the simulation of up-looking and down-looking high-resolution radiance spectra using two different radiative transfer models. *Appl. Optics 41*, 940-956.

Rodriguez, R., Jucks, K.W., Lacome, N., Blanquest, G., Valrand, J., Traub, W.A., Khalil, B., LeDoucent, R., Valentin, A., Camy-Peyret, C., Bonamy, L., and *Hartmann J.M.*, 1999: Model, software, and data-base for computation of line-mixing effects in infrared Q branches of atmospheric CO_2. I. Symmetric isotopomers. *J. Quant. Spectrosc. Ra. 61*, 153-184.

Rothman L.S., Rinsland, C.P., Goldman, A., Massie, T., Edwards, D.P., Flaud, J-M., Perrin, A., Camy-Peyret, C., Dana, V., Mandin, J-Y., Schroeder, J., Cann, A., Gamache, R.R., Wattson, R.B., Yoshio, K., Chance, K.V., Jucks, K.W., Brown, L.R., Nemtchinov, V., and *Varansi, P.,* 1998: The HITRAN molecular spectroscopic database and HAWKS (HITRAN atmospheric workstation): 1996 edition. *J. Quant. Spectrosc. Ra. 60,* 665-710.

Rozanov, A., 2001: *Modeling of Radiative Transfer through a Spherical Planetary Atmosphere: Application to Atmospheric Trace Gases Retrieval from Occultation- and Limb-measurements in UV-Vis-NIR.* Dissertation, Institut für Umweltphysik, Universität Bremen.

Rutten, R.J., 2000: *Radiative Transfer in Stellar Atmospheres.* Lecture notes, Utrecht University. 7th edition.

Schneider, E.K., Kirtman, B.P., and *Lindzen, R.S.,* 1999: Tropospheric water vapor and climate sensitivity. *J. Atmos. Sci. 56,* 1650.

Stephens, G.L. and *Greenwald, T.J.,* 1991: The Earth's radiation budget and its relation to atmospheric hydrology. 1. Observations of the clear-sky greenhouse effect. *J. Geophys. Res. 96,* No. D8, 15311-15324.

Stephens, G.L., Slingo, A., and *Webb, M.,* 1993: On measuring the greenhouse effect of Earth. *NATO ASI Series, Vol. 19,* 396-417.

Tobin, D.C., Best, F.A., Brown, P.D., Dedecker, R.G., Ellingson, R.G., Garcia, R.K., Howell, H.B., Knuteson, R.O., Mlawer, E.J., Revercomb, H.E., Short, J.F., Van Delst, P.F.W., and *Walden, V.P.,* 1999: Down-welling spectral radiance observations at the SHEBA ice station: Water vapor continuum measurements from 17 to 26 μm. *J. Geophys. Res. 104,* No. D2, 2081-2092.

Tuzet, A., 1990: A simple method for estimating downward longwave radiation from surface and satellite data by clear skies. *Int. J. Remote Sens. 11,* 125-131.

Vonder Haar, T., 1986: WCP 115, *WMO ITD,* No. 109, pp. 144.

IDŐJÁRÁS

Quarterly Journal of the Hungarian Meteorological Service
Vol. 108, No. 4, October–December 2004, pp. 253–263

Influence of different sensor positions on leaf wetness duration measurements and their effect on the simulation of grapevine downy mildew (*Plasmopara viticola*)

A. Dalla Marta[1*] S. Orlandini[1], M. Ghironi[1] and F. Sabatini[2]

[1]*Department of Agronomy and Land Management, University of Florence, Piazzale delle Cascine, 18 - 50144 Firenze, Italy*
E-mails: anna.dallamarta@unifi.it; simone.orlandini@unifi.it

[2]*Institute of Biometeorology, National Research Council, Via Caproni, 8 – 50135 Firenze, Italy; E-mail: f.sabatini@ibimet.cnr.it*

(Manuscript received February 6, 2004; in final form September 13, 2004)

Abstract—Leaf wetness duration (LWD) is one of the most important variables responsible for development of plant diseases. Thus, its measurement represents the basis for disease forecasting models, developed and applied with the aim of timing fungicide application, for avoiding environmental damages, waste of resources, and money losses. Despite of its importance, there is no widely accepted standard for LWD measurement, and the different measurement principles, sensor designs, and installation positions are responsible for different results affecting the quality of model simulations. For this reason, four leaf wetness sensors were mounted in a vineyard in two different positions, at one quarter and three quarters of the canopy height, and in two expositions, east and west. Measured LWD was analyzed and compared with visual inspections conducted during the experiment in order to establish the performance obtainable from different sensor positionings, and to asses their impact on the simulation of grapevine downy mildew (*Plasmopara viticola*).

Key-words: disease forecasting, simulation modeling, *Vitis vinifera*.

1. Introduction

In every epidemic system, climatic factors play a role of major concern, affecting the parasite and host development, which, in turn, widely controls the whole evolution of the infective processes. In particular, the factor "water" is really important in many phases of disease development. The presence of free water on a plant surface often represents an indispensable condition for the beginning of the contamination phase (*Egger et al.*, 1996). The exigency of

* Corresponding author

water, in terms of leaf wetness duration (LWD), varies from one pathogen to another, therefore, its knowledge becomes fundamental for plant disease forecasting and, consequently, for crop protection.

Pathogen behavior has been classified in relation with its requirements of leaf wetness for the infection development (*Huber* and *Gillespie*, 1992). Five categories have been identified, starting from pathogens strictly dependent on free water (for example, the Oomycetes) to pathogens which have a minimum or no LWD requirement as powdery mildew (*Erysiphe necator*) or, in some cases, which are obstructed by the presence of water on host tissues. The importance of LWD is confirmed by its use as driving variable of many epidemiological models for the simulation and forecasting of many diseases (*Hoppmann*, 1996). Grapevine downy mildew (*Plasmopara viticola*), apple scab (*Venturia inaequalis*), cercospora leaf spot (*Cercospora beticola*), wheat ear rot (*Fusarium graminearum*), etc., are among the most studied diseases for which accurate simulation models using LWD are available (*Hoppman*, 1996). In the last years, in fact, development of simulation models based on agrometeorological variables became more and more important, especially in the field of phytosanitary defence, with the aims to improve the production quality, reduce the costs, and increase the environment safeguarding (*Campbell* and *Madden*, 1990; *Seem et al.*, 2000). On the other hand, at present not every meteorological variable is measured and available with enough accuracy and spatial and temporal resolution to be successfully used by such agrometeorological models (*Maracchi*, 2003).

The main problem is that LWD is not always observed on a routine basis, and for this reason, there is a lack of agreement about a standard sensor design and protocol for the use of sensors. In addition, as most of the sensors measure LWD indirectly and have different physical properties from leaves, sensors require calibration to represent a specific crop (*Getz*, 1991). A particular care is needed to sensor positioning that has to reflect the leaf exposition and inclination as much as possible (*Gozzini et al.*, 1996). Finally, the variable itself has been poorly defined, so it can be said that the methodology of LWD estimation is in a state of infancy (*Magarey*, 1999).

The differences pointed out by many authors between the real and measured LWD (*Caprara* and *Veronesi*, 1992) as well as among measurements carried on by different sensors (*Egger* and *Marinelli*, 1995), had lead to the exigency to analyze the possible influences, that different methods of LWD assessment could have on the forecasting of pathogens attack.

On these basis, the aim of this work was to compare different LWD sensor positionings in the vineyard, and to establish how these different measurements could affect the output of a model that simulates grapevine downy mildew infections using agrometeorological variables.

2. Materials and methods

The experiment was conducted in the Paretaio vineyard, located in Tuscany (central part of Italy), in the northern part of Chianti region, in the period of April–September 2003. Grapevine (*Vitis vinifera*) were cordon trained and spur pruned, rows were north-south oriented, and the spacing was 1.0 m in the rows and 3.0 m between the rows. The canopy was developed between 90 and 210 cm above the ground (*Fig. 1*).

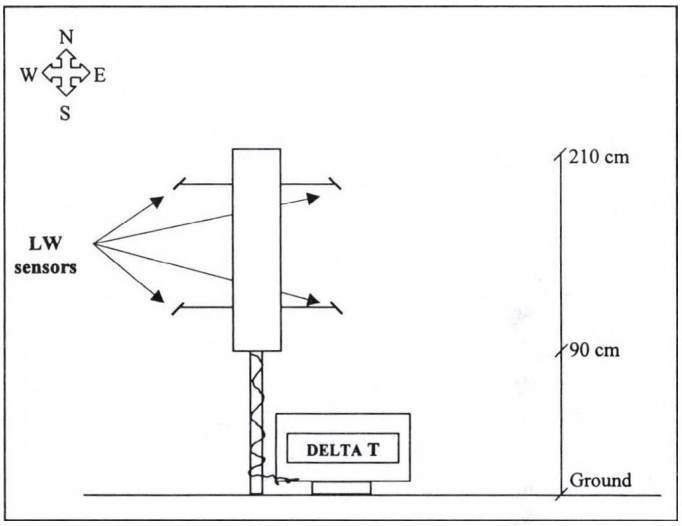

Fig. 1. Scheme of grape canopy and sensor positions connected with the data logger.

Leaf wetness data were collected in 3 different ways: by a single sensor installed on a standard weather station placed near the vineyard; by 4 sensors placed at canopy level; and by visual observations. The sensors (S.W. and W.F. Burrage, Ashford, Kent, U.K.) used in this work were low consumption electronic transducers operating on the basis of resistance variations that occurs in the presence of water. The sensible part of the transducer is constituted by a flat surface made by 3 graphite electrodes separated by a waterproof resin with rough surface in order to increase the active area. The transducer active surface is made by graphite and plastic, then all the complex results to be chemically inert toward the components of phytopathological treatments and organic residuals. The sensor dimensions were 450 mm^2 of active area, 150 mm of length, and 20 mm of diameter. The transducer furnishes a 0-1 logical signal: in fact the presence of water on the active

surface affects the system resistivity and the out signal varies between 0 (dry) and 1 (wet). A drop of distilled water of 1 mm of diameter is sufficient for varying the condition from dry to wet. The sensor response time is lower then 0.5 seconds.

The 4 sensors at canopy level were placed at two different exposures, east and west, and two different heights, one quarter (110 cm above the ground) and three quarters (180 cm above the ground) of the canopy height. Sensors were mounted with an inclination angle of 45° to imitate grapevine leaves position. They were connected with a data logger (Delta-T mod. DL2, Burwell, Cambridge, UK), and the data were recorded with 10 minutes time resolution (*Fig. 1*).

The single sensor was part of the equipment of an agrometeorological station placed just outside of the vineyard. The sensor was exposed to north and mounted with an inclination of 45°. The station was also fitted for air temperature (°C) (Vaisala HMP45, Helsinki, Finland), relative humidity (%) (Vaisala HMP45, Helsinki, Finland), and precipitation (mm) (RGB1, Institute of Hydrology, Wallingford, UK) measurements to collect all the input data required by the epidemiological model. All the sensors were connected to a data logger (Delta-T mod. DL2, Burwell, Cambridge, UK), and in this case the data also were recorded every 10 minutes.

The technique for visual observation of LWD has required some months to be set up. The presence of a layer of water on a leaf, in fact, is clearly visible, the difficulty is to determine the percentage of surface concerned. For this reason two observers were skilled with a series of exercises for determining the percentage of wet surface in special pictures of leaves. At the end of the training the error committed by the two observers was less than 3%.

The visual observations were made in correspondence to the sensor positions in the canopy and the data were recorded every 20 minutes starting from 10 p.m. until the complete surface wetness at night, and from sunrise to the complete dew depletion in the morning. The observations took place during 12 rainless nights and were made on 40 leaves (20 eastward and 20 westward, 10 for each canopy height). The observations were carried on with the help of some powerful electric torches to determine the percentage of leaf surface covered by water, and the threshold for considering a whole leaf as wet was 10% of its surface. LWD beginning and ending were recorded when at least 50% of the sampling was wet or dry. These data were taken separately to compare the visual observations to the sensor measurements, while to compare the observations and sensor measurements to the data recorded by the agrometeorological station outside the vineyard, the 4 positions data were considered together as a single set and LWD was considered to begin and finish, when at least 3 of the 4 positions were wet or dry.

To compare sensor measurements with visual observations, statistical analyses were carried out in two different ways; the first control was made among visual observations, the set of inside canopy sensors, and the outside sensor to compare the proportion of hours correctly classified as wet and dry using a dichotomous categorical verification (*Wilks*, 1995). In this case the statistical indices used were: "Probability of Detection" (POD) representing the probability to measure correctly the observed event; "Critical Success Index" (CSI) representing the ability of the measure to discriminate between yes and no observations; "Bias" that is the ratio of the number of yes measures to the number of yes observations, and it is an index of over- or under-estimation of LWD.

The second control was made by calculating the statistic indices of mean absolute error (MAE), root mean squared error (RMSE), and mean real error (MRE) for the time of wetting and drying and for the length of individual wetness periods both visually observed and recorded by sensors in each position.

Afterwards, LWD data measured at canopy level and outside the vineyard were used to feed the grapevine downy mildew simulation model Plasmo. The mathematical model Plasmo has the purpose to estimate the severity (%) of the grapevine downy mildew disease development through the principal biological stages: primary infection, loss of vitality, sporulation, infection, and incubation (*Orlandini* and *Rosa*, 1997; *Rosa* and *Orlandini*, 1997). Besides LWD, the corresponding meteorological inputs required at hourly interval (temperature (°C), relative humidity (%), precipitation (mm)) were measured by the weather station located outside the vineyard.

In order to compare the simulation model performances obtained using different LWD data, visual surveys of the disease were made during the season in the Paretaio vineyard. The observations were made by two skilled technicians every month from May to September in samples of 100 leaves each randomly chosen in untreated plots of the vineyard. Differences between downy mildew simulations and observations were statistically analyzed by calculating MAE, RME, and RMSE values.

3. Results

3.1 Leaf wetness observations in relation to sensor position

A comparison between the set of sensors placed in the canopy and the set of observations showed a tendency of sensors to underestimate LWD, with a bias of 0.64 (*Table 1*). On the contrary, comparing both the set of observations and

the set of inside canopy sensors with the outside canopy, this latter always overestimated the phenomenon as demonstrated by the bias values, 1.60 and 1.56 for inside canopy sensors and observations, respectively (*Table 1*). POD and CSI values showed that the outside canopy sensor gave the best performance; its measurements, compared with observations, led to a POD of 0.93 with a CSI of 0.57, while the inside canopy sensor measurements gave the definitely worst performance, with a POD of 0.50 and CSI of 0.44. The comparison between inside canopy and outside canopy sensors led to an intermediate result (POD 0.91 and CSI 0.54) (*Table 1*).

Table 1. Comparison of proportions of hours that are correctly classified as wet and dry. Legend: POD = Probability of Detection; CSI = Critical Success Index. Observed is referred to the visual observations, Inside and Outside are referred to the set of inside and outside canopy sensors, respectively

	POD	CSI	BIAS
Observed-Inside	0.50	0.44	0.64
Observed-Outside	0.93	0.57	1.56
Inside-Outside	0.91	0.54	1.60

With regard to the measurements of dew onset, depletion, and duration, the comparative analysis could be divided into two parts. The first one compared the 4 different positions of inside canopy sensors with the same 4 positions of visual inspection, and the second one compared the set of inside canopy sensors and observations with the outside canopy sensor.

Table 2. Comparison between the 4 positions of inside canopy sensors and the respective visual observations. Values are expressed in hours. Legend: MRE = Mean Real Error; RMSE = Root Mean Squared Error; MAE = Mean Absolute Error

	Starting			Ending			Duration		
	MRE	RMSE	MAE	MRE	RMSE	MAE	MRE	RMSE	MAE
Up east	0.02	1.22	1.02	0.17	0.30	0.19	0.11	2.01	1.23
Down east	0.08	0.54	0.29	0.20	0.35	0.20	0.45	3.13	2.10
Up west	0.00	0.53	0.33	0.22	0.38	0.22	0.23	3.16	1.16
Down west	0.04	2.32	1.35	-0.03	0.26	0.17	0.59	3.30	2.44

When comparing the 4 different sensor positions and observations (*Table 2*), it could be noticed that for up east and west positions leaf wetness duration errors were evidently lower than the respective down positions. MAE values

were 1.23 and 1.16 hours, respectively, while those for down positions were 2.10 and 2.44 hours. For leaf wetness depletion the errors are really small for every considered position, with a maximum MAE of 22 minutes and minimum of 17.

When the 4 positions were averaged and considered together for analyzing the outside canopy sensor performance, the errors were generally increased in comparison with the sensors considered singularly (*Table 3*). For every considered phase (onset, duration, and depletion) the inside canopy sensors made lower error than the set of the outside canopy sensors that had a clear tendency to overestimate LWD (*Table 3*).

Table 3. Comparison between the visual observation, set of inside canopy sensors and outside sensor. Values are expressed in hours. Legend: MRE = Mean Real Error; RMSE = Root Mean Squared Error; MAE = Mean Absolute Error. Inside and Outside are referred to the set of inside and outside canopy sensors, respectively

	Starting			Ending			Duration		
	MRE	**RMSE**	**MAE**	**MRE**	**RMSE**	**MAE**	**MRE**	**RMSE**	**MAE**
Observed-Inside	0.06	1.00	0.32	-0.52	1.39	1.04	1.06	3.08	1.56
Observed-Outside	-1.05	2.00	1.35	-2.11	1.10	1.54	-2.15	3.03	2.23

3.2 Sensitivity of simulation model Plasmo to different LWD measurements

Plasmo was applied for the Paretaio vineyard during the season April–September 2003. The model was fed with the agrometeorological data collected by weather station outside the vineyard using the data collected by the set of inside canopy sensors with the 4 separate positions and by the sensor outside the vineyard as LWD input data. The model outputs (i.e., simulated infection periods) were then compared with the real infection data.

In general, all the simulations gave a satisfactory performance: in fact, the severity observed at the end of the season was 4.69% and the simulation ranged between 5.13% and 3.29% (*Table 4*). Thus, the low level of errors was also determined by the low infection pressure of grapevine downy mildew, because climatic conditions of 2003 were not favorable for the disease development. During the period June–August, in fact, mean temperature was very high (26°C), the amount of leaf wetness due to dew were very small (184 hours), and rain was low (86 mm). Nevertheless, some considerations have to be pointed out. For example, the comparison between the severity simulated with LWD measured by the sensor placed outside the vineyard, and the set of inside canopy sensors (*Fig. 2*), respectively, showed a slight overestimation and

underestimation of the disease as regards the final observed value. In fact, the observed severity was 4.69%, the outside canopy sensor measurements led to a value of 5.13% while the severity simulated using the inside canopy sensor measurements was 3.35% (*Table 4*).

Table 4. Severity of downy mildew by the end of the season and number of infection periods simulated using the different leaf wetness measurements. Legend: MRE = Mean Real Error; MAE = Mean Absolute Error; RMSE = Root Mean Squared Error. Errors are calculated for the whole season. Inside and Outside are referred to the set of inside and to the outside canopy sensors respectively

Sensor	Severity (%)	Number of infections	MRE	MAE	RMSE
Outside	5.13	8	-0.05	0.69	0.80
Inside	3.35	5	0.94	0.94	1.28
Up east	3.29	5	0.96	0.96	1.29
Down east	3.77	6	0.69	0.79	1.07
Up west	4.95	8	0.00	0.64	0.79
Down west	4.01	6	0.58	0.74	0.98
Observed	4.69	-	-	-	-

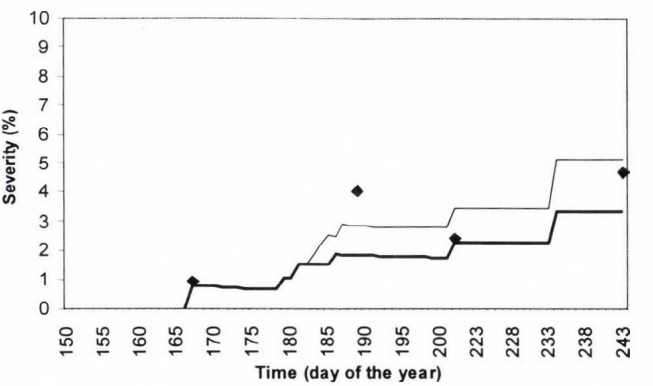

Fig. 2. Downy mildew severity observed (dots), simulated with leaf wetness measured by the outside canopy sensor (thin line) and set of inside canopy sensors (bold line).

A further analysis was carried out by separating the inside canopy sensors according to their single position (*Fig. 3*). It could be noticed that the up west position gave the best result leading to a really unimportant overestimation of the final severity (4.95%) (*Table 4*).

The LWD measurements obtained from the other sensor positions, however, have caused a more or less evident underestimation of downy mildew attack, clearly showed by the positive figures of MRE. Among these, the down west sensor position generated the lowest error (0.58), while the up east generated the highest one (0.96) (*Table 4*). Then, downy mildew severity was best simulated by using the measurements of sensors placed in the west side of the canopy.

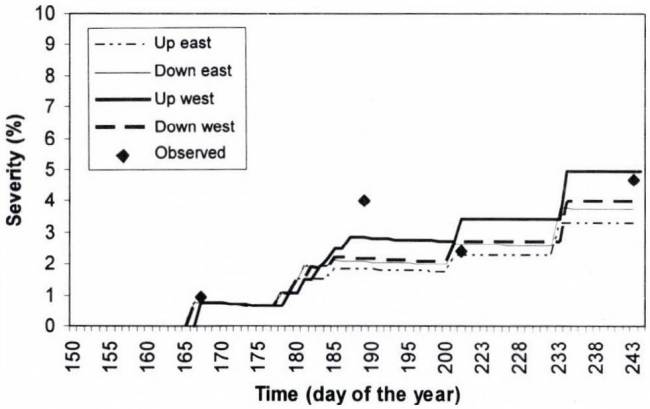

Fig. 3. Downy mildew severity observed (dots) and simulated with leaf wetness measured by the inside canopy sensors.

4. Discussion and conclusions

The analysis of the results highlights, as expected, that the outside canopy sensor always records a longer LWD as compared to the inside canopy sensors. This difference in the amount of wet hours recorded by the instruments was probably due to the fact, that sensors placed directly within the grape canopy were disturbed by the canopy itself. The sensors inside the canopy, in fact, were partly covered by the foliage that, intercepting the sky long wave radiation during the night, causes a slower cooling of the sensor that, in turn, could be traduced in a slower process of dew deposition on its active surface. This idea, in part, is strengthened by the lower error values given by both the upper positions of sensors for LWD. Some previous studies (*Weiss* and *Lukens*., 1981, *Jacobs et al.*, 1990; *Potratz et al.*, 1994) suggested that the best site for a sensor is just below the top of the canopy (approximately at the three quarters of the canopy height) but exposed to the sky radiation, because this position has the greatest surface wetness and, at the same time, some protection from the wind and early morning sun is given.

Looking at the errors made by each single sensor placed within the canopy and set of 4 sensors considered together, this latter raised an averaged value. This result is supported by previous works (*Penrose* and *Nicol*, 1996; *Magarey*, 1999), which indicated that a single sensor, as generally used in standard weather stations, can lead to an imprecise measurement. There are indications that 3 sensors should be used for a mean determination.

According to the previous indications, results of this work suggested that for a good LWD data quality, the best choice would be the positioning of at least 3 LWD sensors placed within the grape canopy. Otherwise, when such a set of sensors is not available, to avoid the variability due to the canopy effect, the choice has to be addressed to the use of a single sensor placed outside the vineyard. Anyway, the required precision of LWD data depends on their further use. In fact, for forecasting plant diseases related to LWD, in order to plan opportunely the crop protection, overestimation of LWD most of the time is more suitable than a slight underestimation, because LWD is a threshold parameter and the model starts to simulate the infections from a certain amount of LW hours. Then, LWD underestimation could induce the model not to detect the disease or to underestimate its severity which, in turn, may induce farmers to avoid treatments which are necessary, because the disease becomes aggressive.

As regards to the simulation of downy mildew attack, it can be safely said that the model was affected by the different LWD measurements. Considering the comparison between the outside canopy sensor, which overestimated LWD, and the set of inside canopy sensors, this latter produced a too low final severity in comparison to the observations (it raised only 3.35%, while the real severity was 4.69%). The outside sensor, determining a slight overestimation of severity, can be considered suitable also regarding farmer requirements.

In general, it can be concluded that LWD sensors do not always supply a precise datum and the precision varies depending on the sensor placement. Furthermore, the need of data precision mainly depend on their further utilization. Disease forecast models, related to LWD, are used to time the application of fungicides and provide effective disease management with the potential to reduce the number of total applications (*Russo, 2000*). These models are then really important in order to carry out a more sustainable and thoughtful agriculture, in respect of the environmental safeguard principles to obtain a safe production of high quality. Because of this extreme importance, besides the need of a suitable standard for sensor design and a protocol for their use, it is necessary to study alternative ways. In particular, the set up of mathematical models, based on agrometeorological variables for the simulation of LWD is a suitable response to the lack of sensor reliability. Moreover, the developments in remote sensing techniques, both with satellite and radar, could

bring a really useful contribution to the assessment of LWD with the advantage to give an output already spatially distributed on the studied territory. The integration of sensors, modeling, and remote sensing, then, could represent the more suitable way for obtaining precise and reliable LWD data.

References

Campbell, C.L. and *Madden, L.V.*, 1990: *Introduction to Plant Disease Epidemiology*. Wiley, New York.

Caprara, C. and *Veronesi, G.*, 1992: La misura dei parametri meteoclimatici in fitoiatria: la bagnatura fogliare. *Informatore Fitopatologico 4*, 29-32.

Egger, E. and *Marinelli, E.*, 1995: Confronto tra diversi sensori ed un metodo per la stima della bagnatura fogliare. *Informatore Fitopatologico 45*, 48-54.

Egger, E., Marinelli, E., and *D'Arcangelo, M.*, 1996: Influenza di diversi metodi per la stima della bagnatura fogliare sulla previsione degli attacchi di peronospora e muffa grigia sulla vite. *Informatore Fitopatologico 3*, 67-61.

Getz, R.R., 1991: Report on the measurement of leaf wetness. *WMO Publication*, No. 2, Geneva, Shwitzerland.

Gozzini, B., Orlandini, S., and *Seghi, L.*, 1996: Influenza della vegetazione e dell'orientamento del sensore sulla rilevazione della bagnatura fogliare. *Informatore Fitopatologico 4*, 55-59.

Hoppmann, D., 1996: *Agarmeteorologische Entscheidungsmodelle im Weinbau am Beispiel der Prognose der Rebenperonospora (Plasmopara viticola)*. Abschlußbericht AM 37, Deutscher Wetterdienst. Geisenheim, pp.75.

Huber, L. and *Gillespie, T.J.*, 1992: Modeling leaf wetness in relation to plant disease epidemiology. *Ann. Rev. Phytopathol. 30,* 53-77.

Jacobs, A.F.G., Van Pul, W.A.J., and *Van Dijken, A.*, 1990: Similarity moisture dew peofiles within a corn canopy. *J. Appl. Meteorol. 29*, 1300-1306.

Magarey, R.D., 1999: A theoretical standard for surface wetness estimation. *Ph.D. Dissertation*. Cornell University, Ithaca, NY.

Maracchi, G., 2003: *Meteorologia e Climatologia applicate* (a cura di). L'Universo, Istituto Geografico Militare, Firenze, Italy.

Orlandini, S. and *Rosa, M.*, 1997: A model for the simulation of grapevine downy mildew. *Petria 7*, Suppl. 1, 47-54.

Penrose, L.J. and *Nicol, H.J.*, 1996: Aspects of microclimate variation within apple tree canopies and between sites in relation to potential *Venturia inequalis* infections. *New Zeal. J. Crop Hort. 24*, 259-266.

Potratz, K.J., Gleason, M.L., Hockmuth, M.L., Parker, S.K., and *Pearston, G.A.*, 1994: Testing the accuracy and precision of wetness sensors in a tomato field and turfgrass. *Journal of Iowa Academic Science 101*, 56-60.

Rosa, M. and *Orlandini, S.*, 1997: Structure and application of the PLASMO model for the control of grapevine downy mildew. *Petria 7*, Suppl. 1, 61-70.

Russo, J.M., 2000: Weather forecasting for IPM. In *Emerging Technologies for Integrated Pest Management: Concepts, Research, and Implementation* (eds.: *G.G. Kennedy* and *T.B Sutton*). APS Press, St. Paul.

Seem, R.C., Magarey, R.D., Zack, J.W., and *Russo, J.M.*, 2000: Estimating disease risk at the whole plant level with general circulation models. *Environ. Pollut. 108*, 389-395.

Weiss, A. and *Lukens, D.L.*, 1981: Electronic circuit for detecting leaf wetness and comparison of wwo sensors. *Plant Disease 65*, 41-43.

Wilks, D.S., 1995: *Statistical Methods in the Atmospheric Sciences*. Academic Press, San Diego, CA.

IDŐJÁRÁS

Quarterly Journal of the Hungarian Meteorological Service
Vol. 108, No. 4, October–December 2004, pp. 265–281

Periodicity of the annual precipitation totals in Serbia and Montenegro

Ivana Tošić and **Miroslava Unkašević**

Institute of Meteorology, University of Belgrade,
P.O. Box 368, 11000 Belgrade, Serbia and Montenegro
E-mail: itosic@afrodita.rcub.bg.ac.yu

(Manuscript received February 18, 2004; in final form August 6, 2004)

Abstract—Annual precipitation totals of 13 stations in different parts of Serbia and Montenegro are analyzed for homogeneity, trend, and periodicities. The data cover time periods ranging from 50 to 70 years. Autocorrelation spectral analysis (ASA) and multitaper method (MTM) are used to investigate the periodicity of precipitation series. Spectral analysis shows peaks at frequencies corresponding to the following time periods: about 2.5–5, 8, and 14–23.3 years. Statistical significance of these peaks is discussed. These results are compared with those of other authors.

Key-words: periodicity, spectral analysis, annual precipitation series.

1. Introduction

Precipitation is one of the key elements that characterize the climate of a region. It is essential to regional water resources, agriculture, and ecosystem environment. Identifying and understanding short timescale precipitation variations is crucial for understanding regional climate variations.

Many authors analyzed the periodicities of annual precipitation in different parts of the world. *Tyson et al.* (1975) found cycles in the South African rainfall data with period ranges of 16–20 years, 3–4 years, and approximately 2 years. *Rodhe* and *Virji* (1976), in their analysis of East African rainfall data, detected spectral peaks at 2–2.5 years, 3.5 years, and 5–5.5 years. *Kousky* and *Chu* (1978), analyzing rainfall series in two large sectors of Northeast Brazil, identified prevalence of spectral peaks with periods of 2–3 years, 3–5 years, and 10–20 years. Also, *Chu* (1984) found

relative maxima of power in the frequency bands of 12.7–14.9, 4.5–4.9, and 2.4 years. A study for Central Europe indicates that short and medium periods with lengths of 2–5 years and 10–16 years appear significant (*Brázdil et al.*, 1985). Over Northern Europe there exists a 16-year cycle, in the southern part of Central Europe there is a longer cycle of 20–22 years, while periods of about 6–7 years (short term) and 10–12 years (medium terms) are evident over much of the continent (*Camuffo*, 1984; *Vines*, 1985).

The present study, motivated by earlier investigations linking regional rainfall anomalies to large-scale circulation, uses time series analysis to identify the dominant bands of these variations.

2. Data used

The basic data consists of annual rainfall totals from 13 stations in Serbia and Montenegro. The stations are shown in *Fig. 1* and listed in *Table 1*. The grouping of stations were done (*Table 1*) subjectively, but using similarities of climatic regimes: Vojvodina lowland and Belgrade, mountainous part of Serbia, and seaside of Montenegro.

Fig. 1. Location of meteorological stations listed in Table 1.

Vojvodina and Serbia have continental climates. The continental regime is characterized by maximum rainfall during summer, especially in June, with a secondary maximum in October, and by minimum precipitation during winter

(in February). Stations at the seaside of Montenegro are under the effect Mediterranean climate. The precipitation regime is controlled mainly by the subtropical Azores anticyclone in summer and the cyclonic circulation over the Tyrrhenian Sea during autumn. Therefore, the minimum precipitation appears in summer, while the maximum is during late autumn. The coast of Montenegro is influenced by the vicinity of littoral chains that exceeds the altitude of 1000 m. These chains enhance the rainfall when moist air is advected from south due to their forced uplift, causing the European maximum (4926 mm/year) of annual precipitation totals (*Ranković et al.* 1981).

Table 1. List of rainfall stations with their latitudes, longitudes, altitudes, and the lengths of available records

Regions and stations	Latitude	Longitude	Altitude (m)	Period
Lowland				
Senta	45°56'	20°05'	80	1926–1995
Kikinda	45°51'	20°28'	81	1926–1995
Zrenjanin	45°24'	20°21'	80	1926–1995
Vršac	45°09'	21°19'	84	1926–1995
Sremska Mitrovica	44°58'	19°38'	81	1926–1995
Belgrade	44°48'	20°28'	132	1926–1995
Mountainous Serbia				
Požega	43°50'	20°02'	310	1926–1995
Kraljevo	43°44'	20°41'	219	1926–1995
Dimitrovgrad	43°01'	22°45'	450	1926–1995
Vranje	42°29'	21°54'	432	1926–1995
Prizren	42°13'	20°44'	402	1926–1995
Coastal Montenegro				
Herceg-Novi	42°27'	18°33'	10	1951–2000
Bar	42°06'	19°06'	4	1951–2000

2.1 Homogeneity

The relative homogeneity of the series was tested according to *Alexandersson* (1986). The standard normal homogeneity test for the precipitation is based on the assumption that the ratio of values at the station being tested (test station) to values of a neighboring station (reference station) is fairly constant in time. The number of reference stations should be large enough to mask any eventual non-homogeneities in the reference data. The appropriate number of reference stations depends on the station network density and data quality. The central idea was to use the reference stations that are best correlated with the test station.

A test parameter T is computed for each of the $N-1$ possible change points in the time series:

$$T(m) = a\overline{P}_1^2 + (N-m)\overline{P}_2^2, \quad a = 1,2,...,N-1, \tag{1}$$

where $\overline{P}_1$ is the mean value of P during the m first years, and $\overline{P}_2$ is the mean value during the $(N-m)$ last years. The value of m is the year most probable for break. The maximum T value in the time series is denoted by T_x:

$$T_x = \max\{T(m)\}, \quad m = 1,2,...,N-1. \tag{2}$$

The critical T values for the 5% significance level (T_{95}) are 8.80 for $N = 70$, and 8.45 for $N = 50$ (*Alexandersson*, 1986). Inhomogeneity was assumed to occur in the year for which T reached its maximum value T_x. The exact year for the break was decided by station history.

In our testing of 13 precipitation series, 12 were found to be homogenous, while series of Prizren (*Fig. 2*) becomes homogeneous after being adjusted by multiplying values of the period before the inhomogeneity with an adjustment factor.

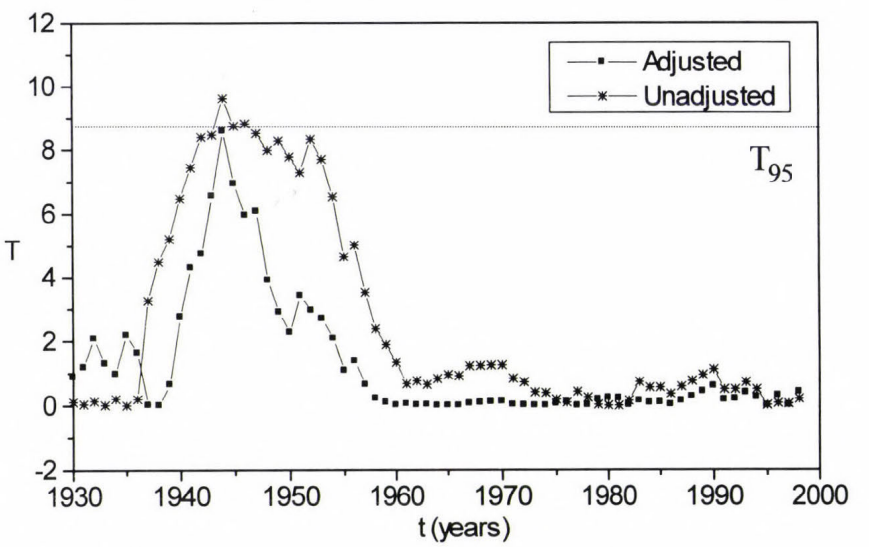

Fig. 2. Results of performing the SNHT on the annual precipitation totals for Prizren.

2.2 Trend

The presence or absence of trend in individual rainfall series have been determined using the Mann-Kendall rank statistic τ (*Kendall* and *Stuart*, 1961). This is defined as:

$$\tau = \frac{4\sum n_i}{N(N-1)} - 1, \tag{3}$$

where n_i is the number of values larger than the ith value in the series subsequent to its position in the series of N values. To apply this statistic to evaluate significance, a comparison is made with:

$$(\tau)_t = \pm t_g \sqrt{\frac{4N+10}{9N(N-1)}}, \tag{4}$$

where t_g is the desired probability point of the standard Gaussian distribution for a two sided test. Linear trend has been determined by conventional least squares regression analysis. In both types of trend evaluation, the 5% level of significance has been taken for the rejection of the null hypothesis of no trend for individual sets of data. For all stations, except for both stations at coastal Montenegro, τ lies within the range $-(\tau)_t$ and $+(\tau)_t$, so the sequence of annual precipitation totals should be assumed random.

To understand the nature of trend, and in order to remove high frequency oscillations, the series were subjected to a low-pass filter. *Hu et al.* (1998) assigned different weights to each of the 11-years in the moving average: 1/24, 1/24, 1/12, 1/8, 1/8, 1/6, 1/8, 1/8, 1/12, 1/24, and 1/24. This removes variations with periods shorter than 10 years in the time series, and retains variations of inter-decadal time scales. The symmetry of the weight distribution guarantees no phase shift of the variations in the time series after the filter is applied. *Fig. 3* shows annual precipitation, moving average, and slopes corresponding to linear trend. Stations in Vojvodina and Montenegro (significant at the 5% level) show negative trends, while stations at the mountain regions of Serbia show positive trends.

According to *Schönwiese* and *Rapp* (1997), there have been marked increases in precipitation in the latter part of the 20th century over Northern Europe with a general decrease southward to the Mediterranean. Hence, our results agree with results obtained by *Schönwiese* and *Rapp* (1997). Dry wintertime conditions over Southern Europe and the Mediterranean and wetter than normal conditions over many parts of Northern Europe and Scandinavia

are linked to strong positive values of the North Atlantic Oscillation (NAO), with more anticyclonic conditions over Southern Europe and stronger westerlies over Northern Europe (*IPCC*, 2001).

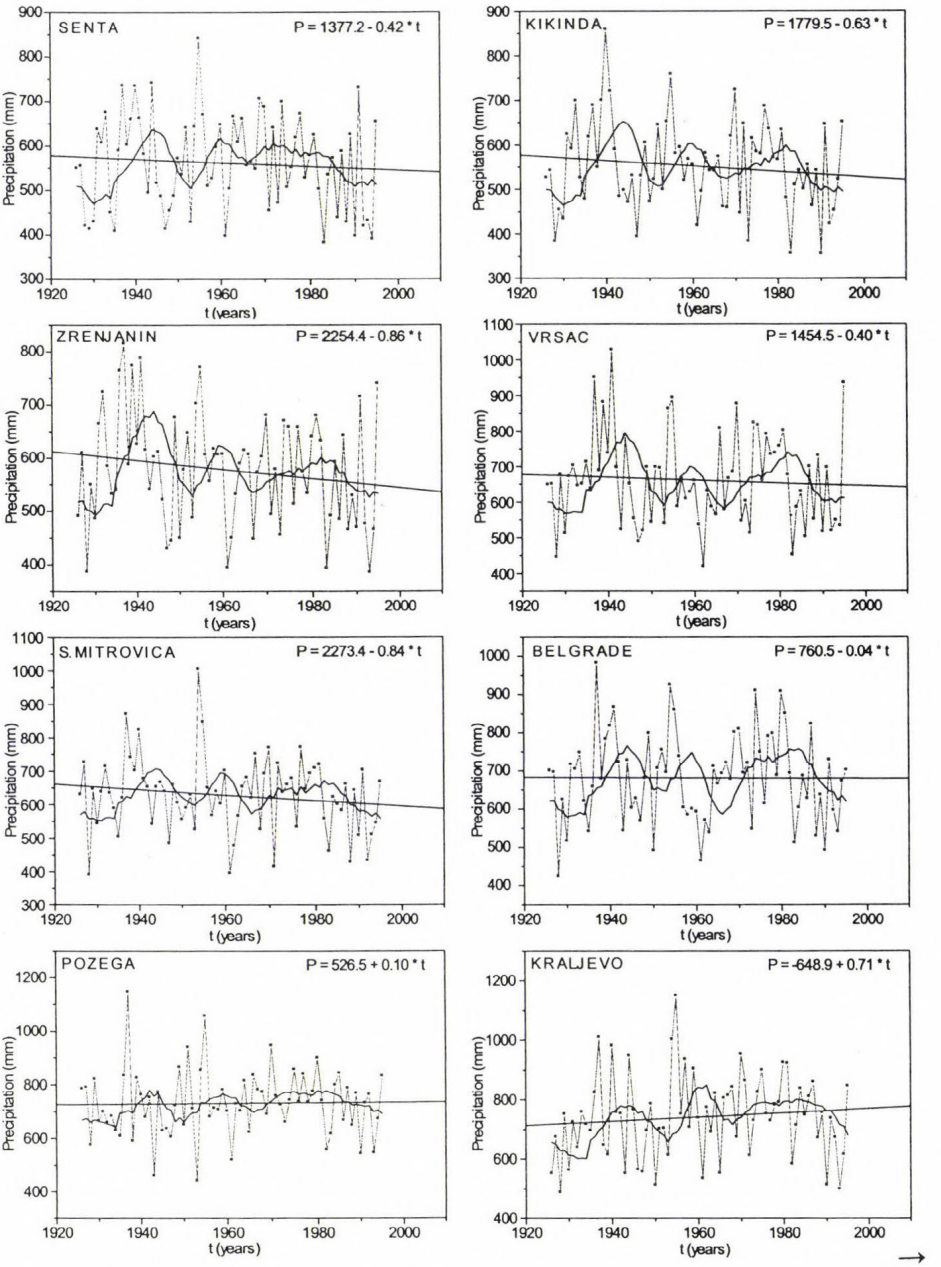

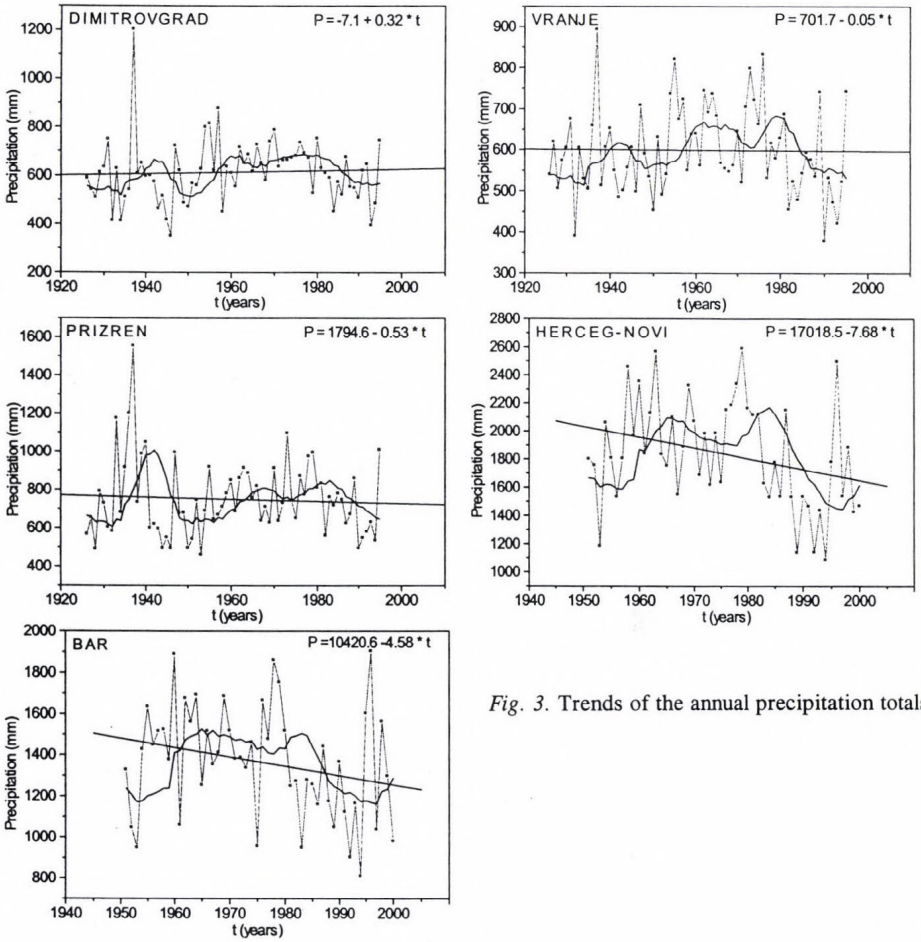

Fig. 3. Trends of the annual precipitation totals.

3. *Spectral analysis*

3.1 Methodology

Spectral analysis of discrete meteorological data sequences plays an important role in data analysis, interpretation, and searches for periodicities. Time series analysis methods aim to examine temporal sequences of data in terms of its frequency content. Various methods for estimating the spectral density function are used. In this study the power spectra of annual standardized anomalies were analyzed using the autocorrelation spectral analysis (ASA) (*Blackman* and *Tukey*, 1958; *Mitchell et al.*, 1966) and the multitaper method (MTM) (*Thompson*, 1982; *Park et al.*, 1987). The ASA is obtained by applying the discrete Fourier transform (DFT) algorithm to the correlation functions

estimated from time series, and taking the classical Hamming window as smoothing function. The averaging operation of raw spectral estimate is necessary in order to obtain a consistent estimate of the spectrum in terms of discrete estimates. In order to determine the significant peaks in the calculated spectra, the theoretical curve (null continuum) along with its associated 95% confidence level has been fitted as described by *Mitchell et al.* (1966).

Following *Tukey* (1950), the ratio between the spectral estimate and the null continuum ("white" or Markov "red noise") for any spectral component follows a Chi-square distribution (χ^2) divided by the degrees of freedom

$$\nu = \frac{2N - \frac{m}{2}}{m}, \tag{5}$$

where N is the record length analyzed, and m is the maximum lag considered in the computation of the correlation function. Thus, if we fix a confidence limit of, e.g., 95%, and compute the probability point for the χ^2 distribution at this percentage, the empirical spectral component will be significant if the ratio of the power associated with a peak in the spectrum to the local power level of the null continuum is greater than this probability point. In our case a maximum lag of $m = N/2$ is considered with a degree of freedom of 3.5, and thus a probability point close to 2.5 is used.

One of the more sophisticated methods is the MTM approach using multiple orthogonal data tapers to describe structures in time series. The statistical information discarded by the first taper is partially recovered by the second taper, the information discarded by the first two tapers is partially retrieved by the third, and so on. Only a few low-order tapers may be employed, as the spectral leakage increases with increasing order. For a given time series $x(t)$, we determine a set of S orthogonal Slepian data tapers (*Slepian*, 1978) $a_s(t)$, and their S associated tapered Fourier transforms or eigenspectra $Y_s(f)$, $s = 1,...,S$, as:

$$Y_s(f) = \sum_{t=1}^{N} a_s(t)x(t)e^{-i2\pi f t\Delta t}, \tag{6}$$

where Δt is the sampling interval.

The multi-taper spectral estimate can provide a description of an irregular oscillatory signal centered at a particular frequency f, since it can describe a variety of amplitude and phase modulations using a suitable linear combination of the S independent eigenspectra. The independent eigenspectra can be combined through a weighted average as follows:

$$\bar{Y}(f) = \frac{\sum_{s=1}^{S} \lambda_s |Y_s(f)|^2}{\sum_{s=1}^{S} \lambda_s}, \tag{7}$$

where the eigenvalues λ_s come from the eigendecomposition. The linear combination of eigenspectra given by $\bar{Y}(f)$ provides a power spectrum with optimal trade-off properties between spectral resolution and variance (*Thompson*, 1982; *Park et al.*, 1987). According to *Park et al.* (1987), only the first $K = 2p$ (p is the time-frequency bandwidth parameter) are known to have the best spectral properties, as their leakage fractions are very close to zero.

The significance of periodic signals or quasi-periodic signals was measured with respect to the noise background. The confidence levels of the noise estimate are calculated by assuming that the spectrum has a χ^2_ν distribution with $\nu \approx 2K$ degree of freedom (*Mann* and *Lees*, 1996). The ratio of the power associated with a peak in the spectrum to the local power level of the background is assumed to be distributed as χ^2/ν, and can be compared to the tabulated χ^2 probability distributions to determine peak significance.

3.2 Analysis of the results

Figs. 4 and *5* show results of the annual anomalies obtained by using ASA and MTM, respectively. There is a general agreement between the two spectral methods for shapes of power spectra. However, there are some differences in their power of spectral resolution and signal detectability. In the case of Prizren and Herceg-Novi, the lag-one autocorrelation coefficients differ significantly from zero. The annual precipitation variance spectra in these two cases can be fitted by Markov "red noise" continuum. For the other stations it should be assumed that the "null" continuum is "white noise", since the lag-one autocorrelation coefficients do not differ significantly from zero. With respect to the significant spectral peaks summarized in *Table 2*, an interesting feature is the absence of peaks with spectral density exceeding the 95% confidence level for the "null" continuum for Dimitrovgrad. Spectral analysis shows that the peaks occur mainly within the following three spectral regions: about 2–5, 8, and 14–23.3 years. The quasi-biennial oscillations (QBO) appear at Požega (2.5 years), Prizren (2.0 years), and Herceg-Novi (2.8 years). *Maheras et al.* (1992) and *Gajić-Čapka* (1994) detected the QBO periodicity when studying annual rainfall in the central Mediterranean and Croatia, respectively. *Brázdil* and *Zolotokrylin* (1995) found the QBO in monthly precipitation fields over Europe. *Lana* and *Burgueño* (2000) detected periodicities greater than 2 years in the monthly and spring analysis of rainfall anomalies for Barcelona.

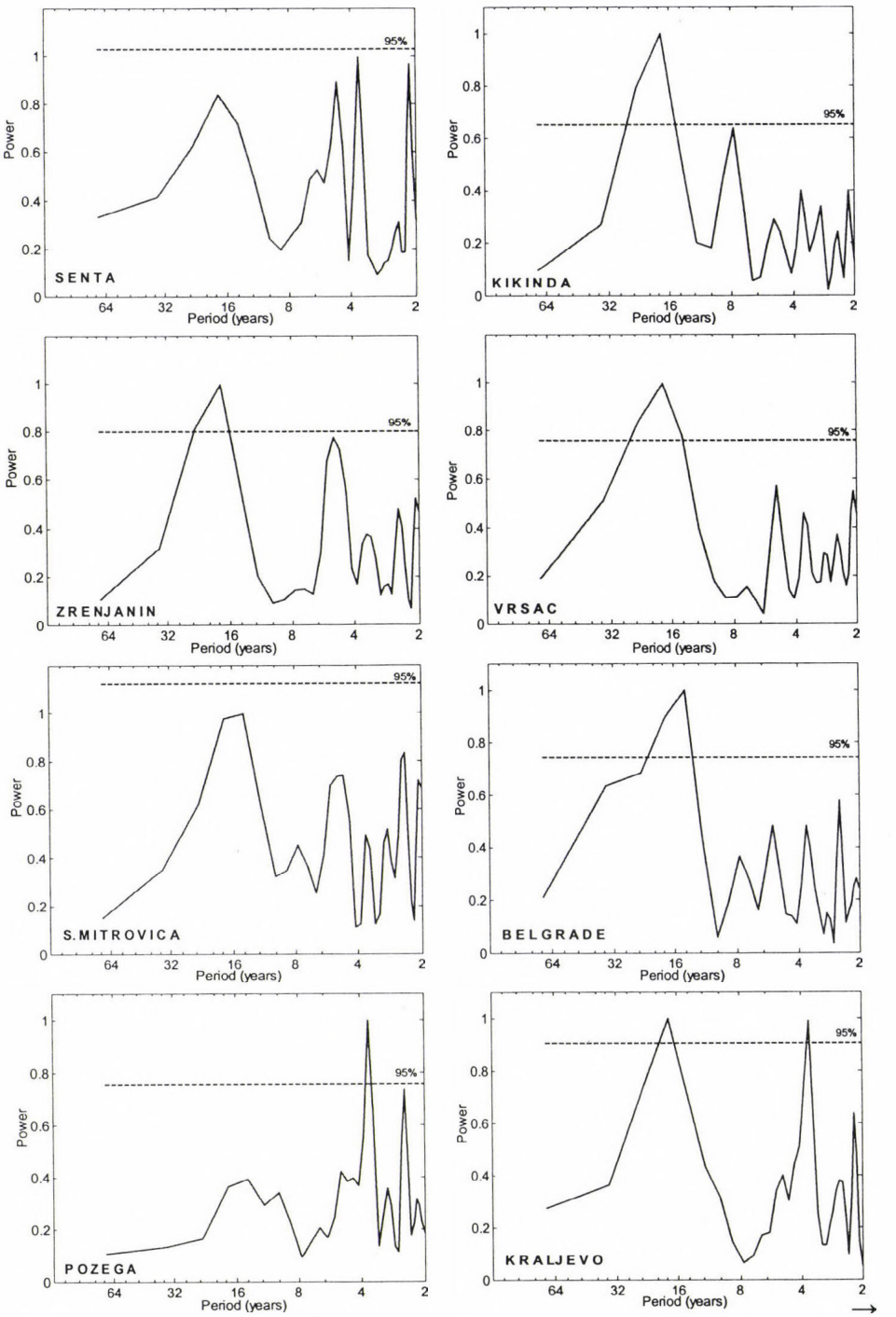
SENTA
KIKINDA
ZRENJANIN
VRSAC
S.MITROVICA
BELGRADE
POZEGA
KRALJEVO
95%
Power
Period (years)
64
32
16
8
4
2
0
0.2
0.4
0.6
0.8
1

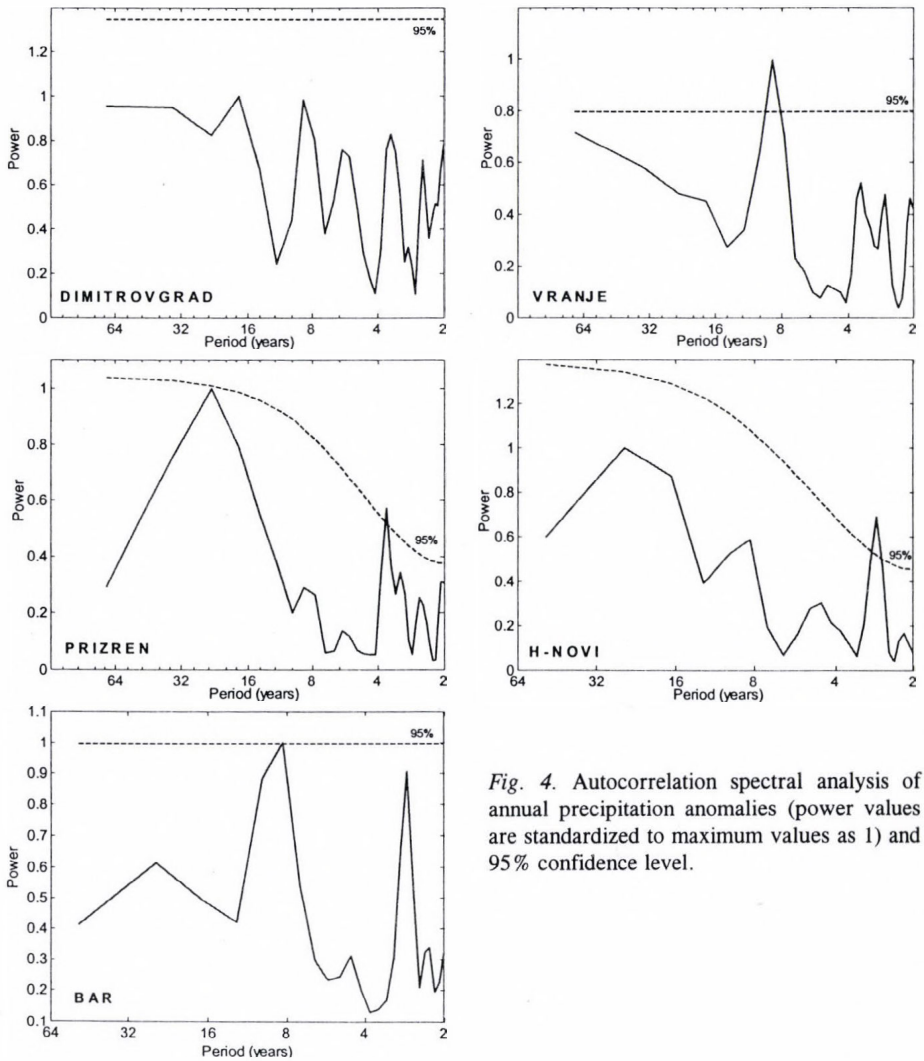

Fig. 4. Autocorrelation spectral analysis of annual precipitation anomalies (power values are standardized to maximum values as 1) and 95% confidence level.

A period of 3.7 years is common for the mountainous part of Serbia: Kraljevo, Požega, and Prizren (*Figs. 4* and *5*). *Brázdil* (1986) found statistically significant cycles in the length of 3.3–3.6 years in Central Europe (Moravia: 3.3 years, Vienna, Poland, Slovakia, Hungary: 3.6 years). *Gajić-Čapka* (1994) detected the periods of 3.6 and 3.7 years for three different climate regions of Croatia. According to *Burroughs* (1992), periodicities in the range of 3–4 and 6 years can be interpreted as higher harmonics of the sunspot cycle. Oscillation of 4.9 years is characteristic for Senta, Sremska Mitrovica, and Zrenjanin annual rainfall anomalies in Vojvodina lowland.

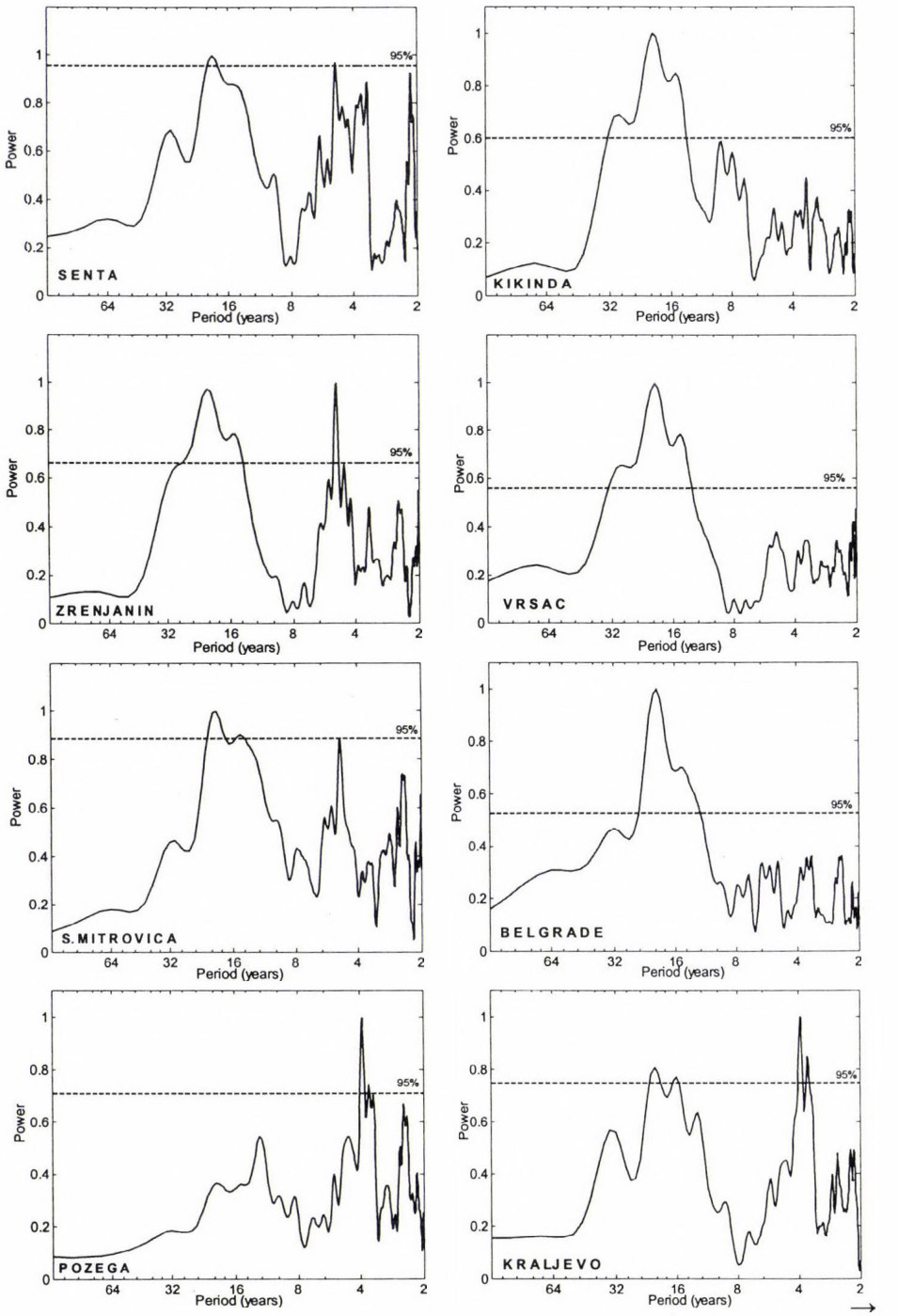
SENTA
KIKINDA
ZRENJANIN
VRSAC
S.MITROVICA
BELGRADE
POZEGA
KRALJEVO
Power
Period (years)
95%
64
32
16
8
4
2
0
0.2
0.4
0.6
0.8
1

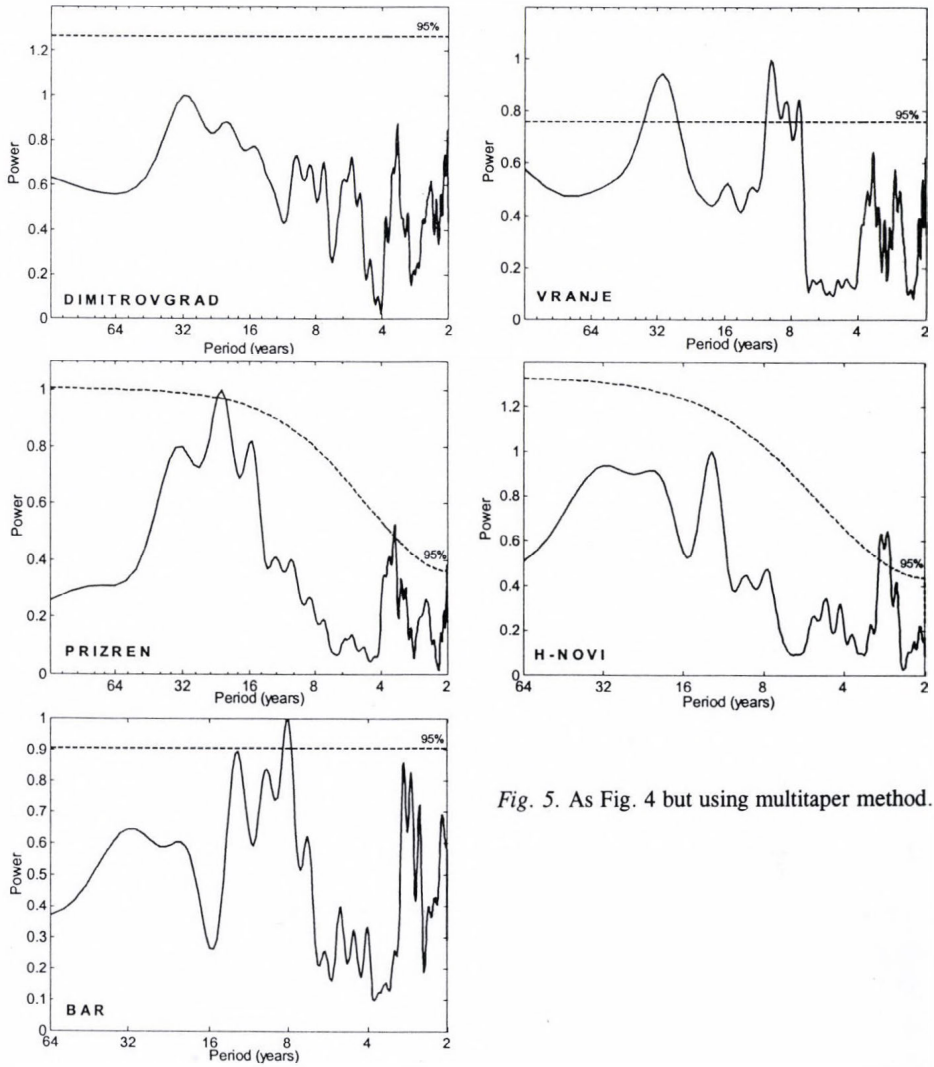

Fig. 5. As Fig. 4 but using multitaper method.

Cycle of about 8 years is detected in the analysis of the precipitation series for Bar (8.3), Kikinda (7.8), and Vranje (8.7). A seven-year period has been reported by several other authors studying different series in the Northern Hemisphere, mainly in Europe, North America, and the North Atlantic Ocean, suggesting that it may be associated with the dynamics of the atmosphere interacting with the North Atlantic Ocean. For example, *Plaut et al.* (1995) and *Banner* (1999) found a cycle of 7.7 years in the Central England temperature time series, *Moron et al.* (1998) found a cycle of 7.5 years in

North Atlantic sea surface temperatures and winter North Atlantic Oscillation Index (NAOI), *Dettinger et al.* (1995) found a cycle of 7.4 years in the United States surface air temperature records.

Table 2. Significant cycles of annual precipitation anomalies according to the 95% confidence level of the power spectra

	2	3	5	8	14	18	23.3
Senta	-	-	4.9	-	-	18.9	-
Kikinda	-	-	-	7.8	-	17.5	23.3
Zrenjanin	-	-	4.9	-	14.0	17.5	23.3
Vršac	-	-	-	-	14.0	17.5	23.3
Sremska Mitrovica	-	-	4.9	-	14.6	17.5	-
Belgrade	-	-	-	-	14.0	17.5	-
Požega	2.5	3.7	-	-	-	-	-
Kraljevo	-	3.7	-	-	-	17.5	-
Dimitrovgrad	-	-	-	-	-	-	-
Vranje	-	-	-	8.7	-	-	-
Prizren	2.0	3.7	-	-	-	-	23.3
Herceg-Novi	2.8	-	-	-	-	-	-
Bar	-	-	-	8.3	12.5	-	-

Oscillation corresponding to medium periods of about 14–23.3 years is a feature of Vršac (14–23.3), Zrenjanin (14–23.3), Kikinda (17.5–23.3), Belgrade (14–17.5), Sremska Mitrovica (14.6–17.5), Senta (18.9), Kraljevo (17.5), and Prizren (23.3). *Vines* (1985) found a cycle of 20–22 years over the southern part of Central Europe and a cycle of about 16 years for the northern part. *Maheras* and *Vafiadis* (1991) found a periodicity close to 22 years by studying annual and spring rainfalls. The double sunspot cycle has been also detected by *Rodríguez et al.* (1999) analyzing monthly series and by *Lana* and *Burgueño* (2000) in the monthly and summer rainfall anomalies for Barcelona. *Tošić* and *Unkašević* (2004) noted an oscillation of 13.3–16 years in the annual and winter precipitation series in Belgrade during the period 1889–2000.

Similarity between our spectral peaks and those for the European studies, cited above, suggests that possibly a feature of the large scale circulation pattern may be responsible for the observed fluctuations. One of the possibilities is a teleconnection with the North Atlantic Oscillation expressed by NAO Index (NAOI) (*Hurrel*, 1995). It is defined as normalized pressure difference between Ponta Delgrada (or Gibraltar) and Reykjavik. *Table 3* shows the correlation between precipitation series and NAOI. All stations

except for Sremska Mitrovica show significant negative correlation with NAO. *Reljin et al.* (2002) found significant influence of the NAO to the climate in Yugoslavia through several linear and non-linear methods of analysis.

Table 3. Correlation coefficient between the North Atlantic Oscillation and annual precipitation series

Stations	NAOI
Senta	-0.4402 **
Kikinda	-0.4336 **
Zrenjanin	-0.4000 **
Vršac	-0.3745 **
Sremska Mitrovica	-0.1949
Belgrade	-0.3323 **
Požega	-0.3723 **
Kraljevo	-0.3493 **
Dimitrovgrad	-0.2539 *
Vranje	-0.2772 *
Prizren	-0.2855 *
Herceg-Novi	-0.4075 **
Bar	-0.4218 **

* significant at 95% confidence level
** significant at 99% confidence level

4. Conclusions

Annual precipitation totals of 13 stations in different parts of Serbia and Montenegro were analyzed for homogeneity, trend, and periodicities. The normalized annual precipitation series reveal significant negative trend at 95% confidence level for coastal Montenegro series, non-significant negative trend for Vojvodina, and non-significant positive trend for mountainous Serbia.

Quasi-biennial (about 2.5 years) and quasi-triennial (3.7 years) oscillations, as well as oscillation with medium periods (14–23.3 years) found over Serbia and Montenegro are consistent with the quasi-periodic oscillation reported in other studies on fluctuations of European annual precipitation. The 7-year period, reported by several authors studying different series in the Northern Hemisphere, mainly in Europe, North America, and the North Atlantic Ocean, has been identified in this study, too. The large scale circulation pattern may be responsible for the observed fluctuations. Strong influence of a large-scale phenomenon, the North Atlantic Oscillation, on the precipitation series in Serbia and Montenegro was found.

References

Alexandersson, H., 1986: A homogeneity test applied to precipitation data. *J. Climatol. 6*, 661-675.

Banner, T.C., 1999: Central England temperatures: long-term variability and teleconnections. *Int. J. Climatol. 19*, 391-403.

Blackman, R.B. and *Tukey, J.W.*, 1958: *The Measurement of Power Spectra*. Dover Publications, New York.

Brázdil, R., 1986: *Variation of Atmospheric Precipitation in the CSSR with Respect to Precipitation Changes in the European Region*. Folia Fac. Sci. Nat. Univ. Purk Brun, Geographia 22, Brno.

Brázdil, R. and *Zolotokrylin, A.N.*, 1995: The QBO signal in monthly precipitation fields over Europe. *Theor. Appl. Climatol. 51*, 3-12.

Brázdil, R., Šamaj, F., and *Valovič, Š.*, 1985: Variation of spatial annual precipitation sums in Central Europe in the period 1881-1980. *J. Climatol. 5*, 617-631.

Burroughs, W.J., 1992: *Weather Cycles, Real or Imaginary*? Cambridge University Press, Cambridge, 201 pp.

Camuffo, D., 1984: Analysis of the series of precipitation at Padova, Italy. *Climatic Change 6*, 57-77.

Chu, P.S., 1984: Time and space variability of rainfall and surface circulation in the northeast Brazil-tropical Atlantic sector. *J. Meteorol. Soc. Japan 26*, 363-369.

Dettinger, M.D., Ghil, M., Strong, C.M., Weibel, C.M., and *Yiou, P.*, 1995: Software expedities singular-spectrum analysis of noisy time series. Eos, Trans. American Geophysical Union *76*(2), 12-21.

Gajić-Čapka, M., 1994: Periodicity of annual precipitation in different climate regions of Croatia. *Theor. Appl. Climatol. 49*, 213-216.

Hu, Q., Woodruff, C.M., and *Mudrick, S.E.*, 1998: Interdecadal variations of annual precipitation in the Central United States. *B. Am. Meteor. Soc. 79*, 221-229.

Hurrel, J.W., 1995: Decadal trends in the North Atlantic Oscillation regional temperatures and precipitation. *Science 269*, 676-679.

IPCC, 2001: *Climate Change 2001: The Scientific Basis*. Cambridge University Press, Cambridge, 881 pp.

Kendall, M.G. and *Stuart, A.*, 1961: *The Advanced Theory of Statistics 2*. Charles Griffen, 483-484.

Kousky, V.E. and *Chu, P.S.*, 1978: Fluctuations in annual rainfall for Northeast Brazil. *J. Meteorol. Soc. Japan 56*, 457-465.

Lana, X. and *Burgueño, A.*, 2000: Statistical distribution and spectral analysis of rainfall anomalies for Barcelona (NE Spain). *Theor. Appl. Climatol. 66*, 211-227.

Maheras, P. and *Vafiadis, M.*, 1991: Fluctuations temporelles des precipitations à Sofia et à Thessaloniki durant la dernière pèriode seculaire. *Societa Geogr. Italiana XVI*, 543-553.

Maheras, P., Balafoutis, C., and *Vafiadis, M.*, 1992: Precipitation in the central Mediterranean during the last century. *Theor. Appl. Climatol. 45*, 209-216.

Mann, M.E. and *Lees, J.M.*, 1996: Robust estimation of background noise and signal detection in climatic time series. *Climatic Change 33*, 409-445.

Mitchell, J.M. et al., 1966: Climatic change. *WMO Tech. Note 79*. WMO No. 179, Geneva, 79 pp.

Moron, V., Vautard, R., and *Ghil, M.*, 1998: Trends, interdecadal and interannual oscillations in global sea-surface temperatures. *Clim. Dynam. 14*, 545-569.

Park, J., Lindberg, C.,. and *Vernon, F.L.*, 1987: Multitaper spectral analysis of high-frequency seismograms. *J. Geophys. Res. 92*, 12675-12684.

Plaut, G.R., Ghil, M., and *Vautard, R.*, 1995: Interannual and interdecadal variability in 335 years of central England temperature. *Science 268*, 710-713.

Ranković, S., Radičević, D. and *Sokolović-Ilić, G.*, 1981: Basic characteristics of the precipitation distribution in Yugoslavia - Contribution to the maps of *Climate Atlas, Note 2*. Federal Hydrometeorological Institute of Yugoslavia, Belgrade, Yugoslavia, 226 pp.

Reljin, I., Jovanović, G., and *Reljin, B.*, 2002: The analyses of FRY climate and NAO teleconnection. *Proc. Conf. on Information Technologies-Present and Future*, IT '02 Zabljak, 33-37.

Rodhe, H. and *Virji, H.*, 1976: Trends and periodicities in East African rainfall data. *Mon. Weather Rev. 104*, 307-315.

Rodríguez, R., Llasat, M.C., and *Wheeler, D.*, 1999: Analysis of the Barcelona precipitation series 1850-1991. *Int. J. Climatol. 19*, 787-801.

Schönwiese, C.D. and *Rapp, J.*, 1997: *Climate Trend Atlas of Europe Based on Observations 1891-1990.* Kluwer Academic Publisher, Dodrecht, 228 pp.

Slepian, D., 1987: Prolate spheroidal wave function, Fourier anaysis and uncertainty, V. The discrete case. *AT&T Tech. J. 57*, 1371-1429.

Thomson, D.J., 1982: Spectrum estimation and harmonic analysis. *Proc. IEEE 70*, 1055-1096.

Tošić, I. and *Unkašević, M.*, 2004: Analysis of precipitation series for Belgrade. *Theor. Appl. Climatol.* (in press).

Tukey, J.W., 1950: The sampling theory of power spectrum estimates. *Symp. on Applications of Autocorrelation Analysis to Physical Problems*. US Office of Naval Research. NAVEX-P-735 47-67, Washington D.C.

Tyson, P.D., Dyer, T.G., and *Mametse, M.N.*, 1975: Secular changes in South African rainfall: 1880 to 1972. *Q. J. Roy. Meteor. Soc. 101*, 817-833.

Vines, R.G., 1985: European rainfall patterns. *J. Climatol. 5*, 607-616.

NEWS

The EMS Young Scientist Award winner in 2004

The European Meteorological Society (EMS) Awards Committee conferred the "Young Scientist Award" on a Hungarian scientist, *Szilvia Horváth* in Nice, France, on September 27, 2004.

Supporting the aspiring young scientists is one of the central activities of the European Meteorological Society. At the first time, the Award was presented at the EMS Annual Meeting in Rome, 2003.

Young scientists from the EMS Member countries are entitled to receive this Award. According to the requirements, the candidate must have written a high quality publication published during the previous three years in a reviewed international scientific journal, or an outstanding PhD thesis. Qualification also needs a supporting statement by the EMS Member Society (in this case by the Hungarian Meteorological Society), too.

In order to support excellence among young European scientists, EMS honors each year one promising candidate with the Award. This Award includes a diploma and a sum of 1000 EUR. The winner is also invited for participation in the EMS Annual Meeting, where the Award is presented.

The year 2004 Award was conferred on the author for her PhD thesis entitled "20th century variations of the soil moisture content in East-Hungary".

The Award Ceremony took place during the opening session of the Fourth Annual Meeting of the European Meteorological Society on September 27, 2004. Participants of the Award Ceremony were addressed by *Prof. Werner Wehry*, President of the European Meteorological Society; *Prof. Susan K. Avery,* President of the American Meteorological Society, and *Dr. Arne Spekat,* Executive Secretary of the European Meteorological Society.

At the end of the ceremony, the author expressed her acknowledge to her PhD supervisors, *Dr. János Mika* (Hungarian Meteorological Service) and *Dr. László Makra* (University of Szeged, Department of Climatology and Landscape Ecology), for their advices, ideas, and non-stop co-operation; her colleagues for their support and help, her family for their patience and frequent assistance; the Hungarian Meteorological Society for the recommendation, and the EMS Awards Committee, for the idea and management of this Award.

Summary of the
EMS Young Scientist Award, 2004 winner PhD thesis

20th century variations of the soil moisture content in East-Hungary

by

Szilvia Horváth

*University of Szeged, Department of Climatology and Landscape Ecology, Szeged, Hungary**

Summary—Hungary and the eastern part of the Great Hungarian Plain have always been characterized by significant hydrological extremities. The aim of the dissertation is to give a modern climatographical analysis on the varied hydrometeorological relations of the region, based on reliable observations of meteorological stations. The analysis includes statistical characteristics of the inter-annual variability, spatial, and temporal correlation of the available soil moisture content and long-range changes, as well as their possible relation with climatic trends for greater regions, respectively. The above-mentioned aims are intended to realize on the basis of the *Palmer's Drought Severity Index* (PDSI) data series, known world-wide in the agroclimatological analysis. Monthly PDSI data series of five stations (Miskolc, Nyíregyháza, Debrecen, Kecskemét, and Szeged) were determined for the 20th century (99 years), in three versions: (*a*) plant-covered surface (maize plant) and homogenized; (*b*) bare (not plant-specific) surface, homogenized; and (*c*) plant-covered surface, but non-homogenized meteorological data. For studying the spatial correlation, PDSI sets of 17 stations were calculated for the period between 1951 and 1992. The results are as follows: place-independence of the PDSI is realized, but season-independence is only partly on the Great Hungarian Plain. By analyzing the PDSI sets of each station and month separately, the distribution of the samples can be considered normal. PDSI can correctly be interpreted as a characteristic of the soil moisture content. PDSI anomalies show regional differences and definite structures in the examined region. The high autocorrelation makes it possible to define so called year-types (dry, wet, medium) objectively. The trends for each month and station are negative. Decreasing soil moisture content is connected not only with the time, but the warming characterizing the average of the northern hemisphere, too. Significant wet sub-periods are detected in the first half of the 20th century, while dry breaks occurred in the second half of the century. The two methods for calculating the index (Thornthwaite, Blaney-Criddle) and the homogenisation of the original parameters influence the statistical characteristics of the index series only slightly.

**Present address: Ministry of Environment and Water, H-1394 Budapest, P. O. Box 351, Hungary; E-mail: horvath@mail.kvvm.hu*

Hans Ertel – a pioneer in meteorological sciences

(A brief historical review on the occassion of his 100th birthday)

In 1946 Hans Ertel was appointed professor of Geophysics at the University of Berlin, and director of the Institute of Meteorology and Geophysics. He died suddenly and unexpectedly in 1971. He was visiting professor at the University of Uppsala (Sweden) and met there his old friend, the theoretical meteorologist, Hilding Koehler as well as Markus Bath. Koehler was the tutor of Bert Bolin and contributed significantly to the scientific career of Carl-Gustaf Rossby. It is of historical interest, that Ertel and Rossby met again after the war in Stockholm and Uppsala, when Uppsala invited Ertel to give some lectures. Rossby was the first foreign guest to visit Ertel's institute in Berlin after the war. Rossby's lecture on the waves, later named after him, have shown that this concept was implicitly included in Ertel's paper but they did not became known to the Anglo-American scientific community. It is sadly true that many important papers by Hans Ertel published in the 1940s in the "Meteorologische Zeitschrift" did not get known to researchers in the United States and England due to the war.

A later publication by Ertel, co-authored by Rossby, remained similarly unknown for a period of time. This situation changed when C. Truesdall studied Ertel's papers and presented a general survey in his well-known paper in the "Handbuch der Physik".

With the re-opening of the Institute of Meteorology, Ertel started many successful projects both as university professor and researcher. His activity became even broader, when in 1948 he was appointed director of the Institute of Physical Hydrology of the German Academy of Sciences (DAW) in Berlin. In this institute he continued his hydrodynamic research and, in addition, he started to tackle, with his staff, important geoecological issues. These activities are considered today as pioneering work. The fields of research of this institute, e.g., theoretical hydrodynamics, the special hydrography of Northern German lakes and coasts (coast protection), hydraulic nomography, hydrographic cartography, and the weather history of Europe, were successfully studied by a small staff and led within a short time to a high international reputation for the institute. Many results were published in the journal of the institute, "Acta Hydrophysica", and Curt Weikinn succeeded in publishing an internationally recognized source-book on weather history. In later years Ertel was increasingly engaged in problems of coast protection in the framework of the activities of the Academy, and this research resulted in new insights in for example the theory of lake embankment, the problem of sudden increases of the sea level, as well as many new results in theoretical geomorphology. Ertel published a considerable part of his work in the "Monatsberichte der Deutschen Akademie der Wissenschaften" (Monthly Reports of the German Academy of Sciences). This journal was not very well

known internationally, and these important papers became better known only later (through, for example, Scheidegger's "Theoretical Geomorphology"). Ertel treated meteorological problems, too, as shown by his studies "Influence of the orography on the development of weather" in the framework of the Conferences on Carpathian Meteorology.

In 1949 Ertel was elected to be an ordinary member of the German Academy of Sciences in Berlin and became its vice president for ten years. During this time many new institutes of the Academy were founded, and German-German co-operation was promoted. For the latter, Ertel joined forces with Julius Bartels, especially within the framework of the International Geophysical Year. Ertel participated intensively in other international projects such as the Decade of Hydrology, and he took part in the Carpathian Co-operation. He attended many conferences and strongly influenced international co-operation in this field.

Ertel was editor of the journals Gerlands Beiträge zur Geophysik, Zeitschrift für Meteorologie, Forschungen und Fortschritte, and Deutsche Literaturzeitung, published with the co-operation of the German academies. He was in the editorial board of "Időjárás" and "Geofisica e applicata". He was also involved in the "Alexander-von Humboldt-Forschung" for which the DAW founded a special commission on his advice and published in 1959 a Humboldt memorial volume.

Ertel's later interests were partly determined by those of his institute, but he returned often to meteorological problems and worked on an extension of geophysically oriented hydrodynamics with its wide ranging applications.

Ertel considered his fields to be theoretical mechanics (thus Theoretical Mechanics was added in 1960 to the name of his university institute) and mathematical physics, and devoted himself to the task of elaborating the laws of physics in forms applicable to the Earth and Universe.

Ertel's vorticity theorems are formulated to be valid and directly applicable in all systems of reference and with many complementary conditions. They make it possible to discuss the dependence of the continuum on non-mechanical parameters, including thermodynamic parameters (such as temperature) and physical-chemical ones (such as air humidity). Thus, they enable us to deduce mathematically the excitation and annihilation of vortices. Ertel's theorems are, however, valid for all continua in which a vortex potential can be defined; thus they are also valid in magnetohydrodynamics.

The problem of the validity limits of the continuum physics and the possibility of deducing them from atomistics have been repeatedly discussed by Hans Ertel and H.-J. Treder. Ertel supposed that this problem would never be solved "in a final form". Ertel supposed a stochastic cause in atomistic variations as in the "macroscopically random" swinging over of unstable weather situations, and generally the basis of the "randomness" both in space and time of the transitions of unstable situations into stable ones.

In the 30's Ertel was known in certain circles as a cosmologist. His corresponding works were supported among others by von Laue, Einstein, and Schrödinger. Treder remarked to Ertel that all universe models, both Newtonian and Einsteinian ones together with their modifications, emerge from the fact that the Hamiltonian of the cosmos is constant. Ertel, as a potential theorist, suggested at once that this is identical with the statement that the average variations of the Newtonian gravity potential disappear in cosmic dimensions.

Selected works of Hans Ertel have recently been collected and published in a Volume of the Beitrage zur Geschichte der Geophysic und Kosmischen Physik Band VI, Heft 3, 2005, entitled Geophysical Fluid Dynamics (ed.: W. Schröder).

In the book many of Ertel's important results are contained, e.g., the Ertel-Cadez theorem for meteorology and hydrography, the Gauss-Argand diagram, the vorticity of streaming about hills, and many others.

Wilfried Schröder.
Geophysical Institute
D 28777 Bremen-Roennebeck
Germany

IDŐJÁRÁS

VOLUME 108 * 2004

BUDAPEST, HUNGARY

AUTHOR INDEX

TABLE OF CONTENTS

I. Papers

II. Book review

III. News

SUBJECT INDEX

GUIDE FOR AUTHORS OF *IDŐJÁRÁS*

The purpose of the journal is to publish papers in any field of meteorology and atmosphere related scientific areas. These may be

- research papers on new results of scientific investigations,
- critical review articles summarizing the current state of art of a certain topic,
- short contributions dealing with a particular question.

Some issues contain "News" and "Book review", therefore, such contributions are also welcome. The papers must be in American English and should be checked by a native speaker if necessary.

Authors are requested to send their manuscripts to

Editor-in Chief of IDŐJÁRÁS

P.O. Box 39, H-1675 Budapest, Hungary

in three identical printed copies including all illustrations. Papers will then be reviewed normally by two independent referees, who remain unidentified for the author(s). The Editor-in-Chief will inform the author(s) whether or not the paper is acceptable for publication, and what modifications, if any, are necessary.

Please, follow the order given below when typing manuscripts.

Title part: should consist of the title, the name(s) of the author(s), their affiliation(s) including full postal and E-mail address(es). In case of more than one author, the corresponding author must be identified.

Abstract: should contain the purpose, the applied data and methods as well as the basic conclusion(s) of the paper.

Key-words: must be included (from 5 to 10) to help to classify the topic.

Text: has to be typed in double spacing with wide margins on one side of an A4 size white paper. Use of S.I. units are expected, and the use of negative exponent is preferred to fractional sign. Mathematical formulae are expected to be as simple as possible and numbered in parentheses at the right margin.

All publications cited in the text should be presented in a *list of references*, arranged in alphabetical order. For an article: name(s) of author(s) in Italics, year, title of article, name of journal, volume, number (the latter two in Italics) and pages. E.g., *Nathan, K.K.,* 1986: A note on the relationship between photo-synthetically active radiation and cloud amount. *Időjárás 90,* 10-13. For a book: name(s) of author(s), year, title of the book (all in Italics except the year), publisher and place of publication. E.g., *Junge, C. E.,* 1963: *Air Chemistry and Radioactivity.* Academic Press, New York and London. Reference in the text should contain the name(s) of the author(s) in Italics and year of publication. E.g., in the case of one author: *Miller* (1989); in the case of two authors: *Gamov* and *Cleveland* (1973); and if there are more than two authors: *Smith et al.* (1990). If the name of the author cannot be fitted into the text: *(Miller,* 1989); etc. When referring papers published in the same year by the same author, letters a, b, c, etc. should follow the year of publication.

Tables should be marked by Arabic numbers and printed in separate sheets with their numbers and legends given below them. Avoid too lengthy or complicated tables, or tables duplicating results given in other form in the manuscript (e.g., graphs)

Figures should also be marked with Arabic numbers and printed in black and white in camera-ready form in separate sheets with their numbers and captions given below them. Good quality laser printings are preferred.

The text should be submitted both in manuscript and in electronic form, the latter on diskette or in E-mail. Use standard 3.5" MS-DOS formatted diskette or CD for this purpose. MS Word format is preferred.

Reprints: authors receive 30 reprints free of charge. Additional reprints may be ordered at the authors' expense when sending back the proofs to the Editorial Office.

More information for authors is available: antal.e@met.hu

Information on the last issues: http://omsz.met.hu/irodalom/firat_ido/ido_hu.html

Published by the Hungarian Meteorological Service

Budapest, Hungary

INDEX: 26 361

HU ISSN 0324-6329